

Design Study for Generating Sub-femtosecond to Femtosecond Electron Bunches for Advanced Accelerator Development at SINBAD

**Dissertation
zur Erlangung des Doktorgrades
an der Fakultät für Mathematik, Informatik und Naturwissenschaften
Fachbereich Physik
der Universität Hamburg**

vorgelegt von

Dipl.-Phys. Jun Zhu
aus Jingdezhen

Hamburg
2017

Gutachter der Dissertation Prof. Dr. Florian Grüner
Dr. Barbara Marchetti

Mitglieder der Prüfungskommission Prof. Dr. Daniela Pfannkuche
Prof. Dr. Florian Grüner
Dr. Barbara Marchetti
Prof. Dr. Wolfgang Hillert
Dr. Klaus Flöttmann

Datum der Disputation December 12, 2017

Abstract

The SINBAD (Short INnovative Bunches and Accelerators at DESY) project is a dedicated, long-term accelerator research and development (R&D) facility currently under construction at the DESY Hamburg campus, aiming to provide an infrastructure for developing several types of novel high-gradient accelerators. The research presented in this thesis addresses the design of the magnetic lattice as well as the modeling and simulations of ultra-short electron bunch generation at the ARES (Accelerator Research Experiment at SINBAD) linac, which is the core of the SINBAD facility. In order to meet the requirements of the high-gradient accelerators, the ARES linac was optimized to provide ~ 100 MeV, low charge (0.5 to 30 picocoulombs) and ultra-short electron bunches (sub-femtosecond to dozens of femtoseconds) with ultra-small spot sizes (less than a few micrometers) and excellent timing stability (rms bunch arrival-time jitter < 10 femtoseconds). As one of the research branches, the generation of a train of dozens-of-femtosecond-long electron bunches with terahertz repetition rate was experimentally investigated at the SPARC_LAB test facility. A novel method was proposed to simultaneously measure the relative misalignments of the individual electron bunches in both planes, which is beyond the reach of up-to-date beam position monitors.

Zusammenfassung

Das SINBAD (Short INnovative Bunches and Accelerators at DESY) Projekt ist eine dedizierte Einrichtung für langfristige Beschleunigerforschung und -entwicklung (Accelerator R&D). Sie wird derzeit mit dem Ziel Infrastruktur zur Entwicklung mehrerer neuartiger Hochgradientenbeschleuniger bereit zu stellen am DESY in Hamburg gebaut. Die in dieser Arbeit vorgestellten Untersuchungen befassen sich mit dem Entwurf des magnetischen Lattice, sowie der Modellierung und Simulation der Erzeugung von ultrakurzen Elektronenbunchen mit Hilfe des ARES (Accelerator Research Experiment at SINBAD) Linacs, welcher Kern der SINBAD Anlage ist. Um den Anforderungen der Hochgradientenbeschleuniger gerecht zu werden, wurde der ARES Linac optimiert, um ~ 100 MeV, niedrige Ladung (0,5 bis 30 Picocoulombs) und ultrakurze Elektronenbunche (Subfemtosekunden bis Dutzenden Femtosekunden) mit ultrakleine Punktgrößen (weniger als ein paar Mikrometer) und hervorragender Timing-Stabilität (RMS-Ankunftszeit-Jitter < 10 Femtosekunden) bereitstellen zu können. Als einer der Forschungszweige wurde in der SPARC_LAB-Testanlage die Erzeugung eines Zuges von 10 Femtosekunden langen Elektronenbunchen mit Terahertz-Wiederholungsrate experimentell untersucht. Hierbei wurde ein neuartiges Verfahren vorgeschlagen, um die relative Fehlausrichtungen einzelner Elektronenbunche gleichzeitig in beiden Ebenen messen zu können, was mit aktuellen Strahlpositionsmonitoren nicht ohne Weiteres möglich wäre.

Contents

ABSTRACT.....	III
ZUSAMMENFASSUNG.....	III
LIST OF FIGURES.....	IX
LIST OF TABLES.....	XV
INTRODUCTION.....	1
1 ELECTRON BUNCH COMPRESSION.....	5
1.1 ELECTRON BEAM PHYSICS.....	5
1.1.1 <i>Beam phase-space</i>	5
1.1.2 <i>Courant-Snyder (Twiss) parameters</i>	7
1.1.3 <i>Transfer matrix</i>	7
1.1.4 <i>Particles with momentum deviation</i>	9
1.1.5 <i>Paraxial envelope equation</i>	9
1.1.6 <i>Space-charge effects</i>	10
1.2 OVERVIEW OF BUNCH COMPRESSION TECHNIQUES.....	12
1.2.1 <i>Magnetic bunch compression</i>	12
1.2.2 <i>Velocity bunching and ballistic bunching</i>	21
1.2.3 <i>Other novel bunch compression schemes</i>	22
2 THE SINBAD FACILITY.....	25
2.1 ARES.....	26
2.1.1 <i>Photoinjector</i>	28
2.1.2 <i>Traveling-wave structure</i>	30
2.1.3 <i>RF station</i>	31
2.1.4 <i>Diagnostics</i>	31
2.2 NOVEL ACCELERATION TECHNIQUES.....	37
2.2.1 <i>Laser Wakefield Accelerators (LWFA)</i>	37
2.2.2 <i>Plasma Wakefield Accelerators (PWFA)</i>	43
2.2.3 <i>Dielectric Laser Accelerators (DLA)</i>	44
2.2.4 <i>Terahertz-driven accelerators</i>	45
2.2.5 <i>Summary of the major parameters of novel acceleration techniques at SINBAD</i>	46
3 SIMULATION CODES AND TOOLS.....	47
3.1 ACCELERATOR CODES.....	48
3.1.1 <i>ASTRA</i>	48
3.1.2 <i>IMPACT-T</i>	48

3.1.3	<i>CSRTrack</i>	49
3.1.4	<i>ELEGANT</i>	51
3.2	<i>LINACOPT</i>	51
3.2.1	<i>pyOpt</i>	51
3.2.2	<i>LinacOpt</i>	53
4	GENERATION OF SUB-FS ELECTRON BUNCH WITH SUB-10 FS BUNCH ARRIVAL-TIME JITTER	57
4.1	LAYOUT OF THE BEAMLINE	58
4.2	TRADE-OFF OF PARAMETERS	59
4.3	BEAM DYNAMIC SIMULATION	60
4.3.1	<i>ASTRA simulation - photoinjector</i>	60
4.3.2	<i>ELEGANT simulation – optics</i>	61
4.3.3	<i>IMPACT-T and CSRTrack simulations – bunch compression</i>	62
4.4	TRANSVERSE WAKEFIELDS AT THE SLIT	74
4.5	TIMING STABILITY	75
4.5.1	<i>Timing system for LWFA experiments</i>	75
4.5.2	<i>Analytical results</i>	77
4.5.3	<i>Start-to-end simulation of timing jitter</i>	80
4.6	SUMMARY.....	85
5.	LATTICE DESIGN OF THE ARES LINAC	87
5.1.	TECHNICAL DESIGN OF THE CHICANE BUNCH COMPRESSOR	87
5.1.1.	<i>Typical chicane designs for existing facilities</i>	87
5.1.2.	<i>Chicane overview</i>	88
5.1.3.	<i>Dipole magnets</i>	90
5.1.4.	<i>Power supply</i>	95
5.1.5.	<i>Slit collimator</i>	95
5.1.6.	<i>BPM</i>	100
5.1.7.	<i>Screen</i>	101
5.2.	MATCHING OF ELECTRON BUNCHES INTO A TINY STRUCTURE	101
5.2.1.	<i>Design consideration</i>	102
5.2.2.	<i>Influence of chromatic effect</i>	103
5.2.3.	<i>Influence of space-charge effects</i>	107
5.3.	DESIGN OF THE DOGLEG BEAMLINE.....	110
5.3.1.	<i>Isochronous beamline</i>	111
5.3.2.	<i>Hybrid compression</i>	114
5.4.	SUMMARY.....	115
6	MISALIGNMENT MEASUREMENT OF FEMTOSECOND ELECTRON BUNCHES WITH THZ	117
	REPETITION RATE	117
6.1	SPARC_LAB OVERVIEW.....	117
6.2	EXPERIMENTAL SETUP.....	118
6.3	THEORY OF MISALIGNMENT MEASUREMENT	119
6.4	SIMULATIONS	122
6.4.1	<i>Simulations without any jitter</i>	123

6.4.2	<i>Simulations with RFD jitter</i>	126
6.4.3	<i>Simulations with beam position and pointing jitter</i>	128
6.5	EXPERIMENTAL RESULTS.....	129
6.6	DISCUSSION.....	132
6.7	SUMMARY.....	133
7.	FINAL DESIGN WORKING POINTS OF THE ARES LINAC	135
7.1.	WORKING POINTS AT ARES LINAC	136
7.2.	APPLICATION IN LWFA DRIVEN FREE-ELECTRON LASER	141
7.2.1.	<i>Basic FEL theory</i>	141
7.2.2.	<i>Challenges in LWFAs</i>	144
7.2.3.	<i>More discussions on LWFA-driven FEL at ARES</i>	145
7.3.	SUMMARY.....	147
	SUMMARY	149
A	THIN LENS FOCUSING	151
A.1	EMITTANCE TERM	151
A.2	CHROMATIC ABERRATION	152
B	MISMATCH FACTOR	153
C	PARAMETERS USED IN THE FINAL WORKING POINTS	155
	BIBLIOGRAPHY	157
	ACKNOWLEDGEMENTS	167
	LIST OF PUBLICATIONS	169
	<i>Journal papers</i>	169
	<i>Conference papers</i>	170
	DECLARATION	171

List of figures

Figure 1.1: Emittance and beam envelope oscillation for a slightly mismatched beam, beginning with a minimum beam size and vanishing correlated emittance.....	12
Figure 1.2: Schematic of electron trajectories with different energies in a magnetic chicane bunch compressor.....	12
Figure 1.3: Illustration of a chicane bunch compressor.	14
Figure 1.4: Illustration of a two-dipole dogleg.....	15
Figure 1.5: Illustration of a chicane bunch compressor with a slit collimator.	17
Figure 1.6: Illustration of the geometry of the CSR effect.....	18
Figure 1.7: Shape of the CSR wakefield of a line charge with Gaussian density distribution. The bunch head is on the left.....	19
Figure 1.8: Illustration of an emittance exchange beamline.....	23
Figure 1.9: Sketch of the double emittance exchange beamline at Argonne National Laboratory.	24
Figure 2.1: Overview of the SINBAD facility.	26
Figure 2.2: Sketch of the ARES linac. The corrector magnets are not shown in the plot due to space constraint. Here BPM refers to beam position monitor, BAC refers to bunch arrival-time cavity and BCM refers to beam current monitor. The diagnostics in the dogleg beamline has not been determined yet.	27
Figure 2.3: Illustration of the photoinjector at ARES.	28
Figure 2.4: Normalized on-axis longitudinal electric field of the gun.	29
Figure 2.5: Normalized B_z of the combination of the “high-charge” and its bucking solenoids (left) and the “low-charge” solenoid (right). The excitation of the two “low-charge” solenoid coils can be controlled independently.	30
Figure 2.6: Cross-section of the 4.2-meter-long traveling-wave structure with four surrounding solenoids.....	31
Figure 2.7: Normalized longitudinal electric field of one regular cell plus the input and output coupling cells of the travelling-wave structure.	31
Figure 2.8: 3D model of the ARES RF gun area.....	32
Figure 2.9: Illustration of the principle of the slit-based emittance measurement method (left) and the TEM grid method (right).	35
Figure 2.10: Illustration of the principle of RFD operation.	36

Figure 2.11: Electron charge density distribution and electric field map for a typical LWFA (simulated by A. F. Pousa). Here $\omega_p = (4\pi n_0 e^2 / m_e)^{1/2}$ is the electron plasma frequency and n_0 is the ambient electron number density.....	38
Figure 2.12: The evolution of a Gaussian laser beam in vacuum.	39
Figure 2.13: Accelerating and focusing field maps in approximately one cycle after the ANGUS laser pulse simulated using OSIRIS (simulated by M. Weikum). The plasma density is 10^{17} cm^{-3} . The focusing field map is extracted at $x \approx 15 \text{ }\mu\text{m}$. An electron beam is placed inside the wakefield which is the reason for the small kink in the field structures at around $z = 1.845 \text{ mm}$	42
Figure 2.14: Illustration of a PWFA with one drive bunch and one witness bunch.....	43
Figure 2.15: Schematic layout of the AXSIS experiment.	45
Figure 3.1: Projected shapes of the sub-bunches in CSRTrack.....	50
Figure 3.2: Plot of the “eggholder” function.....	52
Figure 3.3: Class hierarchy for users in LinacOpt.....	55
Figure 4.1: Layout of the beamline used in the study in this chapter. The blue rectangles represent dipole magnets while the green diamonds are quadrupole magnets.....	58
Figure 4.2: Schematic of the magnetic chicane with a slit.....	59
Figure 4.3: Longitudinal phase-space of the 100-pC bunch at the linac exit.	61
Figure 4.4: Longitudinal phases-space of the 10-pC velocity-bunched beam at the linac exit. ..	61
Figure 4.5: Optics (left) and beta functions of the beam (right) from the exit of the linac to the end of the chicane for the 100-pC beam. The contribution from the dispersion is not subtracted from the horizontal beta function of the beam.	62
Figure 4.6: IMPACT-T and CSRTrack simulation results of the bunch duration and emittance growth of a 100-MeV, 5-pC bunch for different initial bunch durations after a 0.1-m-long drift space. The initial normalized emittance, rms energy spread, rms horizontal and vertical bunch size are $0.25 \text{ }\mu\text{m}$, 0.2%, $112 \text{ }\mu\text{m}$ and $112 \text{ }\mu\text{m}$ respectively. 50,000 macro particles were used. .	64
Figure 4.7: Same as Figure 4.6 but with a reduced initial vertical bunch size of $28 \text{ }\mu\text{m}$	65
Figure 4.8: Transverse phase-spaces of a 100-MeV, 1-fs and 5-pC bunch at the end of the 0.1-m-long drift simulated by using IMPACT-T.	65
Figure 4.9: Same as Figure 4.8 except that CSRTrack was used.....	65
Figure 4.10: Comparisons of the bunch durations, normalized emittances and energy losses simulated by IMPACT-T and CSRTrack. The full-width of the slit is 0.4 mm.	67
Figure 4.11: Final longitudinal phase-spaces for the 2.7-pC bunch without self-force (upper-left), simulated by IMPACT-T without CSR (upper-right), and with both space-charge and CSR effects (middle-left), as well as simulated by CSRTrack (middle-right), CSRTrack with $\sigma_{v,sub} = \sigma_v/5$ (lower-left) and $\sigma_{v,sub} = \sigma_v/20$ (lower-right).....	68
Figure 4.12: Evolutions of the bunch durations and energies in the last dipole magnet simulated by CSRTrack with different vertical sub-bunch sizes. The bunch charge is 2.7 pC.....	69
Figure 4.13: Final bunch duration and normalized horizontal emittance simulated by IMPACT-T and CSRTrack for different beam optics. The bunch charge is 2.7 pC.	70

Figure 4.14: Final longitudinal phase-spaces simulated by IMPACT-T (left column) and CSRTrack (right column). The final vertical bunch sizes are about 54 μm (upper row) and 21 μm (lower row). The bunch charge is 2.7 pC.....	71
Figure 4.15: Final longitudinal phase-spaces simulated by using IMPACT-T (left column) and CSRTrack (right column) for the hybrid compression scheme. The final bunch charge is 2.7 pC and the full-width of the slit is 0.3 mm. The final normalized horizontal emittances are about 0.19 μm and 0.21 μm , respectively.	72
Figure 4.16: Analytical results of the energy losses along the bunch in the first dipole magnet for a short bunch compared to the central slice of a long bunch. The steady state CSR model was assumed.....	72
Figure 4.17: Typical initial longitudinal phase space (left) and the bunch shape in the middle of the chicane (right) when only the central slice of the bunch was tracked.	73
Figure 4.18: Comparisons of the final rms bunch durations and horizontal emittances simulated by IMPACT-T and CSRTrack with different initial bunches.	73
Figure 4.19: Final longitudinal phase-spaces simulated by IMPACT-T (left) and CSRTrack (right) by tracking only the central slice of the bunch. The bunch charge is 2.7 pC.....	73
Figure 4.20: Sketch of a tapered slit collimator.	74
Figure 4.21: Timing structure diagram for the LWFA experiment at the ARES linac. Cathode laser and drive laser are independent.	76
Figure 4.22: Alternative timing structure diagram for the LWFA experiment at the ARES linac. Cathode laser and drive laser are the same.....	76
Figure 4.23: Illustration of dt_{slice} . The slice that passes through the slit usually is not the central slice of the incoming bunch.	79
Figure 4.24: Histograms of the timing jitters for different working points with the tolerance budgets given in Table 4.2. The plot with a gun charge jitter of 0.3% is shown for the 100-pC pure magnetic compression case.	82
Figure 4.25: Histograms of the final bunch length jitters for different working points with the tolerance budgets given in Table 4.2. The plot with a gun charge jitter of 0.3% is shown for the 100-pC pure magnetic compression working point.	83
Figure 4.26: Histograms of the final bunch charge jitters for different working points with the tolerance budgets given in Table 4.2. The plot with a gun charge jitter of 0.3% is shown for the 100-pC pure magnetic compression working point. It should be noted that significantly different initial bunch charge jitters were assumed for different working points.	84
Figure 4.27: Histograms of the final momentum jitters for different working points with the tolerance budgets given in Table 4.2. The plot with a gun charge jitter of 0.3% is shown for the 100-pC pure magnetic compression working point.	85
Figure 5.1: Schematic of the movable chicane layout. The central part of the chicane will be installed in a platform and be able to move horizontally.	90
Figure 5.2: Technical drawing of the FLASH TDB dipole magnet.	91
Figure 5.3: Curve path through an off-beamline (2 nd or 3 rd) dipole magnet.....	91
Figure 5.4: Influences of the field strength error to the emittances and bunch length.	94

Figure 5.5: Influences of field errors of different orders to the emittances and bunch length. ...	94
Figure 5.6: Influences of misalignments to the emittances and bunch length.....	95
Figure 5.7: Geometry of the slit collimator used in the shower simulation.	97
Figure 5.8: Beam transverse profile after passing through an ideal slit (left) and a 2-cm-thick copper slit (right).....	97
Figure 5.9: Longitudinal phase-spaces of the electrons immediately downstream of different slit collimators.....	98
Figure 5.10: Longitudinal phase-spaces of the compressed beam at the end of the chicane using a 1-cm-thick copper slit (left) and a 2-cm-thick copper slit (right).....	98
Figure 5.11: Comparison of the transverse and longitudinal phase-spaces of the compressed beam with an ideal slit collimator (upper row) and a 2-cm-long copper collimator (lower row).	99
Figure 5.12: Evolution of the beam charge along the beamline downstream of a 2-cm-thick copper collimator. A round beam pipe with a 5 cm aperture was assumed.	99
Figure 5.13: Longitudinal phase-spaces of a 200 MeV beam after passing through a 2 cm (left) and 3 cm (right) copper slit.	100
Figure 5.14: Cartoon of the main beamline from the entrance of the matching section to the focus (the entrance of the plasma).....	103
Figure 5.15: Illustration of the triplet optics.....	103
Figure 5.16: Transverse emittance growths at the focus for different beam momentums and rms momentum spreads. The PMQ triplet composed of three 20-mm-long PMQs with gradients of 250 T/m, 500 T/m and 500 T/m respectively. The matched beta functions are 1 mm in both planes. The incoming beta function ranges from 6 m to 22 m.	104
Figure 5.17: Same as Figure 5.16 but the distributions of the mismatch factors in both planes are shown.	104
Figure 5.18: Same as Figure 5.16 but the length of the PMQ is reduced to 10 mm. The incoming beta function ranges from 18 m to 77 m.	105
Figure 5.19: Same as Figure 5.18 but the distributions of the mismatch factors in both planes are shown.	106
Figure 5.20: Same as (5.16) but the gradients of the PMQ triplet are reduced to 70 T/m, 140 T/m and 140 T/m, respectively. Also, the matched beta functions in both planes are 10 mm. The incoming beta function ranges from 6 m to 25 m.	106
Figure 5.21: Same as Figure 5.20 but the distributions of the mismatch factors in both planes are shown.	107
Figure 5.22: Design optics for the 84 MeV bunch (left) and the 150 MeV bunch (right) with the Twiss parameters at the focus being $\beta_x = \beta_y = 1$ mm and $\alpha_x = \alpha_y = 0.0$. The PMQ triplet composed of three 2-cm-long PMQs with gradients of 250 T/m, 500 T/m and 500 T/m respectively.	108
Figure 5.23: Longitudinal and transverse phase-spaces at the exit of the chicane (left column) and at the focus (right column) for the 84 MeV electron bunch. The final bunch charge is ~ 2.9	

pC. The Twiss parameters at the focus are $\beta_x \approx 5.3$ mm, $\alpha_x \approx 2.2$, $\beta_y \approx 2.6$ mm and $\alpha_y \approx 0.8$	109
Figure 5.24: Longitudinal and transverse phase-spaces at the exit of the chicane (left column) and at the focus (right column) for the 150 MeV electron bunch. The final bunch charge is about 3.1 pC. The Twiss parameters at the focus are $\beta_x \approx 4.5$ mm, $\alpha_x \approx 2.1$, $\beta_y \approx 1.8$ mm and $\alpha_y \approx -0.4$	110
Figure 5.25: Cartoon of the beamline from the exit of the linac to the exit of the dogleg.	111
Figure 5.26: Design optics along the isochronous dogleg beamline.	112
Figure 5.27: Evolutions of the first and second order longitudinal dispersions along the isochronous dogleg beamline.	112
Figure 5.28: Longitudinal phase-spaces of a 10-pC bunch before (left) and after (right) the isochronous dogleg beamline.	112
Figure 5.29: Evolution of the bunch length of a 10-pC bunch along the isochronous dogleg beamline.	113
Figure 5.30: Longitudinal phase-spaces of a 0.5-pC bunch before (left) and after (right) the isochronous dogleg beamline.	113
Figure 5.31: Evolution of the bunch length of a 0.5-pC bunch along the isochronous dogleg beamline.	113
Figure 5.32: Design optics along the dogleg beamline with an overall R_{56} of -9 mm.	114
Figure 5.33: Evolutions of the first and second order longitudinal dispersions along the dogleg beamline with an overall R_{56} of -9 mm.	115
Figure 5.34: Longitudinal phase-space of a 10-pC bunch after the dogleg beamline with an overall R_{56} of -9 mm.	115
Figure 5.35: Evolution of the bunch length of a 10-pC bunch after the dogleg beamline with an overall R_{56} of -9 mm.	115
Figure 6.1: Layout of the SPARC_LAB facility. The gun (1) is followed by three travelling-wave structures (2), a THz station (3) and an RFD (4). Four beamlines follow the dipole (5): FEL (6a) both in SASE and with seed laser (6b), beam diagnostics based on THz radiation (7a) and electro-optic sampling (7b), plasma acceleration (8) and X-rays production by Thomson scattering (9) using the FLAME laser (10). Electro-optic sampling shares the laser from the photo-cathode (11) and is delivered by an optical line (12).	118
Figure 6.2: Non-scale layout of the SPARC_LAB diagnostic section beam line. The beam is coming from the left side.	119
Figure 6.3: Typical measured longitudinal phase-space of the train at Flag D1. The bunch head is on the left. D1, D2, D3, D4 are the four drive bunches while W refers to the witness bunch.	119
Figure 6.4: Typical fits for a single bunch in both planes without any jitter.	123
Figure 6.5: Comparisons between the input and simulated misalignments in both planes without any jitter. The bunch train head is on the left. The input $c_{y'}$ are also shown in the plot since they affect the accuracies of c_y	124

Figure 6.6: Comparison between the input and simulated misalignments in the vertical plane without any jitter. The input displacements are ten times as small as those in Figure 6.5. Q1 is used for scanning. The bunch train head is on the left.	125
Figure 6.7: Same as Figure 6.6 but Q3 is used for scanning.	125
Figure 6.8: Sensitivities of the measurement error to the energy used in the transfer matrix calculation. Left: Q1 is used for scanning; right: Q3 is used for scanning.	126
Figure 6.9: Errors of the simulated vertical displacements with 300 random RFD voltages (rms jitter 0.1%) and phases (rms jitter 0.1 degree), respectively. Q1 is used for scanning.	126
Figure 6.10: Fits in the vertical plane for the first (left) and the third (right) bunches in the train. Only the RFD voltage jitter is included. The data points without any jitter are also plotted together for comparison.	127
Figure 6.11: Same as Figure 6.10 except only the RFD phase jitter is included.	127
Figure 6.12: Residuals for the fits with only the RFD phase jitter. The residual is defined as the difference between the predicted value and the data.	127
Figure 6.13: Comparisons between the input and simulated misalignments in the vertical plane with both RFD phase and amplitude jitter included. Q1 is used for scanning.	128
Figure 6.14: Typical fittings in the horizontal plane with an initial rms position jitter of 10 μm and rms pointing jitter of 1 μrad	128
Figure 6.15: Images of the bunch train on the screen (Flag U3) during the quadrupole scan from the No. 170652 experiment.	129
Figure 6.16: Fits for each bunch in the train in the horizontal and vertical planes for the No. 170652 experiment.	130
Figure 6.17: Residuals for the fits in the vertical plane shown in Figure 6.16.	131
Figure 6.18: Measured misalignments of each bunch in the train for the No.170652, No.172023 and No.172659 experiments. The bunch train head is on the left.	132
Figure 7.1: Summary of the applications for the ARES linac.	135
Figure 7.2: Longitudinal and transverse phase-spaces at different locations for WP1.	139
Figure 7.3: Longitudinal and transverse phase-spaces at different locations for WP2.	139
Figure 7.4: Longitudinal and transverse phase-spaces at different locations for WP3. The energy spread increases dramatically during the long drift space from the linac exit to the chicane exit, which results in a huge chromatic aberration in the PMQ triplet. It again demonstrates that 100-MeV electron bunches cannot sustain peak currents higher than 1 kA for a long distance.	140
Figure 7.5: Longitudinal and transverse phase-spaces at different locations for WP4.	141
Figure 7.6: Illustration of the spontaneous emission from an electron and the FEL process in a planar undulator.	142
Figure A.1: Illustration of the change of focus resulting from the chromatic aberration.	151
Figure B.1: Area of Twiss parameters with a 1% mismatch for different definitions. The matched Twiss parameters are $\beta_m = 40$ mm and $\alpha_m = 1.6$	154

List of tables

Table 2.1: Summary of the novel accelerators considered at the SINBAD facility. For LWFA and PWFA, the values refer to externally injected witness beams.....	46
Table 4.1: Summary of bunch parameters at the exit of the linac.....	60
Table 4.2: Summary of jitter sensitivity and tolerance studies. The smaller the sensitivity value, the more sensitive the jitter source is. The total timing jitter was obtained from the randomized simulation results.	81
Table 5.1: Summary of the chicane designs in several facilities. B_{ij} indicates the location is between the i -th and j -th dipole magnets.....	88
Table 5.2: Pros and cons of different chicane technical design options.....	89
Table 5.3: Parameters of the dipole magnet, which is the same as the FLASH TDB.....	90
Table 5.4: Requirements of the dipole magnet good field region and the beam pipe aperture for a fixed chicane and a movable chicane. Here the maximum full-open-width of the slit is assumed to be 10 mm.	92
Table 5.5: Matched beta function for an externally injected 100-MeV electron bunch with a hard edge plasma driven by the ANGUS laser using the formulas in the linear and blow-out regimes. $k_p \xi = -\pi/6$ is used in the formula for the linear regime and $\xi = 0.8r_B$ is used in the formula for the blow-out regime. It should be noted that given these electron and laser parameters, the plasma acceleration should actually be in the transition regime between the linear and blow-out regimes.	101
Table 5.6: Beam parameters at the linac exit used for the final focus study. The 150 MeV electron bunch was obtained by using three travelling-wave structures.	107
Table 6.1: Summary of the input parameters for every bunch in the train used in the simulations. The parameters were chosen to be similar to the experimental working points. D1-D4 denote the drive bunches and W denotes the witness bunch. The centroid coordinates c_x are the values with respect to the accelerator axis, and t refers to the timing with respect to the zero crossing of the RFD.	122
Table 7.1: Summary of beam parameters at the linac exit for different working points.	136
Table 7.2: Summary of beam parameters at the chicane exit for different working points.	136
Table 7.3: Summary of beam parameters at the plasma entrance for different working points. The bunch tail containing 5% of the particles are not included in the calculation since the parameters of these particles largely deviate from the rest, and will most probably be lost during further acceleration and transportation. Slice properties were calculated for the slice centred at	

the current peak (WP1, WP3 and WP4) or the bunch centre if the longitudinal current profile has a plateau (WP2). The length of the slice is about 1/10 of the total bunch length.	136
Table 7.4: Summary of the discussed FEL parameters using the WP2 at ARES.....	147
Table 7.5: Summary of the discussed FEL parameters using the WP4 at ARES.....	147
Table C.1: Summary of parameters used in ASTRA simulations (linac part) for different working points.....	155
Table C.2: Summary of key parameters used in IMPACT-T simulations (lattice part) for different working points.....	155

Introduction

Particle accelerators have been one of the most important instruments for scientific research for the past few decades. Since the invention of particle accelerators, the need for higher beam energies in performing cutting-edge scientific experimentation has pushed the technical progress of accelerator technologies over time. However, conventional particle accelerators rely on the use of either radio-frequency (RF) or pulsed longitudinal electric fields inside a metal structure [Humphries99]. Because of the electrical breakdown of metals in the presence of high electric fields, conventional accelerators typically operate with accelerating gradients less than 50 MV/m, with the possibility to reach 100 MV/m with the state-of-art X-band technology [CLIC12]. Nowadays, even accelerators with modest particle energies (a few hundreds of MeV) are large and expensive facilities which usually can only be found in national laboratories. High energy accelerator facilities, e.g. hard X-ray Free-electron Lasers [LCLS02][EuXFEL06], the Large Hadron Collider [LHC], typically cost billions of dollars and occupy many kilometers of real estate, which are not affordable even for a country.

As a consequence, advanced acceleration concepts, e.g. LWFA (Laser-plasma Wakefield Acceleration) [Tajima79][Esarey09], PWFA (Plasma Wakefield Acceleration) [Blumenfeld07][Litos14] and DLA (Dielectric Laser Acceleration) [Peralta13][England14], sprang up to address these concerns and have made considerable progress during the past 15 years. Plasma-based accelerators (LWFA, PWFA) are of great interest because of their ability to sustain accelerating gradients three orders of magnitude higher than conventional accelerators. In 2014, the generation of 4.2-GeV, 6-pC electron bunches with preformed plasma channels in a 9-cm-long LWFA was achieved [Leemans14]. One year later, the electron bunch pointing fluctuation was reduced to 0.6 mrad rms, which allowed for consistent observation of electron bunches with FWHM divergence less than 1 mrad [Gonsalves15]. Accelerating wakefields in excess of 50 GV/m were achieved in an 85-cm-long PWFA using a 42 GeV drive electron bunch at the Stanford Linear Accelerator Center (SLAC) in 2007 [Blumenfeld07]. More recently, a variant of this scheme has been demonstrated to work for positrons as well [Corde15]. DLAs are complements to LWFAs and PWFAs rather than competitors. DLAs are driven by high-average-power μJ -class lasers and operate with temporally short (tens to hundreds of attoseconds) and low charge (fC) bunches at high repetition rates (10 to 100 MHz), while LWFAs are driven by high-peak-power terawatt or petawatt class lasers and

operate with high-charge (pC to nC) and longer (hundreds of attoseconds to a few tens of fs) bunches at low repetition rates (a few hertz) [England16]. The first demonstration of electron acceleration within an enclosed dielectric structure operating at optical wavelengths was reported in 2013 and accelerating gradients exceeding 300 MV/m were achieved in a fused silica structure at the laser wavelength of 800 nm [Peralta13].

A common feature of the advanced acceleration method is the tiny size of the accelerating structure/channel, in both transverse and longitudinal dimensions. In order to generate electron bunches suitable for user applications, it is required to match and align the externally injected electron bunch into the tiny accelerating structure/channel and, more specifically, its transverse focusing field. It is also required to minimize the phase spread and jitter of the very short accelerating period experienced by the electron bunch. These characteristics result in very stringent requirements on the transverse and longitudinal sizes as well as the timing and position stabilities of externally injected electron bunches. Moreover, applications such as FEL require electron bunches with peak currents on the order of kilo-Ampere (kA) and even higher, which makes it more challenging due to the space-charge effects at low beam energies (< 150 MeV), and the coherent synchrotron radiation (CSR) effect if a curved trajectory is involved in the beamline.

The SINBAD (Short **IN**novative **B**unches and **A**ccelerators at **DESY**) project [Dorda16] is a dedicated, long-term accelerator research and development (R&D) facility currently under construction at the DESY Hamburg campus. It is foreseen to have multiple independent experiments in ultra-fast science and high-gradient accelerators accessing a common infrastructure, e.g. LWFA, DLA, THz-driven dielectric acceleration [Nanni15] and so on. As one of the two experiments at the SINBAD facility, the ARES (Accelerator Research Experiment at SINBAD) linac [Marchetti16] was optimized to provide ~ 100 MeV, low charge (0.5 to 30 pC) and ultra-short electron bunches (sub-fs to dozens of fs) with ultra-small spot sizes (less than a few micrometers) and excellent timing stability (rms bunch arrival-time jitter < 10 fs) at 10 to 50 Hz repetition rates, suitable for external injection into the aforementioned R&D experiments.

The research presented in this thesis addresses the design of the magnetic lattice as well as the modeling and simulations of ultra-short electron bunch generation at the ARES linac. Two beamlines were considered during the design: the main beamline and the dogleg beamline. In the main beamline, a magnetic chicane bunch compressor with a slit collimator located between the 2nd and 3rd dipole magnets will allow to generate ultra-short (sub-fs to dozens of fs) bunches with peak currents of several kA. In particular, meticulous simulation studies have been performed in order to have an in-depth understanding of compressing electron bunches to sub-fs durations when the space-charge and CSR effects are both non-negligible. Moreover, the technical design of the chicane bunch compressor has also been studied. With a permanent magnet

quadrupole (PMQ) triplet located immediately downstream of the chicane, focusing of the compressed bunches to ultra-small beta functions (a few mm) can be achieved numerically, which makes it possible to have a matched bunch for high-gradient accelerating structures, e.g. plasma channels. The dogleg beamline was designed to have a tunable R_{56} between -10 mm to 10 mm, which allows flexible control of the bunch compression at the second beamline. With the above design, several compression techniques, i.e. velocity bunching, magnetic compression and the combination of them (hybrid compression), are able to be investigated at the ARES linac. It is foreseen to push these techniques to their limits in the direction of producing ultra-short, high-brightness electron bunches.

An objective-oriented Python application programming interface (API) has been developed to optimize the beam dynamics using the existing well-benchmarked accelerator codes. Both local search and global optimization algorithms have been implemented. This API facilitated the repeated iterations during the ARES linac beamline design, and will also benefit setting up different experiments in the future.

As a possible research interest at the ARES linac in the future, the generation of a train of dozens-of-femtosecond-long bunches with THz repetition rate was experimentally investigated at the SPARC_LAB test facility [Ferrario13]. A novel method was proposed to simultaneously measure the relative misalignments of the individual electron bunches in a train in both planes by applying a single quadrupole scan together with a radio-frequency deflector (RFD), which is crucial for the control of the alignments of individual bunches in the train.

This thesis is organized as follows. In Chapter 1, the principles of electron beam physics are introduced and the different bunch compression techniques are comprehensively reviewed. Chapter 2 presents an overview of the SINBAD facility – the ARES linac and examples of novel acceleration techniques for possible future experiments. In Chapter 3, different accelerator codes used in the simulations are summarized and the Python optimization API is introduced. Chapter 4 presents the detailed analytical and start-to-end simulation studies of generating ~100 MeV electron bunches with sub-fs bunch durations and sub-10-fs bunch arrival-time jitter via bunch slicing in a magnetic chicane bunch compressor. In Chapter 5, various considerations in the technical design of the chicane bunch compressor, matching different electron bunches down to extremely small beta functions as well as the physical design of the dogleg beamline are presented. The experimental study of misalignment measurement of a train of dozens-of-femtosecond-long bunches with THz repetition rate is presented in Chapter 6. Chapter 7 summarizes the final design of the ARES linac with several typical working points and their foreseen applications. Following the summary, the appendix includes the derivation of the thin lens focusing, a discussion on the mismatch factor as well as a list of parameters used in the simulations of several optimized working points.

1 Electron bunch compression

Novel accelerators and linac-based light sources require very short electron bunches (down to attosecond) with peak currents up to the order of ten kilo-Amperes. This kind of bunch cannot be produced directly in the electron source because of the strong space-charge effects. Therefore, it is preferred to first generate bunches with low peak currents in the gun and then accelerate them to higher energies where the space charge forces are weakened sufficiently. Afterwards these bunches can be manipulated to shorten the bunch length and increase the peak current.

In this chapter, the basics of the accelerator beam physics are shortly reviewed first, including emittance, Courant-Snyder (Twiss) parameters, transfer matrix, dispersion function, paraxial envelope equation and space-charge effects. Afterwards, a comprehensive overview of different compression schemes and their limits are presented.

1.1 Electron beam physics

1.1.1 Beam phase-space

In accelerator physics, the coordinates of an electron in 6D phase space are usually denoted as $\mathbf{X} = [x, x', y, y', z, \delta]^T$. Here x and y are the horizontal and vertical distances from the reference trajectory (design orbit) s , $x' = p_x/p_z$ and $y' = p_y/p_z$ are horizontal and vertical divergences with p_x , p_y and p_z being the particle momentums at each coordinate, z denotes the longitudinal distance (along the reference trajectory) from the center of the beam, and $\delta = \Delta p/p$ denotes the relative momentum spread with p_0 being the reference momentum and $\Delta p = p - p_0$. Based on the above definition, the covariance beam matrix within the six-dimensional phase-space is given by

$$\mathbf{\Sigma} = \begin{bmatrix} \mathbf{\Sigma}_{XX} & \mathbf{\Sigma}_{XY} & \mathbf{\Sigma}_{XZ} \\ \mathbf{\Sigma}_{YX} & \mathbf{\Sigma}_{YY} & \mathbf{\Sigma}_{YZ} \\ \mathbf{\Sigma}_{ZX} & \mathbf{\Sigma}_{ZY} & \mathbf{\Sigma}_{ZZ} \end{bmatrix} = \begin{bmatrix} \langle x^2 \rangle & \langle xx' \rangle & \langle xy \rangle & \langle xy' \rangle & \langle xz \rangle & \langle x\delta \rangle \\ \langle x'x \rangle & \langle x'^2 \rangle & \langle x'y \rangle & \langle x'y' \rangle & \langle x'z \rangle & \langle x'\delta \rangle \\ \langle yx \rangle & \langle yx' \rangle & \langle y^2 \rangle & \langle yy' \rangle & \langle yz \rangle & \langle y\delta \rangle \\ \langle y'x \rangle & \langle y'x' \rangle & \langle y'y \rangle & \langle y'^2 \rangle & \langle y'z \rangle & \langle y'\delta \rangle \\ \langle zx \rangle & \langle zx' \rangle & \langle zy \rangle & \langle zy' \rangle & \langle z^2 \rangle & \langle z\delta \rangle \\ \langle \delta x \rangle & \langle \delta x' \rangle & \langle \delta y \rangle & \langle \delta y' \rangle & \langle \delta z \rangle & \langle \delta^2 \rangle \end{bmatrix} \quad (1.1)$$

with $\mathbf{\Sigma}_{XX}, \dots, \mathbf{\Sigma}_{ZZ}$ being the 2×2 covariance matrices. The rms quantities of a beam are denoted as

$$\sigma_x = \sqrt{\langle x^2 \rangle}, \sigma_y = \sqrt{\langle y^2 \rangle}, \sigma_z = \sqrt{\langle z^2 \rangle}, \sigma_\delta = \sqrt{\langle \delta^2 \rangle}. \quad (1.2)$$

One of the most important properties of the beam is called emittance, which describes the average spread of electrons in the position-momentum phase-space. The so-called trace-space emittance is defined as:

$$\varepsilon_{tr} = \sqrt{\langle x^2 \rangle \langle x'^2 \rangle - \langle xx' \rangle^2}. \quad (1.3)$$

Since the trace-space emittance decreases as the momentum increases (adiabatic damping), the normalized emittance is usually considered

$$\varepsilon_{n,tr} = \beta\gamma\varepsilon_{tr}, \quad (1.4)$$

where β is the average speed relative to the speed of light c and γ is the average Lorentz factor.

In contrast to the normalized trace-space emittance, the normalized rms emittance is defined as

$$\varepsilon_{n,rms} = \frac{1}{m_e c} \sqrt{\langle x^2 \rangle \langle p_x^2 \rangle - \langle xp_x \rangle^2} \quad (1.5)$$

with m_e being the electron mass. The counterpart of the trace-space emittance is the geometric emittance, which is given by

$$\varepsilon_{rms} = \frac{\varepsilon_{n,rms}}{\beta\gamma}. \quad (1.6)$$

The difference between the trace-space emittance and geometric emittance is negligible unless both the divergence and the energy spread of the beam are striking [Floettmann03]. For beams with these extreme parameters, the emittance definitions given by equation (1.5) and (1.6) should be used. In this thesis, the output emittances from beam dynamics simulations always refer to the *normalized rms emittance* unless specified otherwise.

According to Liouville's theorem, the density in phase-space of non-interacting particles in a conservative or Hamiltonian system, measured along the trajectory of a particle is invariant. It implies that the phase-space volume of a beam with n particles is conserved in the 6-D phase-space if only conservative forces are present:

$$\int n dx dy dz dp_x dp_y dp_z = const. \quad (1.7)$$

Liouville's theorem is also valid in any sub-space (x - p_x , y - p_y or z - p_z) of the six-dimensional phase-space if it is uncoupled with the others. This ensures that the emittance in equation (1.5) is a conserved value [Reiser08].

1.1.2 Courant-Snyder (Twiss) parameters

The paraxial (linear) motion of a charged particle in a periodic system is described by the Hill's equation

$$x'' + K(s)x = 0, \quad (1.8)$$

where $K(s)$ is the periodic focusing function. It is interesting to have a solution to equation (1.8) as a harmonic oscillator [Wangler08]

$$x(s) = A\sqrt{\beta(s)} \cos(\phi(s) + \phi_0), \quad (1.9)$$

where $\beta(s)$ and $\phi(s)$ are amplitude and phase functions respectively, and A and ϕ_0 are constants determined by the initial condition. The functions $\beta(s)$ and $\phi(s)$ are related by

$$\phi(s) = \int \frac{ds}{\beta(s)}. \quad (1.10)$$

It is customary to define other two functions as

$$\alpha(s) = -\frac{1}{2} \frac{d\beta(s)}{ds}, \quad \gamma(s) = \frac{1 + \alpha(s)^2}{\beta(s)}. \quad (1.11)$$

The quantities $\alpha(s)$, $\beta(s)$ and $\gamma(s)$ are called either Courant-Snyder or Twiss parameters. The coordinates x and x' satisfy the equation

$$\gamma(s)x^2 + 2\alpha(s)xx' + \beta(s)x'^2 = A^2, \quad (1.12)$$

which is the general equation of an ellipse with area πA^2 centered at the origin of the x - x' phase-space. Equation (1.12) only describes the trajectory of a single particle in the phase-space. By choosing the amplitude of the oscillation $A\sqrt{\beta(s)} = \sigma_x$ and defining $A^2 = \varepsilon_{tr}$, equation (1.12) can be extended to describe the collective behavior of the particles in a beam, which gives

$$\gamma_x x^2 + 2\alpha_x x x' + \beta_x x'^2 = \varepsilon_{tr} \quad (1.13)$$

with the corresponding Twiss parameters given by

$$\beta_x = \frac{\langle x^2 \rangle}{\varepsilon_{tr}}, \quad \gamma_x = \frac{\langle x'^2 \rangle}{\varepsilon_{tr}}, \quad \alpha_x = -\frac{\langle x x' \rangle}{\varepsilon_{tr}}. \quad (1.14)$$

Although the standard reference of the above theory deals with circular accelerators [Courant58], the method and results apply equally to beam transport systems in linear accelerators.

1.1.3 Transfer matrix

Equation (1.8) also has the solution related to an initial location $[x_i, x'_i]$ and a final location $[x_f, x'_f]$ in the matrix form, which is given by [Brown84]

$$\begin{aligned} \begin{bmatrix} x_f \\ x'_f \end{bmatrix} &= \begin{bmatrix} C(s) & S(s) \\ C'(s) & S'(s) \end{bmatrix} \begin{bmatrix} x_i \\ x'_i \end{bmatrix} \\ &= \begin{bmatrix} \frac{\beta_{x_f}}{\beta_{x_i}} (\cos\mu + \alpha_{x_i} \sin\mu) & \sqrt{\beta_{x_f} \beta_{x_i}} \sin\mu \\ -\frac{(1 + \alpha_{x_i} \alpha_{x_f}) \sin\mu + (\alpha_{x_f} - \alpha_{x_i}) \cos\mu}{\sqrt{\beta_{x_f} \beta_{x_i}}} & \frac{\beta_{x_i}}{\beta_{x_f}} (\cos\mu - \alpha_{x_f} \sin\mu) \end{bmatrix} \begin{bmatrix} x_i \\ x'_i \end{bmatrix}, \end{aligned} \quad (1.15)$$

where $\mu = \Delta\phi$ is the phase advance between them. The 2×2 matrix is called a transfer matrix.

The transfer matrix can be extended to the 6-D phase-space, where it is denoted as

$$\mathbf{R} = \begin{bmatrix} R_{11} & R_{12} & R_{13} & R_{14} & R_{15} & R_{16} \\ R_{21} & R_{22} & R_{23} & R_{24} & R_{25} & R_{26} \\ R_{31} & R_{32} & R_{33} & R_{34} & R_{35} & R_{36} \\ R_{41} & R_{42} & R_{43} & R_{44} & R_{45} & R_{46} \\ R_{51} & R_{52} & R_{53} & R_{54} & R_{55} & R_{56} \\ R_{61} & R_{62} & R_{63} & R_{64} & R_{65} & R_{66} \end{bmatrix}. \quad (1.16)$$

The transformation between the initial and final coordinates of a single particle and the covariance matrix of a beam are given by

$$\mathbf{X}_f = \mathbf{R}\mathbf{X}_i \quad (1.17)$$

and

$$\mathbf{\Sigma}_f = \mathbf{R}\mathbf{\Sigma}_i\mathbf{R}^T, \quad (1.18)$$

respectively. The Twiss parameters at two locations can also be related by the elements of the transfer matrix, which gives

$$\begin{bmatrix} \beta_f \\ \alpha_f \\ \gamma_f \end{bmatrix} = \begin{bmatrix} R_{11}^2 & -2R_{11}R_{12} & R_{12}^2 \\ -R_{11}R_{21} & R_{11}R_{22} + R_{12}R_{21} & -R_{12}R_{22} \\ R_{21}^2 & -2R_{21}R_{22} & R_{22}^2 \end{bmatrix} \begin{bmatrix} \beta_i \\ \alpha_i \\ \gamma_i \end{bmatrix}. \quad (1.19)$$

By further denoting the second and third order matrix elements as T_{ijk} and U_{ijkl} , respectively, the relationship between the final phase-space coordinate X_i and the initial phase-space coordinates $\mathbf{X}(0)$ can be extended to

$$\begin{aligned}
X_i = & \sum_{j=1}^6 R_{ij} X_j(0) + \sum_{j=1}^6 \sum_{k=j}^6 T_{ijk} X_j(0) X_k(0) \\
& + \sum_{j=1}^6 \sum_{k=j}^6 \sum_{l=k}^6 U_{ijkl} X_j(0) X_k(0) X_l(0).
\end{aligned} \tag{1.20}$$

1.1.4 Particles with momentum deviation

For a particle with a small momentum deviation δ , equation (1.8) becomes

$$x'' + K(s)x = \frac{\delta}{\rho(s)}, \tag{1.21}$$

where $\rho(s)$ is the radius of the reference orbit. The general solution of equation (1.21) is the sum of the complete solution of the homogeneous equation (1.8) and a particular solution of the above inhomogeneous equation. In the matrix form, it is given by

$$\begin{bmatrix} x_f \\ x'_f \\ \delta \end{bmatrix} = \begin{bmatrix} C(s) & S(s) & \eta(s) \\ C'(s) & S'(s) & \eta'(s) \\ 0 & 0 & 1 \end{bmatrix} \begin{bmatrix} x_i \\ x'_i \\ \delta \end{bmatrix}, \tag{1.22}$$

where $\eta(s)$ and $\eta'(s)$ are the dispersion function and its derivative, respectively. It is obvious that $\eta(s)$ should be a particular solution of the following equation

$$\eta''(s) + K(s)\eta(s) = \frac{1}{\rho(s)}. \tag{1.23}$$

The above equation can be solved by using the Green's function [Brown84] and the dispersion function is given by

$$\eta(s) = S(s) \int_{s_0}^s \frac{C(\tau)}{\rho(\tau)} d\tau - C(s) \int_{s_0}^s \frac{S(\tau)}{\rho(\tau)} d\tau. \tag{1.24}$$

Moreover, the first-order path length change introduced by the momentum deviation δ can also be related to the dispersion function by

$$\Delta s = \int_{s_0}^s \frac{\Delta x(\tau)}{\rho(\tau)} d\tau = \int_{s_0}^s \frac{\eta(\tau)}{\rho(\tau)} \delta d\tau = R_{56} \delta. \tag{1.25}$$

1.1.5 Paraxial envelope equation

In a cylindrical symmetric system, the motion of a paraxial beam ($v_z \approx v$) is governed by the paraxial envelope equation, which describes the evolution of a beam with rms transverse radius $\sigma_r(s)$ and current I under the effect of an external linear focusing channel of strength $K_r(s)$ by [Serafini97]

$$\sigma_r''(s) + \sigma_r'(s) \frac{\gamma'}{\beta^2 \gamma} + K_r(s) \sigma_r(s) - \frac{I}{2I_A \beta^3 \gamma^3 \sigma_r(s)} - \frac{\varepsilon_{n,tr}^2}{\beta^2 \gamma^2 \sigma_r^3(s)} = 0, \quad (1.26)$$

where $I_A = ec/r_e \approx 17$ kA with r_e being the classical electron radius and the emittance in the case of cylindrical symmetry is defined as

$$\varepsilon_{n,tr} = \frac{\beta \gamma}{2} \sqrt{\langle r^2 \rangle \langle r'^2 \rangle - \langle r r' \rangle^2} \quad (1.27)$$

with r being the radial coordinate of the electron. For a so-called space-charge-dominated beam, the fourth term on the left hand side of equation (1.26) is much larger than the fifth one. While for a so-called emittance dominated beam, the fifth term is much larger than the fourth one.

A constant focusing channel is a good starting point to study the intrinsic beam physics in many cases. In the case of a constant focusing channel and beam current profile, there is a special solution (equilibrium radius) for equation (1.26) where $\sigma_r(s) = \sigma_{r,eq} = \text{const}$, $\sigma_r'(s) = 0$ and $\sigma_r''(s) = 0$, and hence the beam envelope is a straight line. This special case is known as the *matched beam*, with the radius being the solution of

$$K_r \sigma_{r,eq} - \frac{I}{2I_A \beta^3 \gamma^3 \sigma_{r,eq}} - \frac{\varepsilon_{n,tr}^2}{\beta^2 \gamma^2 \sigma_{r,eq}^3} = 0. \quad (1.28)$$

1.1.6 Space-charge effects

The fourth term on the left hand side of equation (1.26) is introduced because of the space-charge effects. With increasing beam intensity the interaction between the charged beam particles becomes more important. The charges produce mutually repulsive electric fields that act in opposition to the focusing forces, and also magnetic fields that produce attractive forces. The magnetic forces are smaller than the electric forces, and are unimportant except for relativistic particles. Considering a continuous beam of cylindrical symmetric distribution with charge density $\rho(r)$ that moves at a constant velocity βc , the radial force on an electron at radius r produced by the rest of the bunch charge is given by [Wangler08]

$$F_r(r) = \frac{e}{\gamma^2 \varepsilon_0 r} \int_0^r \rho(r) r dr, \quad (1.29)$$

where ε_0 is the permittivity in free space. Therefore, the space-charge effects mitigate quickly as the beam energy increases.

The space-charge forces are given by the composition of linear and nonlinear functions of the displacement from the centroid. Assuming the space-charge increases the divergence by $\Delta x' = Ax^n$, equation (1.3) becomes

$$\varepsilon_{tr} = \sqrt{(\langle x^2 \rangle \langle x'^2 \rangle - \langle x x' \rangle^2) + A^2 (\langle x^2 \rangle \langle x^{2n} \rangle - \langle x^{1+n} \rangle^2)}, \quad (1.30)$$

where A and n both are constants. Obviously, the linear space-charge force component ($n = 1$) only defocuses the beam but conserves emittance (the second term on the right hand side of equation (1.3) vanishes). The nonlinear space-charge force components ($n \neq 1$), however, increase the effective emittance by distorting the phase-space distribution.

Space-charge effects can also cause misalignment of longitudinal slices of a bunch in the transverse phase-space, which will result in project emittance growth or oscillation. Considering a space-charge-dominated beam in a constant focusing channel without acceleration, equation (1.26) can be reduced to

$$\sigma_r''(z, s) + K_r \sigma_r(z, s) - \frac{I(z)}{2I_A \beta^3 \gamma^3 \sigma_r(z, s)} \approx 0. \quad (1.31)$$

Here the z coordinate is included since different slices of a bunched beam normally have different currents and radius. The equilibrium radius for a slice at location z is thus given by

$$\sigma_{r,eq} = \sqrt{\frac{I(z)}{2I_A \beta^3 \gamma^3 K_r}}. \quad (1.32)$$

The projected emittance growth can be examined by considering a small perturbation of the equilibrium radius $\delta\sigma_r(z, s)$ in each slice

$$\sigma_r(z, s) = \sigma_{r,eq} + \delta\sigma_r(z, s). \quad (1.33)$$

Inserting equation (1.33) into (1.31) and keeping only the first order term of the small perturbation, we have

$$\delta\sigma_r''(z, s) + 2K_r \delta\sigma_r(z, s) \approx 0. \quad (1.34)$$

The above equation indicates that the oscillation frequency of the small perturbation in each slice is only dependent on the external focusing strength. Assuming all the slices initially have the same size $\sigma_{r,0}$, the projected emittance of the bunch can be derived as [Serafini97]

$$\varepsilon_{tr} \cong \frac{1}{2} \sqrt{K_r} \sigma_{r,0} \sigma_{r,eq} (I_{peak}) \frac{\sigma_I}{I_{peak}} |\sin(\sqrt{2K_r} s)|, \quad (1.35)$$

where I_{peak} is the peak current of the whole bunch and σ_I is the rms current over all the slices. The beam emittance and envelope oscillations for a slightly mismatched beam are shown in Figure 1.1. We observe two subsequent local minima for the emittance after the starting point in one cycle. One is reached when the beam size is at its maximum and the other is reached when the beam size returns to its original size. The emittance oscillation is the basis for the emittance compensation in a photoinjector,

which will be introduced in the next chapter. A more complicated model which takes both the space-charge and emittance terms into account can be found in [Floettmann17].

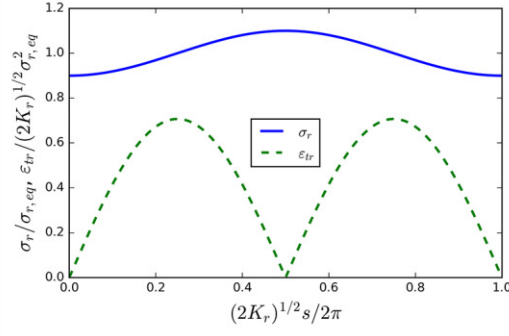


Figure 1.1: Emittance and beam envelope oscillation for a slightly mismatched beam, beginning with a minimum beam size and vanishing correlated emittance.

1.2 Overview of bunch compression techniques

To compress a bunch longitudinally, the time of flight through a certain beamline must be shorter for the tail of the bunch than it is for the head. The usual technique is to send a bunch with energy chirp imprinted by the accelerating field through a beamline with longitudinal dispersion.

1.2.1 Magnetic bunch compression

Figure 1.2 illustrates the principle of the magnetic bunch compression. An energy chirp of the bunch, a linear correlation between the energy and longitudinal position, is introduced before the bunch compressor by off-crest acceleration. The path length difference between the reference particle and the particle with relative energy error δ can be written as

$$\Delta s = R_{56}\delta + T_{566}\delta^2 + U_{5666}\delta^3 + o(\delta^4), \quad (1.36)$$

where R_{56} , T_{566} and U_{5666} are the coefficients of the Taylor expansion.

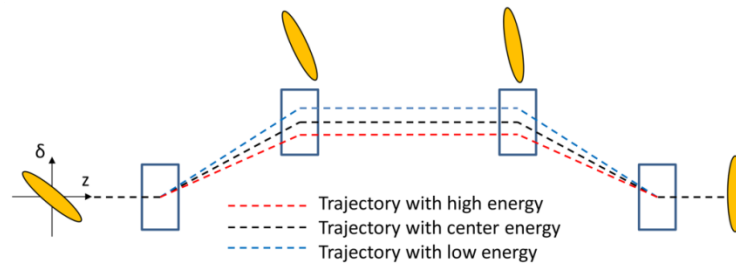


Figure 1.2: Schematic of electron trajectories with different energies in a magnetic chicane bunch compressor.

To first order, the longitudinal coordinate of an electron bunch after a dispersion section is given by

$$z_f = z + \Delta s = R_{56}\delta_u + (1 + R_{56}h)z, \quad (1.37)$$

where δ_u is the uncorrelated energy spread, $h = \langle \delta z \rangle / \langle z^2 \rangle$ is the bunch chirp. The final rms bunch length is thus

$$\sigma_{z_f} \approx \sqrt{R_{56}^2 \sigma_{\delta_u}^2 + (1 + R_{56}h)^2 \sigma_z^2}. \quad (1.38)$$

Under the condition of full compression ($1 + R_{56}h = 0$), the bunch length is minimized to

$$\sigma_{z_f, \min} \approx |R_{56}| \sigma_{\delta_u}. \quad (1.39)$$

In real world, the high-order terms of both the magnetic compressor and the longitudinal phase-space of the bunch dominate the final bunch length if the compression factor is high. The incoming longitudinal phase-space of an electron bunch can be expressed as

$$\delta = \delta_u + h_1 z + h_2 z^2 + h_3 z^3 + h_4 z^4 + o(z^5), \quad (1.40)$$

where h_i ($i=1\sim 4$) are the coefficients of the Taylor expansion. Utilizing equation (1.36) and (1.40) and ignoring most of the terms with δ_u (very small quantities), the final longitudinal position of the electron with respect to the bunch center is given by

$$\begin{aligned} z_f \approx & R_{56}\delta_u + (1 + R_{56}h_1)z + (R_{56}h_2 + T_{566}h_1^2)z^2 + \\ & (R_{56}h_3 + 2T_{566}h_1h_2 + U_{5666}h_1^3)z^3 + \\ & [R_{56}h_4 + T_{566}(2h_1h_3 + h_2^2) + 3U_{5666}h_1^2h_2]z^4. \end{aligned} \quad (1.41)$$

The second and third order terms in equation (1.41) can be eliminated by finely tuning the phase and amplitude of a high-order harmonic cavity [Floettmann01], which is usually located immediately upstream of the bunch compressor, to meet

$$h_2 = -\frac{T_{566}h_1^2}{R_{56}} \quad (1.42)$$

and

$$h_3 = \frac{h_1^3}{R_{56}} \left(\frac{2T_{566}^2}{R_{56}} - U_{5666} \right). \quad (1.43)$$

However, the 4th-order term in equation (1.41) will still dominate the final bunch length if the compression factor is high, e.g. 1000 for compressing a bunch from 1 ps to 1 fs. Therefore, multiple compression stages are generally required in a FEL facility.

Chicane bunch compressor

Chicane bunch compressors are the most widely used magnetic bunch compressor in modern electron linacs. A typical chicane bunch compressor is illustrated in Figure 1.3.

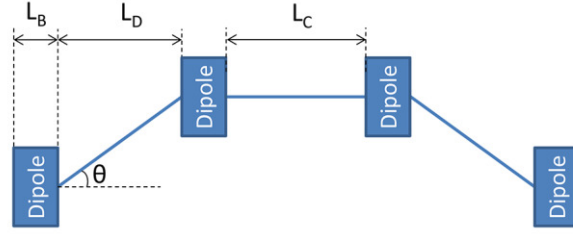


Figure 1.3: Illustration of a chicane bunch compressor.

The path length of an electron passing through a chicane is

$$s = 2L_D \frac{1}{\cos \theta} + 4L_B \frac{\theta}{\sin \theta} + L_C. \quad (1.44)$$

When $\theta \ll 1$, the path length difference between the chicane and the straight path is given by

$$\Delta s \approx \theta^2 \left(L_D + \frac{2}{3} L_B \right), \quad (1.45)$$

where the relationships

$$\frac{1}{\cos \theta} = 1 + \frac{1}{2} \theta^2 + o(\theta^4) \quad (1.46)$$

and

$$\frac{\theta}{\sin \theta} = 1 + \frac{1}{6} \theta^2 + o(\theta^4) \quad (1.47)$$

have been used. For an electron with a small momentum deviation δ , equation (1.45) becomes

$$\Delta s \approx \theta^2 (1 - 2\delta + 3\delta^2 - 4\delta^3) \left(L_D + \frac{2}{3} L_B \right). \quad (1.48)$$

By comparing the above equation and equation (1.36), one gets

$$R_{56} = -2\theta^2 \left(L_D + \frac{2}{3} L_B \right), \quad (1.49)$$

$$T_{566} \approx -\frac{3}{2} R_{56} \quad (1.50)$$

and

$$U_{5666} \approx 2R_{56}. \quad (1.51)$$

In addition to the standard four-dipole chicane, some other derivative designs exist. An S-chicane [Vogt13] offers potential compensation of projected emittance growth induced by the CSR effect. Quadrupoles inserted in between the dipoles can be used to adjust the longitudinal dispersion R_{56} . However, misalignments of these quadrupoles can cause tremendous emittance growth [Sun11].

Dogleg bunch compressor

A dogleg is usually used to shift the beam to another parallel beamline. Unlike the chicane, the transverse dispersion does not disappear naturally after a dogleg. Therefore, quadrupole magnets are required to close the dispersion and control the Twiss parameters.

Two-dipole dogleg

The simplest two-dipole dogleg consisting of two identical dipole magnets and three quadrupole magnets is shown in Figure 1.4.

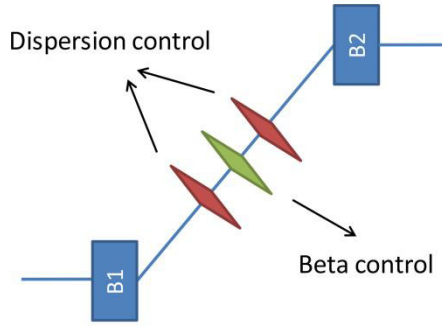


Figure 1.4: Illustration of a two-dipole dogleg.

The R_{56} of the two-dipole dogleg is given by

$$R_{56} = \int \frac{\eta(s)}{\rho(s)} ds = \frac{1}{\rho} \left(\int_{B1} \eta(s) ds + \int_{B2} \eta(s) ds \right). \quad (1.52)$$

Suppose η_B and η'_B are the dispersion and its derivative respectively at the entrance of the second dipole magnet, the dispersion and its derivative immediately downstream the second dipole magnet are given by

$$\eta_f = \eta_B / \cos \theta + \eta'_B \rho \sin \theta - \rho(1 - \cos \theta) \quad (1.53)$$

and

$$\eta'_f = \eta'_B \cos \theta - \sin \theta \quad (1.54)$$

respectively. Since the dispersion and its derivative are required to vanish downstream the dogleg, it gives

$$\eta_B = \rho(\cos \theta - 1) = -\eta_A \quad (1.55)$$

and

$$\eta'_B = \tan \theta = -\eta'_A, \quad (1.56)$$

where η_A and η'_A are the dispersion and its derivative respectively at the exit of the first dipole magnet. Therefore, the quadrupoles in between the two dipole magnets are supposed to flip the signs of the dispersion and its derivative. Accordingly, equation (1.52) can be written as

$$R_{56} = 2\rho \int_0^\theta (1 - \cos \mu) d\mu = 2\rho(\theta - \sin \theta) \approx L_B \theta^2 / 3. \quad (1.57)$$

It should be noted that the R_{56} in a drift space must also be included when the beam energy is low. A main disadvantage of the two-dipole dogleg is that its R_{56} cannot be adjusted.

Sextupole magnets placed between the dipole magnets can be used to suppress or manipulate the T_{566} of the dogleg, several designs with different combinations of quadrupole and sextupole magnets have been adopted [England05].

Multi-dipole dogleg

A Multi-dipole dogleg (spreader, switchyard) can usually be found in a FEL facility to connect the end of the linac and the entrance to the FEL [LCLS02][Zholents07] or to switch the beam to another parallel beamline [Milas10]. One of the main considerations in this type of dogleg design is to suppress the CSR-induced emittance growth by properly adjusting the phase advance between the dipole magnets via tuning the quadrupole magnets in between [DiMitri13]. In principle, the R_{56} of this type of dogleg should be almost zero (isochronous) since the bunch length is supposed to be kept constant after the linac. At FERMI@Elettra [Zholents07], for example, the nominal R_{56} of the dogleg is 0.9 mm but it can be increased to 5.5 mm.

Multi-dipole dogleg was also designed in purpose to compress the incoming bunch, for instance, at CTF3 [Sharma09]. However, the bunch length is so long (\sim ps) at CTF3 that the CSR effect does not need to be taken into account.

Bunch compressor with slit collimator

Due to the nonlinearity of the longitudinal phase-space of the electron bunch, a slit collimator can be used in a chicane or dogleg to allow only the central slice of a bunch to pass through. This technique was first proposed by Borland [Borland01+] to generate 10-20 fs electron bunches at the Advanced Photo Source (APS) Linac. Recently, it has been demonstrated that this technique can also be used for ultra-short FEL pulse generation [Emma04], beam diagnostics [DiMitri13-1], as well as removing of the double-horn structure in the current profile to improve the FEL performance [Zhou15]. In a chicane, the slit collimator is usually located between the second and the third dipole magnets to maximize the transverse dispersion at the slit, as illustrated in Figure 1.5.

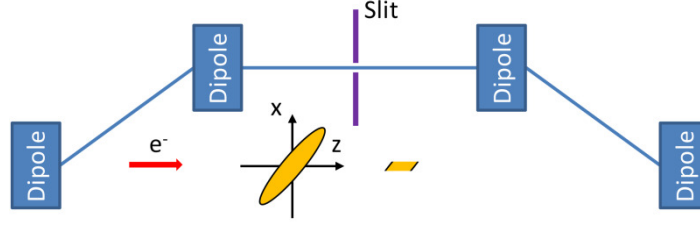


Figure 1.5: Illustration of a chicane bunch compressor with a slit collimator.

To first order, the horizontal position of an electron at the location with transverse dispersion η is given by

$$x = x_\beta + \eta(\delta_u + hz), \quad (1.58)$$

where x_β is the betatron component of the transverse coordinate. Solving equation (1.58) for z and substituting the solution into equation (1.37) gives

$$z_f = \frac{(1 + R_{56}h)(x - x_\beta)}{\eta h} - \frac{\delta_u}{h}. \quad (1.59)$$

Suppose the horizontal distribution of electrons is uniform in the central slice (accordingly $\langle x x_\beta \rangle = 0$), the rms bunch length after compression is given by

$$\sigma_z = \frac{1}{|h|} \sqrt{\frac{(1 + R_{56}h)^2 (\sigma_{x_\beta}^2 + \Delta x^2/12)}{\eta^2} + \delta_u^2}, \quad (1.60)$$

where $\sigma_{x_\beta} = \sqrt{\varepsilon_x \beta_x}$ is the rms betatron beam size and Δx is the full width of the slit. It should be noted that when the slit width is comparable to the betatron beam size, reducing the slit width will not significantly reduce the final bunch length. Instead, the bunch charge (peak current) will be reduced considerably [Emma04].

CSR effects

As it is known, an ultra-relativistic charged particle bunch moving in a curved trajectory in a magnetic field radiates electromagnetic energy in a wide frequency spectrum, i.e. the synchrotron radiation. In the region of the full coherent radiation ($\sigma_z \ll \rho/\gamma^3$), the radiation power from a bunch consisting of N_p electrons is proportional to $N_p^2 \gamma^4 / \rho^2$, which is N_p times the power radiated incoherently by a much longer bunch with the same number of electrons. Between these two limits there is the region where the radiation is still coherent ($\sim N_p^2$) but the radiation power depends on the bunch length instead of the bunch energy [Dohlus05].

When the radius of the curved trajectory is small, the electromagnetic fields emitted by the particle in the bunch tail can overtake the particle in the bunch head via the shorter straight trajectory. As illustrated in Figure 1.6, the overtaking length is defined as

$$L_0 = |AB| = 2\rho \sin \frac{\theta}{2} \approx (24\sigma_z \rho^2)^{1/3}. \quad (1.61)$$

In the above equation, the relation between the bunch length and the angle θ is purely determined by the geometry, which gives

$$\sigma_z = \text{arc}(AB) - |AB| = \rho\theta - 2\rho \sin \frac{\theta}{2} \approx \frac{\rho\theta^3}{24}. \quad (1.62)$$

At a storage ring, the overtaking length is typically longer than tens of meters and the effect can be neglected. However, in the magnetic bunch compressor of a FEL facility, assuming a bending radius of 1.5 m and a bunch length of 10 μm , the overtaking length is only 0.08 m.

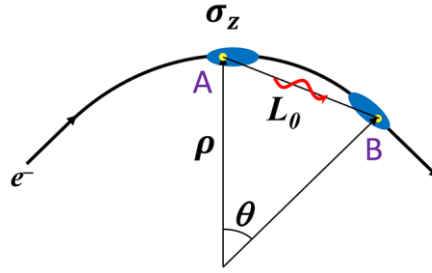


Figure 1.6: Illustration of the geometry of the CSR effect.

1-D CSR effect

Investigating of 3-D CSR effect requires extreme expensive numerical simulations. Fortunately, in most practical situations, the transverse bunch size is small enough to meet the Derbenev criterion [Derbenev95]

$$\frac{\sigma_{\perp}}{\sigma_z} \ll \left(\frac{\rho}{\sigma_z}\right)^{1/3} \quad (1.63)$$

so that the bunch can be treated as a line charge. Considering an electron bunch with longitudinal particle density λ given by

$$\int_{-\infty}^{+\infty} \lambda(s) ds = N_p, \quad (1.64)$$

the 1-D steady state CSR wakefield generated by the bunch as it propagates in a bend has the form of

$$W_{\parallel}(s) = -\frac{2r_c mc^2}{3^{1/3} \rho^{2/3}} \int_{-\infty}^s \frac{1}{(s-s')^{1/3}} \frac{d\lambda(s')}{ds'} ds', \quad (1.65)$$

where r_c denotes the classical electron radius and is the longitudinal particle density. In the case of the Gaussian distribution

$$\lambda(s) = \frac{N_p}{(2\pi)^{1/2}\sigma_z} \exp\left(-\frac{s^2}{2\sigma_z^2}\right), \quad (1.66)$$

the wakefield is given by

$$W_{||}(s) = \frac{2N_p r_c m c^2}{(2\pi)^{1/2} 3^{1/3} \sigma_z^{4/3} \rho^{2/3}} F\left(\frac{s}{\sigma_z}\right), \quad (1.67)$$

where

$$F(\xi) = \int_{-\infty}^{\xi} \frac{\xi' \exp\left(-\frac{\xi'^2}{2}\right)}{(\xi - \xi')^{1/3}} d\xi', \quad (1.68)$$

The shape of the wakefield calculated by equation (1.67) is shown in Figure 1.7, where the amplitude of the wakefield is normalized by

$$W_c = \frac{2N_p r_c m c^2}{(2\pi)^{1/2} 3^{1/3} \sigma_z^{4/3} \rho^{2/3}}. \quad (1.69)$$

It is found that the head of the bunch is slightly accelerated while the majority of the bunch experiences a decelerated field.

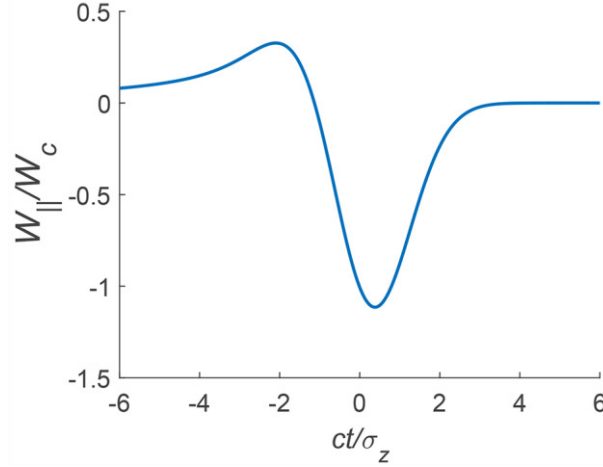


Figure 1.7: Shape of the CSR wakefield of a line charge with Gaussian density distribution. The bunch head is on the left.

The bunch as a whole loses its energy due to the CSR effect. The total radiation power is then given by

$$\int_{-\infty}^{+\infty} \lambda(s) W(s) ds \approx 0.279 \frac{N_p^2 r_c m c^2}{\epsilon_0 \sigma_z^{4/3} \rho^{2/3}}. \quad (1.70)$$

As introduced at the beginning of this sub-section, the CSR power is proportional to N_p^2 but the radiation power depends on the bunch length instead of the bunch energy.

Emittance growth induced by 1D-CSR effect

The energy redistribution along the bunch caused by the CSR effect produces varying transverse offsets and divergences along the bunch (only in the bending plane) in the dispersion section, which will result in projected emittance growth. To first order, the second moments of the whole bunch can be written as

$$\langle x^2 \rangle = \langle (x_0 + \eta \sigma_{\delta, CSR})^2 \rangle \cong \varepsilon_0 \beta + \eta^2 \sigma_{\delta, CSR}^2, \quad (1.71)$$

$$\langle x'^2 \rangle = \langle (x'_0 + \eta' \sigma_{\delta, CSR})^2 \rangle \cong \varepsilon_0 \frac{1 + \alpha^2}{\beta} + \eta'^2 \sigma_{\delta, CSR}^2 \quad (1.72)$$

and

$$\langle xx' \rangle = \langle (x_0 + \eta \sigma_{\delta, CSR})(x'_0 + \eta' \sigma_{\delta, CSR}) \rangle \cong -\varepsilon_0 \alpha + \eta \eta' \sigma_{\delta, CSR}^2, \quad (1.73)$$

where $\sigma_{\delta, CSR}$ is the CSR effect induced energy spread. Accordingly, the projected emittance increases to

$$\varepsilon \cong \varepsilon_0 \sqrt{1 + \frac{H}{\varepsilon_0} \sigma_{\delta, CSR}^2}, \quad (1.74)$$

where

$$H = \frac{\eta^2 + (\eta' \beta + \eta \alpha)^2}{\beta}. \quad (1.75)$$

Assuming the beam has a waist ($\alpha \cong 0$) between the 3rd and 4th dipole magnets, equation (1.75) reduces to

$$H \cong \frac{\eta^2}{\beta} + \eta'^2 \beta. \quad (1.76)$$

At the third dipole magnet, we have $\langle \eta^2 \rangle \cong \eta_{max}^2$ and $\langle \eta'^2 \rangle \cong \theta^2/2$. Therefore, equation (1.76) becomes

$$H \cong \frac{\eta_{max}^2}{\beta} + \frac{1}{2} \theta^2 \beta. \quad (1.77)$$

At the last dipole magnet, we have $\langle \eta^2 \rangle \cong 0$ and $\langle \eta'^2 \rangle \cong \theta^2/2$. Thus equation (1.76) reduces to

$$H \cong \frac{1}{2} \theta^2 \beta. \quad (1.78)$$

Since the bunch length reaches its minimum at the end of the 3rd dipole magnet in most cases, the CSR effect in the 4th dipole magnet dominates the projected emittance growth. Therefore, it is of importance to have a small beta function at the 4th dipole magnet.

However, when the final bunch length is very small (ultra-short bunch) or the transverse emittance is very large (flat beam), the bunch length will still be very long at the end of the 3rd dipole magnet. To first order, the bunch length after the third dipole magnet of a chicane is given by [Zhu14]

$$\sigma_{z_3} = \sqrt{\left(1 + hR_{56}^{(3)}\right)^2 \sigma_{z_0}^2 + R_{56}^{(3)2} \sigma_{\delta_u}^2 + \frac{\varepsilon_x}{\gamma\beta_{x_0}} \left[R_{52}^{(3)2} + \left(R_{52}^{(3)} \alpha_{x_0} - R_{51}^{(3)} \beta_{x_0} \right)^2 \right]}, \quad (1.79)$$

where $R_{51}^{(3)}$, $R_{52}^{(3)}$ and $R_{56}^{(3)}$ are the elements of the transfer matrix from the entrance of the chicane to the exit of the third dipole magnet, and α_{x_0} , β_{x_0} are the horizontal C-S parameters of the beam at the entrance of the chicane. The contribution of the emittance [the second term on the right-hand side of equation (1.79)] to the bunch length dominates in the aforementioned two extreme cases. Nevertheless, the CSR effect in the 4th dipole magnet still dominates the projected emittance growth. However, since the bunch is still long at the entrance of the 4th dipole magnet, the CSR effect can be mitigated considerably. Also, it is important to maximize the bunch length at the entrance of the 4th dipole magnet by choosing proper beam optics.

1.2.2 Velocity bunching and ballistic bunching

Velocity bunching relies on the longitudinal phase-space rotation of the electrons and the phase slippage between the electrons and the RF wave which both occur during the acceleration of non-ultra-relativistic electrons [Serafini01]. The longitudinal electric field in a traveling-wave structure can be expressed as

$$E = E_0 \sin \phi, \quad (1.80)$$

where

$$\phi(z, t) = k_{rf}z - \omega t + \phi_0. \quad (1.81)$$

The evolutions of ϕ and γ are then given by

$$\frac{d\phi}{dz} = k_{rf} - \omega \frac{dt}{dz} = k_{rf} \left(1 - \frac{1}{\beta} \right) = k_{rf} \left(1 - \frac{\gamma}{\sqrt{\gamma^2 - 1}} \right), \quad (1.82)$$

and

$$\frac{d\gamma}{dz} = \frac{e}{m_e c^2} E_0 \sin \phi = \alpha k_{rf} \sin \phi \quad (1.83)$$

respectively with

$$\alpha = \frac{e}{m_e c^2 k_{rf}} E_0. \quad (1.84)$$

The above two coupled differential equation (1.82) and (1.83) describe the motion of an electron in the traveling-wave structure, and the solution is

$$\gamma - \sqrt{\gamma^2 - 1} + \alpha \cos \phi = C. \quad (1.85)$$

Substituting equation (1.85) with the initial and final conditions respectively, the relationship between the initial and final phases can be obtained to be

$$\cos \phi_f \approx \cos \phi_i + \frac{1}{2\alpha\gamma_i}, \quad (1.86)$$

where the two approximations $\gamma_i - \sqrt{\gamma_i^2 - 1} \cong 1/(2\gamma_i)$ and $\gamma_f - \sqrt{\gamma_f^2 - 1} \cong 0$ have been used. Finally, by differentiating equation (1.86) on both sides, the final phase extension (i.e. the bunch length) can be written as

$$d\phi_f = \frac{\sin \phi_i}{\sin \phi_f} d\phi_i + \frac{1}{2\alpha\gamma_i^2 \sin \phi_f} d\gamma_i \quad (1.87)$$

Hence, the incoming energy, phase extents and the injection phase in the RF structure can be tuned to minimize the bunch length after extraction. The key point for velocity bunching is that the compression and acceleration happen at the same time within the same RF structure.

Similarly to velocity bunching, ballistic bunching occurs for non-ultra-relativistic electron bunches. In such a scheme, an energy chirp is imparted along the bunch and the compression occurs in the downstream drift. Ballistic bunching is of common use in conjunction with DC-gun electron sources [Curtoni01].

Velocity and ballistic bunching both have to start at a low energy, i.e. downstream of the electron source. In the case of a RF-gun, the accelerating structure located immediately downstream of the gun, plays also an important role in the emittance compensation process [Carlsten89][Wang07]. An invariant envelope matching condition, which is a special equilibrium solution of the beam envelope equation, is desired. However, such a requirement is incompatible with operating the first accelerating structure far off-crest. A solenoid surrounding the first accelerating structure was proposed to prevent significant transverse emittance growth, which has also been demonstrated experimentally [Ferrario10]. Nevertheless, this technique is not applicable for a superconducting linac because of the size of the whole superconducting structure.

1.2.3 Other novel bunch compression schemes

Emittance exchange

The basic idea behind the emittance exchange is to swap the phase-spaces of a bunch between two planes by applying a proper transfer matrix [Cornacchia02], e.g .

$$\begin{aligned}
\begin{bmatrix} \Sigma_{XX,f} & 0 \\ 0 & \Sigma_{ZZ,f} \end{bmatrix} &= \begin{bmatrix} 0 & \mathbf{A}^T \\ \mathbf{B}^T & 0 \end{bmatrix} \begin{bmatrix} \Sigma_{XX,i} & 0 \\ 0 & \Sigma_{ZZ,i} \end{bmatrix} \begin{bmatrix} 0 & \mathbf{B} \\ \mathbf{A} & 0 \end{bmatrix} \\
&= \begin{bmatrix} \mathbf{A}^T \Sigma_{ZZ,i} \mathbf{A} & 0 \\ 0 & \mathbf{B}^T \Sigma_{XX,i} \mathbf{B} \end{bmatrix}.
\end{aligned} \tag{1.88}$$

Since $|\mathbf{A}| = |\mathbf{B}| = 1$, the horizontal and longitudinal phase-spaces are exchanged. It was found that a transverse deflection cavity (TDC) flanked by two doglegs is a feasible choice, as shown in Figure 1.8. In order to strongly compress the incoming bunch, a proper optics is required to set up before the emittance exchange beamline to achieve a direct mapping between the final longitudinal coordinate z_f and the initial transverse coordinate x_i [Carlsten11]

$$z_f = \left| \frac{\varepsilon_x}{\eta} \right| x_i, \tag{1.89}$$

where η is the dispersion at the TDC. Hence, bunch compression can be achieved by starting with a transversely tight focused bunch.

Bunch compression using an emittance exchange beamline has several advantages over the traditional chicane bunch compressor [Carlsten11]. The initial energy chirp is not required and the residual chirp of the final bunch can also be eliminated. The final bunch length is also less susceptible to the CSR induced bunch length broadening and microbunching instability [Huang04]. However, a key disadvantage of this method is that the final horizontal emittance tends to strongly depend on the initial bunch length and beam energy.

Emittance exchange has already been experimentally demonstrated in Fermilab [Ruan11]. However, using the emittance exchange beamline as a bunch compressor has not been experimentally proved.

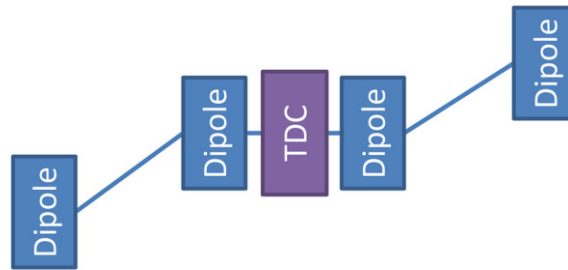


Figure 1.8: Illustration of an emittance exchange beamline.

Double emittance exchange

A more complicated double emittance exchange beamline was proposed by Zholents in 2011 [Zholents11]. Instead of achieving a direct mapping between the transverse and longitudinal coordinates, the bunch compression is achieved by first swapping the longitudinal and transverse phase-spaces and then using the magnetic

telescope to expand the horizontal beam size and squeeze its angular size. Finally, the emittance exchange is reversed, but in a new state with compressed bunch length and increased energy spread. This double emittance exchange method has the similar advantages as the single one. A unique feature of this new method is that the bunch is only partially compressed after the double emittance exchange. This allows acceleration of bunches with smaller peak currents in the linac, and the full compression can be achieved anywhere before beam utilization, e.g. in the dogleg beamline before the undulator. Figure 1.9 shows the sketch of the double emittance exchange beamline set up in Argonne National Laboratory [Ha16ppt]. However, this beamline was mainly designed and constructed for demonstrating the generation of arbitrary current profile [Ha16].

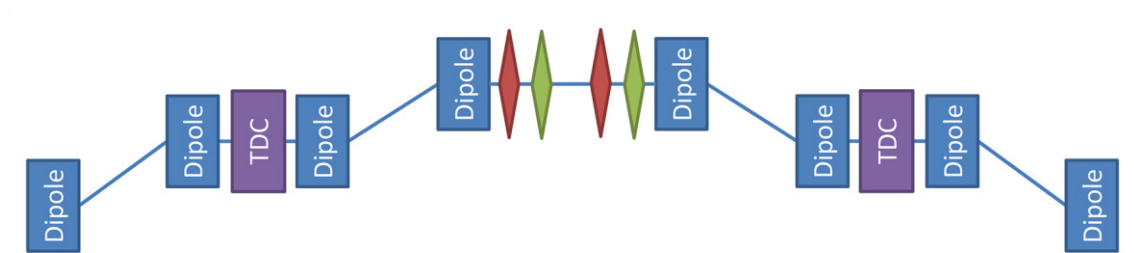


Figure 1.9: Sketch of the double emittance exchange beamline at Argonne National Laboratory.

2 The SINBAD Facility

A common feature of advanced acceleration methods, e.g. LWFA (Laser-plasma Wakefield Acceleration) [Tajima79][Esarey09], PWFA (Plasma Wakefield Acceleration) [Blumenfeld07][Litos14] and DLA (Dielectric Laser Acceleration) [Peralta13][England14], is the tiny size of the structure or accelerating channel which can sustain accelerating fields several orders of magnitude higher than conventional accelerators. However, it is required to match and align the externally injected electron bunch into the very small aperture. It is also required to minimize the phase spread and jitter of the very short accelerating period experienced by the electron bunch. These specifications result in very stringent requirements on the transverse and longitudinal bunch sizes as well as the timing and position stabilities.

The SINBAD (**S**hort **I**Nnovative **B**unches and **A**ccelerators at **D**ESY) project is a dedicated, long-term accelerator research and development facility currently under construction at the DESY Hamburg campus. It is foreseen to have multiple independent experiments in ultra-fast science and high-gradient accelerators accessing a common infrastructure [Dorda16]. The initial project goals are:

- [1] Production of ultra-short electron bunches for ultra-fast science.
- [2] Construction of a plasma accelerator module with usable beam quality for applications.
- [3] Test of a DLA structure (the “accelerator on a chip” project).
- [4] Setup of an attosecond radiation source with advanced technologies.

In the initial phase, SINBAD will host two independent experiments: ARES (Accelerator Research Experiment at SINBAD) and AXSIS (Frontiers in Attosecond X-ray Science: Imaging and Spectroscopy). The former is located in one of the two long straight sections, consisting of a linac and associated research beamlines. The latter will be installed in one of the two arcs and direct X-rays into the outside user areas. The layout of the SINBAD facility is shown in Figure 2.1.

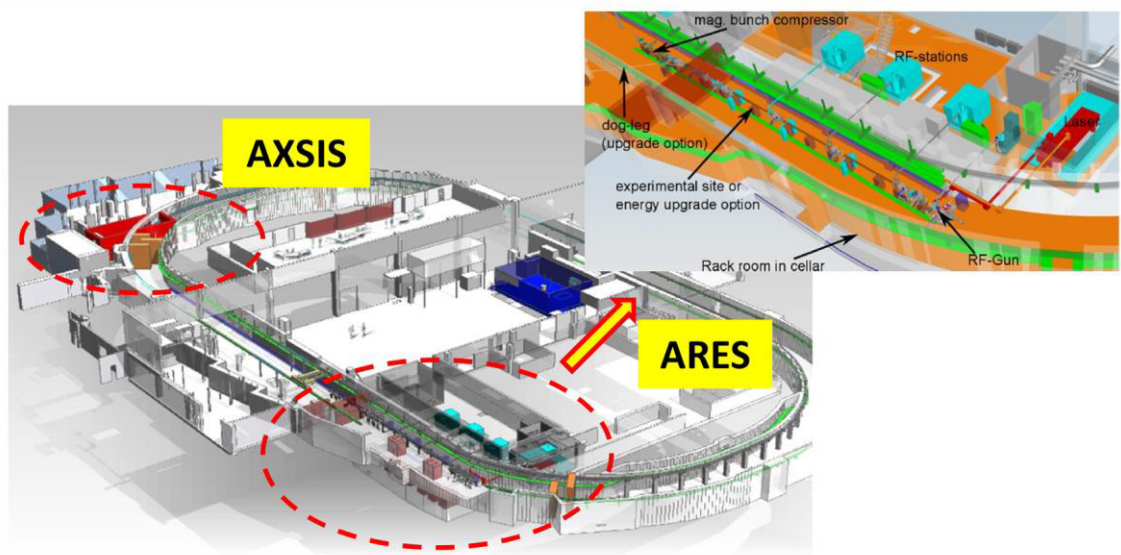


Figure 2.1: Overview of the SINBAD facility.

In the first part of this chapter, the layout of the ARES experiment is introduced, including the photoinjector, the traveling-wave structure, the RF station, the magnetic lattice and the diagnostics. In the second part, different novel acceleration schemes currently being considered at the SINBAD facility are reviewed. Particularly, more details are presented for LWFA since the design of the ARES linac mainly focuses on the requirements of LWFA experiments.

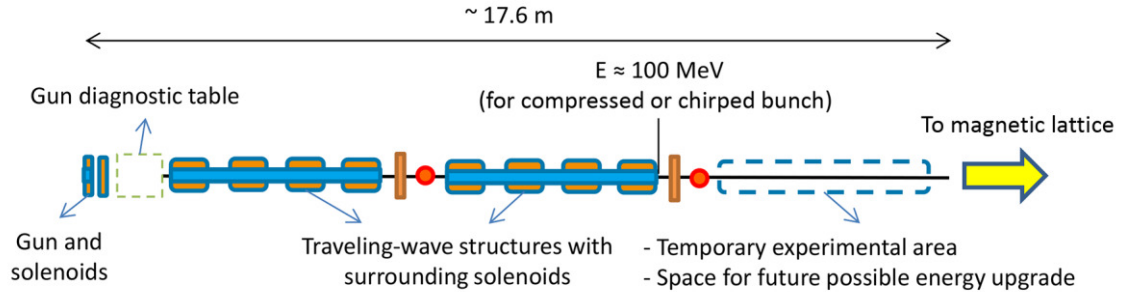
2.1 ARES

The ARES linac is foreseen to provide electron bunches suitable for experiments in the following fields of Accelerator Research and Development [Marchetti16]:

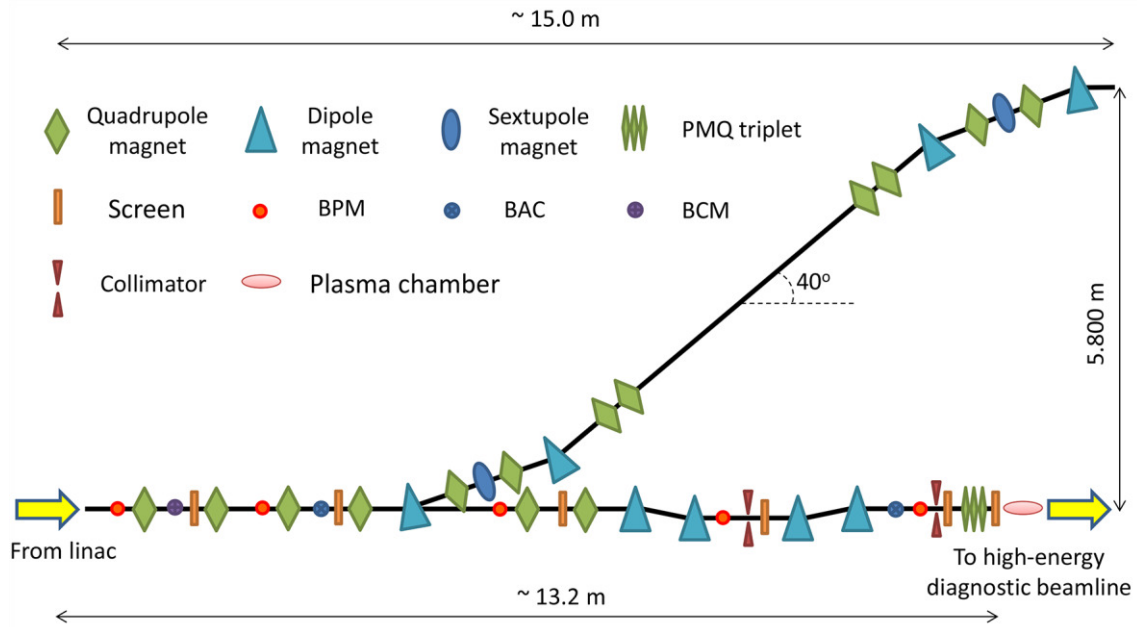
- [1] A source of sub-fs-long, pC electron bunches with energies of ~ 100 MeV (10 to 50 Hz repetition rate) and excellent timing stability (rms bunch arrival-time jitter < 10 fs), adequate to characterize novel accelerators, e.g. allowing high resolution temporal sampling of the phase.
- [2] An extended charge range ($0.5 \sim 30$ pC) corresponding to a wider range of bunch lengths (sub-fs \sim dozens of fs), suitable for experiments requiring high-brightness electron bunches for radiation generation, e.g. Free-Electron Laser.
- [3] In a possible upgraded version in the future, trains of bunches having total charges up to 1 nC are foreseen to be produced. This choice leaves open the possibility for PWFA experiments in which the trailing witness bunch can be accelerated by the plasma wave excited by a leading electron bunch (train).

The layout of the ARES linac is shown in Figure 2.2. The ~ 5 MeV electron beams generated by the 1.5-cell S-band photocathode RF-gun will be accelerated by two 4.2-meter-long S-band traveling-wave structures. Downstream of the traveling-wave structures the main (straight) beamline includes the matching section, the magnetic chicane bunch compressor, the final focusing section, the plasma experiment area, the

beam capture section and the diagnostics beamline (the last two parts are not shown in the figure). Between the second traveling-wave structure and the matching section, space is reserved for another traveling-wave structure for the possible upgrade in the near future. A dogleg starting from the middle of the matching section will deliver beams to the second experimental area.



The baseline design



The lattice (upgraded) design

Figure 2.2: Sketch of the ARES linac. The corrector magnets are not shown in the plot due to space constraint. Here BPM refers to beam position monitor, BAC refers to bunch arrival-time cavity and BCM refers to beam current monitor. The diagnostics in the dogleg beamline has not been determined yet.

The slit collimator located between the second and third dipole magnets of the chicane will allow to generate ultra-short (sub-fs to dozens of fs) electron bunches with peak currents of several kA, while the dogleg will have tunable R_{56} which allows flexible control of the bunch compression at the second beamline. The designs of these two beamlines as well as detailed beam dynamics simulations are presented in Chapter 4 and Chapter 5. Several compression techniques (velocity bunching, magnetic compression and hybrid compression) will be investigated at the ARES linac. It is

foreseen to push these techniques to their limits in the direction of producing ultra-short electron bunches with high peak currents.

2.1.1 Photoinjector

The photoinjector consists of a laser driven electron source embedded in an RF accelerating field combined with a magnetic system (solenoids) which preserves and matches the beam into an accelerating structure, as shown in Figure 2.3.

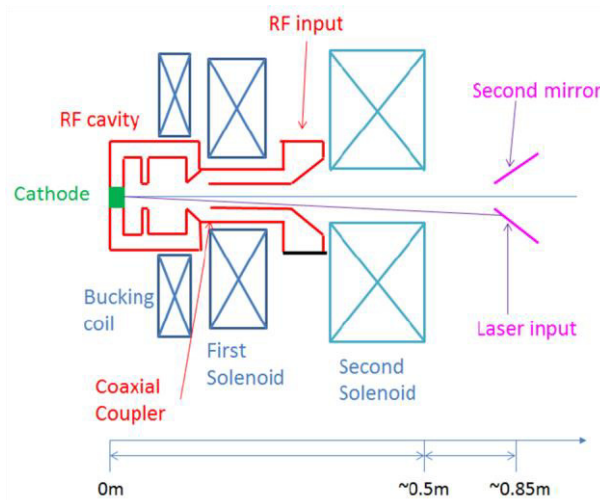


Figure 2.3: Illustration of the photoinjector at ARES.

Photocathode laser

The photocathode laser is a 1 mJ Yb doped laser with a tunable FWHM pulse length between 190 fs and 10 ps. In the baseline version of the linac it is foreseen to use a laser pulse having a transversally flat-top and longitudinally Gaussian profile. The minimum rms laser spot size on the cathode is expected to be 20 μm .

RF gun

The RF gun is similar to the one currently running at REGAE [Hada12], which is a 1.5-cell S-band (2998 MHz) gun. The normalized field map of the on-axis longitudinal electric field of the gun is shown in Figure 2.4. The maximum allowed electric field gradient is about 110 MV/m and the corresponding energy of the beam is about 5 MeV. A new balanced single output Mach-Zehnder modulator based laser-to-RF synchronization setup will be implemented and a long term sub-50 fs timing stability between the photocathode laser and the RF master oscillator can be achieved [Titberidze15].

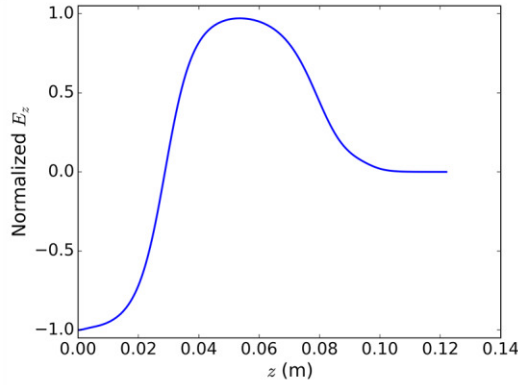


Figure 2.4: Normalized on-axis longitudinal electric field of the gun.

Both the semiconductor (Cs_2Te) and metallic (e.g. copper) cathodes are going to be used at the ARES linac. A load-lock vacuum system will allow for in-vacuum cathode exchange. The semiconductor cathode will be used in high average current applications because of its high quantum efficiency (QE). Here QE is defined as the ratio of the number of emitted electrons to the number of incident photons. Since the response time of the semiconductor cathode is on the picoseconds scale (possibly shorter), it will also only be used at working points with laser pulse durations longer than 1 ps so that the electron bunch's temporal profile is similar to the laser's. Metallic cathodes can be used for low average current applications since their high work functions lead to low dark currents even in high electric fields. Moreover, they can be used at working points with short laser pulse durations since their emission times are as short as dozens of femtoseconds [Rao12].

Gun solenoid

There will be three solenoids around the RF gun. A so-called “low-charge” solenoid located at about 0.4 m downstream of the cathode will allow the transverse focusing of the low charge bunches (0.5 ~ 10 pC). The so-called “high-charge” solenoid located before the on-axis coaxial coupler of the RF-gun will be implemented in the future to allow transport and focus of beams having charges higher than 10 pC. Since the “high-charge” solenoid is so close to the cathode that it leaves a tail of the longitudinal magnetic field B_z at the cathode, any longitudinal magnetic field at the cathode will cause the electron beam to have an angular momentum about its longitudinal axis. This angular momentum is conserved as described by Busch's theorem [Reiser08]. Such a magnetized beam has an intrinsic emittance due to the angular momentum, which is given by [Kim03]

$$\varepsilon_{rms} = \frac{eB_z}{2m_e c} \sigma_x^2. \quad (2.1)$$

The above expression gives 0.29 μm for a magnetic field of 10 Gauss and an rms beam size of 1 mm. Therefore, it is of importance to cancel the longitudinal magnetic field at the cathode with another bucking solenoid which will be mounted upstream of the

cathode. The normalized on-axis field maps of the “low-charge” solenoid and the combination of the “high-charge” and its bucking solenoids are shown in Figure 2.5. The peak longitudinal magnetic fields for the high-charge and low-charge solenoids are 0.24 T and 0.40 T, respectively.

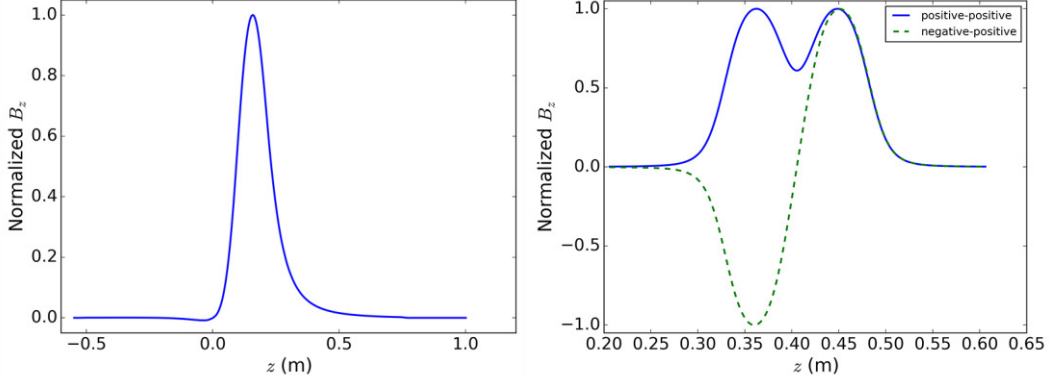


Figure 2.5: Normalized B_z of the combination of the “high-charge” and its bucking solenoids (left) and the “low-charge” solenoid (right). The excitation of the two “low-charge” solenoid coils can be controlled independently.

The solenoids are critical for the emittance compensation process [Carlsten89], which reverses the projected emittance growth induced by the linear space-charge effects between the cathode and the first accelerating structure, particularly in high charge working points. In order to compensate the projected emittance growth, the electron bunch is required to be matched into the first accelerating structure: the RF focusing of the accelerating structure is matched to the invariant envelope to damp the emittance to its final value at a relativistic energy. The required matching condition is referred to as Ferrario’s working point [Ferrario00], and it requires the emittance to be a local maximum and the envelope to be at a waist at the entrance to the first accelerating structure. A more in-depth discussion can be found in [Floettmann17].

2.1.2 Traveling-wave structure

The traveling-wave structure is a disk-loaded cylindrical waveguide and operates at 2998 MHz and $2\pi/3$ phase advance per cell, as illustrated in Figure 2.6. It consists of 120 regular cells and 2 coupling cells at both ends [Raguin12]. The on-axis longitudinal electric field map used in the simulation is shown in Figure 2.7. The fields in both the input and output coupling cells are treated as standing waves, while the field of the periodic section is treated as traveling wave and repeated 120 times. The peak electric field of the structure is 25.5 MV/m, which corresponds to a maximum energy gain of about 77 MeV per structure. Four solenoids around the cavity with peak fields up to 0.1 T provide additional focusing to the beam. The alignment of the individual solenoid can be adjusted independently, which alleviates the misalignment issue of using a single long solenoid.

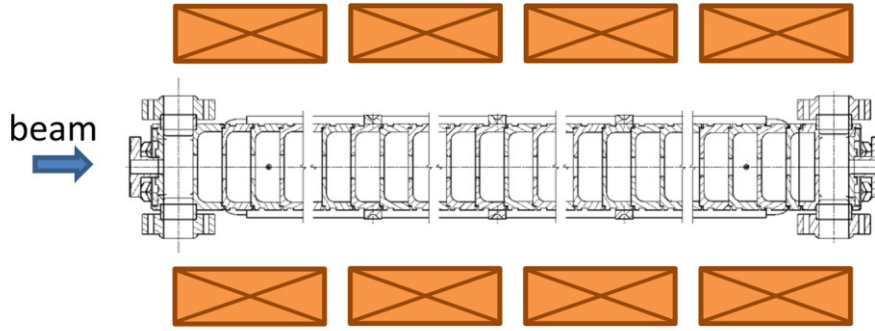


Figure 2.6: Cross-section of the 4.2-meter-long traveling-wave structure with four surrounding solenoids.

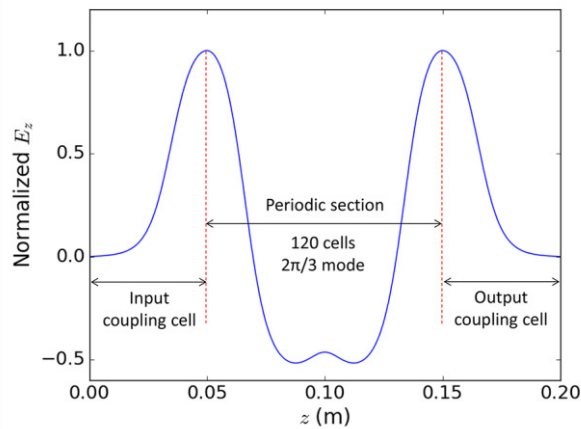


Figure 2.7: Normalized longitudinal electric field of one regular cell plus the input and output coupling cells of the travelling-wave structure.

2.1.3 RF station

In order to minimize the bunch arrival-time jitter, each RF cavity in the ARES linac will be fed by an independent RF station (the reason will be discussed in Chapter 4). The RF pulse lengths of the gun RF station and the linac RF station are as long as $6 \mu\text{s}$ and $4.5 \mu\text{s}$, respectively, in favor of the stabilization of the accelerating field. The distances among the cavities, the RF stations and the racks containing parts of the LLRF were also minimized and meet the requirements for digital feedback regulation in microsecond range.

2.1.4 Diagnostics

In addition to many distributed diagnostics (e.g. beam position monitors, screens), there will be two major diagnostic areas at the ARES linac. One is the gun diagnostic table and the other is the high-energy diagnostic beamline.

The 3D model of the integration of the gun and the diagnostics at the gun diagnostic table is shown in Figure 2.8. The first diagnostic section will include a Faraday Cup for the charge measurement, an LYSO:Ce scintillator screen for the measurement of the transverse spot size, a collimator and a fourth entry possibly hosting

a TEM (Transmission Electron Microscopy) grid for emittance measurements. The second diagnostics section will host a scintillator screen. Transverse emittance can also be measured here via the solenoid scan method. A 90-deg dipole spectrometer magnet will be used for energy and energy spread characterization. For this purpose a third diagnostic section will be located in a branch beamline perpendicular to the main one.

The high-energy diagnostic beamline which will be located downstream of the plasma experiment area is still under design.

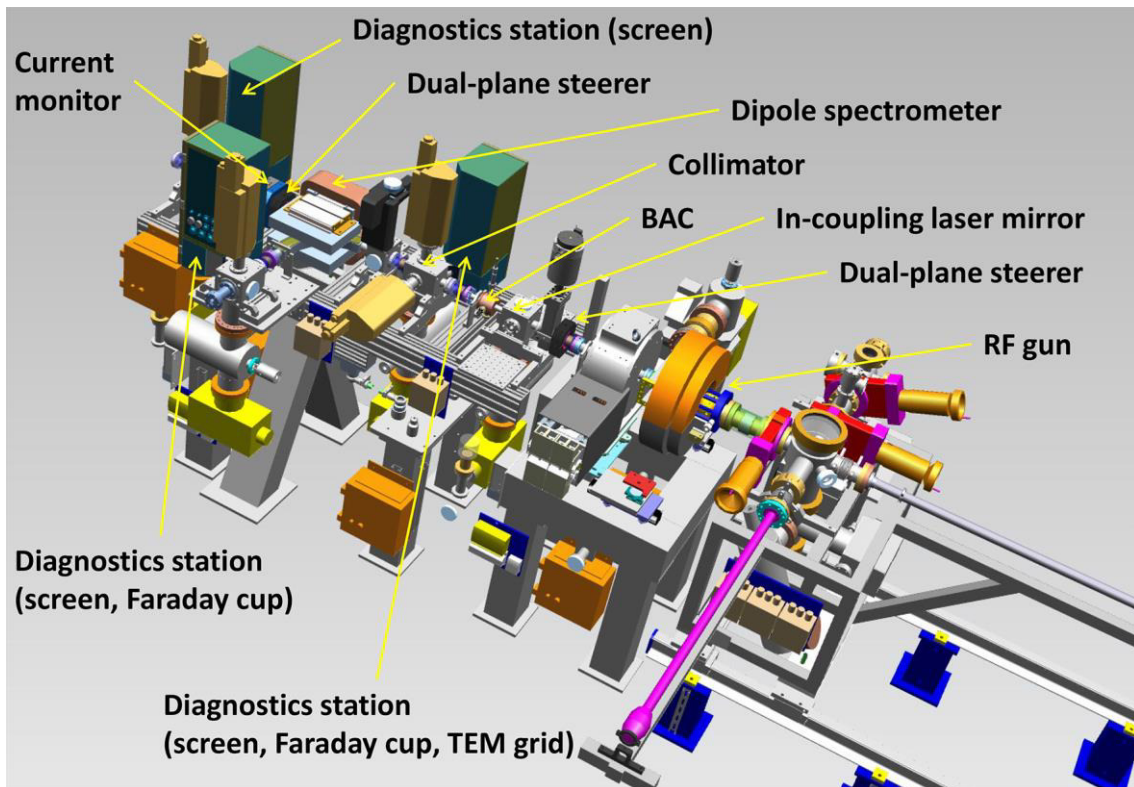


Figure 2.8: 3D model of the ARES RF gun area.

Beam position monitor

Beam Position Monitors (BPMs) are the most widely used, non-destructive diagnostics at nearly all accelerators. In addition to the beam position measurement, the BPM can also measure the relative charge of the beam. In general, a BPM couples the electromagnetic fields generated by charge particle beams. The most frequently used BPMs are the button BPM and the stripline BPM. The cavity BPM has much higher resolution but is typically also much more expensive. It is used throughout the SwissFEL [Keil2015] beamline and part of other accelerators, e.g. the undulator section [Smith09], where a very high position resolution is required.

In a button BPM, four pick-up electrodes (buttons) are mounted around the beam pipe. Both circular arrangement (for round beam pipes) and planar arrangement (for flat beam pipes) can be used. The beam centroid is evaluated by comparing the signals measured through the electrodes. The small size of the button BPM and the short vacuum feed-through allows for a compact installation [Forck08]. A position resolution

of $\sim 5 \mu\text{m}$ for single bunch with charge higher than 50 pC has been achieved using the button BPM [Treyer13].

In comparison to other types of BPMs, only the cavity BPM has the potential to achieve resolutions of smaller than $1 \mu\text{m}$ in a bunch by bunch time-scale. When a bunched beam traverses a cavity BPM, a subset of resonant modes will be excited. The output voltage of a cavity BPM with impedance Z is given by [Inoue08]

$$V_{out} = \frac{\omega q}{2} \sqrt{\frac{Z}{Q_{ext}}} (R/Q) \exp\left(-\frac{\omega^2 \sigma_z^2}{2c^2}\right), \quad (2.2)$$

where R is the shunt impedance, Q and Q_{ext} are the quality factor and external quality factor, respectively. In the dipole mode (TM110), the signal amplitude is proportional to the bunch charge q and the transverse offset d of bunch ($R/Q \propto d^2$), and its phase flips at the center. However, the signal amplitude in the monopole mode (TM010) does not depend on the bunch position but is proportional to the bunch charge, and its phase is determined by the bunch arrival-time. Therefore, by combining the measurements for the dipole and monopole mode cavities, it is possible to calculate the beam position. The higher order modes are damped much more strongly so that their contributions are negligible and the linearity of the measurement is guaranteed. A position resolution of less than $0.8 \mu\text{m}$ for a single bunch has been demonstrated experimentally for a 16-mm-aperture cavity BPM with a bunch charge of 135 pC [Schietinger16].

A new cavity BPM is currently under design for the ARES linac aiming to improve the precision at the low-charge working points. For the 0.5-pC bunch, the goal for the precision after averaging over 50 points is $5 \mu\text{m}$ while the goal for the single-shot precision is about $25 \mu\text{m}$.

Beam Profile monitor

Optical transition radiation screen

Transition radiation is emitted when a charged particle at a constant velocity crosses a sharp boundary of two media with different dielectric properties. For an incidence normal to the surface, transition radiation is emitted symmetrically forward and backward around the direction of motion of the particle. The radiation is radially polarized. It has zero intensity around the axis and maximum intensity at on a cone at an angle equal to $1/\gamma$. For a non-normal incidence, the forward radiation is still emitted around the direction of the particle. However, the backward radiation is emitted around the direction of specular reflection.

For the purpose of monitoring the beam profile, an aluminum-coated silicon wafer is typically used. The screen is rotated so that the incident angle of the charged particle is 45 degree and the backward radiation is emitted perpendicularly to the beam axis. The transition radiation in the optical wavelength range (OTR) is recorded by a camera. The OTR intensity from a small area of the screen is proportional to the charge density

at the screen in this area, as long as the coherent emission does not occur. The OTR is essentially a surface effect and the emission time is approximately on the same scale as the electron bunch length [Castellano99]. Although the OTR screen provides good spatial resolution, it is not suitable for beams with low energies and intensities due to the low signal to noise ratio in this region [Rimjaem11]. It must be noted that the spatial resolution for the transverse beam size measurements is also limited by the optical readout system, the lens imperfection and the pixel size of the CCD camera.

Scintillator screen

The scintillator screen is another type of widely used beam profile monitor in accelerators. When the beam energy is deposited in the crystal by ionization, either directly by charged particles or by the conversion of photons into electrons or positrons which subsequently produce ionization, the energy is transferred to the luminescent centers which then radiate scintillation photons [Beringer13].

A common scintillator screen in electron linacs is made of Yttrium Aluminum Garnet (YAG) doped with Cerium, which is a non-hygroscopic, chemically inert inorganic scintillator. It is also a radiation stable material and has good mechanical, thermal and vacuum properties. The wavelength of the maximum emission at 550 nm is well matched to the CCD (charge-coupled device) sensitivity. The light yield from a YAG screen increases linearly as the total energy deposition increases within a certain range. The decay time of the light emission is about 70 ns which is several orders of magnitude longer than the electron bunch length [Saint-gobain]. The impact of the OTR generated at the scintillator surface can be circumvented by only recording the tail of the scintillation light.

Although the scintillator screen has a higher light yield than the OTR screen, its spatial resolution is usually worse. The scintillator screen is prone to be saturated by the high intensity beam, which results in non-linearity of the light yield. In addition, space-charge ionization enhancement may contribute to the image blurring [Murokh00]. The degradation of the resolution of the scintillator screen can also be explained by the transverse extension of the electron-hole formation region and the index of refraction of the scintillator [Kube10].

At the ARES linac, the up-to-date LYSO:Ce screen designed for the European XFEL will be installed and the resolution is expected to be smaller than 22 μm [Wiebers13].

Transverse emittance measurement

Magnet scan methods

In order to measure the transverse emittance, e.g. horizontal emittance given by equation (1.3), the covariance matrix elements $\langle x^2 \rangle$, $\langle x'^2 \rangle$ and $\langle xx' \rangle$ have to be known. When a beam profile monitor intercepts the entire beam, however, only the rms beam size $\sqrt{\langle x^2 \rangle}$ can be directly measured. According to equation (1.18), in a decoupled

beamline ($R_{13} = R_{14} = R_{15} = R_{16} = 0$), the final quantity $\langle x_f^2 \rangle$ is related to the initial ones by

$$\langle x_f^2 \rangle = R_{11}^2 \langle x_i^2 \rangle + 2R_{11}R_{12} \langle x_i x_i' \rangle + R_{12}^2 \langle x_i'^2 \rangle. \quad (2.3)$$

Therefore, the initial covariance matrix elements can be determined by three measurements of $\langle x_f^2 \rangle$ with different transfer matrices. The different measurements can be carried out by measuring the beam sizes at different screens separated by drift spaces or by varying the strength of a quadrupole. The latter is the well-known quadrupole scan method. In practice, measurements of the rms beam size are subject to errors. Therefore, more than three measurements are required and the covariance matrix elements can be deduced using the linear least square method. The accuracy of the measurement is limited by the ratio of the detector spatial resolution to the size of the beam waist achievable at the monitor. [McDonald89]. Similarly, solenoid scan is also used in emittance measurement, typically for low energy electron beams [Hachmann16].

It should be noted that equation (2.3) only holds when the space-charge effects are negligible. For the space-charge dominated beam, the slit-based method is normally used [Anderson02].

Slit-based method [McDonald89]

The slit-based method is able to measure the emittance of a space-charge dominated beam, e.g. in a photoinjector. The basic idea of this method is to produce emittance dominated beamlets by inserting a single-slit/multi-slit collimator or a “pepper-pot” to select tiny portions of the space-charge dominated beam. By combining with a drift, which reveals the angular spread as spatial information at an intensity-sensitive detector, allows a full reconstruction of one of the beam's transverse phase planes, as illustrated in Figure 2.9.

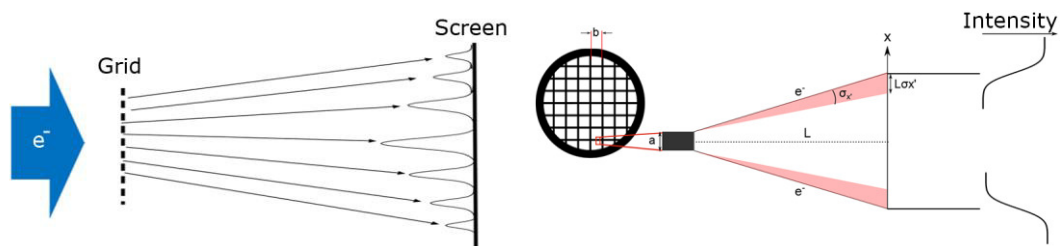


Figure 2.9: Illustration of the principle of the slit-based emittance measurement method (left) and the TEM grid method (right).

The precision of the slit-based method is determined by trade-offs among several considerations. First, the smearing of the angular profile and the amount of signal both decreases as the open-width of the slit decreases. Second, the spatial resolution and the overlapping of beamlets on the screen both increases as the slit spacing increases. Third, a slit thick enough to stop the beam or at least minimize the scattered beam is desired,

but the finite length of the holes (which may be much greater than their transverse size) may complicate the interpretation of the beamlet profiles.

For the single-slit method, the trace-space distribution can be obtained by scanning the slit position across the bunch, assuming a very good shot-to-shot stability [Abrahamyan04]. While for the multi-slit/pepper-pot method, the measurement can be accomplished with a single shot. Moreover, the pepper-pot method can obtain the emittances in both transverse planes at the same time. However, the disadvantage of the multi-slit/pepper-pot method is the possibility of overlapping the beamlet images on the screen, which could underestimate the real divergence.

At the ARES gun diagnostic table, a TEM grid is planned for the single-shot emittance measurement, as illustrated in Figure 2.9. Unlike the pepper-pot method, the angular spread of the electrons at the TEM grid method is obtained by analyzing the beam profile at the edge of each bar. Moreover, the opening area of the TEM grid is larger, which makes it more practicable for bunches with ultra-low charges comparing to the traditional pepper-pot method [Bayesteh14].

Bunch length measurement

RF deflecting cavity

The RF deflecting cavity (RFD), also known as transverse deflecting structure (TDS), is the most widely used device for characterizing the longitudinal phase-spaces of electron bunches. In an RFD, electrons are transversely deflected by the electromagnetic force, typically at TM_{11} mode, which is linearly dependent on their longitudinal positions within a bunch. The first Iris-loaded RF deflecting structure was built first at SLAC in the 1960's for particle separation and called "LOLA" after the name of its three inventors [Larsen64]. The basic working principle of an RFD is illustrated in Figure 2.10.

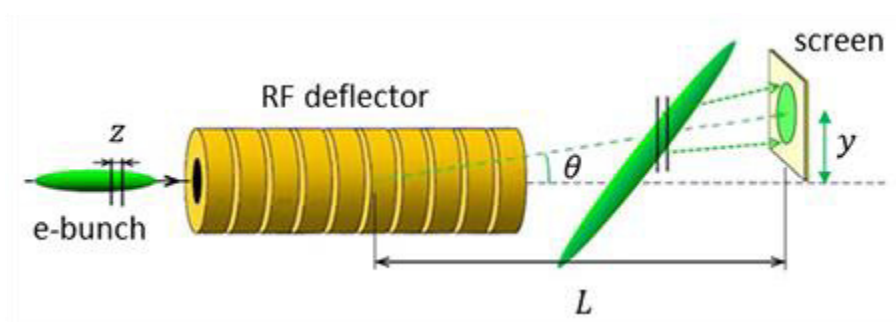


Figure 2.10: Illustration of the principle of RFD operation.

The shear parameter of a vertical RFD, which defines the linear relationship between a particle's position y on the screen and its longitudinal coordinate z , is defined as [Ding11]

$$S = \frac{y}{z} = R_{34} \frac{2\pi f e V_{RFD}}{pc^2} = \sqrt{\beta_{y,scr} \beta_{y,RFD}} \frac{2\pi f e V_{RFD}}{pc^2} |\sin \Delta\phi|, \quad (2.4)$$

where R_{34} is the element of the transfer matrix from the TDS center to the screen, V_{RFD} is the equivalent peak deflecting voltage, f is the RF frequency, $\beta_{y,scr}$, $\beta_{y,RFD}$ are the vertical beta functions at the screen and the center of the RFD, respectively, and $\Delta\phi$ is the phase advance between them.

The resolution of an RFD is simply given by [Ding11]

$$\sigma_{z,min} = \frac{\sqrt{\varepsilon_{y,tr} \beta_{y,scr}}}{S} = \sqrt{\frac{\varepsilon_{y,tr}}{\beta_{y,RFD}} \frac{pc^2}{2\pi f e V_{RFD} |\sin \Delta\phi|}}. \quad (2.5)$$

It indicates that besides increasing the deflecting voltage, the resolution can also be improved by decreasing the emittance of the beam, increasing the RF frequency (X-band is much better than S-band) and making the phase advance near $\pi/2$. In the LCLS experiment, a temporal resolution of less than 1 fs rms has been achieved with the electron beam energy of ~ 4.7 GeV using an X-band RFD [Behrens14].

At the ARES linac, the planned X-band TDS will allow the characterization of the 3D charge density profile of an electron bunch to femtosecond longitudinal resolution [Marx17].

Beam Energy measurement

The beam energy can be determined by measuring the transverse displacement of the beam downstream of a dipole magnet (spectrometer). Through combining with an RFD, the longitudinal phase-space of the beam can also be reconstructed [Behrens14]. The energy resolution after a horizontal bend spectrometer is given by

$$\sigma_\delta = \frac{\sqrt{\varepsilon_{x,tr} \beta_{x,scr}}}{R_{16}}. \quad (2.6)$$

2.2 Novel Acceleration Techniques

2.2.1 Laser Wakefield Accelerators (LWFA)

In an LWFA, an ultra-short, intense laser pulse excites strong radial and longitudinal electromagnetic fields via the ponderomotive force. The ponderomotive force expels the electrons from the plasma, generating a co-propagating “bubble” in which strong accelerating and focusing fields are present. These electric fields can be used to accelerate and focus either electrons captured directly from the plasma background or injected externally. A typical electron charge density and electric field distribution in an LWFA are shown in Figure 2.11.

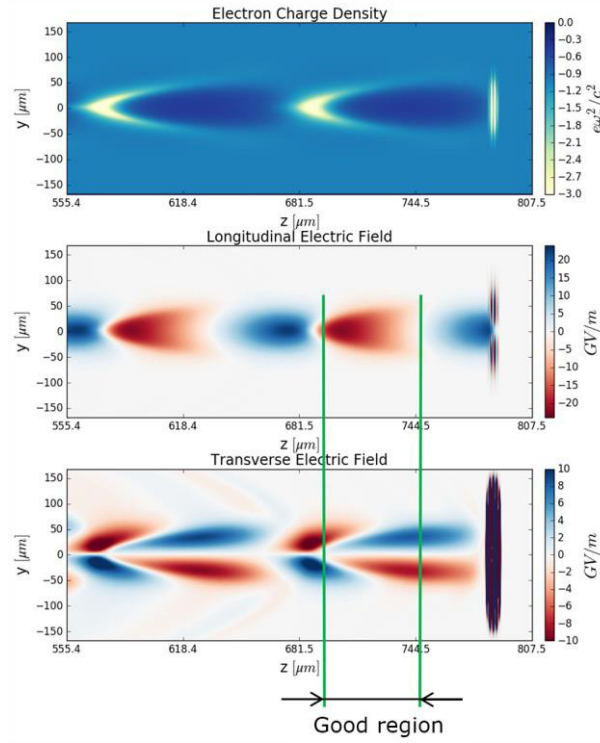


Figure 2.11: Electron charge density distribution and electric field map for a typical LWFA (simulated by A. F. Pousa). Here $\omega_p = (4\pi n_0 e^2 / m_e)^{1/2}$ is the electron plasma frequency and n_0 is the ambient electron number density.

Basic theory [Esarey09]

Ionized plasma can sustain electron plasma waves with electric fields in excess of $E_0 = cm_e \omega_p / e$ or

$$E_0(\text{GV/m}) \cong 9.6 \times 10^{-8} \sqrt{n_0(\text{cm}^{-3})}. \quad (2.7)$$

Equation (2.7) is referred to as the cold nonrelativistic wave breaking field. For instance, it yields a field gradient of 96 GV/m with a plasma density of $n_0 = 10^{18} \text{ cm}^{-3}$, which is approximately three orders of magnitudes greater than that obtained in conventional accelerators. However, the length of the accelerating wave in a plasma-based accelerator is approximately the plasma wavelength $\lambda_p = 2\pi c / \omega_p = 2\pi / k_p$ or

$$\lambda_p(\mu\text{m}) \cong 3.3 \times 10^{10} / \sqrt{n_0(\text{cm}^{-3})}, \quad (2.8)$$

which yields an extremely short wavelength of about 33 μm for a plasma density of $n_0 = 10^{18} \text{ cm}^{-3}$.

In an LWFA, the accelerating wave is excited by a short-pulse, high-intensity laser beam via the ponderomotive force. When a focused laser field is propagating along the z axis in vacuum, the laser spot size and intensity evolve as

$$w(z) \cong w_0 \sqrt{1 + \frac{z^2}{Z_R^2}} \quad (2.9)$$

and

$$I_L(z) \cong I_{L,pk} \frac{w_0^2}{w^2(z)} \exp\left(-\frac{2r^2}{w^2(z)}\right), \quad (2.10)$$

respectively, where w_0 is the laser spot size at focus, $Z_R = k_L w_0^2/2$ is the Rayleigh length, $k_L = \omega_L/c = 2\pi/\lambda_L$ with λ_L the laser wavelength and ω_L the laser frequency in vacuum, and a fundamental Gaussian mode is assumed. The evolution of the laser spot size in vacuum is also illustrated in Figure 2.12. It should be noted that the laser spot size $w(z)$ is defined as the transverse distance from the beam axis where intensity drops to $1/e^2$ of the intensity on axis (for a Gaussian beam $w = \sqrt{2}\text{FWHM}/2\sqrt{\ln 2} \approx 0.849\text{FWHM}$).

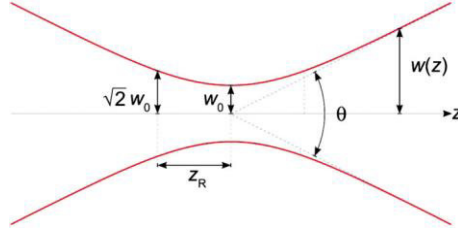


Figure 2.12: The evolution of a Gaussian laser beam in vacuum.

An important parameter of a high-intensity laser beam is the laser strength parameter a_0 , which is related to the normalized vector potential of the laser field $\mathbf{a} = e\mathbf{A}/m_e c^2$ by

$$\mathbf{a} = \frac{1}{\sqrt{2}} a_0 \exp\left(-\frac{r^2}{w^2(z)}\right) \exp\left(-\frac{\xi^2}{4\sigma_{z,L}^2}\right) \cos(k_L \xi) \mathbf{e}_x, \quad (2.11)$$

where a linearly polarized laser field with Gaussian laser profile is assumed, \mathbf{A} is the vector potential, $\xi = z - ct$, $\sigma_{z,L}$ is the rms laser pulse length and \mathbf{e}_x is the unit vector. For a laser beam with power $P_L = \pi w_0^2 I_{L,pk}/2$, the laser strength parameter is also related to the peak laser intensity by $I_{L,pk} = (\pi c/4)(m_e c^2 a_0/e\lambda_L)^2$, which yields

$$a_0^2 \cong 7.3 \times 10^{-19} (\lambda_L [\mu\text{m}])^2 I_{L,pk} [\text{W}/\text{cm}^2]. \quad (2.12)$$

In the linear regime ($a_0^2 \ll 1$, $E_{z,max}/E_0 \ll 1$), the longitudinal wakefield inside the plasma for such a Gaussian laser profile is given by (utilizing equation (37) in [Esarey09] and substituting a_0^2 and L with $a_0^2/2$ and $\sqrt{2}\sigma_{z,L}$, respectively)

$$E_z(r, \xi) = \frac{m_e c^2 k_p^2 \sigma_{z,L}}{2e} \sqrt{\frac{\pi}{2}} a_0^2 \exp\left(-\frac{k_p^2 \sigma_{z,L}^2}{2} - \frac{2r^2}{w^2(z)}\right) \cos(k_p \xi). \quad (2.13)$$

For a given k_p , the maximum longitudinal field is achieved when $\sigma_{z,L} = 1/k_p = \lambda_p/2\pi$ which means that a longer laser pulse is required for a plasma with lower density. The transverse wakefields are related to the axial wakefield by the Panofsky-Wenzel theorem $\partial E_z/\partial r = \partial(E_r - \beta c B_\theta)/\partial z$, which gives

$$E_r(r, \xi) - \beta c B_\theta(r, \xi) = -r \frac{2m_e c^2 k_p \sigma_{z,L}}{e} \sqrt{\frac{\pi}{2}} \frac{a_0^2}{w^2(z)} \exp\left(-\frac{k_p^2 \sigma_{z,L}^2}{2} - \frac{2r^2}{w^2(z)}\right) \sin(k_p \xi). \quad (2.14)$$

The plasma wave is a simple sinusoidal oscillation with frequency ω_p and a wave phase velocity v_p in the linear regime with accelerating gradient $E_z \ll E_0$. The phase velocity v_p is approximately equal to the group velocity v_g of the drive laser, which gives

$$v_p \cong v_g = c \sqrt{\left(1 - \frac{\omega_p^2}{\omega_L^2}\right)} \quad (2.15)$$

in the 1D limit. The phase velocity of the plasma wave and the group velocity of the drive laser are usually presented in the form of

$$\gamma_p = (1 - v_p^2/c^2)^{-1/2} \text{ and } \gamma_g = (1 - v_g^2/c^2)^{-1/2}, \quad (2.16)$$

which are the Lorentz factors associated with v_p and v_g , respectively. In the linear regime, it gives $\gamma_p \cong \gamma_g = \omega_L/\omega_p$. In reality, the group velocity of the drive laser is reduced by the diffraction of the laser beam and the distortion of the drive pulse.

The energy gain of an LWFA is limited by several factors: laser diffraction, electron dephasing, pump depletion and laser plasma instabilities. Due to the diffraction of the laser, the laser-plasma interaction distance will be limited to a few Z_R without some form of optical guiding since the laser intensity drops rapidly outside this region. For a relativistic electron bunch, the bunch will eventually outrun the plasma wave and move into the decelerating phase region since the phase velocity of the plasma $v_p < c$. The dephasing length L_{dps} is defined as the length the electron must travel before it slips by one-half of a plasma wave period. The linear dephasing length is approximately given by $L_{dps} = \gamma_p^2 \lambda_p$, assuming $\gamma_p \gg 1$. The pump depletion refers to the energy loss of the drive laser after it excites a plasma wave. In the linear regime, the depletion length $L_{dpt} \gg L_{dps}$. Therefore, the electron energy gain is limited by dephasing. The dephasing limitation can be overcome by increasing the plasma density along the direction of propagation, thus the phase velocity of the wakefield can be increased.

As the laser strength parameter increases, the plasma wave will become non-linear. Typically, numerical methods are required to solve the exact wakefields in the mildly non-linear regime ($a_0^2 \gtrsim 1$, $E_{z,max}/E_0 \gtrsim 1$). Analytical solutions can only be given under specific conditions. Considering a linearly polarized laser pulse with a square longitudinal profile in the 1D limit $k_p w_0 \gg 1$, the maximum amplitude of the wakefield is given by

$$E_{z,max} = \frac{a_0^2}{\sqrt{4 + 2a_0^2}} E_0. \quad (2.17)$$

In general, the electron energy gain is limited by pump depletion instead of dephasing in the non-linear region.

The regime of complete expulsion of the plasma electrons from some region around the axis, leaving behind a cavity of massive and stationary plasma ions surrounded by a thin layer of the expelled electrons, is called the blow-out regime ($a_0^2 \gg 1$). The wakefields in the blow-out regime are given by

$$E_z \cong \frac{k_p \xi}{2} E_0 \quad \text{and} \quad E_r - \beta c B_\theta \cong \frac{k_p r}{2} E_0 \quad (2.18)$$

for any shape of cavities [Mehrling14]. The longitudinal force on an electron hence has a linear dependence on the co-moving variable ξ and the transverse force has a linear dependence on the radius. The axial electric field is at its maximum when $\xi = r_B$, where $r_B \approx w_0$ is the radius of the cavity.

The high-power laser system ANGUS which is used as a driver for the plasma wakefields at the LUX beam line [<http://lux.cfel.de/>], as well as for the planned REGAE experiment [Zeitler17], is also possibly going to be used at the SINBAD facility. ANGUS is a Titanium-sapphire based laser system with a central wavelength of 815 nm. It is optimized for stability in terms of low energy fluctuations and in particular minimization of variations in beam pointing. The nominal parameters for the ANGUS laser are $I_{L,pk} = 196.2$ TW, $\sigma_{z,L} = 25$ fs, $w_0 \approx 42.3$ μm and $a_0 \approx 1.8$. The typical accelerating and focusing field maps in approximately one cycle after the drive laser pulse simulated by OSIRIS are shown in Figure 2.13.

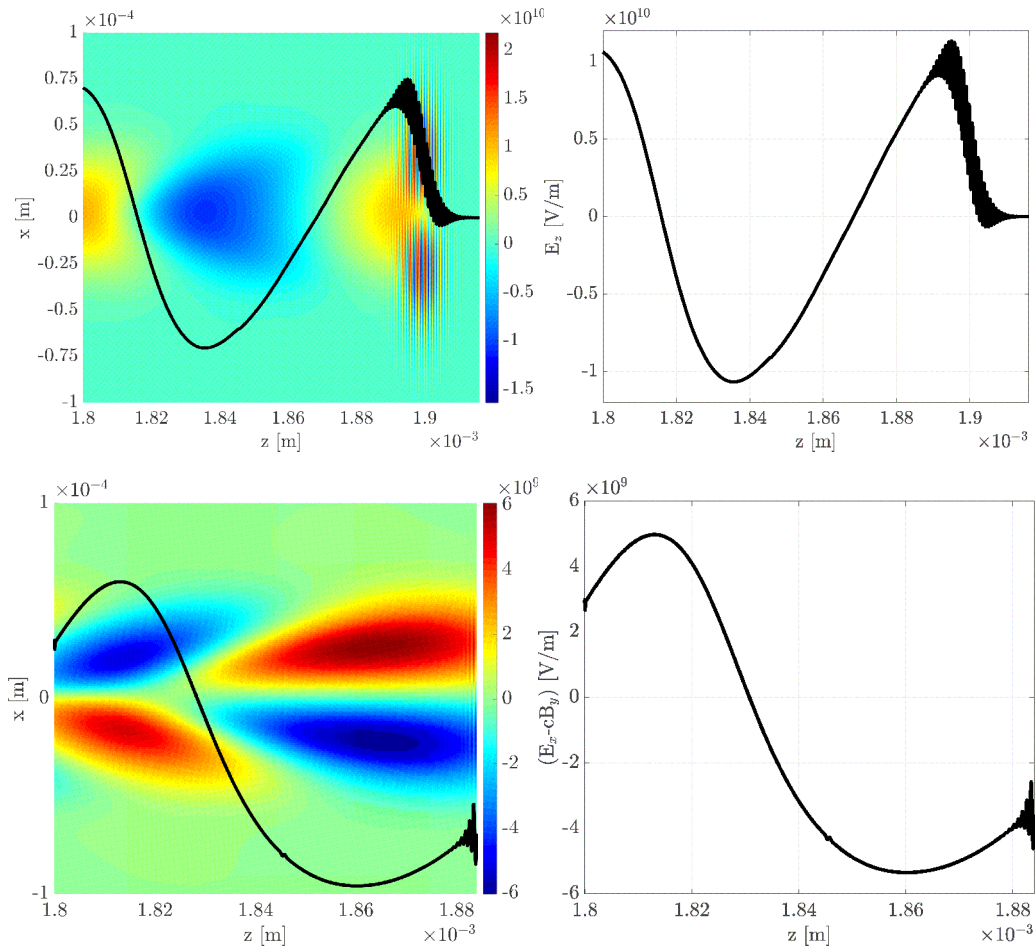


Figure 2.13: Accelerating and focusing field maps in approximately one cycle after the ANGUS laser pulse simulated using OSIRIS (simulated by M. Weikum). The plasma density is 10^{17} cm^{-3} . The focusing field map is extracted at $x \approx 15 \text{ }\mu\text{m}$. An electron beam is placed inside the wakefield which is the reason for the small kink in the field structures at around $z = 1.845 \text{ mm}$.

Recent experimental results

Although it is straightforward to achieve acceleration gradients on the orders of tens to hundreds of GeV/m in LWFA experiments, the energy spreads of the accelerated electron beams were as high as 100% in early days, which makes it hard to use [Esarey09]. A breakthrough in energy spread was obtained in 2004 by three groups by interacting intense laser pulses with millimeter-scale gas jets to generate 70 ~ 200 MeV electron bunches with energy spreads of only a few percent [Faure04][Geddes04][Mangles04]. Afterwards, using a plasma-channel-guided laser, high-quality electron bunches up to the energy of 1 GeV were achieved within a 30 mm plasma capillary [Leemans06]. In 2014, the generation of electron bunches with energies of 4.2 GeV using only 16 J of laser energy with preformed plasma channels in a 9-cm-long capillary was achieved [Leemans14]. One year later, the electron bunch pointing fluctuation was reduced to 0.6 mrad rms, which allowed for consistent observation of electron bunches with FWHM divergence less than 1 mrad [Gonsalves15].

External injection and internal injection

In the aforementioned experiments, self-injected electron bunches generated inside the plasma were accelerated by the wakefields. The energy spreads of the accelerated bunches were typically larger than 1%, which makes further transport and applications difficult [Migliorati13]. Nevertheless, there are several on-going projects which aim to improve the self-injection scheme, e.g. the LUX project [LUX] and the BELLA project [Tilborg17]. As an alternative to the self-injection scheme, external injection of beams generated and manipulated by conventional accelerator technologies allows precise manipulation of the phase-spaces of an externally injected electron bunch. It therefore provides the possibility to optimize the beam dynamics inside the plasma. Moreover, external injection is required whenever a staged plasma accelerator is considered, regardless of the injection scheme.

2.2.2 Plasma Wakefield Accelerators (PWFA)

In PWFAs, a leading high-charge drive bunch (or train of bunches) is used to ionize a gas (or a partially ionized gas produced by a laser) into plasma by the radial electric field of the drive bunch itself. In the so-called blow-out regime with $k_p \sigma_r < 1$, $k_p \sigma_z < 1$ and electron density higher than the plasma density, the plasma electrons are expelled from the volume of the electron pulse, leaving a column of massive ions behind. Subsequently, the expelled plasma electrons are pulled back by the ions behind the drive bunch, overshoot, and set up space-charge oscillations and strong wakefields. The longitudinal wakefield decelerates the drive bunch but accelerates a witness bunch with an appropriate time delay with respect to the driver. The ion column also provides a focusing force that can guide these bunches over a long distance, which allows an effective energy transfer from the drive bunch to the witness one. The illustration of a PWFA is shown in Figure 2.14. These wakefields have phase velocities equal to the velocity of the ultrarelativistic electron beam. As a result, there is no relative phase slippage between the witness bunch and the wakefields over meter-scale plasmas. The wakefields generated in the blow-out regime of a PWFA are similar to those in an LWFA, which are given by equation (2.18) [Lu06][Mehrling14].

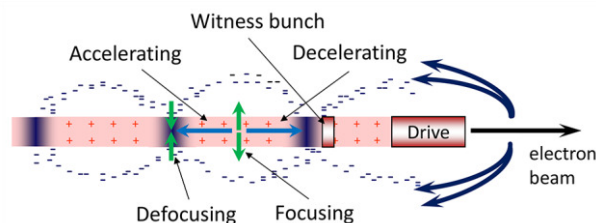


Figure 2.14: Illustration of a PWFA with one drive bunch and one witness bunch.

Accelerating wakefields higher than 50 GeV/m were achieved in an 85 cm long plasma using a 42 GeV drive electron bunch at the Stanford Linear Accelerator Center (SLAC) in 2007 [Blumenfeld07]. It should be noted that there was only one bunch in this

experiment, where the head of the bunch was decelerated while the tail of the bunch was accelerated. Later in 2014, the driver bunch was split into a driver bunch (~ 1 nC) and a witness bunch (~ 780 pC). About 10% of the charge contained in the core of the witness bunch was accelerated at an accelerating gradient of about 4.4 GeV/m. The energy gains of these core electrons were about 1.6 GeV with rms energy spread of about 0.7% [Litos14]. More recently, a variant of this scheme has been shown to work for positrons, as well, where a single positron bunch was demonstrated to excite a plasma wake in which the energy of the particles in the front half of the bunch was efficiently transferred at a high accelerating gradient to positrons in the back of the same bunch [Corde15].

A further improvement of the PWFA is to use a train of bunches as the driver. When a train of identical electron bunches separated by one plasma wavelength is matched into the plasma, the individual wakefields add up and the amplitude of the final wakefield scales linearly with the number of bunches [Kallos07]. Furthermore, the transformer ratio (maximum energy gain of the witness bunch/maximum energy loss of the drive bunch) of the acceleration can be greatly enhanced when the bunch charge increases along the train [Jing07].

2.2.3 Dielectric Laser Accelerators (DLA)

The use of infrared lasers to power optical-scale lithographically fabricated particle accelerators is a developing area of research that has garnered increasing interest in recent years [England14]. According to the Lawson-Woodward theorem, a paraxial free space laser field in an infinite vacuum cannot produce any net acceleration on a passing particle. However, this problem can be solved by modulating or redirecting the laser-generated electromagnetic fields using a material medium or structure. Because of the high power loss in metals at optical frequencies, dielectrics are the only viable candidate for confinement of the electromagnetic energy in such schemes. The damage thresholds of dielectric materials exposed to a pulsed laser beam corresponds to accelerating fields in the range of 1 to 10 GV/m, which are 1 to 2 orders of magnitudes above conventional accelerators. The first demonstration of electron acceleration within an enclosed dielectric structure operating at optical wavelengths was reported in 2013 and accelerating gradients exceeding 300 MV/m were achieved in a fused silica structure at the laser wavelength of 800 nm [Peralta13].

The DLA is distinguished from the LWFA in several ways. The fields in DLAs are confined in static dielectric structures instead of dynamic plasmas. DLAs are driven by high-average-power μ J-class lasers and operate with temporally short (tens to hundreds of attoseconds) and low charge (fC) bunches at high repetition rates (10 to 100 MHz), while LWFAs are typically driven by high-peak-power terawatt or petawatt class lasers and operate with high-charge (pC to nC) and longer (hundreds of attoseconds to a few tens of fs) bunches at low repetition rates (a few hertz) [England16].

The Accelerator on a Chip International Program (ACHIP) funded by the Gordon and Betty Moore Foundation aims to demonstrate a working prototype of a particle accelerator on a chip until 2021. Being part of the ACHIP collaboration DESY aims to carry out related test experiments at the SINBAD facility. The goal is to inject ultra-short relativistic electron bunches produced by the ARES linac into a DLA structure for further acceleration or deflection. In the planned ACHIP experiment at the ARES linac, the 1033 nm cathode laser beam will be split into two beams. One will be down-converted to 257 nm and delivered to the cathode, while the other will be up-converted to 2000 nm to drive the DLA [Mayet17].

2.2.4 Terahertz-driven accelerators

Terahertz (THz) radiation occupies a region between radio frequency and infrared light waves. Similar to the conventional RF travelling-wave structure, THz radiation is a practical option to accelerate co-propagating electrons in a waveguide. On one hand, its wavelength is long enough that waveguides can be fabricated with conventional machining techniques. Moreover, the required synchronization between the THz wave and the electron bunch is achievable. For instance, at 0.3 THz, the wavelength is 1 mm and 1 degree of phase jitter corresponds to 10-fs timing jitter. On the other hand, its frequency is high enough that the threshold of the electric field for high-voltage surface breakdown can reach several GV/m. In addition, very short (<100 ps) THz pulses can be generated which allows for a limited amount of average power loading at high repetition rates (on the order of kHz and above). Using a traveling-wave THz waveguide to accelerate electrons was experimentally demonstrated in 2015 [Nanni15].

The AXISIS experiment is a collaboration between DESY, CFEL (Center for Free-Electron Laser Science) and the University of Arizona aiming to develop a compact, fully coherent attosecond X-ray source for attosecond serial X-ray crystallography and spectroscopy using a THz-driven accelerator [Kaertner16]. The AXISIS experimental setup is illustrated in Figure 2.15. The ultra-compact, THz-driven, dielectric-loaded gun and traveling-wave structures will be used to generate electron bunches of 0.1 ~ 5 pC charge and then accelerate them to 15 ~ 26 MeV at kHz repetition rate. The bunch length is expected to be less than 1 fs due to the ultra-short accelerating wavelength and very high accelerating gradient. The electrons are subsequently focused and collide with a high power laser to create photons at 12 keV by coherent inverse Compton scattering. The electrons are subsequently focused and collide with a high power laser to create photons at 12 keV by coherent inverse Compton scattering.

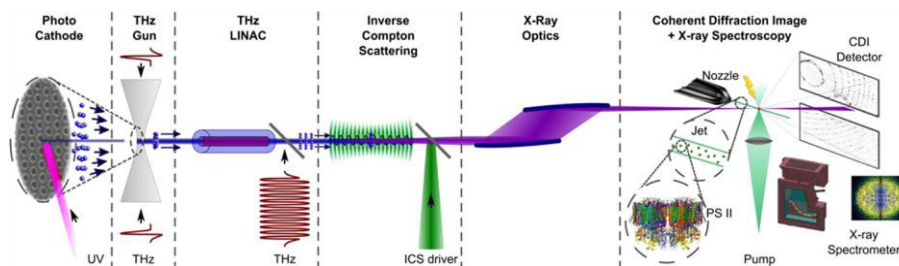


Figure 2.15: Schematic layout of the AXISIS experiment.

2.2.5 Summary of the major parameters of novel acceleration techniques at SINBAD

The characteristics of the above mentioned different novel accelerators are summarized below. Ultra-short (sub-fs to dozens of fs) electron bunches with a few μm transverse spot sizes which are foreseen to be produced at the ARES linac will serve as ideal probes for optimizing the acceleration qualities by using all these different methods.

Table 2.1: Summary of the novel accelerators considered at the SINBAD facility. For LWFA and PWFA, the values refer to externally injected witness beams.

	LWFA ¹	PWFA	DLA ²	THz-driven accelerators ³
Accelerating gradient	< 100 GeV/m	< 10 GeV/m	< 5 GeV/m	< 1 GeV/m
Accelerating period	< 330 μm	< 330 μm	$\sim 2 \mu\text{m}$	< 1 mm
Bunch charge	< 30 pC	< 30 pC	< 1 pC	< 5 pC
Bunch length (rms)	< 30 fs	< 30 fs	< 1 fs	< 100 fs
Repetition rate	< 10 Hz	< 50 Hz	> 10 MHz	> 0.1 kHz
Aperture	< 10 μm	< 10 μm	< half of the accelerating period	$\sim 1 \text{ mm}$

¹ A. F. Pousa and E. Svystun, private communication

² F. Mayet, private communication

³ T. Vinatier, private communication

3 Simulation Codes and Tools

Beam dynamics simulations are essential to understanding important issues that affect present and proposed accelerator facilities. The beam dynamics effort covers topics such as beam-beam effects, space-charge effects, synchrotron radiation, wakefield effects, high-order optics, intrabeam collisions and so on. During the design of the ARES linac, the influences of the space-charge and CSR effects have been investigated in depth by different codes. Besides, the high-order optics is also important during the design of the dogleg beamline. In the first part of this chapter, the major features of the accelerator codes used in the ARES linac design are highlighted.

The purpose of the beam dynamics simulation is to find out one or several optimized working points. Usually, the optimization is performed with extensive start-to-end simulations. However, simulations of the collective effects are normally computationally expensive. Moreover, a large number of parameters have to be tuned with different kinds of constraints being considered. Therefore, the optimization of a linac design can be a long, complicated and boring process. Optimization algorithms have thus been introduced to solve this kind of problems automatically. For example, the evolutionary algorithm was successfully applied to optimize a DC photoinjector [Bazarov05] and a linac-driven FEL [Bartolini12]. In recent years, Paul Scherrer Institut (PSI) has been developing a very powerful accelerator library OPAL which almost covers the usages of all the other accelerator codes [Adelmann]. A multi-objective optimization package built on top of PISA [Fonseca03] is included in this library, but a high performance computing cluster is required.

In order to have a relative computationally cheap and user-friendly tool to perform the optimization tasks with space charge and CSR effects included, an objective-oriented Python application programming interface - LinacOpt, has been developed by the author. In addition to the ARES linac design, the planning ACHIP experiment is also using LinacOpt to optimize the beam dynamics [Mayet17]. In the second part of this chapter, a brief introduction of LinacOpt is presented.

3.1 Accelerator Codes

3.1.1 ASTRA

The code ASTRA (A Space Charge Tracking Algorithm) [Floettmann-website] is a quasi-static code that tracks particles through user defined external field taking into account the space-charge field of the particles as well as the mirror charge near the cathode. Here, the quasi-static means that the static electric field is calculated in the beam frame and both electric and transverse magnetic fields are included in the laboratory frame. It should be pointed out that the validity of the quasi-static model breaks down for beams with large relative momentum spread. There are both 2-D cylindrical symmetric and 3-D space-charge algorithms implemented in ASTRA. A cubic spline interpolation is employed within the cylindrical symmetric grid while only a linear interpolation is applied to the grid in the 3-D algorithm. Also, the 3-D space charge algorithm is not applicable for the emission of particles from the cathode. Therefore, only the 2-D cylindrical-symmetric algorithm was used in this thesis. For the calculation of the 2-D cylindrical-symmetric space-charge field, user-defined grids consisting of rings in the radial direction and slices in the longitudinal direction are set up, and two more rings and four more slices are added outside of the bunch. The grids are Lorentz transformed into the average rest system of the bunch, and the static electric field is calculated by integrating numerically over the rings. A constant charge density inside each ring is assumed. The field contributions of the individual rings are added up and then transformed back into the laboratory system. Outside of the grid the space-charge field is approximated by a $1/r$ extrapolation so that the space charge field is defined over the whole space.

A very useful feature in ASTRA is the automatic procedure which scales the space charge field and the grid dimensions with the variation of the beam size, the beam energy and so on, which makes it much faster than other codes and suitable for parameter scan, optimization and jitter study of the photoinjector. This algorithm is applicable because the space-charge field of the bunch is (at least at sufficient high energies) a slow time-varying function. A new calculation of the field on the grid center points is initiated every time the scaling factor of the field exceeds a user-defined limit.

3.1.2 IMPACT-T

IMPACT-T [Qiang06] is a fully three-dimensional quasi-static beam dynamics code in time domain for modeling high-brightness electron beams in photoinjectors and RF linacs. It can take into account space charge forces, short-range longitudinal and transverse wakefields and CSR effect [Qiang12]. However, since it is totally in time domain, i.e. the accuracy of the timing is the time step, it cannot be used for timing jitter study.

An outstanding feature of IMPACT-T is that it includes mean-field space-charge solvers based on an integrated Green function to efficiently and accurately model beams

with large aspect ratio, e.g., during emission of electrons from a cathode or ultra-short bunches. It also includes a shifted Green function which can efficiently treat image charge effects of a cathode. Another important feature of IMPACT-T is that the initial laser pulse can be divided into a number of short slices, which results in a small velocity spread of electrons within each slice. When calculating the space-charge forces, the Poisson equation is solved in the beam frame and the electromagnetic fields are Lorentz transformed back to the laboratory frame individually for each slice. The total space-charge fields at a given location are then added up from the contributions from all the slices. This scheme is useful when electrons emit from a photo-cathode, where the difference between the momentum of electrons in the tail and in the head is significant and nonrelativistic so that there is no single Lorentz transform available.

It is worth noting that it is rather unphysical to separate the velocity and the radiation fields which both come from the same Liénard-Wiechert (LW) potential. However, since CSR requires the bunch phase space history to be recorded and then used to estimate the effects of the retarded field at the present time, in order to carry out the simulation with a reasonable time, the separation is the approach commonly being used.

3.1.3 CSRTrack

CSRtrack [Dohlus04][Dohlus06] is a code for the simulation of CSR effect on the beam dynamics of linear accelerators. There are two different types of CSR models in CSRTrack. One is the 1-D CSR model, which is similar to the 1-D model implemented in IMPACT-T. The other is the so-called ‘sub-bunch’ model, in which the beam is tracked by the following procedure in each time step:

- First, the 3-D distributed particles are projected onto the bending plane and the retarded trajectories are calculated by back-tracking without the inclusion of the self-force.
- Second, the “point-to-point” L-W potentials are evaluated by replacing each source particle with a 3-D Gaussian sub-bunch having equal charge and shape, i.e. the “sub-bunch-to-point” interaction is calculated with all the “points” on the bending plane. Since the center of each sub-bunch is the location of the corresponding source particle, the self-force has no vertical component because of the symmetry of the bending plane.
- Finally, the initial 3-D distributed particles are pushed by the 2-D self-force and 3-D external forces (e.g. the magnetic field of the dipole magnet). A hard-edge model of the dipole magnet was included in CSRTrack.

According to the above description, the projected shapes of the sub-bunches in x-z and y-z planes in CSRTrack are shown in Figure 3.1.

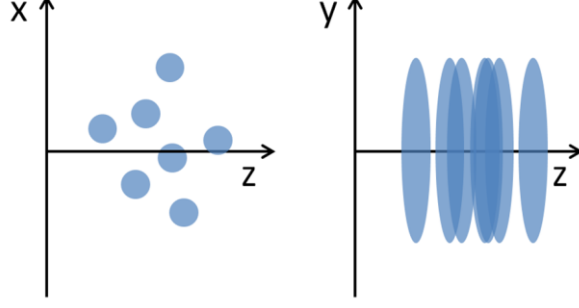


Figure 3.1: Projected shapes of the sub-bunches in CSRTrack.

In CSRTrack, the 3D integration of the retarded source is calculated by the convolution of the quantities of a line charge density $\lambda(s, t)$ traveling along the path $\mathbf{r}_s(s)$ with a transverse density function $\eta(x, y)$ [Dohlus00][Dohlus03]

$$\mathbf{X}(\mathbf{r}, t) = \int \mathbf{X}^{(\lambda)}(\mathbf{r} - \mathbf{r}_\eta(x, y), t) \eta(x, y) dx dy, \quad (3.1)$$

where \mathbf{X} and $\mathbf{X}^{(\lambda)}$ are the 3D and 1D quantities respectively. In the Lorentz gauge, the 1-D scalar and vector potential are given by

$$\Phi^{(\lambda)}(\mathbf{r}, t) = \frac{1}{4\pi\epsilon_0} \int \frac{\lambda(s, t')}{R(\mathbf{r}, s)} ds, \quad (3.2)$$

and

$$\mathbf{A}^{(\lambda)}(\mathbf{r}, t) = \frac{\beta}{4\pi\epsilon_0 c} \int \frac{\lambda(s, t')}{R(\mathbf{r}, s)} \mathbf{u}_s(s) ds, \quad (3.3)$$

where ϵ_0 is the permittivity of free space, $R(\mathbf{r}, s) = \|\mathbf{r} - \mathbf{r}_s\|$, $t' = t - R(\mathbf{r}, s)/c$ and $\mathbf{u}_s(s)$ is the unity vector in the tangential direction of the trajectory. Since the bending plane is the symmetric plane for all the sub-bunches, the vertical sub-bunch size changes the volume of the 3D charge distribution during the self-force calculation, while the longitudinal and horizontal sub-bunch sizes determine the resolution of the 2-D self-force. It is obvious that the strength of the self-force increases as the vertical sub-bunch size decreases. In addition, the integration for the line charge is split into a singular part and a residual part. The latter is assumed to be weakly dependent on the transverse offset. Therefore, in principle, the sub-bunch method in CSRTrack is not suitable for sub-bunches with very large transverse-to-longitudinal aspect ratios.

The most time consuming part in the sub-bunch method is the 3-D integration of the retarded force. For the *p_to_p* method, $M \times N$ 3-D integrations need to be done in each step, where N is the number of sub-bunches and M is the number of test particles. For the *g_to_p* method, the electromagnetic fields of a reference sub-bunch that travels along a reference trajectory are used to approximate the fields of other sub-bunches. Therefore, only M_g 3-D integrations are performed at each step, where M_g is the number of grids on the horizontal plane. Although additional $M \times N$ interpolations on the mesh

are required at each step, the g_to_p method was tested to be much faster than the p_to_p method when the number of particles is significantly larger than 1000 [Dohlus06].

It is worth noting that the transverse focusing force of a dipole magnet behaves like a quadrupole magnet in CSRTrack. Namely, the horizontal and vertical kicks are proportional to the horizontal offset and the vertical offset individually (with the same strength but the opposite sign). Because of the significant numerical effort, the absence of the vertical force and the quadrupole-like dipole focusing force, CSRTrack was only used to benchmark the simulation results from IMPACT-T in this thesis, i.e. to make sure that IMPACT-T did not largely underestimate the 3-D CSR effect.

3.1.4 ELEGANT

ELEGANT (ELEctron Generation ANd Tracking) is a very powerful accelerator simulation code developed by Borland for circular and one-pass accelerators [Borland00]. In addition to calculation and optimization of beam optics, ELEGANT has capabilities of 6-D tracking using matrices up to third order, canonical integration, and numerical integration using standard beamline elements as well as 1-D CSR [Borland01], wakefields, RF elements, kickers, apertures, scattering, and so on.

Since ELEGANT cannot handle transverse space charge effects, it is normally used to track the beam downstream of the photoinjector, where the space charge forces have been weakened enough.

3.2 LinacOpt

A general nonlinear optimization problem can be formulated as solving the objective function

$$\text{minimize } f(\mathbf{x}), \quad \mathbf{x} = (x_1, \dots, x_n) \in \mathcal{R}^n, \quad (3.4)$$

where

$$x_{i,l} \leq x_i \leq x_{i,u}, i \in \{1, \dots, n\} \quad (3.5)$$

with m_e equality constraints

$$h_j(\mathbf{x}) = 0, j \in \{1, \dots, m_e\} \quad (3.6)$$

and $m - m_e$ inequality constraints

$$g_j(\mathbf{x}) \leq 0, j \in \{m_e + 1, \dots, m\}. \quad (3.7)$$

In beam dynamics simulations, since the derivative of the objective function is typically not available, only non-derivative optimization algorithms can be used.

3.2.1 pyOpt

pyOpt [pyopt-website] is an object-oriented framework for formulating and solving optimization problems in an efficient, reusable and portable manner. There are more than ten optimizers in pyOpt with most of them being derivative based optimization

algorithms. Only ALPSO, NSGAI and SDPEN have been found to be suitable for solving the beam dynamics optimization problem. Here, ALPSO stands for Augmented Lagrange Particle Swarm Optimization, NSGAI stands for Non-dominated Sorting Genetic Algorithm II and SDPEN is a sequential penalty derivative-free method for nonlinear constrained optimization. The first two algorithms are useful in global optimization while the last one is only suitable for local optimization. In a very preliminary benchmark, ALPSO was faster and obtained a better solution in a photoinjector optimization compared with NSGAI, where the emittance of the beam is the objective function. Therefore, only ALPSO and SDPEN algorithms were extensively used during the optimization of the ARES beamline.

A global optimizer is powerful and required in practice since the solution is independent of the starting point of the optimization. Here, a simple example is used to show the performances of the three above-mentioned optimizers. The so-called “eggholder” function is defined as

$$f(\mathbf{x}) = -(x_2 + 47) \sin\left(\sqrt{\left|x_2 + \frac{x_1}{2} + 47\right|}\right) - x_1 \sin\left(\sqrt{|x_1 - x_2 - 47|}\right). \quad (3.8)$$

The plot of the above function is shown in Figure 3.2. It shows that there are many local minimums for the function with the global minimum being -959.64 at $(x_1, x_2) = (512.00, 404.23)$. This sort of function is difficult for a local search optimizer since it will be trapped by one of the local minimums based on the location of the starting point. Hence a global optimizer is desired. With the default setting of the solver ALPSO, the global minimum was found after 1480 evaluations. However, the local search minimizer SDPEN could only find a local minimum -935.34 at $(x_1, x_2) = (439.48, 453.98)$.

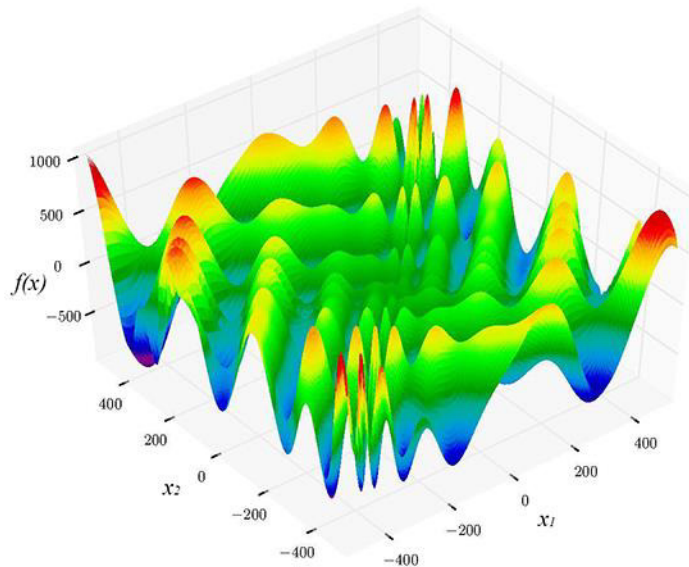


Figure 3.2: Plot of the “eggholder” function.

ALPSO

The particle swarm optimization (PSO) algorithm was first introduced by Kennedy and Eberhart [Kennedy95]. This algorithm is based on the observation of individuals of bird flocks or fish schools as well as their collective behavior as a swarm, and it utilizes the swarm intelligence to find the best place in the search space. In the very basic PSO method, the location and velocity vectors of the i -th particle at iteration $k+1$ are updated as

$$\mathbf{x}_i^{k+1} = \mathbf{x}_i^k + \mathbf{v}_i^{k+1}\Delta t \quad (3.9)$$

and

$$\mathbf{v}_i^{k+1} = w\mathbf{v}_i^k + c_1r_{1,i}^k \frac{\mathbf{x}_{i,best}^k - \mathbf{x}_i^k}{\Delta t} + c_2r_{2,i}^k \frac{\mathbf{x}_{swarm}^k - \mathbf{x}_i^k}{\Delta t} \quad (3.10)$$

respectively. Here Δt denotes the time step size, $\mathbf{x}_{i,best}^k$ and \mathbf{x}_{swarm}^k are the best position of the i -th particle and the swarm have obtained before iteration $k+1$ respectively, $r_{1,i}^k$ and $r_{2,i}^k$ are uniformly distributed in $[0, 1]$ and represent the stochastic behavior of the algorithm, c_1 and c_2 are “trust” parameters indicating how much confidence a particle has in itself (c_1) and how much confidence it has in the swarm (c_2), and w is the inertia weight.

Similar to other stochastic optimization algorithms, the basic PSO algorithm is defined for unconstrained problems. In order to be able to handle various real-life complex engineering optimization problems with equality and inequality constraints, the Augmented Lagrange PSO (ALPSO) was proposed by Sedlaczek and Eberhard [Sedlaczek06].

SDPEN

SDPEN is a derivative-free algorithm for local general constrained optimization problems [Liuzzi10]. The algorithm solves the original nonlinear constrained optimization problem by a sequence of approximate minimizations of a merit function where penalization of constraint violation is progressively increased. At each sequence, a line-search based method is used with convergence to stationary points enforced using a suitable combination of the penalty parameter updating and different sampling strategies.

3.2.2 LinacOpt

LinacOpt is a light-weight object-oriented Python application programming interface (API) built on top of pyOpt, which was developed by the author to solve the optimization problems in beam dynamics simulations with ASTRA and IMPACT-T. It can also be easily extended to include other codes. The motivation of writing this API is to provide a tool for linac optimization when the photoinjector must be included for a start-to-end optimization or the space-charge effects are non-negligible in the magnetic

lattice. Therefore, it serves as a complement for the optimization module included in ELEGANT.

The design of LinacOpt adopts the following principles:

- Take advantage of existing, well-benchmarked accelerator codes;
- Take advantage of existing optimization algorithms and implementations;
- Object-oriented programming;
- Open source;
- Friendly API.

The hierarchy of the classes that the user will need is shown in Figure 3.3. Three optimizers (ALPSO, NSGAI and SDPEN) from pyOpt have been integrated into LinacOpt. Both equality constraints and inequality constraints can be set by using the “Constraint” class. “FitPoints” class can be considered as a set of screens where the local beam parameters can be used in the objective or the constraint function. “Sections” class can be considered as a set of sections in the beamline, where the statistic values (e.g. mean, standard deviation) of certain beam parameters can be visited. Three different kinds of variable classes are provided in LinacOpt: “Variable” class, “CoVariable” class and “StaticVariable” class. “Variable” class defines the common variable with boundaries which is going to be optimized. “CoVariable” class offers the possibility to optimize two or more components which will change dependently. “StaticVariable” class is very useful in the multi-step optimization as a placeholder. It should be pointed out that, although the optimization problem defined in LinacOpt is single objective, multi-objective problem can also be solved by taking advantage of the local search optimizer in a multi-step optimization. Visualization classes (“PhaseSpacePlot” and “LinePlot”) have also been developed.

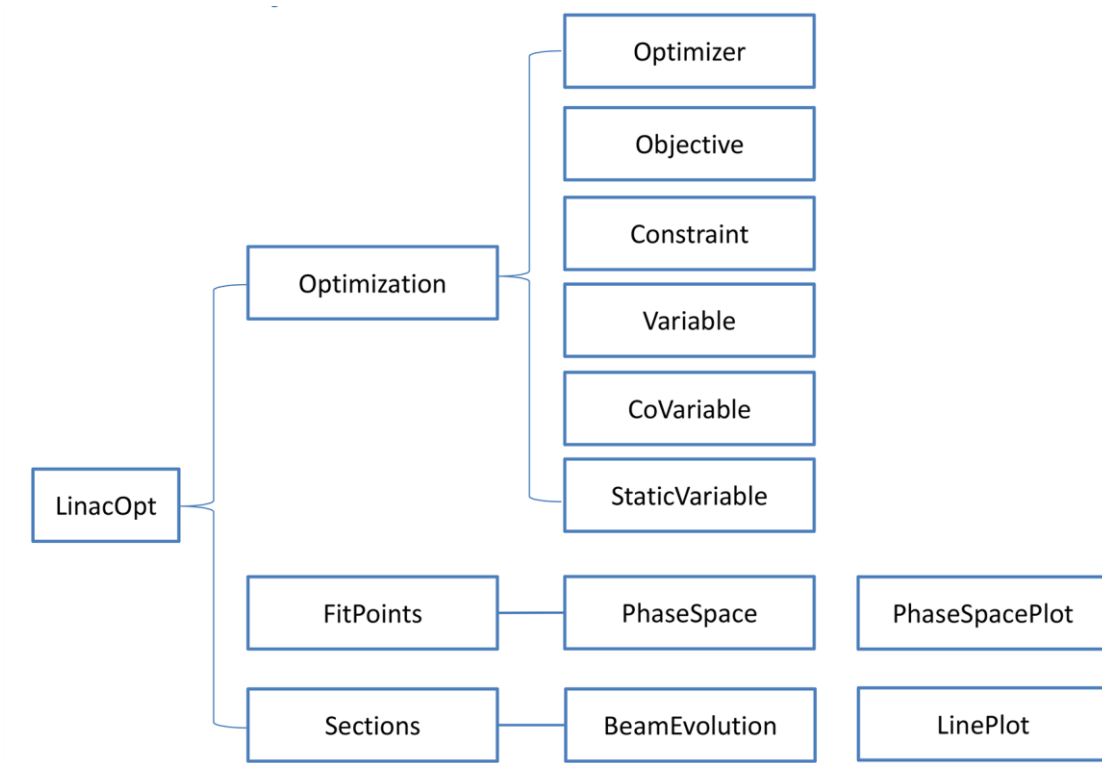


Figure 3.3: Class hierarchy for users in LinacOpt.

4 Generation of Sub-fs Electron Bunch with Sub-10 fs Bunch Arrival-time Jitter

A unique feature of the ARES linac is the ability of generating precisely synchronized electron bunches shorter than one femtosecond, reaching the attosecond region. In this chapter, generation of ~ 100 MeV electron bunches with bunch durations of sub-femtosecond (fs) and bunch arrival-time jitters of less than 10 fs via bunch slicing in a magnetic chicane are presented with analytical studies and detailed start-to-end simulations. These simulations were carried out with the combination of four different codes: ASTRA, ELEGANT, IMPACT-T and CSRTrack. The major results in this chapter have been published at

<https://doi.org/10.1103/PhysRevAccelBeams.19.054401>.

It is worth mentioning that the bunch compression simulations were benchmarked by using two different codes in order to have an in-depth understanding of compressing electron bunches to sub-fs durations when the space-charge and CSR effects are both non-negligible. The impact of the CSR effect on the beam quality during the bunch compression, when the space-charge effects are negligible, has been investigated comprehensively during the past thirty years [Saldin97][Dohlus05][Mitchell13][Hall15]. In recent years, there has been increasingly interest in compressing electron bunches at low energy, where the space-charge effects are still strong enough to spoil the beam quality [Prokop13][Zhu14][He15]. There are generally two types of models (codes) to simulate the space-charge and CSR effects simultaneously. The first model separates them in a three-dimensional (3D) quasi-static space-charge model and a one-dimensional (1D) CSR model, e.g. PARMELA_B [Koltenbah02], IMPACT-T and IMPACT-Z [Qiang-website]. As this allows for fast computations it is thus adopted in most of the reported studies. In principle, however, the space-charge and CSR forces cannot be separated as they originate from the same Liénard-Wiechert (L-W) potential, and the 1D CSR approximation only works well under certain conditions. The second model starts from the first-principle calculation, e.g. CSRTrack, Trafic4 [TraFiC4], Tredi [Giannessi03] and the L-W particle-mesh code reported by R. Ryne [Ryne13]. However, simulations with these codes are significantly more time-consuming. Prokop et al. [Prokop13] compared the simulation results from IMPACT-Z and CSRTrack for the full compression of ~ 40 -MeV electron bunches with bunch charges and durations down to 20 pC and 40 fs

respectively. While it was found that the emittance growth in the bending plane simulated by the latter is much higher than by the former, the reason was not clear. In order to better understand the magnetic bunch compression with non-negligible space-charge effects, especially when the final bunch duration is shorter than 1 fs, detailed beam dynamics studies using IMPACT-T and CSRTrack are presented in this chapter in order to understand the difference between the results from the two self-force models.

4.1 Layout of the beamline

The layout of the beamline used in this chapter is shown in Figure 4.1. The ~ 5 -MeV electron bunches generated by the 1.5-cell S-band photocathode RF-gun are accelerated off-crest to approximately 100 MeV by two 5.2-m-long S-band traveling-wave structures. There is only one gun solenoid which is the same as that being used in the SPARC lab [Ferrario13]. The distance between the cathode and the entrance of the first traveling-wave structure is about 2.5 m. Downstream of the traveling-wave structures the beamline includes four quadrupole magnets (matching section) and a magnetic chicane bunch compressor with a slit located in the middle of it, as shown in Figure 4.2.

Since the studies in this chapter were carried out in the early phase of the ARES design, the layout of the beamline is different from the layout in the final design presented in Chapter 2 and Chapter 7. However, the concepts and methods developed in this chapter apply equally to the final design.

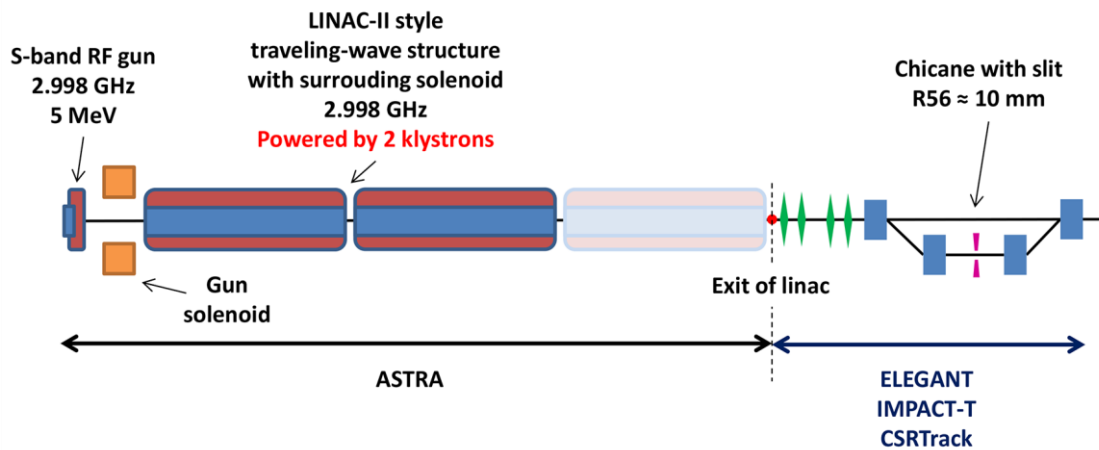


Figure 4.1: Layout of the beamline used in the study in this chapter. The blue rectangles represent dipole magnets while the green diamonds are quadrupole magnets.

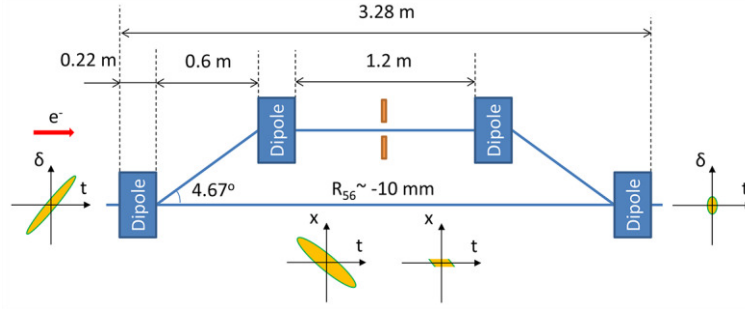


Figure 4.2: Schematic of the magnetic chicane with a slit.

4.2 Trade-off of parameters

In order to make the final bunch length as short as possible, only the full compression of the initial bunch is considered. Therefore, the chirp of the bunch at the entrance of the chicane is approximately $h \approx -1/R_{56}$. The nominal R_{56} of the chicane was -10 mm, which was identified as the optimal trade-off of the constraints discussed below.

Neglecting the high-order effect and the collective effects, at maximum compression the bunch duration achievable by a chicane is given by equation (1.39). It indicates that R_{56} should be as weak as possible in order to obtain sub-fs bunches. For instance, the minimum achievable bunch duration is 1.0 fs for $R_{56} = -30$ mm and $\delta_u = 10^{-5}$ (1 keV for a 100-MeV bunch). Furthermore, during the compression of the electron bunch in a magnetic chicane, the energy spread of the bunch will increase due to the CSR effect, which in turn will result in a longer final bunch length. The CSR effect can be reduced by using a weak chicane and a large initial correlated energy spread.

Moreover, the contributions from the RF amplitude jitter of the traveling-wave structure and the magnetic field jitter of the dipole magnet to the rms timing jitter both scale as R_{56}/c . For example, an RF amplitude jitter or a magnetic field jitter of 0.01% corresponds to a contribution of 10.0 fs for $R_{56} = -30$ mm. Therefore, a weak R_{56} is strongly desired.

However, on the other hand, reducing the R_{56} implies working more off-crest in the RF cavities and therefore reduces the overall achieved energy gain for a given RF power. A maximum gradient of 24 MV/m is required for two 5.2-m-long traveling-wave structures, which are operated at the same gradient and phase, to accelerate electrons to 100-MeV with a chirp of 100 m^{-1} ($R_{56} = -10$ mm).

In practice, the linac must be able to operate at several working points with different bunch charges. The simplest method to tune the final bunch charge is changing the slit width. However, for the sub-fs bunch generation, the non-linearity of the longitudinal phase-space and the high-order terms of the bunch compressor dominate the final bunch length. The current profile associated with the fully-compressed bunch generally consists of a high peak in the bunch head with a long trailing tail. Therefore,

the final bunch length increases quickly while the peak current remains unchanged as the slit width increases.

There is also the possibility to employ a longitudinal phase-space linearizer [Floettmann01] before bunch compression. Then a slit with larger aperture can be used to slice more electrons from the initial bunch. However, this method requires additional, costly hardware and intrinsically implies an increase of the final energy spread of the beam, which will result in significant emittance growth due to chromatic aberration in the matching section and spot size dilution at the entrance of the plasma.

To first order, the chromatic dilution of the beam size at the focal point is given by [Raubenheimer00]

$$\frac{\Delta\sigma_{\perp}}{\sigma_{\perp}} \approx \sigma_{\delta} \frac{L}{\beta_{\perp}}, \quad (4.1)$$

where σ_{\perp} is the rms transverse beam size, σ_{δ} is the rms energy spread, L is the focal length and β_{\perp} is the beta function at the focal point. At the entrance of the chicane, the rms energy spread σ_{δ} of the bunch with length σ_{z_0} and linear longitudinal phase space is approximately $\sigma_{\delta} \approx \sigma_{z_0}/|R_{56}|$. Assuming $R_{56}=-10$ mm, $\sigma_{z_0}=0.1$ mm, $\beta_{\perp}=1$ mm and $L=0.3$ m, we have $\sigma_{\delta}=0.01$ and $\Delta\sigma_{\perp}/\sigma_{\perp}=3$.

Instead of using a linearizer, the bunch charge extracted from the photocathode can be adjusted while keeping the slit width sufficiently small. The latter method was adopted in this study.

4.3 Beam dynamic simulation

4.3.1 ASTRA simulation - photoinjector

The electron bunch was first transported from the cathode to the exit of the linac by using ASTRA with four million macro particles. A two-dimensional cylindrical-symmetric space-charge algorithm was used. The photocathode laser was assumed to follow a Gaussian longitudinal distribution with rms duration of 3 ps, and a uniform transverse laser intensity distribution was taken at the photocathode. An initial kinetic energy of 0.75 eV was used to simulate the thermal emittance contribution due to photoemission from the cathode.

The two traveling-wave structures are operated at the same gradient and phase (off-crest) in order to minimize the timing jitter. Five different bunch charges were simulated and the parameters of these bunches at the exit of the linac are summarized in Table 4.1. Typically, the longitudinal phase-space of the 100-pC bunch is shown in Figure 4.3.

Table 4.1: Summary of bunch parameters at the exit of the linac.

Bunch charge (pC)	10	20	50	100	200
RMS bunch length (ps)	2.0	2.1	2.2	2.5	2.8

Normalized projected emittance (μm)	0.056	0.063	0.13	0.18	0.31
Normalized slice emittance (μm)	0.044	0.081	0.10	0.15	0.26

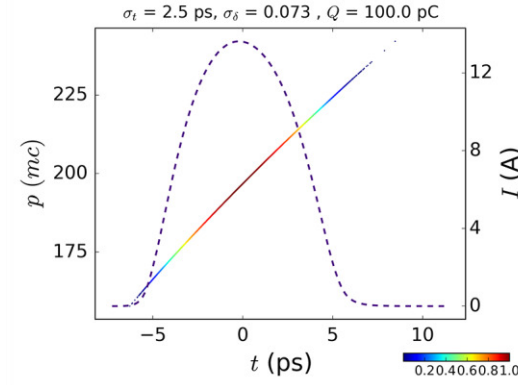


Figure 4.3: Longitudinal phase-space of the 100-pC bunch at the linac exit.

The major disadvantage of the bunch slicing method on high-charge bunches, is that a significant amount of charge will be lost at the slit, which might cause radiation protection problems. In order to reduce the losses while keeping the same overall performance, a hybrid compression scheme is also proposed. In this scheme, the electron bunch is first compressed significantly by velocity bunching in the linac and can be further compressed by the chicane with a slit. As a demonstration, a 10-pC bunch was produced at the cathode with a 200-fs-long laser pulse. Using the first traveling-wave structure as an RF compressor, the rms bunch length upstream of the chicane is reduced to 183 fs while the shape of the longitudinal phase space is almost linear. The second traveling-wave structure is operated slightly off-crest in order to increase the chirp of the bunch to about $-1/R_{56}$. The simulated projected and slice emittance are $0.14 \mu\text{m}$ and $0.15 \mu\text{m}$ respectively. The longitudinal phase-space is shown in Figure 4.4.

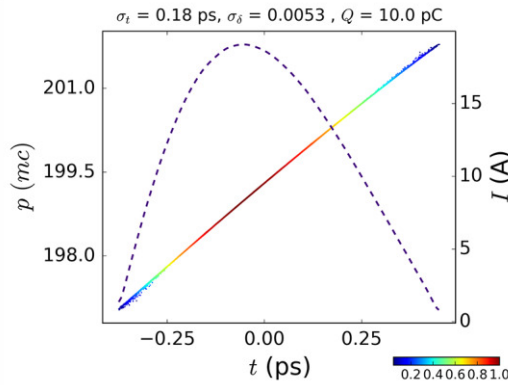


Figure 4.4: Longitudinal phases-space of the 10-pC velocity-bunched beam at the linac exit.

4.3.2 ELEGANT simulation – optics

When the bunch is fully compressed, the bunch length given by equation (1.60) is the same as equation (1.39). However, as being discussed previously, the second order

term dominates the bunch length for a fully-compressed bunch. Similarly, solving equation (1.58) for z and substituting the solution into equation (1.41) gives

$$z_f \approx R_{56}\delta_u + (R_{56}^3 h_2 + T_{566}) \left(\frac{x - x_\beta}{\eta} - \delta_u \right)^2, \quad (4.2)$$

where the third and fourth order terms have been ignored and the relationship $h \approx h_1$ has been used. Further considering $\delta_u \ll (x - x_\beta)/\eta$ and the horizontal distribution of electrons is uniform, the rms bunch length after compression is given by

$$\sigma_z \approx |R_{56}| \sqrt{\delta_u^2 + \left(R_{56}^2 h_2 + \frac{T_{566}}{R_{56}} \right)^2 \frac{(\langle x_\beta^4 \rangle + \Delta x^4 / 80)}{\eta^4}}. \quad (4.3)$$

It is not surprising to find out that the betatron beam size has a strong impact on the final bunch length via the second-order effect. As a result, the betatron beam size at the slit cannot be too large.

With the output from the ASTRA simulations, ELEGANT was then used to find the proper optics from the entrance of the matching section to the exit of the chicane. The optics was finely tuned in order to achieve the beam's beta functions of about 10 m in both planes and a horizontal beam waist at the exit of the last dipole magnet of the chicane. The final Twiss parameters of the optics largely deviate from the beam's beta functions since the abrupt changes of the Twiss parameters at the slit could not be taken into account in the optics (there is no transfer matrix for the slit), as shown in Figure 4.5. Moreover, the contribution from the dispersion was not subtracted from the beam's beta function in the horizontal plane. The full-width of the slit is 0.4 mm for the pure magnetic compression working points and 0.3 mm for the hybrid compression working point.

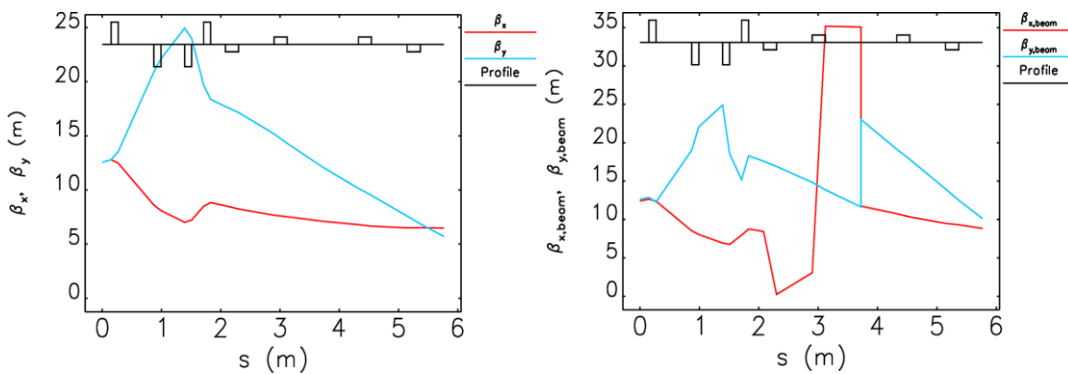


Figure 4.5: Optics (left) and beta functions of the beam (right) from the exit of the linac to the end of the chicane for the 100-pC beam. The contribution from the dispersion is not subtracted from the horizontal beta function of the beam.

4.3.3 IMPACT-T and CSRTrack simulations – bunch compression

In this section, bunches from the exit of the linac to the exit of the chicane were simulated using IMPACT-T and CSRTrack. Four million macro particles from the

ASTRA simulation were used in the IMPACT-T simulations. Due to the limit of the number of macro particles in CSRTrack, only two million macro particles could be used. A large number of macro particles are necessary in these simulations since a smooth current profile is required for the simulation of the CSR effect, while only a few percent of macro particles can pass through the slit collimator.

Before going into the details of these simulations, let's recall the discussion in Chapter 1. When the final bunch duration is of the order of sub-fs, the coupling between the transverse and longitudinal phase spaces makes the bunch length at the end of the third dipole magnet still much longer than the final value. For this reason, the impacts of the space-charge and CSR effects are mitigated considerably, which makes it possible to achieve sub-fs electron bunches with relatively high charges via a magnetic bunch compressor. In other words, only the collective effects near the end of the last dipole magnet are important in these simulations.

Numerical setup

The time steps and grid sizes used in these simulations were determined after a careful benchmark study. Because of the significant numerical effort, it is difficult to simulate millions of particles in CSRTrack using the sub-bunch model. Considering that the space-charge effects before the slit are negligible, the projected model was used before the slit with a 1-ps time step, while the sub-bunch model using the pseudo Green's function (*g_to_p* force in CSRTrack) was employed afterwards with a 50-ps time step before the last dipole magnet and a 20-ps time step inside it.

The rms longitudinal sub-bunch size was set to 1/20 of the local rms bunch length. According to the discussion in Chapter 3, the vertical sub-bunch size in CSRTrack has a strong impact on the simulation result. Therefore, three different vertical sub-bunch sizes ($\sigma_{v,sub} = \sigma_v/20$, $\sigma_{v,sub} = \sigma_v/5$ and $\sigma_{v,sub} = \sigma_v$) were compared, where σ_v is the local rms vertical bunch size. In the simulation with $\sigma_{v,sub} = \sigma_v$ the bunch almost has the same volume as the original bunch, while a sheet-like bunch was simulated actually in the other two cases. In the following, The results from CSRTrack will always be referred to as being simulated by using $\sigma_{v,sub} = \sigma_v$, unless specified otherwise.

In order to avoid a huge vertical-to-longitudinal aspect ratio of the sub-bunch, which was found to introduce unphysical energy modulation in the simulation, the longitudinal sub-bunch size was not allowed to be smaller than 1/1000 of the vertical sub-bunch size. As a consequence, the longitudinal sub-bunch size will be much larger than 1/20 of the longitudinal bunch size at the end of the compression when the vertical sub-bunch size is large. Moreover, since the code does not allow the horizontal sub-bunch size to be set as a function of the local rms horizontal bunch size, the horizontal rms sub-bunch size was fixed to be 1/20 of the rms horizontal bunch size at the exit of the chicane.

In the IMPACT-T simulations, the time step was set to 1 ps and the grid sizes in *x*, *y* and *z* planes were set to 32, 32 and 128 respectively.

Benchmark of the Space-charge effects

Although the CSR forces in IMPACT-T and CSRTrack should be quite different, the space-charge forces in both the codes are expected to be similar except in the vertical plane. In order to compare the space-charge forces simulated by the two codes, the beam dynamics of a 100-MeV, 5-pC cylindrical-symmetric Gaussian bunch was simulated. The simulations were performed for various initial bunch durations and two initial vertical bunch sizes (112 μm and 28 μm). The beam starting at its waist was tracked along a 0.1-m-long drift space, where the self-force only originates from the space-charge effects.

As shown in Figure 4.6 and Figure 4.7, the results from IMPACT-T and CSRTrack match well except for the 1-fs case in Figure 4.6. This study indicates that it is valid to set the vertical sub-bunch size equal to the vertical bunch size in the CSRTrack simulations. If the vertical sub-bunch size is chosen much smaller than the actual vertical size of the beam, the dynamics of a sheet-like bunch is simulated which overestimates the space-charge effects compared to reality. However, if the vertical-to-longitudinal aspect ratio of the bunch is chosen too large (e.g. on the left side of the plots in Figure 4.6), in order to avoid a huge vertical-to-longitudinal aspect ratio of the sub-bunch, we were forced to select a big value for the longitudinal sub-bunch size. This choice made the longitudinal sub-bunch size too large to simulate the longitudinal space-charge effect correctly.

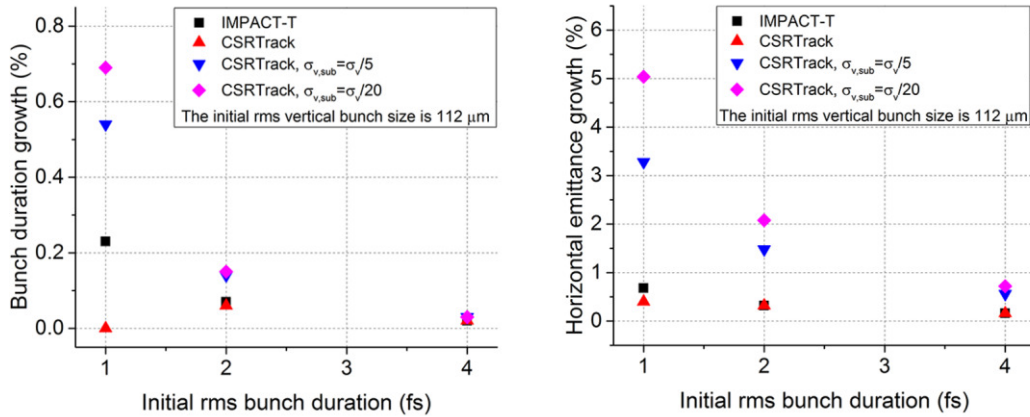


Figure 4.6: IMPACT-T and CSRTrack simulation results of the bunch duration and emittance growth of a 100-MeV, 5-pC bunch for different initial bunch durations after a 0.1-m-long drift space. The initial normalized emittance, rms energy spread, rms horizontal and vertical bunch size are 0.25 μm , 0.2%, 112 μm and 112 μm respectively. 50,000 macro particles were used.

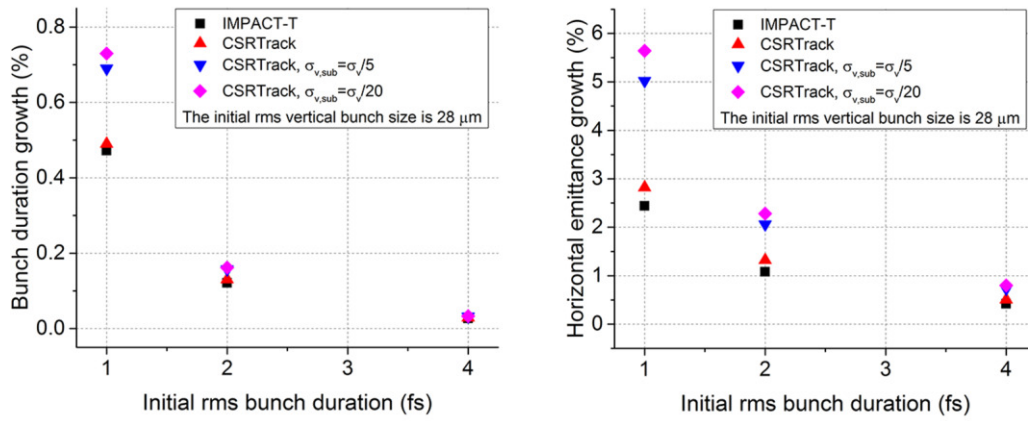


Figure 4.7: Same as Figure 4.6 but with a reduced initial vertical bunch size of $28 \mu\text{m}$.

The transverse phase-spaces of the 100-MeV, 1-fs and 5-pC bunch at the end of the 0.1-m-long drift simulated by using both codes are shown in Figure 4.8 and Figure 4.9. It is obvious that only the vertical phase-space simulated by using CSRTrack did not rotate during the beam propagation, which confirms the absence of the vertical force in CSRTrack.

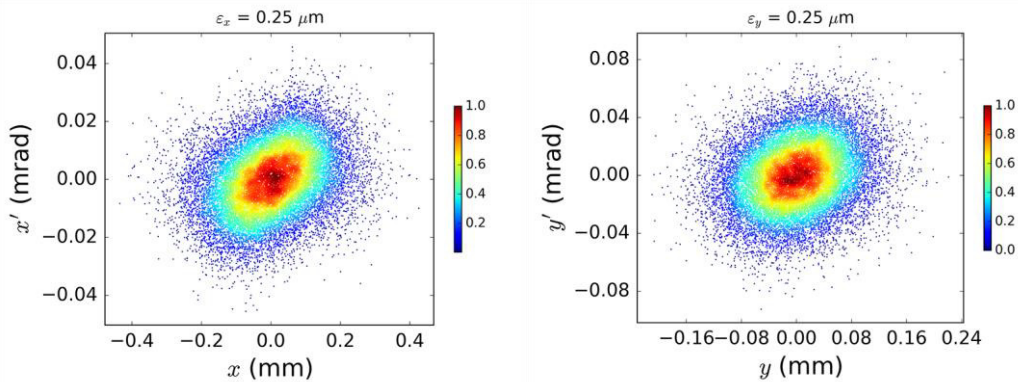


Figure 4.8: Transverse phase-spaces of a 100-MeV, 1-fs and 5-pC bunch at the end of the 0.1-m-long drift simulated by using IMPACT-T.

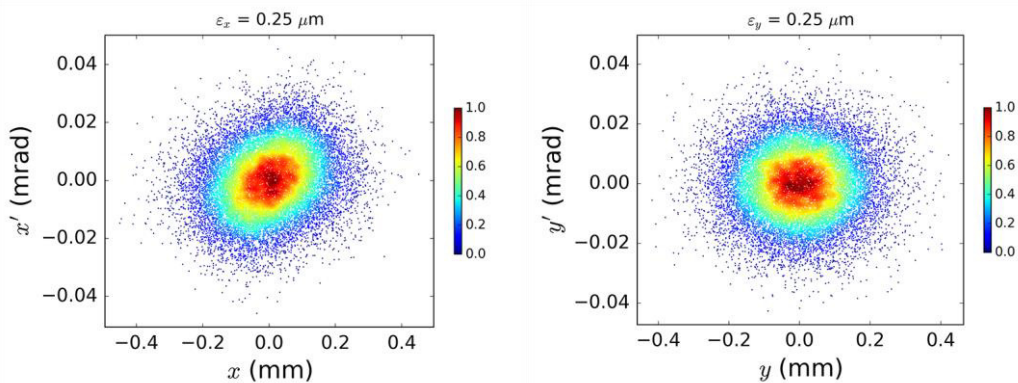
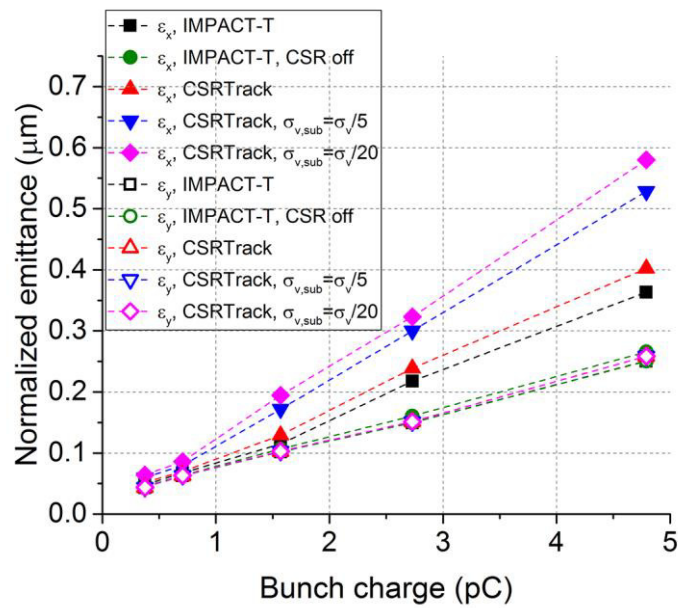
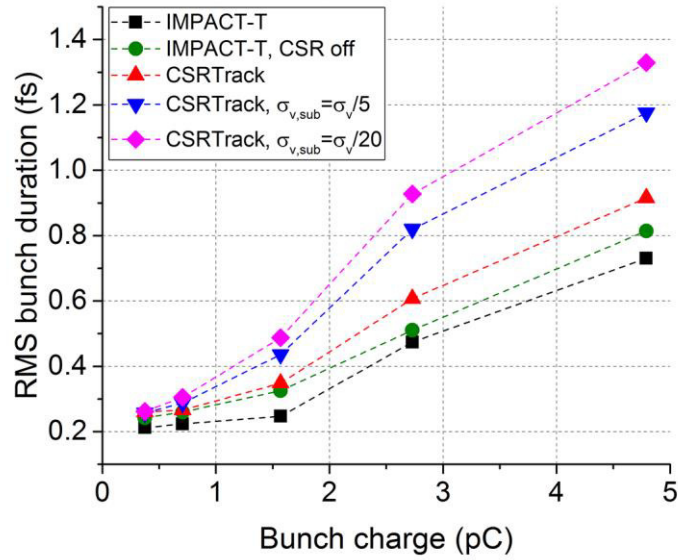


Figure 4.9: Same as Figure 4.8 except that CSRTrack was used.

Sub-fs bunch simulation results

The final bunch duration, transverse emittances and energy loss as a function of the final bunch charge are shown in Figure 4.10. The final longitudinal phase-spaces at the working point with final bunch charge of ~ 2.7 pC, simulated by both codes and under different conditions, are shown in Figure 4.11.



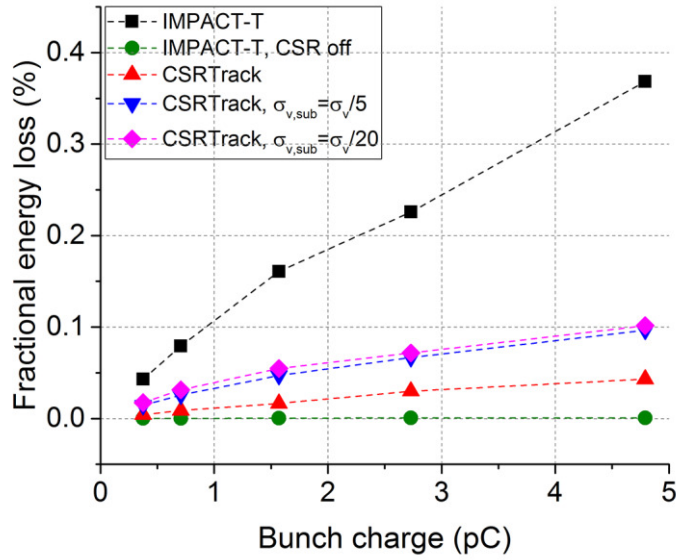
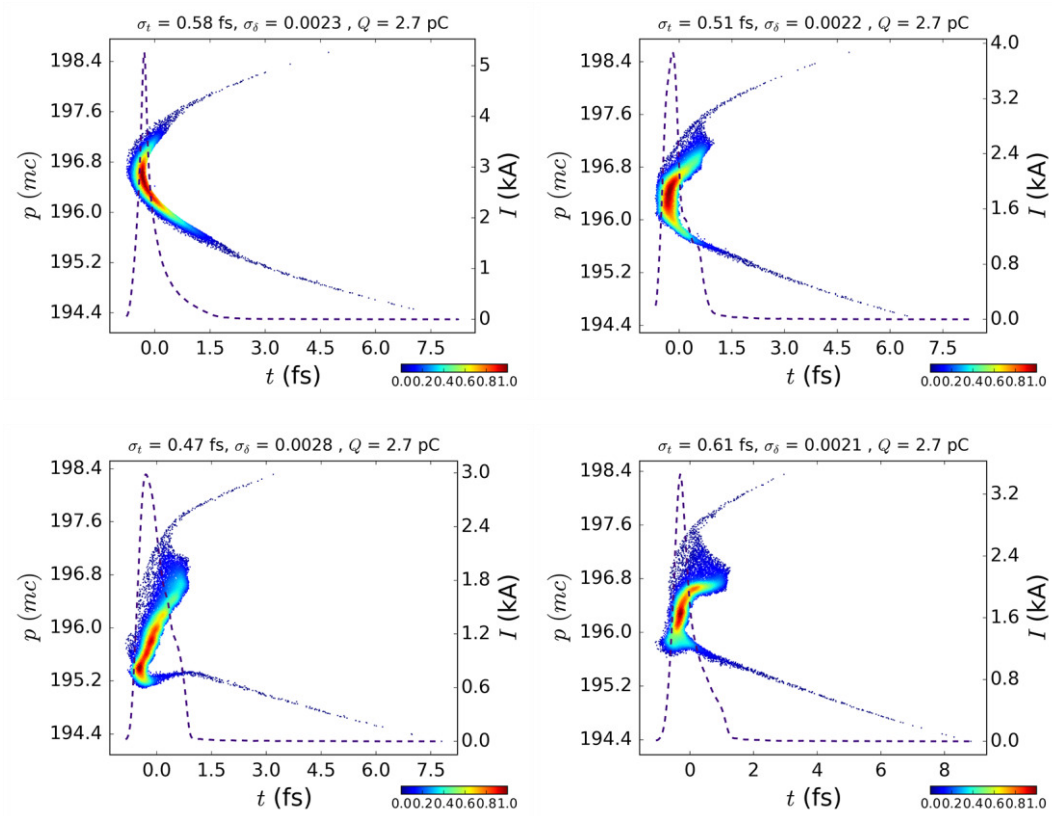


Figure 4.10: Comparisons of the bunch durations, normalized emittances and energy losses simulated by IMPACT-T and CSRTrack. The full-width of the slit is 0.4 mm.



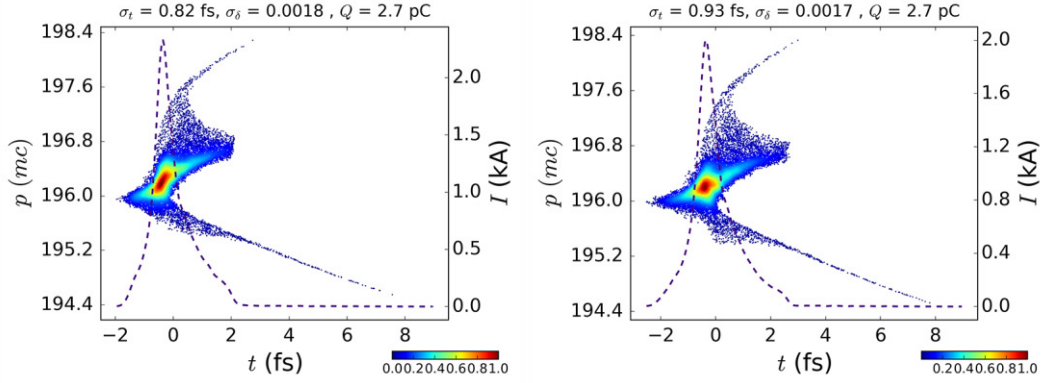


Figure 4.11: Final longitudinal phase-spaces for the 2.7-pC bunch without self-force (upper-left), simulated by IMPACT-T without CSR (upper-right), and with both space-charge and CSR effects (middle-left), as well as simulated by CSRTrack (middle-right), CSRTrack with $\sigma_{v,sub} = \sigma_v/5$ (lower-left) and $\sigma_{v,sub} = \sigma_v/20$ (lower-right).

The horizontal emittance increases quickly as the bunch charge increases. The IMPACT-T simulations without CSR effect show that the horizontal emittance growths are no more than 5%. Moreover, according to the benchmark simulations in the previous section, the emittance growth induced by the space-charge effects is expected to be small even for a sheet-like bunch. Therefore, one can conclude that the CSR effect accounts for most of the horizontal emittance dilution. On the other hand, the vertical emittances are preserved in the CSRTrack simulations because of the lack of the vertical self-force, while they increase only slightly in the IMPACT-T simulations since the space-charge effects are not strong.

Although the final longitudinal phase spaces obtained by CSRTrack and IMPACT-T are similar, the bunch durations obtained by CSRTrack are 19% to 41% longer than those from IMPACT-T, and the horizontal emittances obtained by CSRTrack are up to 13% higher than those from IMPACT-T. Since the CSR effect dominates, this difference is clearly explained by the different CSR models. In the 1D CSR model, the longitudinal CSR force of the bunch causes the longitudinally dependent energy loss in the dispersion section, which leads to the projected emittance growth. However, since the horizontal CSR force and the horizontal dependence of the longitudinal CSR force are both neglected, the horizontal emittance growth could be underestimated, especially when the bunch has a large horizontal-to-longitudinal aspect ratio. In addition, the results obtained by CSRTrack for a sheet-like bunch indicate that the vertical sub-bunch size also has a significant impact on the calculated CSR effect: the smaller the vertical sub-bunch size, the stronger the CSR effect. According to the algorithm used in CSRTrack, using a smaller vertical sub-bunch size is equivalent to simulating a bunch with a smaller vertical bunch size.

The final bunch duration increases fast as the bunch charge increases. Even if a very narrow slit is used, the second-order effect still dominates the final bunch duration when both the space-charge and CSR effects are not included. It is interesting to find

that both the space-charge and CSR effects linearize the longitudinal phase space in the IMPACT-T simulations, which makes the bunch duration even shorter. However, the final bunch duration increases considerably as the CSR effects become stronger, e.g. in the case of the sheet-like bunch results obtained by CSRTrack. The evolution of the bunch duration of the 2.7-pC bunch in the last dipole magnet is shown in Figure 4.12. As predicted by equation (1.79), the bunch duration at the entrance is significantly longer than that at the exit.

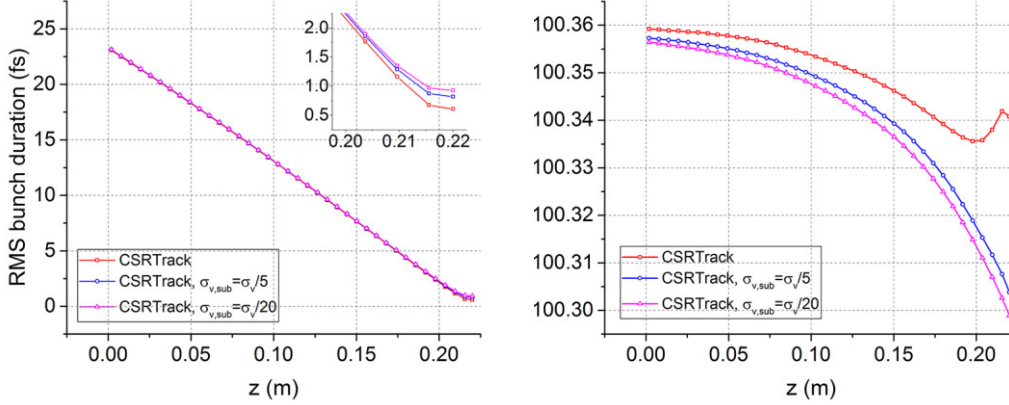


Figure 4.12: Evolutions of the bunch durations and energies in the last dipole magnet simulated by CSRTrack with different vertical sub-bunch sizes. The bunch charge is 2.7 pC.

Energy loss with different CSR models

It is notable that the energy losses obtained by CSRTrack are significantly lower than those obtained by IMPACT-T. To the largest extent this difference can be attributed to the difference in the geometry of the layouts implemented in the two codes. Due to the presence of the fringe field of the dipole magnet included in IMPACT-T, the exit of the last dipole magnet in the IMPACT simulation is about 0.11 m downstream of the one in the CSRTrack simulation. Strictly speaking, a drift space should be added in the CSRTrack simulation to include the additional energy loss in order to be able to compare the two codes. It should be pointed that the energy loss in the drift space after the last dipole magnet will not affect the bunch emittance and duration because the dispersion is closed.

Another factor that can explain the difference in the energy loss between the two codes is that the 1D CSR model is only valid when the dimension of the bunch meets the Derbenev criterion [equation (1.63)]. Rigorous benchmarking simulations with point-to-point L-W solver also prove that the 1D CSR model over-estimates the on-axis longitudinal CSR wakefield when the Derbenev criterion is not met [Ryne12]. For the beam parameters in our design, the Derbenev criterion is not met in most of the last dipole magnet. Therefore, the 1D CSR model will over-estimate the energy loss.

Finally, to a certain extent, the different energy loss can also be attributed to the different final bunch lengths as the CSR power is directly proportional to $\sigma_z^{-4/3}$.

More discussions on the results from CSRTrack

As discussed before, the sub-bunch model implemented in CSRTrack is not adequate for ultra-short bunches with a very large vertical-to-longitudinal aspect ratio. During the bunch compression simulation, it is also found that the energy loss simulated by CSRTrack unphysically increases at the end of the last dipole magnet, as shown in Figure 4.12. However, this is not the case if the vertical sub-bunch size or the vertical bunch size in the last dipole magnet is small. An example of the former case is the sheet-like bunch results in Figure 4.12. For the latter case, we compared the IMPACT-T and CSRTrack simulations with the bunch being more vertically convergent at the entrance of the chicane, so that the vertical bunch size in the last dipole magnet was reduced. The results are shown in Figure 4.13 and Figure 4.14.

On the one hand, the results imply that the abnormal energy change in the CSRTrack simulation does not change the final results abruptly. In fact, since this happens at the end of the last dipole magnet where the dispersion is almost closed, it should have little impact on the final results. On the other hand, these simulations once again show that the vertical bunch size has notable impact on the horizontal emittance and bunch duration. With decreasing vertical bunch size, the 1D CSR model thus increasingly underestimates the horizontal emittance and bunch duration. In addition, the longitudinal phase space distribution in the CSRTrack simulations is affected by the change in the vertical bunch size, while the longitudinal phase space are almost completely unchanged in the IMPACT-T simulations. The results indicate that a large vertical bunch size in the last dipole magnet is required in order to generate a high-quality sub-fs electron bunch.

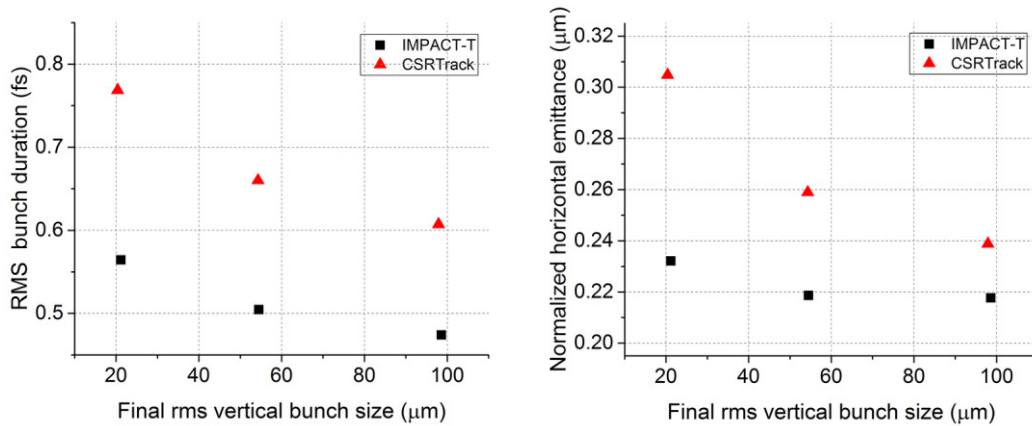


Figure 4.13: Final bunch duration and normalized horizontal emittance simulated by IMPACT-T and CSRTrack for different beam optics. The bunch charge is 2.7 pC.

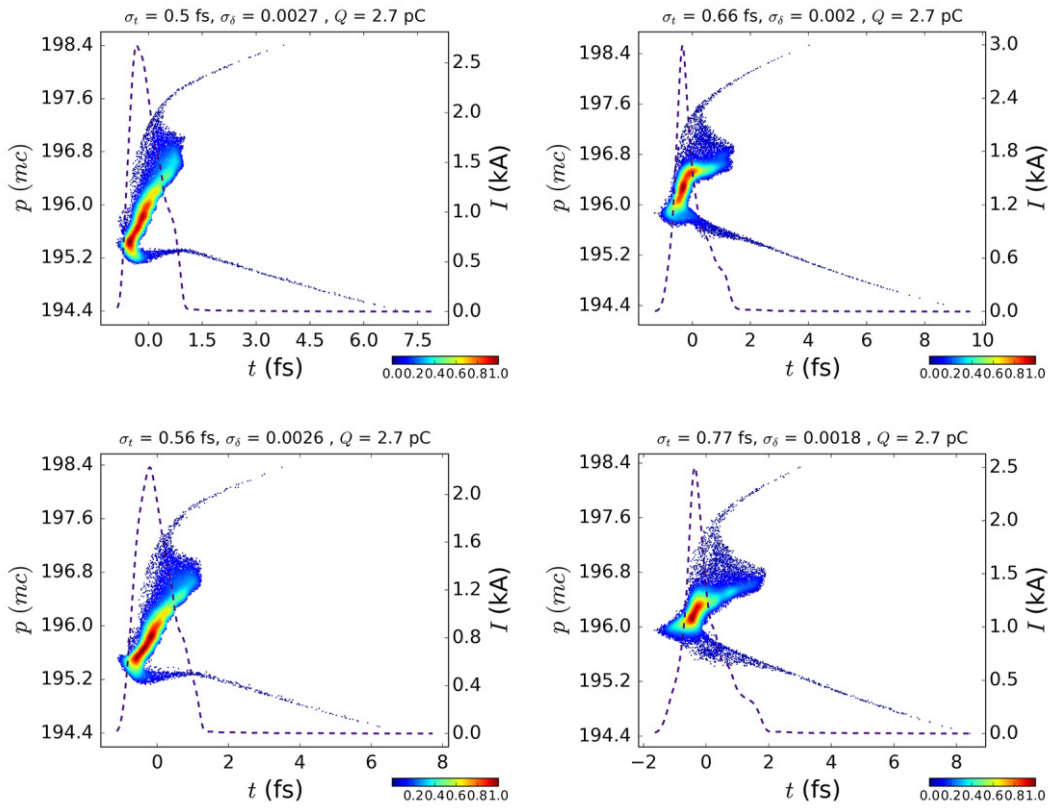


Figure 4.14: Final longitudinal phase-spaces simulated by IMPACT-T (left column) and CSRTrack (right column). The final vertical bunch sizes are about 54 μm (upper row) and 21 μm (lower row). The bunch charge is 2.7 pC.

Hybrid compression

Starting from the 10-pC velocity-bunched beam shown in Figure 4.4, a 2.7-pC bunch can be transported to the exit of the chicane by using a 0.3-mm-wide slit. The bunch durations obtained by IMPACT-T and CSRTrack are both well below 1 fs, as shown in Figure 4.15. Although the bunch durations are slightly longer than those obtained from pure magnetic compression, the final horizontal emittances become smaller. It is worth noting that only 7.3 pC electrons are lost at the slit, which is more than one order of magnitude smaller than the charge lost in the previous case with the same final bunch charge.

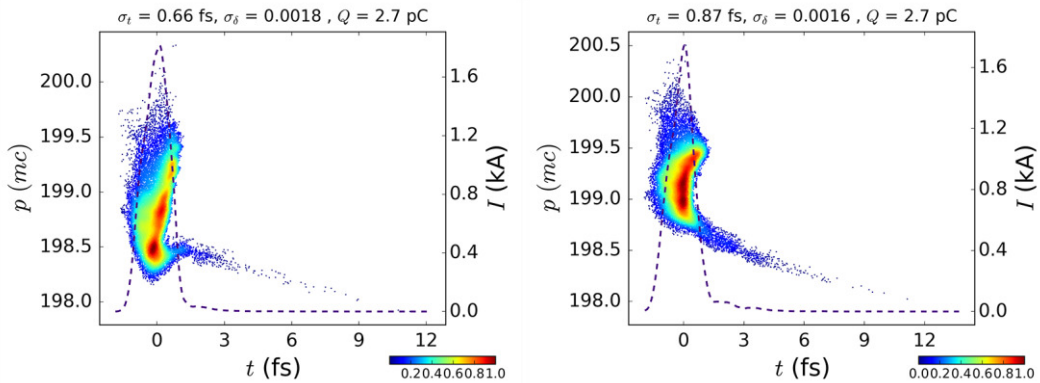


Figure 4.15: Final longitudinal phase-spaces simulated by using IMPACT-T (left column) and CSRTrack (right column) for the hybrid compression scheme. The final bunch charge is 2.7 pC and the full-width of the slit is 0.3 mm. The final normalized horizontal emittances are about 0.19 μm and 0.21 μm , respectively.

Compression without slit

Ideally, it is desirable to obtain a bunch short enough at the entrance of the chicane to eliminate the need for a slit. However, when the initial bunch length becomes too short, the CSR effect in the first and second dipole magnets becomes important. The energy loss in the first dipole magnet along a short bunch and along the central slice of a long bunch (the one which survives the transit in the slit) were calculated by equation (1.67) and are compared in Figure 4.16. It is obvious that the energy modulation induced by the CSR effect in a short bunch is significantly higher.

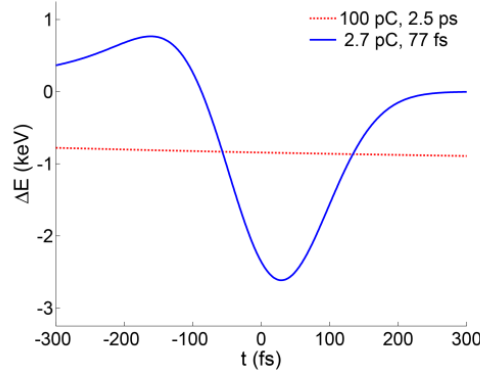


Figure 4.16: Analytical results of the energy losses along the bunch in the first dipole magnet for a short bunch compared to the central slice of a long bunch. The steady state CSR model was assumed.

The compression of such short initial bunches was also simulated by IMPACT-T and CSRTrack. For simplicity, the electrons expected to pass through the slit were filtered out from the complete bunch distribution at the entrance of the chicane and tracked afterwards. Since the initial number of the macro particles was reduced significantly, the sub-bunch model was employed throughout the complete chicane in the CSRTrack simulations. The typical longitudinal phase space of the central slice of the bunch at the entrance of the chicane and the bunch shape in the middle of the chicane are shown in Figure 4.17. The initial portion of the electrons ending up in the surviving slice is only 77 fs long. A comparison of the final bunch durations and horizontal emittances for different bunch charges and the two different codes is shown in Figure 4.18, and typical final longitudinal phase-spaces of the 2.7-pC bunch are shown in Figure 4.19. It is obvious that if the bunch charge is high, the final bunch duration obtained by tracking only the central slice of the bunch is much longer than by starting with the complete bunch. The final longitudinal phase space with the self-force switched off in the 3rd and 4th dipole magnets was also simulated. It was found that the final bunch becomes longer because of the energy modulation in the first half of the

chicane. On the other hand, the CSR effect in the first two dipoles has little impact on the final emittance. It is noteworthy that in the case of tracking only the central slice of a high-charge bunch, the final bunch durations obtained by IMPACT-T and CSRTrack match each other much better than when tracking the complete initial bunches. However, the difference between the final horizontal emittances almost does not change in the two cases.

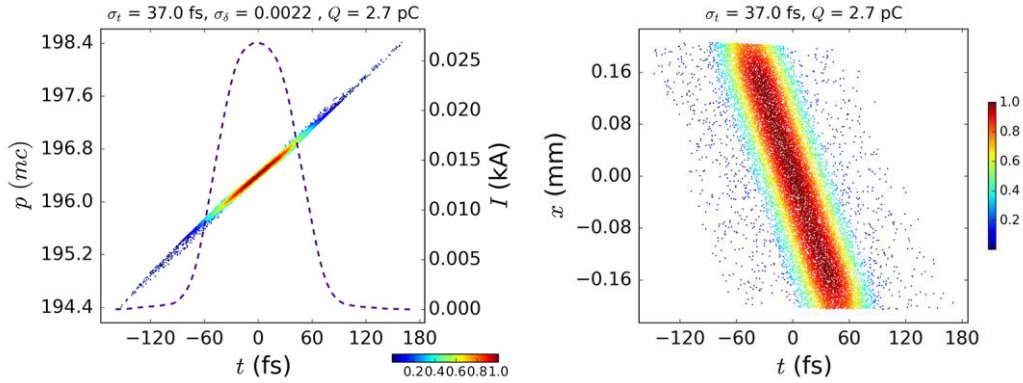


Figure 4.17: Typical initial longitudinal phase space (left) and the bunch shape in the middle of the chicane (right) when only the central slice of the bunch was tracked.

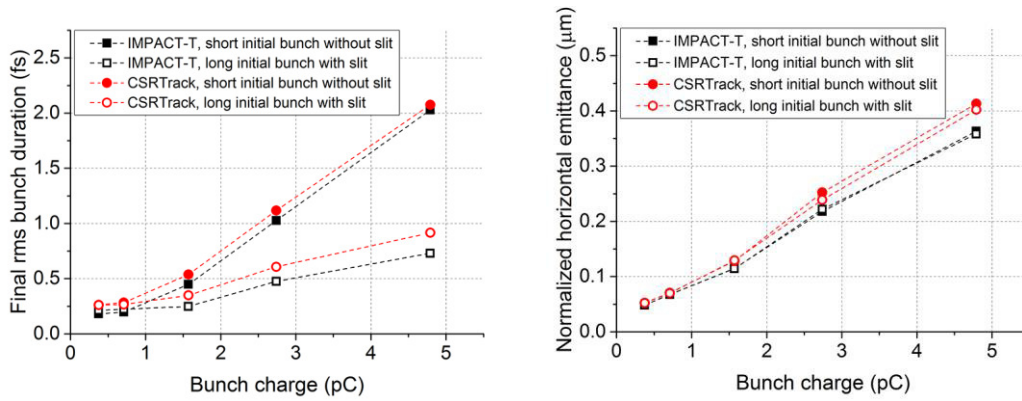


Figure 4.18: Comparisons of the final rms bunch durations and horizontal emittances simulated by IMPACT-T and CSRTrack with different initial bunches.

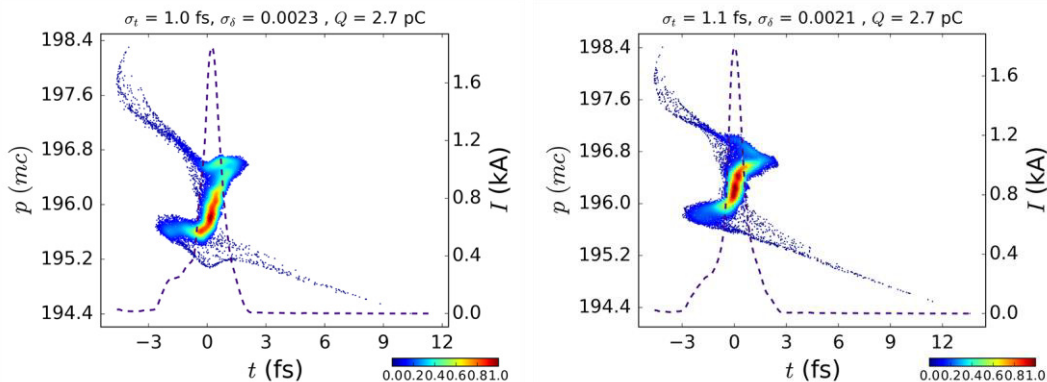


Figure 4.19: Final longitudinal phase-spaces simulated by IMPACT-T (left) and CSRTrack (right) by tracking only the central slice of the bunch. The bunch charge is 2.7 pC.

4.4 Transverse wakefields at the slit

The transverse wakefields that arise due to a change in dimensions of the vacuum chamber at the collimator are collectively referred to as the geometric wakefields. The incoming bunch which is not centered in a collimator will receive a net centroid deflection. In addition, the variation of the kick along the length of a single bunch can cause a net increase in the transverse projected emittance.

The geometry of a tapered collimator is sketched in Figure 4.20. We define $W(\tau)$ as the potential experienced by the witness particle following along the same path at the time τ behind a unit charge. It is easy to see from Causality that $W(\tau) = 0$ for $\tau < 0$. At time t , the potential in and behind an arbitrary current distribution $I(t)$ can be expressed as

$$V(t) = \int_{-\infty}^t W(t - \tau) I(\tau) d\tau = - \int_0^t W(\tau) I(t - \tau) d\tau \quad (4.4)$$

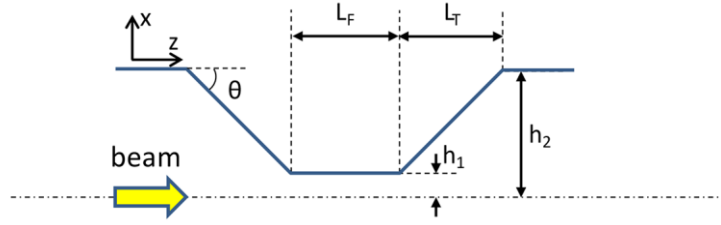


Figure 4.20: Sketch of a tapered slit collimator.

When a relativistic electron bunch with energy E passes through a symmetric flat collimator (the beam will not be collimated in the y direction) at a horizontal distance $\Delta x \ll h_1$, the mean centroid kick is given by [Tenenbaum07]

$$x'[\mu rad] = \frac{\Delta x[mm] Q[pC] \kappa[V/pC/mm]}{E[MeV]}, \quad (4.5)$$

where Q is the charge of the bunch in pC, κ is the horizontal kick factor (horizontal kick average over the length of the bunch). Analytical solution of κ can be found when the parameter $\alpha = \theta h_1 / \sigma_z$ is either smaller than 1 (inductive regime) or larger than 1 (diffractive regime). With the typical parameters at ARES: $\sigma_z \approx 11 \mu m$, $h_1 = 0.2 \text{ mm}$ and $\theta = \pi/2$, κ should be calculated in the diffractive regime.

In the diffractive regime, there are analytical formulas in the limits of short ($L_F \rightarrow 0$) and long collimators ($L_F \rightarrow \infty$). For a flat short collimator, κ is given by

$$\kappa = \frac{Z_0 c}{4\pi h_1^2} \quad (4.6)$$

with $Z_0 = 377 \Omega$. While for a flat long collimator, κ is approximately given by

$$\kappa = \frac{Z_0 c}{2\pi} \left(\frac{1}{h_1^2} - \frac{1}{h_2^2} \right) \approx \frac{Z_0 c}{2\pi h_1^2}. \quad (4.7)$$

For a long flat collimator with $h_1 = 0.2$ mm, κ is approximately 450 V/pC/mm. Generally, the horizontal kick factor of a long collimator is about twice as large as of a short collimator.

A long flat collimator is used to estimate the emittance growth induced by the horizontal wakefields here. In the case of a 10-pC bunch with 0.2- μ m emittance traveling through a collimator with $\Delta x = 0.05$ mm, we have $x' \approx 2.25$ μ rad. Assuming the horizontal beta function at the slit is 10 m, the emittance growth is then given by

$$\frac{\Delta \varepsilon_x}{\varepsilon_x} \approx \frac{\gamma \beta_x}{2 \varepsilon_x} x'^2 \approx 0.025, \quad (4.8)$$

which is negligible. In reality, since the bunch before the slice has a nearly uniform distribution in the central slice, the bunch after the collimator will be transversely uniform distributed and thus be centered relative to the axis of the slit even if the bunch is off-axis before the collimator. The experiments at FERMI@Elettra FEL [DiMitri13] and LCLS [Zhou15] with higher bunch charge and energy both confirmed that the slit collimator has little effect on the beam quality.

4.5 Timing stability

In advanced accelerators, the externally injected electron bunch is required to be synchronized with the extremely short accelerating wave. For instance, in LWFA experiments, the requirement on the synchronization of the electron bunch to the drive laser is extremely stringent in order to reduce the shot-to-shot energy variation of the electron beam. Considering a plasma with $n_e = 10^{16}$ cm⁻³ (period ~ 1.1 ps) in the linear regime with average $k_p \xi = -\pi/12$, a timing jitter of 10 fs corresponds to an energy jitter of $\sim 1.6\%$.

4.5.1 Timing system for LWFA experiments

There are two possible setups to synchronize an LWFA experiment, as shown in Figure 4.21 and Figure 4.22. In the first scenario, the timing jitter of the beam with respect to the drive laser is given by

$$\sigma_t = \sqrt{\sigma_{B2RF}^2 + \sigma_{L2RF}^2 + \sigma_A^2}, \quad (4.9)$$

where σ_{B2RF} is the jitter of the bunch arrival-time (at the plasma) relative to the master oscillator, σ_{L2RF} is the timing jitter of the drive-laser oscillator relative to the master oscillator, and σ_A is the timing jitter of the drive-laser amplifier. This is a similar situation as the seeding experiment for FEL [Maltezopoulos14], where the laser amplifier jitter is about 10 fs [Lechner14]. In the second scenario, a small split of the drive laser

will be used as the cathode laser. Hence, the timing jitter of the beam relative to the drive-laser is simply the time of flight jitter of the beam

$$\sigma_t = \sigma_{TOF}. \quad (4.10)$$

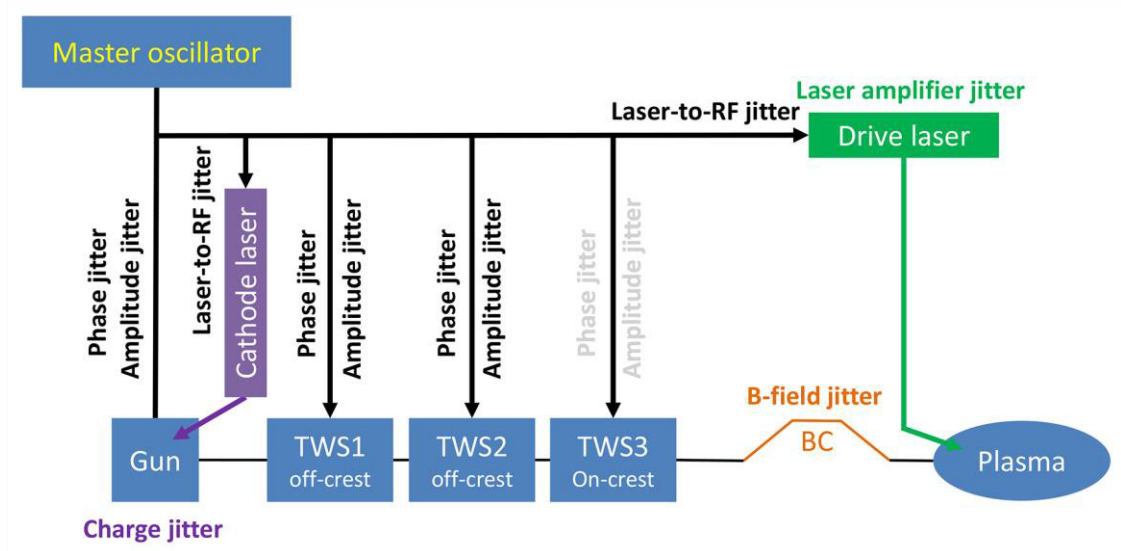


Figure 4.21: Timing structure diagram for the LWFA experiment at the ARES linac. Cathode laser and drive laser are independent.

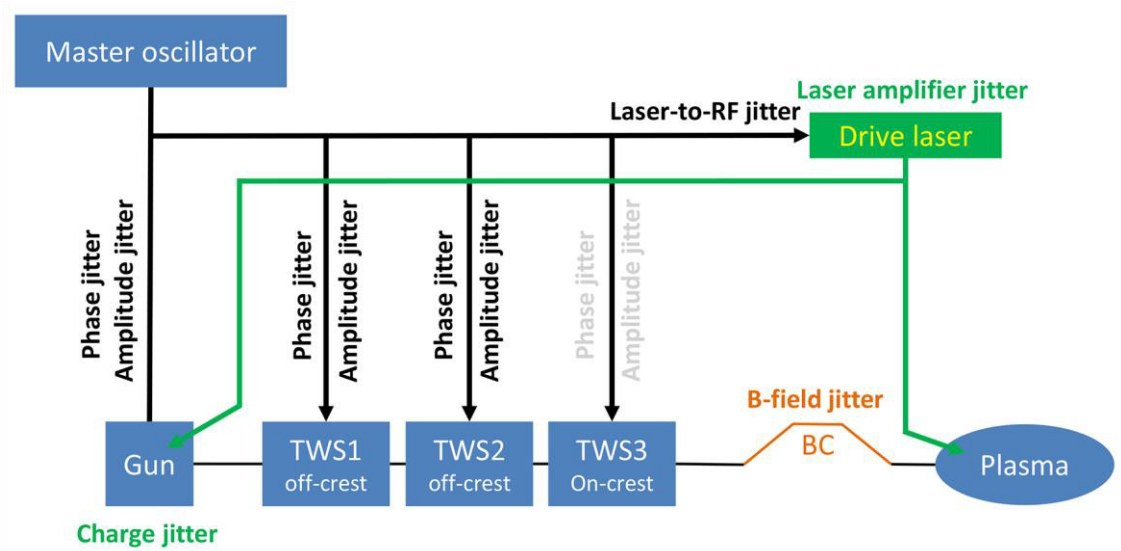


Figure 4.22: Alternative timing structure diagram for the LWFA experiment at the ARES linac. Cathode laser and drive laser are the same.

It needs to be emphasized that when σ_{B2RF} is being calculated in the first scenario, the reference for all the jitter sources (e.g. the cavity phase jitter) is the master oscillator. However, when σ_{TOF} is being calculated in the second scenario, the reference for all the jitter sources should be changed to the drive laser. Accordingly, the cavity phase jitter becomes

$$\tilde{\sigma}_\phi = \sqrt{\sigma_\phi^2 + c^2 k_{RF}^2 (\sigma_{L2RF}^2 + \sigma_A^2)}, \quad (4.11)$$

where σ_ϕ is the phase jitter relative to the master oscillator and k_{RF} is the RF wave number. It is worth noting that $ck_{RF}\sigma_{L2RF}$ and $ck_{RF}\sigma_A$ are both correlated jitters for all the cavities, no matter whether they are powered by individual klystrons or a single klystron.

4.5.2 Analytical results

Bunch arrival-time jitter after a general chicane

Considering a linac consisting of a gun with energy E_0 and N accelerating cavities powered by N independent klystrons, the final energy E can be written as

$$E = E_0 + \sum_{i=1}^N V_i \sin \phi_i, \quad (4.12)$$

where V_i and $\phi_i = ck_{RF}t_i + \phi_{i,0}$ are the voltage and phase of the i th accelerating cavity respectively, t_i is the timing jitter of the beam at the entrance of the i th accelerating cavity and $\phi_{i,0}$ is the reference phase. Here we have assumed that the phase slippage in the accelerating cavity can be neglected, i.e. the velocity bunching is weak.

In this case, the arrival-time of the beam downstream of the chicane is given by

$$dt_{B2RF} = dt_0 + dt_{bc}, \quad (4.13)$$

where dt_0 is the incoming timing jitter of the whole bunch at the entrance of the traveling-wave structure, dt_{bc} is the travelling timing difference of the bunch in the chicane. Following [Craievich13], the rms timing jitter after the chicane is given by

$$\sigma_{B2RF} \approx \sqrt{\frac{R_{56}^2}{c^2} \left[\left(\frac{E_0}{E} \right)^2 \sigma_{\delta_{E_0}}^2 + \sum_{i=1}^N V_i^2 (\sin^2 \phi_i \sigma_{\delta_{V_i}}^2 + \cos^2 \phi_i \sigma_{\phi_i}^2) + \sigma_{\delta_B}^2 \right] + (1 + hR_{56})^2 \sigma_{t_0}^2}, \quad (4.14)$$

where $\delta_{E_0} = dE_0/E_0$, $\delta_{V_i} = dV_i/V_i$, $\delta_{\phi_i} = d\phi_i/\phi_i$, $\delta_B = dB/B$ and

$$h = ek_{rf} \sum_{i=1}^N \frac{V_i \cos \phi_i}{E}. \quad (4.15)$$

For given energy and chirp, assuming the rms phase and amplitude jitters of each accelerating cavity are the same, equation (4.14) reaches its minimum

$$\sigma_{B2RF,min} \approx \sqrt{\frac{R_{56}^2}{c^2} \left[\left(\frac{E_0}{E}\right)^2 \sigma_{\delta_{E_0}}^2 + \frac{1}{N} \left(\frac{E-E_0}{E}\right)^2 \sigma_{\delta_V}^2 + \frac{h^2}{Nk_{rf}^2} \sigma_{\phi}^2 + \sigma_{\delta_B}^2 \right] + (1+hR_{56})^2 \sigma_{t_0}^2} \quad (4.16)$$

when all the cavities have the same voltage and phase.

Difference between timing systems

The total timing jitter for the first scenario of the two timing systems can be obtained by simply substituting equation (4.16) into (4.9), and one gets

$$\sigma_t \approx \sqrt{\frac{R_{56}^2}{c^2} \left[\left(\frac{E_0}{E}\right)^2 \sigma_{\delta_{E_0}}^2 + \frac{1}{N} \left(\frac{E-E_0}{E}\right)^2 \sigma_{\delta_V}^2 + \frac{h^2}{Nk_{rf}^2} \sigma_{\phi}^2 + \sigma_{\delta_B}^2 \right] + (1+hR_{56})^2 \sigma_{t_0}^2 + \sigma_{L2RF}^2 + \sigma_A^2}. \quad (4.17)$$

Similarly, the total timing jitter for the second scenario can be obtained by first substituting equation (4.11) into (4.14), and then following the similar procedure from equation (4.14) to (4.16) but taking into account that $ck_{RF}\sigma_{L2RF}$ and $ck_{RF}\sigma_A$ are both correlated jitters of all the cavities, and finally one gets

$$\tilde{\sigma}_t \approx \sqrt{\frac{R_{56}^2}{c^2} \left[\left(\frac{E_0}{E}\right)^2 \sigma_{\delta_{E_0}}^2 + \frac{1}{N} \left(\frac{E-E_0}{E}\right)^2 \sigma_{\delta_V}^2 + \frac{h^2}{Nk_{rf}^2} \sigma_{\phi}^2 + \sigma_{\delta_B}^2 \right] + (1+hR_{56})^2 \tilde{\sigma}_{t_0}^2 + h^2 R_{56}^2 (\sigma_{L2RF}^2 + \sigma_A^2)}, \quad (4.18)$$

where the tilde on $\tilde{\sigma}_{t_0}$ emphasizes that it is different from the one in the first scenario.

It is found that the second scenario can reduce the total timing jitter significantly only when the compression factor of the electron beam is small, i.e. hR_{56} is close to 0. In this case, only a small fraction of the laser-to-RF jitter and the laser amplifier jitter can be transferred to the total timing jitter. However, when the compression factor is high ($hR_{56} \approx -1$), the two scenarios yield almost the same result. In reality, a compression factor higher than 10 is normal for this kind of experiment. Therefore, the second setup does not significantly outperform the first one.

Bunch arrival-time after a chicane with slit

When a slit is put in the middle of the chicane, although the path length of the beam inside the chicane is well defined by the slit, the energy jitter upstream of the chicane will still be converted into the timing jitter downstream of the chicane. In this scenario, the timing jitter downstream of the chicane is given by

$$dt_{B2RF} = dt_0 + dt_{slice}, \quad (4.19)$$

where dt_{slice} is the timing offset jitter of the reference slice with respect to the longitudinal centroid of the whole bunch at the entrance of the chicane, as illustrate in Figure 4.23.

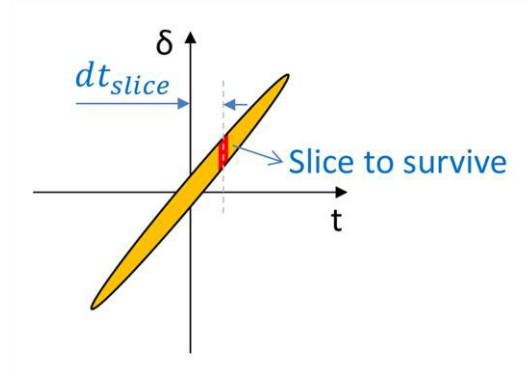


Figure 4.23: Illustration of dt_{slice} . The slice that passes through the slit usually is not the central slice of the incoming bunch.

Assuming the longitudinal phase-space has a linear chirp h , we have

$$dt_c \approx -\frac{1}{hc} \frac{dE}{E}. \quad (4.20)$$

Substituting (4.20) into (4.19), one gets

$$dt_{B2RF} \approx dt_0 \left(1 - \frac{ek_{rf}}{hE} \sum_{i=1}^N V_i \cos \phi_i \right) + \frac{1}{hc} \frac{dB}{B} - \frac{e}{hcE} \sum_{i=1}^N \sin \phi_i dV_i - \frac{e}{hcE} \sum_{i=1}^N V_i \cos \phi_i d\phi_i, \quad (4.21)$$

where we have used the following relationships

$$\begin{aligned} dE &= dE_0 - \frac{\partial E}{\partial B} dB + e \sum_{i=1}^N \left(\frac{\partial E}{\partial V_i} dV_i + \frac{\partial E}{\partial \phi_i} d\phi_i + \frac{\partial E}{\partial t_0} dt_0 \right) \\ &= dE_0 - \frac{E}{B} dB + e \sum_{i=1}^N (\sin \phi_i dV_i + V_i \cos \phi_i d\phi_i + ck_{rf} V_i \cos \phi_i dt_0). \end{aligned} \quad (4.22)$$

The magnetic field jitter is included in Equation (4.22) because the energy of the survival bunch is proportional to the magnetic field of the dipole magnet. By using Equation (4.15), the first term on the right-hand side of Equation (4.21) vanishes. Finally, the rms timing jitter is written as

$$\sigma_{B2RF} \approx \frac{1}{c} \sqrt{\left(\frac{E_0}{hE}\right)^2 \sigma_{\delta_{E_0}}^2 + \frac{\sigma_{\delta_B}^2}{h^2} + \left(\frac{e}{hE}\right)^2 \sum_{i=1}^N V_i^2 (\sin^2 \phi_i \sigma_{\delta_{V_i}}^2 + \cos^2 \phi_i \sigma_{\phi_i}^2)}. \quad (4.23)$$

Similarly, the minimum timing jitter downstream of the chicane is given by

$$\sigma_{B2RF,min} \approx \frac{1}{c} \sqrt{\left(\frac{E_0}{hE}\right)^2 \sigma_{\delta_{E_0}}^2 + \frac{\sigma_{\delta_B}^2}{h^2} + \frac{1}{N} \left(\frac{E - E_0}{hE}\right)^2 \sigma_{\delta_V}^2 + \frac{1}{Nk_{rf}^2} \sigma_{\phi}^2} \quad (4.24)$$

when all the cavities have the same voltage and phase. It is obvious that, regardless of the compression factor of the bunch, the incoming timing jitter will be totally “compressed” while the phase jitter of the accelerating cavity will be fully converted into the timing jitter downstream. Similar to the discussion on equation (4.17) and (4.18), the total timing jitters for the two timing systems mentioned previously will be almost the same in this case.

At the ARES linac, taking into account the timing jitter introduced by the gun charge jitter observed in the simulations [Zhu15-1], the timing jitter downstream of the chicane at a magnetic compression working point is then given by

$$\sigma_{B2RF} \approx \frac{1}{c} \sqrt{R_{56}^2 \left[\frac{E_0^2}{E^2} \sigma_{\delta_{E_0}}^2 + \sigma_{\delta_B}^2 + \frac{1}{2} \left(1 - \frac{E_0}{E}\right)^2 \sigma_{\delta_V}^2 \right] + \frac{1}{2k_{rf}^2} \sigma_{\phi}^2 + D \sigma_{\delta_q}^2}, \quad (4.25)$$

where $\delta_q = dq/q$ is the gun charge jitter and D is a coefficient depending on the bunch charge. One possible explanation for the gun charge jitter term is that the charge jitter could introduce perturbation into the longitudinal phase-space shape due to the space-charge effects, which will in turn affect the location of the reference slice. The gun energy jitter only slightly increases the timing jitter, e.g. a gun energy jitter of 0.1% corresponds to a timing jitter of 1.7 fs.

4.5.3 Start-to-end simulation of timing jitter

The timing jitters downstream of the chicane for working points with different bunch charges and different compression schemes were studied by S2E simulations. Since IMPACT-T is not suitable for timing jitter studies, ELEGANT was used instead to simulate the beam dynamics downstream of the traveling-wave structures. A pure velocity bunching working point with 0.5 pC bunch charge is also included for completeness, although the final bunch length is about 2.6 fs.

The sensitivity of each jitter sources was first studied individually, i.e. the particles were tracked by assigning an artificial jitter to one of the sources while assuming no additional jitter from the other sources. Within the studied ranges, the timing jitter was found to be a linear function of the jitter amplitude for each of the jitter sources. Once the sensitivities of all the jitter sources are known, the expected rms timing jitter for a certain tolerance budget is approximately given by

$$\sigma_{tb} \approx 10 \sqrt{\sum_{i=1}^n \left(\frac{j_{tol,i}}{j_{sen,i}} \right)^2} [fs], \quad (4.26)$$

where $j_{sen,i}$ refers to the amplitude of the i -th jitter source corresponding to a 10-fs timing jitter and $j_{tol,i}$ is the rms tolerance of the i -th jitter source. Equation (4.26) can be used to quickly form a tolerance budget. The statistic total rms timing jitter with the tolerance budget was calculated after 300 randomized S2E simulations, where a 3-sigma Gaussian distribution for each jitter source was assumed. The simulation results are summarized in Table 4.2 and the histograms of the timing jitter results are shown in Figure 4.24.

Table 4.2: Summary of jitter sensitivity and tolerance studies. The smaller the sensitivity value, the more sensitive the jitter source is. The total timing jitter was obtained from the randomized simulation results.

Jitter source	Unit	Sensitivity for 10-fs timing jitter				RMS Tolerance			
		20 pC	100 pC	10 pC hybrid	0.5 pC VB	20 pC	100 pC	10 pC hybrid	0.5 pC VB
Laser-to-RF	fs	42437	5950	160	125	200	200	50	50
Gun Charge	%	5.8	1.6	301.6	1010.1	1.0	0.3 (1.0)	4.0	4.0
Gun Phase	deg	1.75	0.78	0.61	0.49	0.06	0.06	0.06	0.06
Gun Amplitude	%	0.61	1.14	0.72	0.40	0.06	0.06	0.06	0.06
TWS*1 Phase	deg	0.021	0.021	0.011	0.010	0.013	0.013 (0.010)	0.009	0.009
TWS2 Phase	deg	0.022	0.022	0.130	4.214	0.013	0.013 (0.010)	0.011	0.011
TWS1 Amplitude	%	0.055	0.055	0.073	0.098	0.013	0.013 (0.010)	0.009	0.009
TWS2 Amplitude	%	0.064	0.064	0.040	1.155	0.013	0.013 (0.010)	0.011	0.011
Magnetic field	%	0.03	0.03	0.03	\	0.01	0.01	0.01	\
Total timing jitter (rms)	fs	\	\	\	\	9.98	10.13 (10.49)	9.72	9.80

*TWS: Travelling-wave structure

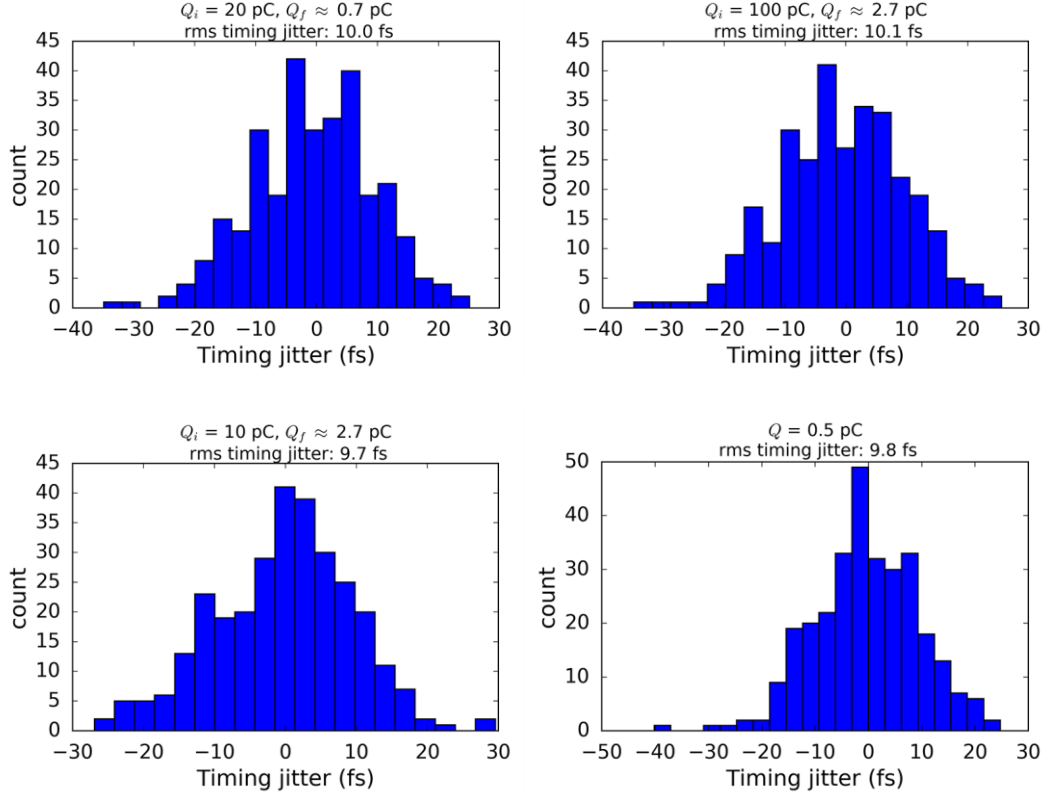


Figure 4.24: Histograms of the timing jitters for different working points with the tolerance budgets given in Table 4.2. The plot with a gun charge jitter of 0.3% is shown for the 100-pC pure magnetic compression case.

For the pure magnetic compression working point, the tolerances for the RF phase and amplitude jitter are demanding, being 0.013 degree and 0.013% respectively. The charge jitter is required to be 1% for the 20 pC working point, and as low as 0.3% for the 100 pC working point in order to keep the same stability requirements for the traveling-wave structure. Alternatively, if the charge jitter can only be limited to 1%, the tolerance on the phase and amplitude has to be reduced to 0.01 degree and 0.01% respectively.

For the hybrid compression working point, the tolerances of the traveling-wave structure are even more demanding. Especially, the phase and amplitude tolerances of the first traveling-wave structure are as small as 0.009 degree and 0.009% respectively. However, the gun charge jitters in the hybrid compression and pure velocity bunching working points are both negligible. It is worth mentioning that the phase and amplitude sensitivities of the first traveling-wave structure (0.011 and 0.073%) for the hybrid compression working point are close to those (0.010 and 0.098%) for the pure velocity bunching working point. The difference comes from the slightly different operation phases of the first traveling-wave structure. It is -85.0 degree for the hybrid compression working point but -90.3 degree for the pure velocity bunching working point.

The final bunch length jitter is generally not a linear function of the jitter amplitude for each of the jitter sources [Zhu15-2]. Therefore, only the statistics results are

investigated. The histograms of the final bunch length jitters are also shown in Figure 4.25. For the pure magnetic compression working point, the rms bunch length jitter also increases as the bunch charge increases. It is worth noting that the rms bunch length jitter for the hybrid compression working point is much smaller than for the other working points. This is similar to the difference between a single compression stage and two compression stages in a FEL facility: the bunch length in a single compression stage is much more sensitive to various jitters [LCLS02].

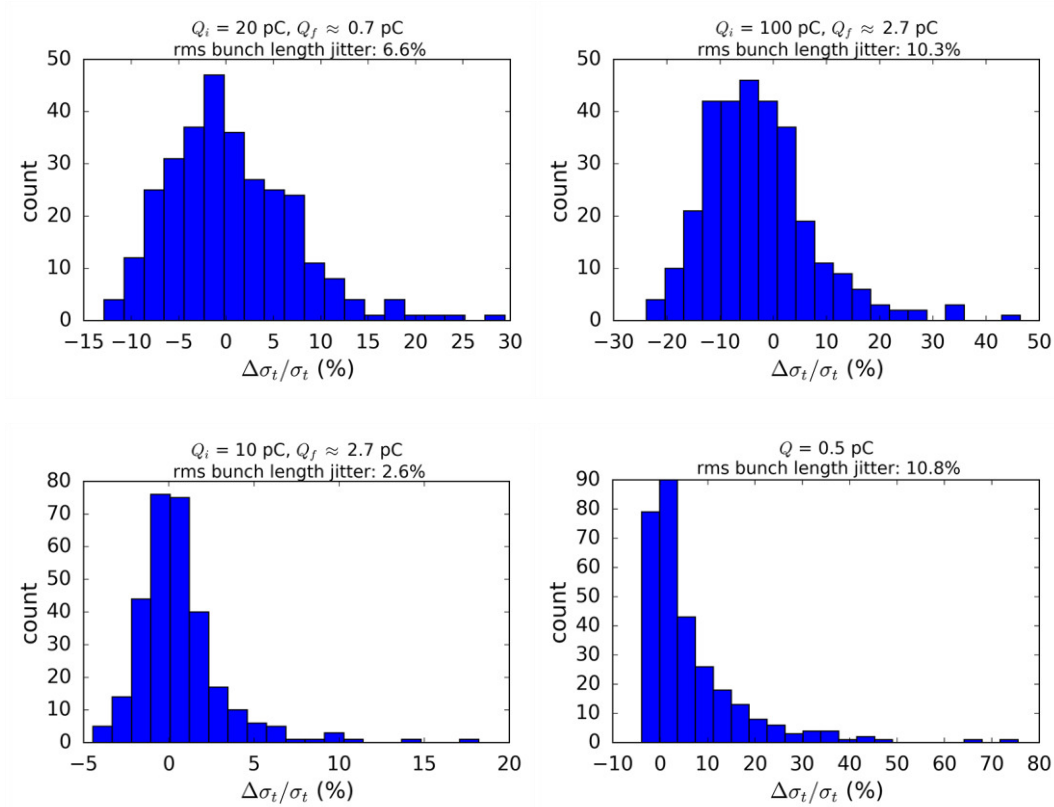


Figure 4.25: Histograms of the final bunch length jitters for different working points with the tolerance budgets given in Table 4.2. The plot with a gun charge jitter of 0.3% is shown for the 100-pC pure magnetic compression working point.

The histograms of the rms final bunch charge jitters for different working points are shown in Figure 4.26. It should be noted that significantly different initial bunch charge jitters were assumed for different working points. In general, the final bunch charge jitter is almost the same as the initial bunch charge jitter for the 20-pC pure magnetic compression and velocity bunching working points. However, for the 100-pC pure magnetic compression working point, the final bunch charge jitter is twice as much as the initial one. While for the hybrid compression working point, the final bunch charge jitter is reduced by a factor of 4.

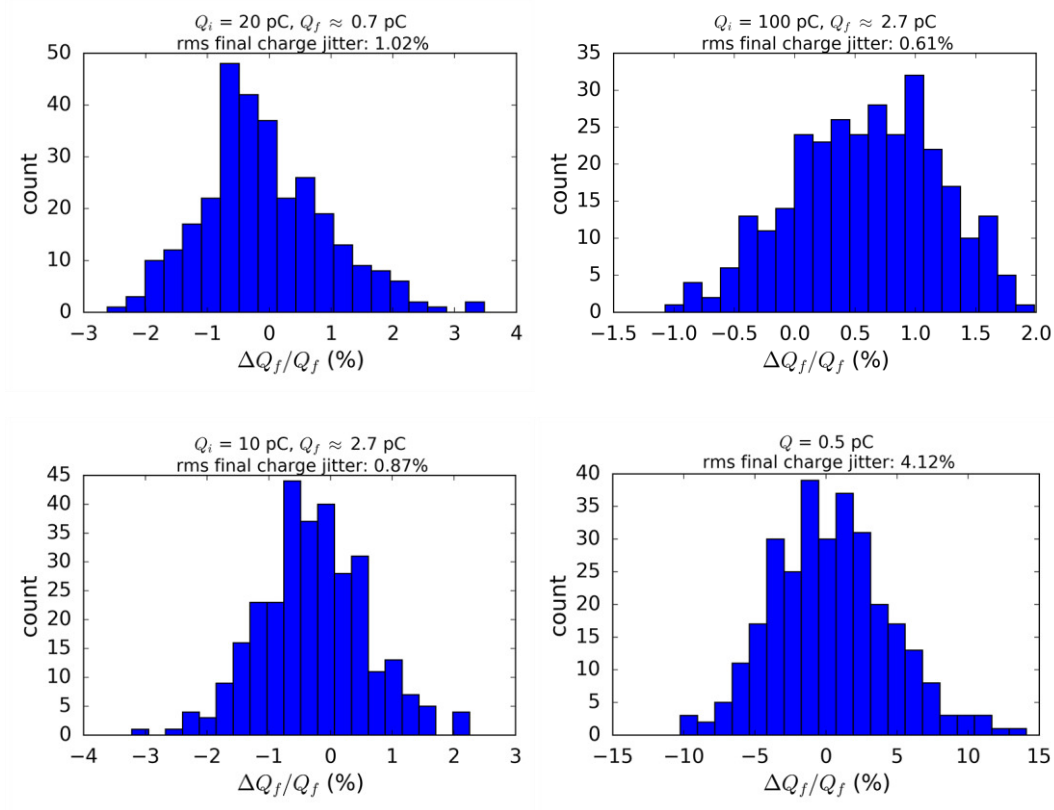
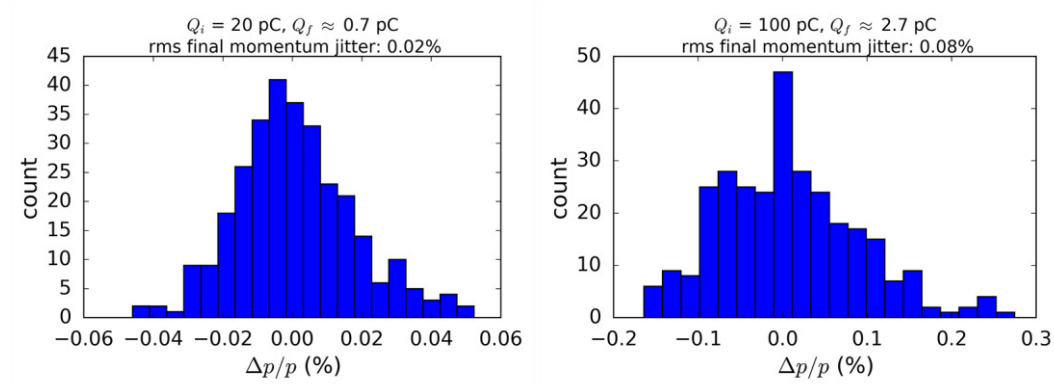


Figure 4.26: Histograms of the final bunch charge jitters for different working points with the tolerance budgets given in Table 4.2. The plot with a gun charge jitter of 0.3% is shown for the 100-pC pure magnetic compression working point. It should be noted that significantly different initial bunch charge jitters were assumed for different working points.

The histograms of the rms final momentum jitters for different working points are shown in Figure 4.27. It is not surprising that the pure magnetic compression working points can benefit from the narrow slit collimator. Nevertheless, the final momentum jitter still increases quickly as the bunch charge increases. The hybrid compression working point has the lowest final momentum jitter, which is only 0.01%. A small final momentum jitter is critical for the final focus of the electron bunch since the momentum is proportional to the focal length.



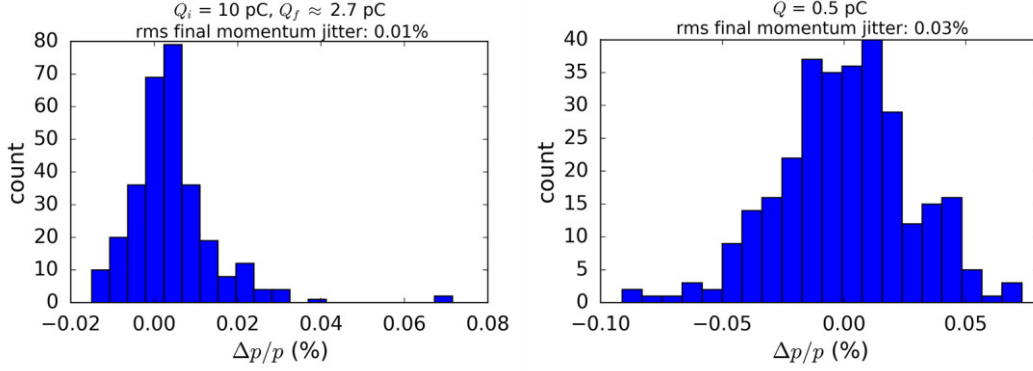


Figure 4.27: Histograms of the final momentum jitters for different working points with the tolerance budgets given in Table 4.2. The plot with a gun charge jitter of 0.3% is shown for the 100-pC pure magnetic compression working point.

4.6 Summary

In this chapter, generation of 100 MeV, sub-fs electron bunches with sub-10-fs bunch arrival-time jitter (timing jitter) has been investigated at a similar beamline as the ARES linac. A weak magnetic chicane ($R_{56} \approx -10$ mm) with a sub-mm-wide slit collimator between the 2nd and the 3rd dipole magnets is used to fully compress the central slice of an incoming long bunch. Because of the slit, the bunch length in the first half of the chicane can be long enough to ensure a negligible energy modulation induced by the CSR effect. This feature is of vital importance in generating sub-fs bunches with high bunch charges.

The beam dynamics inside the chicane was studied by using IMPACT-T and CSRTrack with different space-charge and CSR models. Due to the coupling between the horizontal and longitudinal phase-spaces, the bunch duration at the entrance of the last dipole magnet is still much longer than the final value. This fact mitigates considerably the impact of the space-charge and CSR effects on the beam quality. Simulations from both codes proved that sub-fs electron bunches with charges up to 4.8 pC are achievable, which is one order of magnitude higher than the simulation results obtained by using other compression schemes [Kan10][Bacci14]. It is found that the CSR effect dominates the horizontal emittance growth, and the different CSR models account mostly for the difference between the results obtained by the two codes. Compared to the 3D CSR model in CSRTrack, the 1D CSR model in IMPACT-T underestimates the final bunch duration and emittance when the transverse-to-longitudinal aspect ratio of the bunch is very large. Particularly, the CSR effect is also strongly affected by the vertical bunch size. Our studies also show that in CSRTrack simulations it is important to set the vertical sub-bunch size equal to the vertical bunch size in order *not* to overestimate the space-charge and CSR effects. When the vertical sub-bunch size is set to a value much smaller than the actual vertical bunch size, the beam dynamics of a sheet-like bunch will be simulated actually, which could lead to incorrect result.

In order to achieve a bunch arrival-time jitter of less than 10 fs, it is of vital importance to use a weak chicane, and the stabilization of the phase and amplitude jitter of the traveling-wave structures is critical and challenging. When operating with low charge bunches (e.g. 20 pC at the cathode) and low charge jitter ($< 1\%$), these requirements can be relaxed to 0.013 degree and 0.013% respectively by driving each of the traveling-wave structures with independent klystrons. When operating with high charge bunches (e.g. 100 pC), the extracted charge jitter at the photocathode or the phase and amplitude of the traveling-wave structures need to be further stabilized. The tolerance budget of the accelerator for the sub-10-fs timing jitter is very challenging but not unreasonable. At REGAE (Relativistic Electron Gun for Atomic Exploration), the amplitude and phase jitter of the gun is expected to be 0.01% and 0.01 degree respectively [Felber12], and a similar technology is foreseen to be implemented at the SINBAD facility later. At the SwissFEL Injector Test Facility, a shot-to-shot rms stability of 0.02 deg for the phase and 0.02 for the amplitude has been achieved at the S-band system several years ago [Beutner10].

A two-stage hybrid compression scheme has also been proposed in order to reduce the charge loss at the slit for high-charge working points. Simulations show that the final bunch duration becomes slightly longer while the horizontal emittance dilution is mitigated with respect to the corresponding pure magnetic compression working point. Since the two traveling-wave structures are operated at different phases and amplitudes, the stabilization of the traveling-wave structures is even more challenging than for the pure magnetic compression working point. However, the timing jitter for the hybrid compression working point is not sensitive to the initial bunch charge. Moreover, the final bunch length and momentum jitters are significantly smaller than those for the pure magnetic compression working point. These characteristics make the hybrid compression scheme more suitable for generating ultra-short and low-jitter electron bunches with relatively high bunch charges.

5. Lattice Design of the ARES Linac

This chapter starts with the technical design of the chicane bunch compressor. Different technical design options are compared comprehensively. Key parameters and requirements of the chicane and its components are discussed and specified. In particular, the influences of the field quality and misalignments of the dipole magnets on the emittance and bunch length are simulated. Moreover, the interaction of the beam with a real slit collimator is investigated by Monte-Carlo simulations in order to prove the validity of using a perfect knife edge slit model in the beam dynamics simulation.

Afterwards, the design of the final focus beamline is introduced. Focusing of ultra-short, space-charge dominated electron bunches down to a few μm rms spot sizes (the corresponding beta functions are a few mm) is investigated by start-to-end simulations. The ultra-small spot size is typically required by advanced accelerating structures due to the tiny size of these structures and the requirement of matching the beam to the focusing field of these structures.

Finally, the design of the dogleg beamline is presented. The setup of the dogleg beamline at the ARES linac will not only offer an additional experimental area for users, but also provide a unique opportunity to compare the hybrid compression with a chicane and a dogleg [Marchetti16]. The design of the dogleg is very flexible with a tunable R_{56} ranging from -10 mm to 10 mm.

5.1. Technical Design of the Chicane Bunch Compressor

The design of the magnetic chicane bunch compressor at the SINBAD-ARES linac should meet the following goals:

- 1) The chicane should generate an R_{56} which ranges at least from -8 mm to -30 mm at a maximum electron energy of 200 MeV.
- 2) The beam must be able to pass through the chicane straightly with the dipole magnets switched off. Complete degaussing of the dipoles must be possible routinely.
- 3) It is required to have a slit collimator with continuously adjustable open-width between the 2nd and the 3rd dipole magnets.

5.1.1. Typical chicane designs for existing facilities

The main features and components of the magnetic chicane bunch compressor in several existing facilities are listed in Table 5.1. From the mechanical point of view,

they fall into two major categories: movable and non-movable. The components of a movable chicane can be moved with one or two degrees of freedom, while everything is fixed in a non-movable chicane. A comprehensive comparison of pros and cons of different technical design options is summarized in Table 5.2.

Although the mechanical design of a movable chicane is complicated and expensive, it is preferred since the requirement of the size of good field region for the dipole magnet can be significantly relaxed if the R_{56} has a wide range. Moreover, the implementations of different diagnostic instruments (typically BPM) are much easier for a movable chicane, and the implementations of correction and skew quadrupole magnets are possible. Consequently, most XFEL facilities chose the movable chicane design. However, since the requirement for the vacuum in superconducting accelerators is much higher than that in normal conducting accelerators, particularly the material produced by scratching at the joint could contaminate the superconducting cavities, the fixed chicane design was therefore chosen for EuXFEL.

Table 5.1: Summary of the chicane designs in several facilities. B_{ij} indicates the location is between the i -th and j -th dipole magnets.

Facility name	Q (pC)	Movable	BPM	Correction Quad	Skew Quad	Screen	Collimator
ATF I [Agustsson04]	300	No	N/A	N/A	N/A	B23	N/A
LCLS [LCLS02]	20~250	Yes	B23	B12, B34	N/A	B23	B23
FERMI@ ELETTRA [Veronese06] [Lacivita10]	800~1000	Yes	B23	B12, B34	N/A	B23	B23
SwissFEL [Beutner13]	10~200	Yes	B12, B34	B12, B34	B12, B34	B23	B23
PAL-XFEL [Lee14]	>200	Yes	B12, B23	B12, B34	B34	B23	B23
EuXFEL [Decking11] [Decking13]	20~1000	No	B23	N/A	N/A	B23	B23

5.1.2. Chicane overview

Since ARES is an R&D facility, a movable chicane is highly desired. It not only allows the installation of a high-resolution BMP between the 2nd and 3rd dipole magnets, but also provides the possibility to reach much larger R_{56} which is important for experiments demanding small energy spread of the beam. The schematic of the movable

Table 5.2: Pros and cons of different chicane technical design options.

	Ummovable chicane with one pipe		Ummovable chicane with separate pipes		Movable pipe and fixed dipoles	Movable pipe and movable dipoles
R_{56}	Fixed	Variable	Fixed	Variable	Variable	Variable
Mechanical structure	Cheap	Depend on the range of R_{56}	Cheap	Depend on the range of R_{56}	Expensive. Position reproducibility?	More expensive. Position reproducibility?
Dipole magnets	C-shape dipole with small aperture (cheap) or H-shape dipole with large aperture (expensive)	C-shape dipole with large aperture (expensive) or H-shape dipole with very large aperture (More expensive)	Small aperture and cheap	Large aperture and expensive	Large aperture and expensive	Small aperture and cheap
BPM	Only the stripline BPM is applicable, and the resolution for the low-charge bunch is poor	Only the stripline BPM is applicable, and the resolution for the low-charge bunch is poor	The cavity BPM with high resolution for the low-charge bunch is applicable	Only the stripline BPM is applicable, and the resolution for the low-charge bunch is poor	The cavity BPM with high resolution for the low-charge bunch is applicable	The cavity BPM with high resolution for the low-charge bunch is applicable
Correction quadrupole magnets	Not possible	Not possible	Might be possible (space constraint)	Not possible	Applicable, but complicate (alignment)	Applicable, but complicate (alignment)

chicane bunch compressor designed for the ARES linac is shown in Figure 5.1. In the following paragraphs, the dipole magnets, BPM, slit collimator and the screen will be discussed.

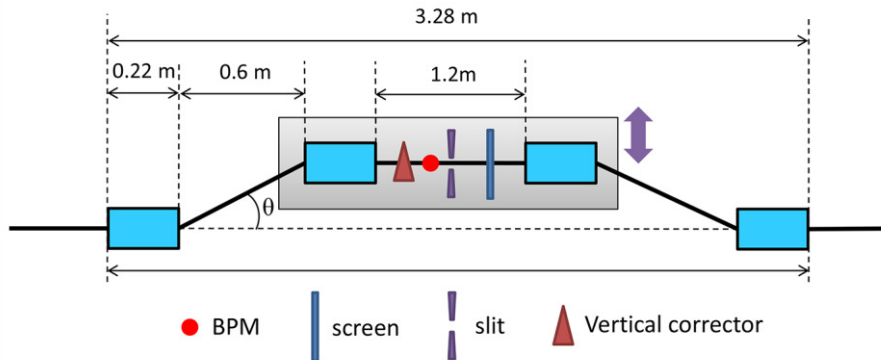


Figure 5.1: Schematic of the movable chicane layout. The central part of the chicane will be installed in a platform and be able to move horizontally.

5.1.3. Dipole magnets

The chosen dipole magnet design is the FLASH-TDB which has already been installed in the FLASH facility [Vogt13] at DESY. The FLASH-TDB has a very large good field region which also meets the requirement for a fixed chicane design with R_{56} ranging from -8 mm to -30 mm. The parameters of the FLASH TDB are summarized in Table 5.3 and the technical drawing is shown in Figure 5.2.

Table 5.3: Parameters of the dipole magnet, which is the same as the FLASH TDB.

Description	Value	Unit
Total length	350	mm
Effective magnetic length	220	mm
Peak magnetic field	0.5	T
Pole face full-width	200	mm
Pole face full-height	40	mm
Good field region ($\Delta B_{ds} / B_{0ds} < 0.1\%$) full-width	100	mm
Good field region ($\Delta B_{ds} / B_{0ds} < 0.1\%$) full-height	40	mm
Current of the main coil	342	A
Current of the correction coil	15	A
Power dissipation of the main coil	1.95	kW
Power dissipation of the correction coil	0.03	kW

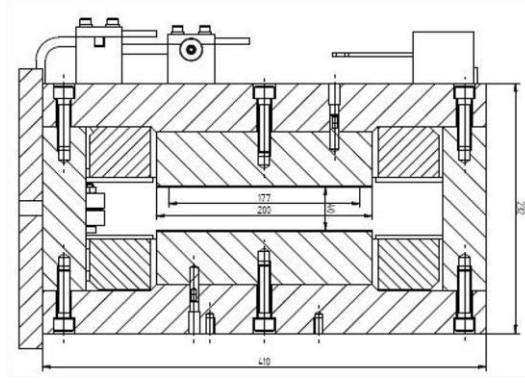


Figure 5.2: Technical drawing of the FLASH TDB dipole magnet.

Good field region and aperture

For a given R_{56} , as illustrated in Figure 5.3, the minimum good field region required for the second dipole magnet in a movable chicane is given by

$$w_{D2,m} \approx \frac{\theta L_B}{2} + 8\eta_{pk}\sigma_\delta, \quad (5.1)$$

where $\eta_{pk} = x_c \approx \theta(\Delta L + L_B)$ is the peak dispersion of the chicane and a 4-sigma beam-size clearance has been considered. The corresponding minimum horizontal inner aperture of the beam pipe at the exit of the second dipole magnet is given by

$$A_{x,D2,m} \approx 8\eta_{pk}\sigma_\delta. \quad (5.2)$$

It should be noted that, the good field region of the second dipole magnet and the aperture of the beam pipe afterwards could be reduced since most of the bunch charge will be collimated by the slit. However, in order to avoid a routine charge loss along the dipole magnet and the beam pipe, it is better to transport all the charges to the slit.

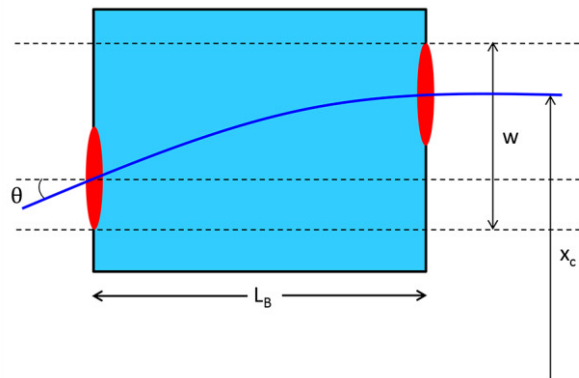


Figure 5.3: Curve path through an off-beamline (2nd or 3rd) dipole magnet.

For a fixed chicane with the bending angle ranging from θ_{min} to θ_{max} , the good field region required for the second dipole magnet increases to

$$w_{D2,f} \approx (\theta_{max} - \theta_{min})(L_B + \Delta L) + \frac{\theta_{min}L_B}{2} + 4\sigma_{\delta,\theta_{min}}\eta_{pk,\theta_{min}} + 4\sigma_{\delta,\theta_{max}}\eta_{pk,\theta_{max}}, \quad (5.3)$$

and the minimum horizontal inner aperture of the beam pipe at the exit of the second dipole magnet also increases to

$$A_{D2,x,f} \approx (\theta_{max} - \theta_{min})(L_B + \Delta L) + 4\sigma_{\delta,\theta_{max}}\eta_{pk,\theta_{max}} + 4\sigma_{\delta,\theta_{min}}\eta_{pk,\theta_{min}}. \quad (5.4)$$

Because of the slit collimator, the requirement for the third dipole magnet relaxes significantly. Compared with the second one, the required widths of the good field region of the third one for a movable and a fixed chicane reduce considerably to

$$w_{D3,m} \approx \frac{\theta_{min}L_B}{2} + \Delta x \quad (5.5)$$

and

$$w_{D3,f} \approx (\theta_{max} - \theta_{min})(L_B + \Delta L) + \frac{\theta_{min}L_B}{2} + \Delta x, \quad (5.6)$$

respectively, where Δx is the full-open-width of the slit. The required apertures of the inner beam pipe at the entrance of the third dipole magnet are even smaller, which give

$$A_{x,D3,f} = \Delta x \quad (5.7)$$

and

$$A_{x,D3,f} \approx (\theta_{max} - \theta_{min})(L_B + \Delta L) + \Delta x, \quad (5.8)$$

respectively.

According to equations (5.3) to (5.8), the required good field regions of the dipole magnets and apertures of the beam pipes are summarized in Table 5.4. It is obvious that the requirement for a fixed chicane is much higher than that for a movable one. A large beam pipe aperture is not compatible with the high resolution BPM, which typically has an aperture of 38 mm or even much smaller [Keil2015].

Table 5.4: Requirements of the dipole magnet good field region and the beam pipe aperture for a fixed chicane and a movable chicane. Here the maximum full-open-width of the slit is assumed to be 10 mm.

R_{56} range (mm)	-8 ~ -30			
Parameter	w_{D2} (mm)	$A_{x,D2}$ (mm)	w_{D3} (mm)	$A_{x,D3}$ (mm)
Fixed chicane	91.6	83.5	65.3	57.2
Movable chicane	44.1	36.0	16.6	10.0

Misalignment and field quality of dipole magnets

The significant linear and nonlinear field non-uniformities of the dipole magnets in a bunch compressor can generate large horizontal dispersion errors downstream, which will dilute the transverse beam emittance. In addition, the field strength and misalignment errors have the similar effect. Moreover, the final bunch length can also be affected by the field and longitudinal misalignment errors since they change the longitudinal dispersion. The field quality could also have an impact on the bunch length due to the correlation between the transverse and longitudinal plane.

The field quality of the dipole magnet can be expressed in terms of multipole components, which are defined as

$$B_y(x, y = 0) = \sum_{n=0}^{\infty} b_n \left(\frac{x}{a}\right)^n = B_0 \left(1 + \sum_{n=1}^{\infty} \frac{\tilde{b}_n}{n!} x^n\right), \quad (5.9)$$

where b_n is a traditional definition of the multipole coefficient, a is a reference radius chosen for convenience (it is usually *not* the bending radius of the dipole magnet), B_0 is the magnetic field at the origin and \tilde{b}_n is the multipole coefficient used in ELEGANT [Borland00][Welch07]. Accordingly, the i -th multipole error can then be represented in ELEGANT as

$$\frac{b_i}{b_0} = \frac{\tilde{b}_i a^i}{i!}. \quad (5.10)$$

Since the multipole components cannot be included in IMPACT-T or CSRTrack, the simulation study was carried out by using ELEGANT without including any collective effects. The influences of the field strength error ΔB_0 , the multipole components, the misalignments (Δx , Δy , Δz) and the tilt about the incoming longitudinal axis $\Delta\phi$ have been simulated for a 100-MeV, 100-pC incoming beam with a 0.4-mm-wide slit in the middle of the chicane.

The influence of the field strength error is shown in Figure 5.4. It is worth noting that the four dipole magnets will be powered by a single power supply. Therefore, every dipole magnet will have also an identical field strength error introduced by the current ripple of the power supply. The influence of the current ripple has been studied in chapter 4. Here, the field strength error refers to the inhomogeneity of the different dipole magnets, which can be corrected by the correcting coil.

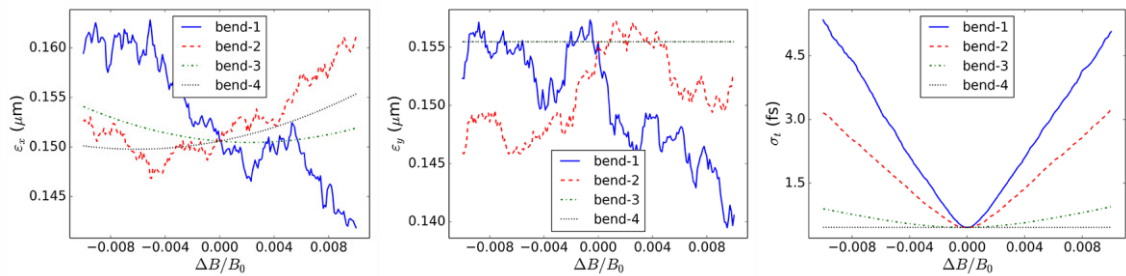


Figure 5.4: Influences of the field strength error to the emittances and bunch length.

The influences of different multipole components are shown in Figure 5.5. It is found that only the quadrupole (b_1/b_0) and sextupole (b_2/b_0) components take effect. The tolerance budget for a $0.01 \mu\text{m}$ emittance growth and 0.1 fs bunch length increasing is $b_1/b_0 \approx 0.001$ and $b_2/b_0 \approx 0.02$, which is not demanding [Welch07]. This is mainly due to the ultra-small horizontal bunch size in the chicane, which is defined by the width of the slit collimator.

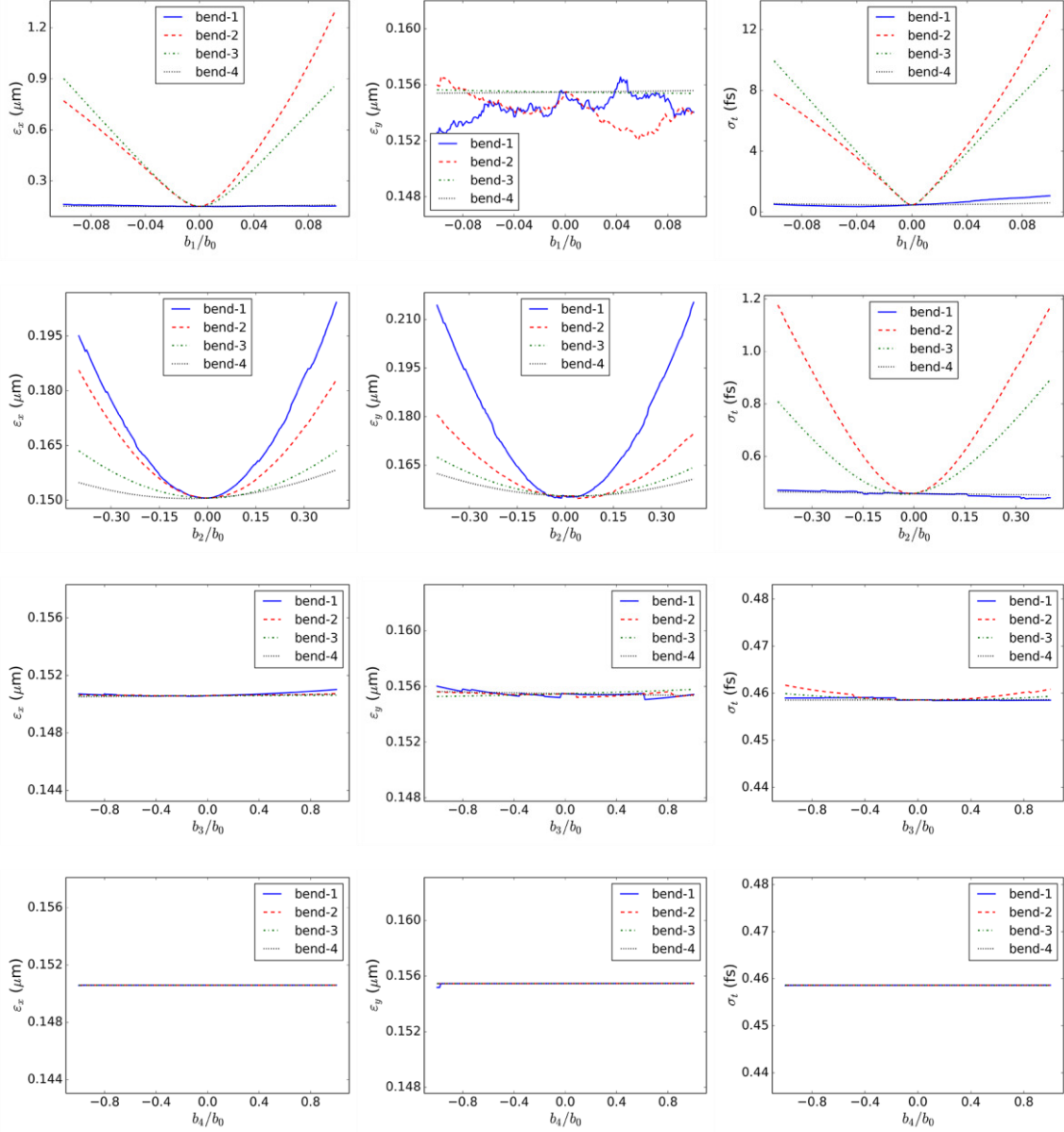


Figure 5.5: Influences of field errors of different orders to the emittances and bunch length.

The influences of the dipole magnet misalignments are shown in Figure 5.6. Only the longitudinal misalignment and the tilt are worthy of notice. The tolerance budget for a $0.01 \mu\text{m}$ emittance growth and 0.1 fs bunch length increasing is $\Delta z \approx 0.4 \text{ mm}$ and $\Delta\phi \approx 0.2 \text{ deg}$.

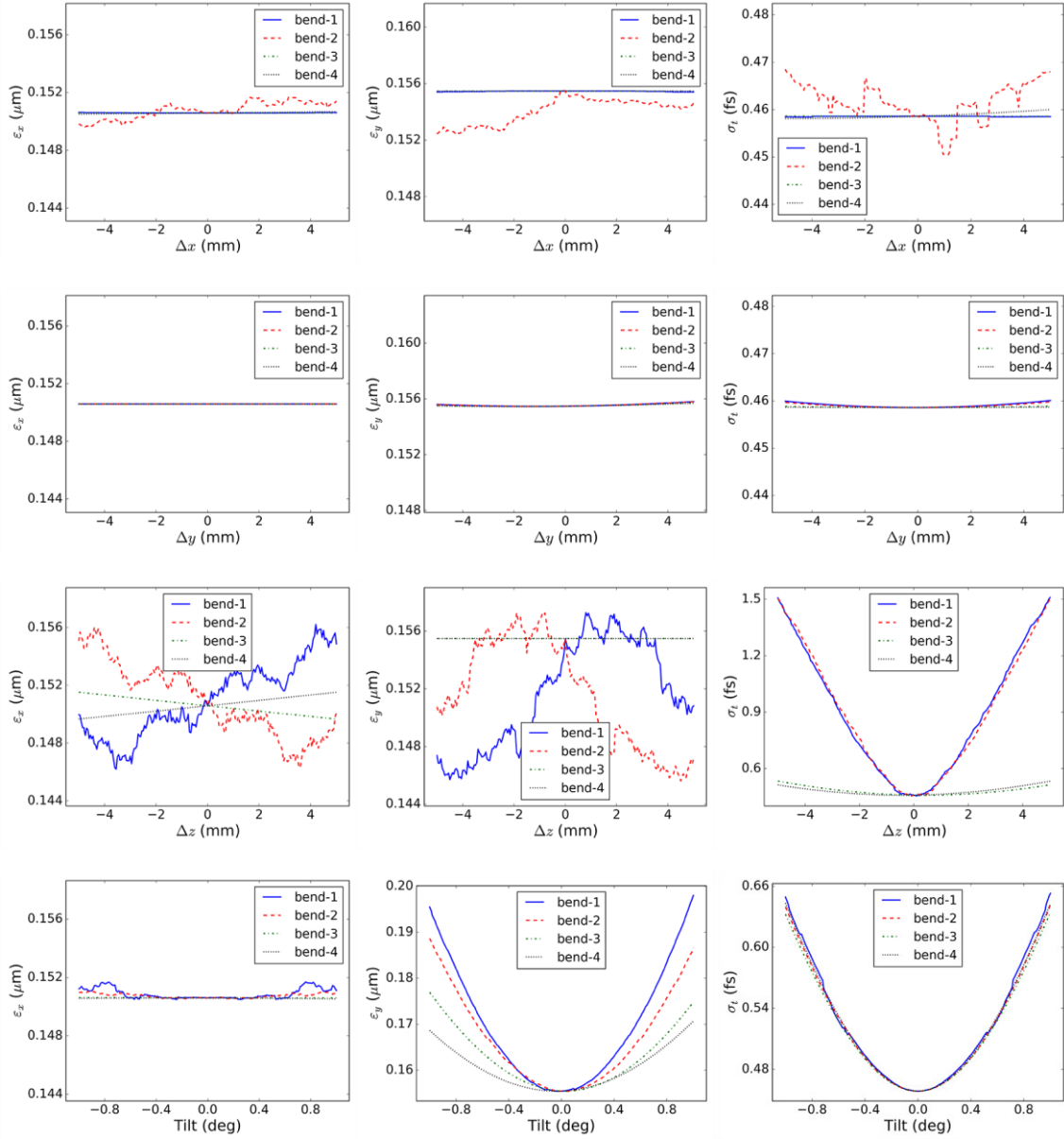


Figure 5.6: Influences of misalignments to the emittances and bunch length.

5.1.4. Power supply

The four dipole magnets will be powered by the same power supply to minimize the influence from the current ripple. According to the budget for the bunch arrival-time jitter of 10 fs shown in Chapter 4, the rms power supply ripple should be smaller than 0.0001.

5.1.5. Slit collimator

Assuming a 200 pC charge loss at the mean energy of 200 MeV and the repetition rate of 10 Hz, the average beam power is only 0.4 W. Based on the experiences at other facilities, water cooling is not necessary at ARES. For example, there is no water cooling for the collimator system in the first bunch compressor of LCLS, where the power of the beam loss is even higher than that in our design [Zhou16]. In another

example at FERMI@Elettra [DiMitri13], the thermal load of the collimator was simulated under the assumption of a 500 pC electron bunch at the mean energy of 300 MeV and the repetition rate of 50 Hz, where the average beam power is about 7.5 W. The simulation code predicted a maximum temperature of 698°C on the rod's surface in the transient regime. Therefore, the temperature rise in our design is expected to be much lower.

Concerning the radiation generated by the interaction of the beam and the collimator as well as other surrounding materials, the electronics (e.g. the camera) around the collimator must be carefully located and protected according to the experiences at FERMI@Elettra and LCLS. Otherwise, they can be easily damaged by the radiation.

Beam and slit interaction

In reality, the interaction of the electrons with the slit collimator is a complicated process. Electrons lose energies by collision and radiation as they traverse matters. At low electron energies the collision loss mechanism dominates while at high energies the bremsstrahlung process is the most important. The energy loss by radiation is fairly uniformly distributed among secondary photons of all energies from zero up to the energy of the electron itself. These photons also interact with the matter and one of the three photo-processes (electron-positron pair production, Compton scattering and photoelectric effect) dominate, depending on the energy of the photon and the nature of the medium. The first two processes provide a return of energy to the system in the form of electrons which, with the repetition of the bremsstrahlung process, results in a multiplicative process known as an electromagnetic cascade shower [Nelson85].

In order to validate the use of an ideal knife edge slit model in the beam dynamics simulation, the interaction of the electron beam and slit collimator was simulated by using the Monte-Carlo code shower [Emery03]. A 100-MeV, 100-pC and ~2.5-ps incoming beam before the chicane was considered. The geometry of the slit is shown in Figure 5.7, which consists of two blocks of coppers separated by 0.4 mm in the x direction. Copper was chosen as the slit material because of its high conductivity. Copper collimators are also adopted in other facilities with the similar applications. For example, the collimator at FERMI@Elettra is made of two identical, cylindrical and individually movable rods of copper. The rod diameter is 13 mm wide. In the first bunch compressor of LCLS, the ~8-cm-long flat collimator is tapered at both ends and coated with Titanium (for stiffness). It is the old SLC (SLAC Linear Collider) collimator which is not specially designed for LCLS [Zhou16].

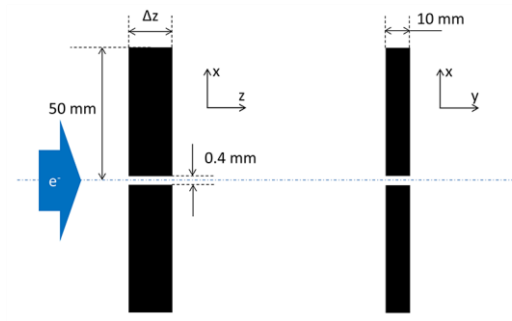


Figure 5.7: Geometry of the slit collimator used in the shower simulation.

The transverse beam profile after passing through an ideal slit and a 2-cm-thick copper slit are compared in Figure 5.8. Because of the electromagnetic shower, a large amount of secondary electrons were produced around the unaffected beam. The longitudinal phase-spaces of the electrons immediately downstream of an ideal slit and slits with thicknesses from 1 cm to 3 cm are also compared in Figure 5.9. With a real slit collimator, the electron energy spectrum is rather broad, ranging from zero up to the maximum value. It is found that, when the slit is thicker than 2 cm, the energies of most of the secondary electrons are well below the energy of the unaffected beam.

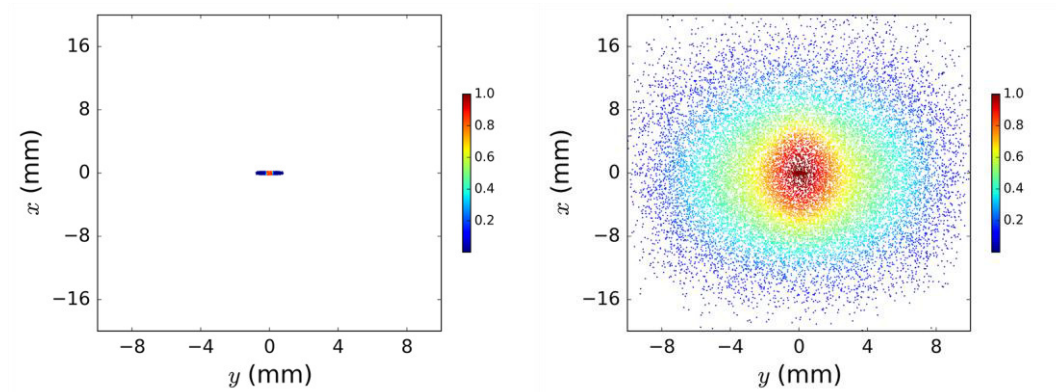
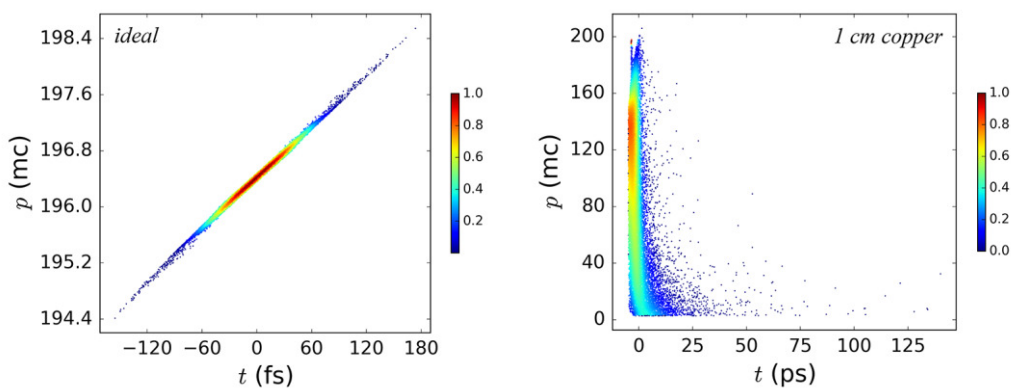


Figure 5.8: Beam transverse profile after passing through an ideal slit (left) and a 2-cm-thick copper slit (right).



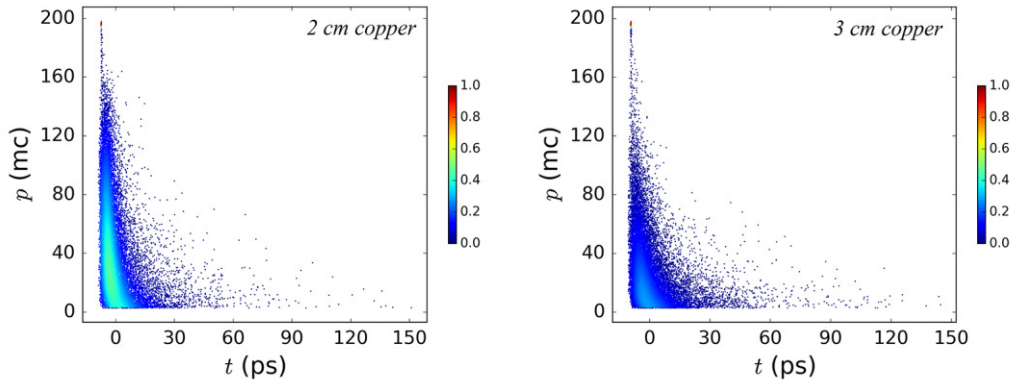


Figure 5.9: Longitudinal phase-spaces of the electrons immediately downstream of different slit collimators.

It is of importance to have a thick enough slit collimator to slow down the unwanted electrons. Figure 5.10 compares the longitudinal phase-spaces of the compressed beams downstream of the chicane with slits of two different thicknesses. With a 1-cm-thick copper slit, about 10% of the electrons in the final phase-space are secondary electrons. However, the fraction of the secondary electrons reduces to about 1% when the thickness of the slit increases to 2 cm.

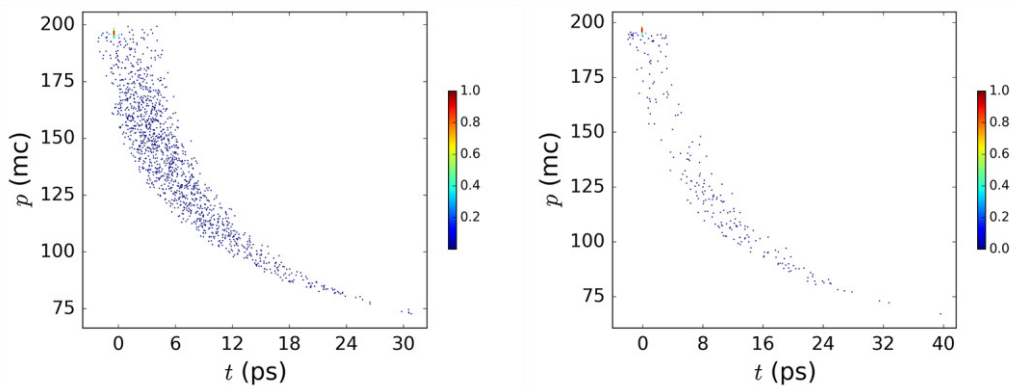


Figure 5.10: Longitudinal phase-spaces of the compressed beam at the end of the chicane using a 1-cm-thick copper slit (left) and a 2-cm-thick copper slit (right).

The transverse and longitudinal phase-spaces of the compressed beam with an ideal slit and 2-cm-thick copper slits, after removing $\sim 1\%$ outliers, are compared in Figure 5.11. It is obvious that the difference between the two cases is negligible. The space-charge and CSR effects were not included in these simulations since the secondary electrons distribute in a very large space so that the main beam will basically not be influenced by the collective effects from the secondary electrons. The result confirms that it is reasonable to approximate the real slit collimator with an ideal knife edge in the beam dynamics simulation.

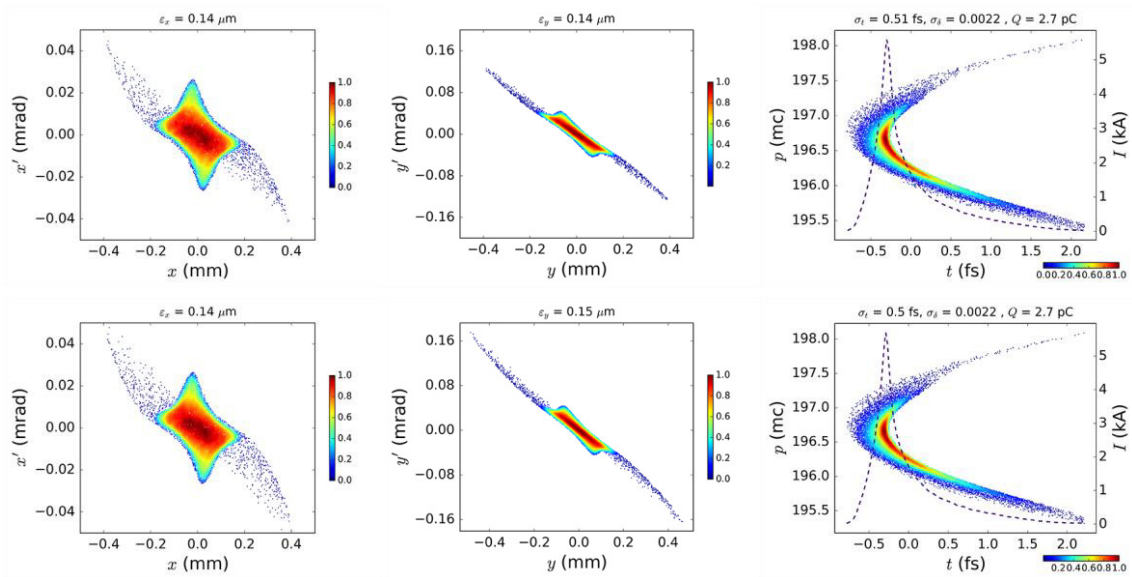


Figure 5.11: Comparison of the transverse and longitudinal phase-spaces of the compressed beam with an ideal slit collimator (upper row) and a 2-cm-long copper collimator (lower row).

The evolution of the beam charge after passing through a 2-cm-thick copper collimator is shown in Figure 5.12. A round beam pipe with an inner diameter of 5 cm was assumed in the simulation. It is found that most of the secondary electrons lost before the third dipole magnet due to the very large divergences.

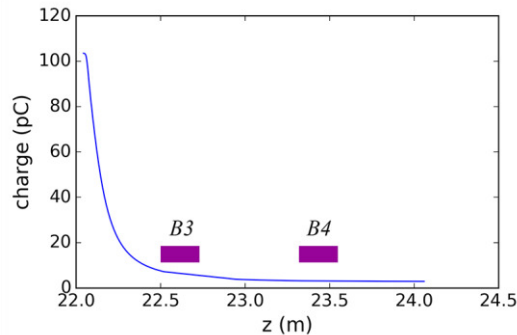


Figure 5.12: Evolution of the beam charge along the beamline downstream of a 2-cm-thick copper collimator. A round beam pipe with a 5 cm aperture was assumed.

The interactions of a 200 MeV beam with copper slit collimators of different thicknesses were also simulated. It was found that the slit should be thicker than 3 cm in order to slow down most of the secondary electrons.

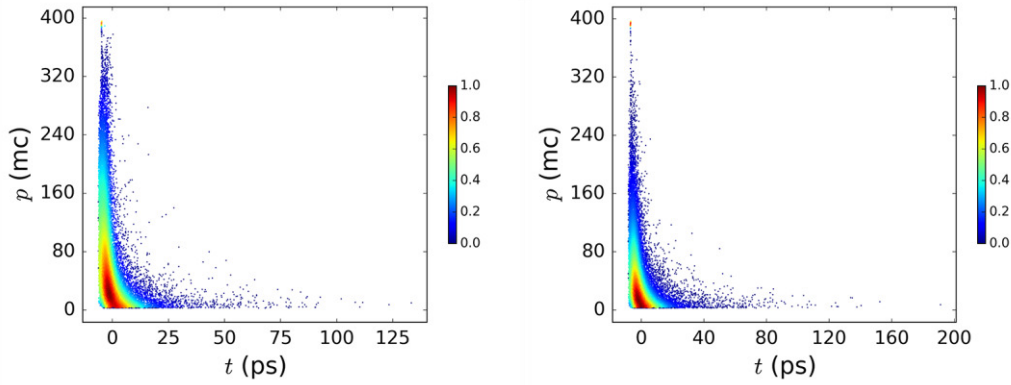


Figure 5.13: Longitudinal phase-spaces of a 200 MeV beam after passing through a 2 cm (left) and 3 cm (right) copper slit.

5.1.6. BPM

The BPM between the second and third dipole magnets are mainly used for the online, non-intercepting energy measurement for the energy feedback [Hacker10]. The energy change of the beam can be derived by the horizontal position change of the beam in a dispersion section, which gives

$$\delta = \frac{\Delta x}{R_{16}}. \quad (5.11)$$

Suppose the BPM is located in the middle of the chicane, a resolution of $6.7 \mu\text{m}$ corresponds to an energy resolution of 1.0×10^{-4} . It is obvious that the choice of a weak chicane in our design limits the energy resolution. It is worth noting that the incoming orbit jitter (displacement and divergence) must be measured using two BPMs before the chicane. It is also important that these BPMs have the comparable resolution to that of the chicane BPM and there are no quadrupole magnets between these BPMs.

It must be pointed out that the BPM used for energy stabilization should be installed before the slit because the bunch arrival-time jitter after the chicane is contributed by the timing offset jitter of the survival electrons with respect to the longitudinal centroid of the bunch at the entrance of the chicane. It can be stabilized by stabilizing the energy of the whole bunch before the slit. However, the energy of the beam after the slit is well defined by the transverse position of the slit.

The measurement of the energy change can also be performed by measuring the time-of-flight change of the bunch through the chicane using the two bunch arrival-time cavities (BACs) before and after the chicane, and it gives

$$\delta = \frac{c}{R_{56}} \Delta t. \quad (5.12)$$

A resolution of 3.3 fs is required to reach the same energy resolution of 1.0×10^{-4} .

In practice, it is helpful to use the BAM and BPM to cross-check the result because both of them are sensitive to the longitudinal profile change of the bunch and the temperature variation. Comparatively speaking, the BPM is less sensitive to temperature

variation because it can be carried out within a single temperature stabilized enclosure, but it is possibly more sensitive to the longitudinal bunch shape change than the BAM [Hacker10]. Moreover, both the resolutions of BAM and BPM for electron bunches with charges down to around 1 pC need to be verified.

5.1.7. Screen

The screen is used to monitor the beam profile with and without the slit collimator. It is important to separate the screen and the collimator as much as possible in order to reduce the noise from the secondary electrons.

5.2. Matching of electron bunches into a tiny structure

Matching of electron bunches into the focusing field of an accelerating structure is of vital importance for preserving the beam quality. According to equation (1.28), the Twiss parameters for a matched emittance-dominated beam are given by

$$\beta_x = \beta_y \approx \frac{1}{\sqrt{K_r}}, \alpha_x = \alpha_y \approx 0, \quad (5.13)$$

where the focusing strength K_r can be calculated by (under the paraxial approximation)

$$K_r(\xi) = \frac{e}{\gamma m_e c^2} \left. \frac{\partial(E_r - \beta c B_\theta)}{\partial r} \right|_{r=0}. \quad (5.14)$$

For a plasma accelerator, substituting equation (2.14) and (2.18) into equation (5.14), respectively, we have

$$K_r(\xi) = \frac{2k_p \sigma_{z,L}}{\gamma} \sqrt{\frac{\pi}{2}} \frac{a_0^2}{w^2(z)} \exp\left(-\frac{k_p^2 \sigma_{z,L}^2}{2}\right) \sin(k_p \xi) \quad (5.15)$$

in the linear regime and

$$K_r = \frac{k_p^2}{2\gamma} \quad (5.16)$$

in the blow-out regime. With the parameters of the ANGUS laser, the matched beta function is extremely small (< 1 mm) for a ~ 100 MeV externally injected beam, as listed in Table 5.5 for plasmas with different densities. Nevertheless, the requirement on the matched beta function can be relaxed by using a tailored longitudinal plasma profile (up-ramp) [Dornmair15], i.e. a proper density transition from the vacuum to the plasma channel with constant density. A mismatched beam will undergo betatron oscillation inside the plasma. The varying betatron frequency along the bunch, which is caused by both the finite bunch length (only in the linear regime) and the energy chirp, will result in a considerable projected emittance growth [Mehrling14].

[Table 5.5: Matched beta function for an externally injected 100-MeV electron bunch with a hard edge plasma driven by the ANGUS laser using the formulas in the linear and blow-out regimes.](#)

$k_p \xi = -\pi/6$ is used in the formula for the linear regime and $\xi = 0.8r_B$ is used in the formula for the blow-out regime. It should be noted that given these electron and laser parameters, the plasma acceleration should actually be in the transition regime between the linear and blow-out regimes.

	Linear regime			Blow-out regime		
	10^{16}	10^{17}	10^{18}	10^{16}	10^{17}	10^{18}
Plasma density (cm^{-3})						
Accelerating gradient (GeV/m)	2.3	20.9	106.7	3.1	31.1	311.2
Matched beta function (mm)	0.80	0.47	0.39	1.04	0.33	0.10

5.2.1. Design consideration

In order to achieve a small beta function at the focus, a high-gradient quadrupole focusing array (e.g. triplet) is required for beams with energies around 100 MeV or higher. By taking into account the beam emittance and the chromatic aberration, the beta function at the focal point is given by [Appendix A]

$$\beta_{x_f} = \frac{f^2}{\beta_{x_i}} + \sigma_\delta^2 \beta_{x_i}. \quad (5.17)$$

The final beta function is also affected by the quality of the focusing field (e.g. the spherical aberration) and the misalignments of the beam and the quadrupoles. However, those factors are beyond the scope of this thesis. According to equation (5.17), the minimum achievable beta function is $2f\sigma_\delta$ at $\beta_{x_i} = f/\sigma_\delta$. Since a considerable energy spread must be introduced to compress the bunch, a small focal length is desired. For conventional electromagnetic quadrupoles triplets, the focal length is typically longer than tens of centimeters. A very large incoming beta function is thus required to achieve a final beta function of ~ 1 mm, which will introduce tremendous chromatic emittance growth [Appendix A]. On the other hand, the gradient of the permanent magnet quadrupole (PMQ) can reach as high as 600 T/m [Cesar16], and the focal length of a PMQ triplet can be as short as several cm for a ~ 100 MeV beam.

A PMQ triplet with a symmetric incoming beam at its waist is considered for the final focus system, as illustrated in Figure 5.15. The transfer matrix of this triplet is given by

$$\begin{aligned} M_{FF} &= \begin{bmatrix} 1 & f \\ 0 & 1 \end{bmatrix} \begin{bmatrix} 1 & 0 \\ \mp 1/f & 1 \end{bmatrix} \begin{bmatrix} 1 & f \\ 0 & 1 \end{bmatrix} \begin{bmatrix} 1 & 0 \\ \pm 1/f & 1 \end{bmatrix} \begin{bmatrix} 1 & f \\ 0 & 1 \end{bmatrix} \begin{bmatrix} 1 & 0 \\ \mp 1/(2f) & 1 \end{bmatrix} \\ &= \begin{bmatrix} 0 & 2f \\ -1/(2f) & \mp 1 \end{bmatrix}. \end{aligned} \quad (5.18)$$

This solution maximizes the convergence angle at the focus for a given maximum obtainable focusing strength of a single PMQ [Lim05], and the beam at the focus is also symmetric.

Due to the strong space-charge effects of the compressed beam downstream of the chicane [zhu16], a long transfer beamline between the chicane and the final focus triplet should be avoided. This excludes the choice of using sextupole magnets to correct the chromatic aberration. As a result, a PMQ triplet is used to strongly focus the transverse beam size immediately downstream of the chicane, as shown in Figure 5.14. The distance between the exit of the chicane and the focal point is about 1.4 m in consideration of the spaces for the BAC, BPM, screen, collimator, vacuum valve, etc. The Twiss parameters of the beam at the entrance of the PMQ triplet can be finely adjusted by six quadrupole magnets upstream of the chicane.

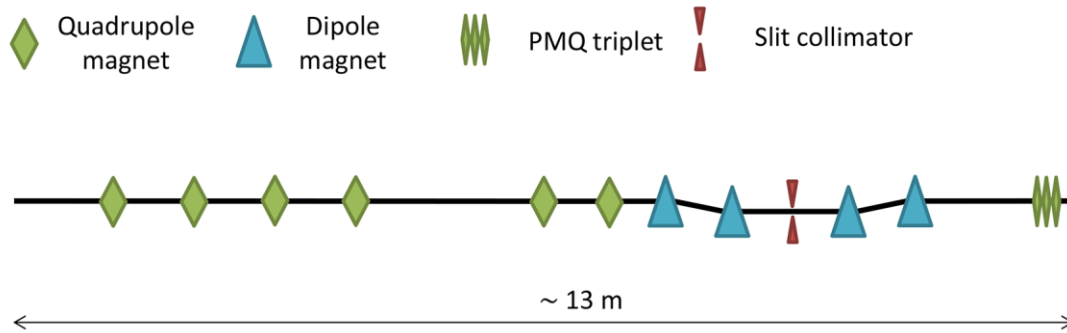


Figure 5.14: Cartoon of the main beamline from the entrance of the matching section to the focus (the entrance of the plasma).

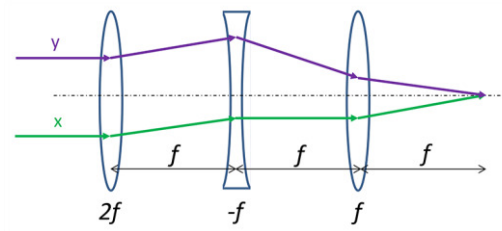


Figure 5.15: Illustration of the triplet optics.

5.2.2. Influence of chromatic effect

The influence of the chromatic effect was first evaluated by beam dynamics simulations from the entrance of the PMQ triplet to the focus using ELEGANT. An incoming cylindrical symmetric Gaussian beam ($\alpha = 0$) with transverse emittances of $0.2 \mu\text{m}$ was assumed. The PMQ triplet used in these simulations composed of three 20-mm-long PMQs with gradients of 250 T/m, 500 T/m and 500 T/m respectively. The beta functions of the incoming beam and the locations of the PMQs were adjusted to focus beams with different energies to $\beta_x = \beta_y \approx 1 \text{ mm}$ and $\alpha_x = \alpha_y \approx 0$ at the fixed focal spot. The results are shown in Figure 5.16 and Figure 5.17. The mismatch factor shown in Figure 5.17 is defined as [Appendix B]

$$M_S = B_{mag} + \sqrt{B_{mag}^2 - 1}, \quad (5.19)$$

where B_{mag} is given by

$$B_{mag} = \frac{1}{2}(\beta\gamma_m + \beta_m\gamma - 2\alpha\alpha_m) \quad (5.20)$$

with α_m , β_m and γ_m the matched Twiss parameters. For a perfectly matched beam, the mismatch factor is 1.0.

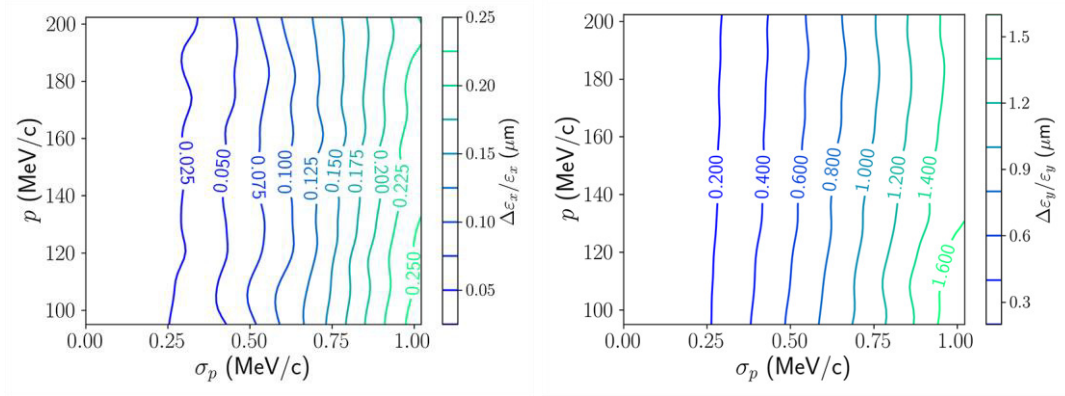


Figure 5.16: Transverse emittance growths at the focus for different beam momenta and rms momentum spreads. The PMQ triplet composed of three 20-mm-long PMQs with gradients of 250 T/m, 500 T/m and 500 T/m respectively. The matched beta functions are 1 mm in both planes. The incoming beta function ranges from 6 m to 22 m.

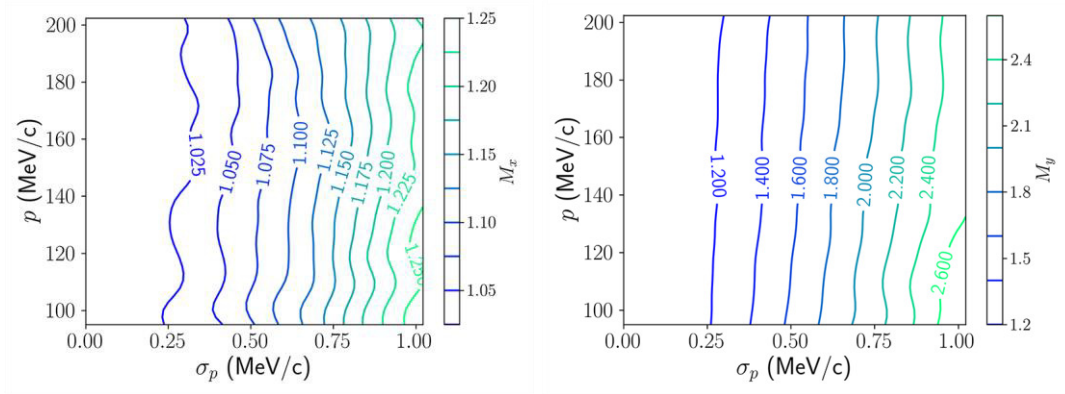


Figure 5.17: Same as Figure 5.16 but the distributions of the mismatch factors in both planes are shown.

Although the incoming beam is cylindrical symmetric, the influences of the chromatic effect in the horizontal and vertical planes are not equal. At the first PMQ, the beam will be focused in one plane and defocused in the other. In the plane where the beam is defocused, the emittance growth due to the chromatic effect will be stronger because of the larger beta function. Therefore, one should be careful about the sign of the PMQ gradient if the emittance and mismatch factor in one plane are more important than those in the other plane.

The beam energy affects the chromatic effect in several competitive ways. Although the relative energy spread of the beam decreases as the energy increases, the beta function of the incoming beam increases as the beam energy increases given the PMQ gradients. Moreover, the focal length and the distances between PMQs also increase as the beam energy increases, which affect the beta functions at the second and the third PMQ. The simulation results show that the beam energy does not have a significant impact on the emittance and the mismatch factor given the absolute energy spread. However, it must be pointed out that the matched beta function increases as the beam energy increases according to equation (5.15) and (5.16). In other words, the matching condition is more relaxed for beams with higher energies. In practice, nevertheless, one must also consider the constraint of beam optics at the entrance of the PMQ triplet.

According to the simulation, the chromatic effect increases monotonically as the absolute energy spread increases given the beam energy. For an energy spread of about 0.25 MeV (0.25% for a 100 MeV beam), the emittance growth and beam mismatch in the horizontal plane are both negligible. However, the emittance growth in the vertical plane is about 20% and the mismatch factor is about 1.2.

As a comparison, the simulation results using shorter (1-cm-long) PMQs with the same gradients are shown in Figure 5.18 and Figure 5.19. It is apparent that the chromatic effect becomes much more significant due to the much larger incoming beta functions. The trade-off can be further explained by equation (A.12) and (5.17). According to the first term on the right-hand side of equation (5.17), if the focal length doubles, the incoming beta function should quadruple to keep the final beta function unchanged. However, according to equation (A.12), this change will also quadruple the emittance growth. In the simulation, the incoming beta function only approximately tripled since the length of the 2-cm PMQs is comparable to the distance between them, which violates the thin lens approximation. It indicates that strong PMQs are preferred unless the space-charge effects start to dominate the beam quality.

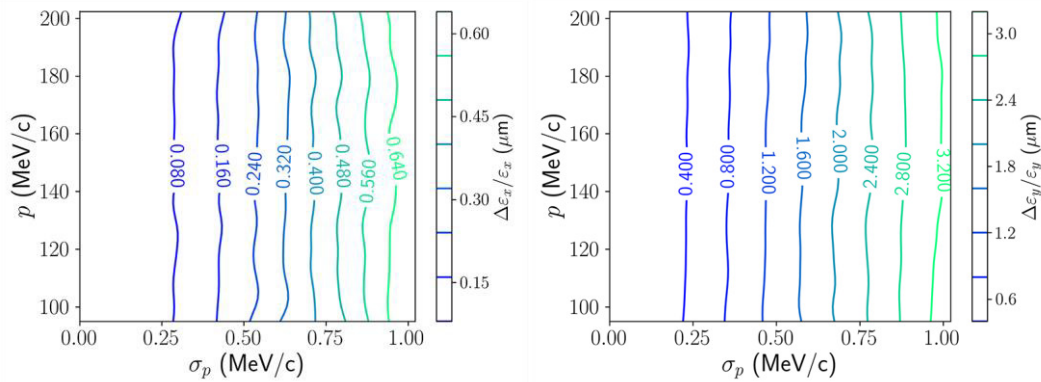


Figure 5.18: Same as Figure 5.16 but the length of the PMQ is reduced to 10 mm. The incoming beta function ranges from 18 m to 77 m.

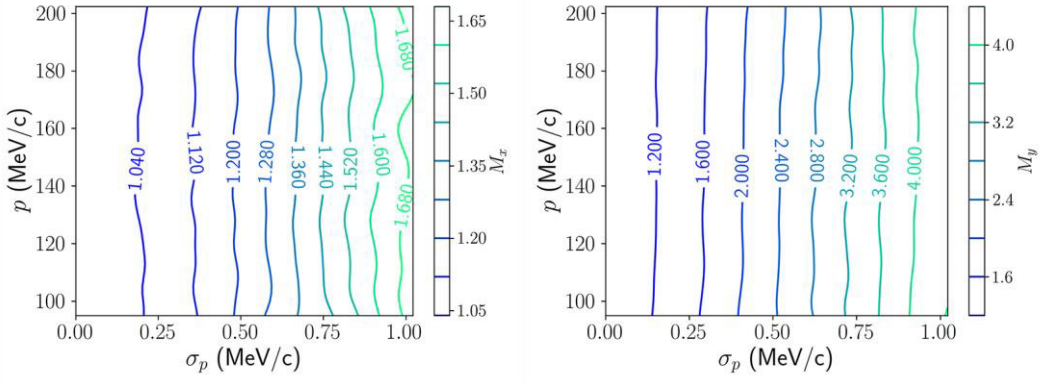


Figure 5.19: Same as Figure 5.18 but the distributions of the mismatch factors in both planes are shown.

As mentioned previously, the matched beta function can be increased by using a tailored longitudinal plasma profile. Considering that the matched beta functions increase to $\beta_x = \beta_y \approx 10$ mm, there are two options to adapt the focusing system in the previous case. One is to reduce the incoming beta functions, and the other is to use a weaker PMQ triplet.

Considering a 100-MeV incident electron bunch, the incoming beta functions need to be smaller than 2 m in order to use the same PMQ triplet. However, this choice will significantly increase the space-charge effects before the PMQ triplet, particularly during the bunch compression in the chicane.

For the other option, a weaker PMQ triplet (70 T/m, 140 T/m and 140 T/m) is considered in order to make the incoming beta functions comparable to the simulations shown in (5.16). The simulation results are shown in Figure 5.20 and Figure 5.21. Although the chromatic effects are suppressed significantly and the incoming beta functions are comparable to the first case, the total length of the triplet largely increases from ~ 0.13 m to ~ 0.39 m. For a space-charge dominated electron bunch, the degradation of the beam quality due to the space-charge effects in this extra distance must be taken into account.

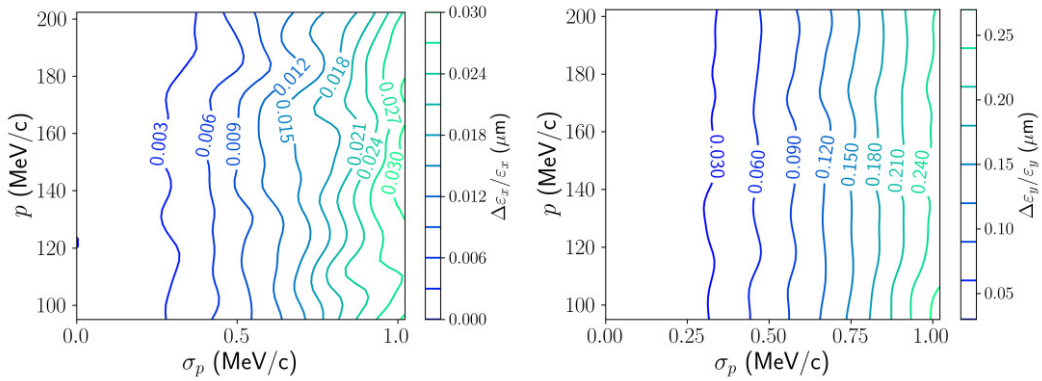


Figure 5.20: Same as (5.16) but the gradients of the PMQ triplet are reduced to 70 T/m, 140 T/m and 140 T/m, respectively. Also, the matched beta functions in both planes are 10 mm. The

incoming beta function ranges from 6 m to 25 m.

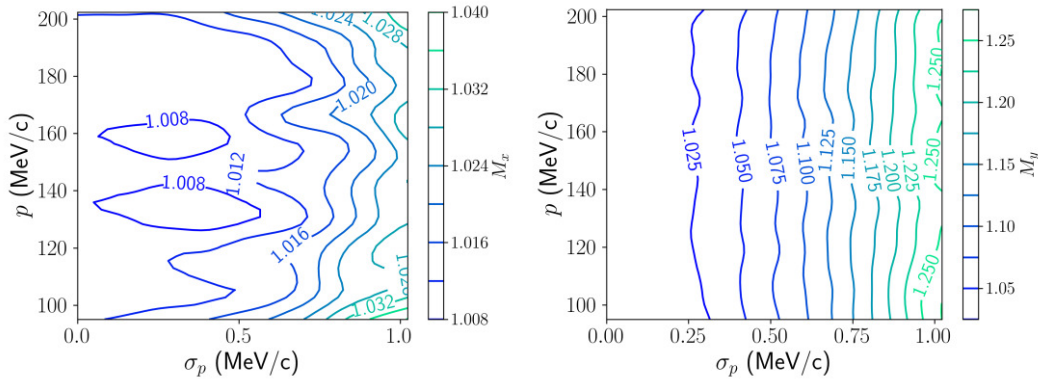


Figure 5.21: Same as Figure 5.20 but the distributions of the mismatch factors in both planes are shown.

5.2.3. Influence of space-charge effects

In this part, two working points with significant different energies were simulated in order to demonstrate the impact of space-charge effects. The beam parameters at the linac exit simulated by ASTRA are summarized in Table 5.6. Downstream of the linac, the beam dynamics were simulated by using Impact-T with both the space-charge and CSR effects included.

Table 5.6: Beam parameters at the linac exit used for the final focus study. The 150 MeV electron bunch was obtained by using three travelling-wave structures.

Bunch charge (pC)	100	100
Energy (MeV)	84	150
RMS bunch length (ps)	2.4	2.7
Normalized projected emittance (μm)	0.29	0.33
Normalized slice emittance (μm)	0.19	0.21

The optics was optimized by considering only the central slice (containing 2.5% charge) of the bunch. The results for the above two working points are shown in Figure 5.22. The design beta functions at the focus are both 1 mm at their waists.

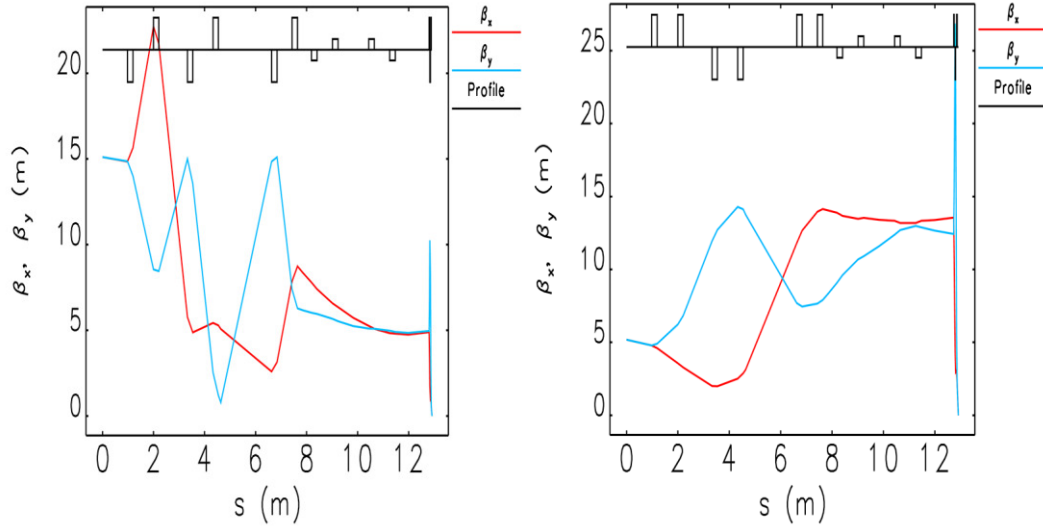


Figure 5.22: Design optics for the 84 MeV bunch (left) and the 150 MeV bunch (right) with the Twiss parameters at the focus being $\beta_x = \beta_y = 1$ mm and $\alpha_x = \alpha_y = 0.0$. The PMQ triplet composed of three 2-cm-long PMQs with gradients of 250 T/m, 500 T/m and 500 T/m respectively.

With a 0.4-mm slit in the middle of the chicane, the charges of the survival electrons are about 3.0 pC and the energy spread are below 0.3% in both cases. The simulated phase-spaces are shown in Figure 5.23 and Figure 5.24. The beta functions at the focus in both cases are much larger than 1 mm because of the high non-linearity of the system. For the 84-MeV working point, the sub-fs electron bunch elongates rapidly because of both the space-charge effects and the relative large R_{56} ($\propto 1/\gamma^2$). As a result, the final peak current is well below 1 kA. The emittances also increase substantially due to the combination of the chromatic aberration and the space-charge effects, especially in the vertical plane. It should be noted that the energy spread of the bunch grows quickly due to the space-charge effects, which further strengthens the chromatic aberration. However, as the electron bunch energy increases to 150 MeV, the beam quality at the focus is improved considerably. The bunch length remains below 1 fs with a peak current over 2 kA. The emittance in the horizontal plane is conserved, while the emittance growth in the vertical plane is significantly reduced. This opens the possibility to implement the sextupole magnets to compensate the chromatic aberration. Still, the beamline must be short enough in order to generate sub-fs electron bunches because of the non-negligible R_{56} in a drift space.

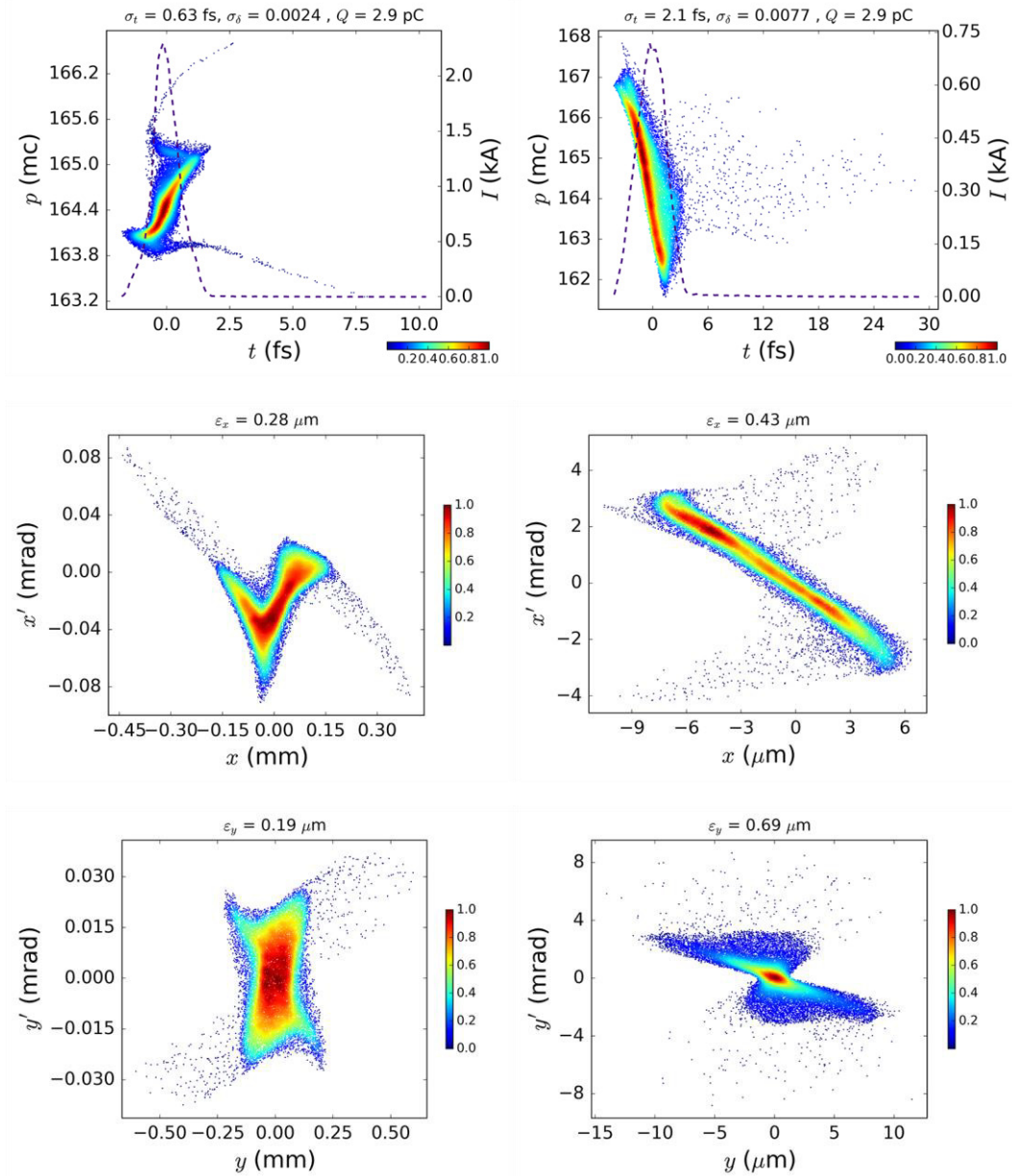
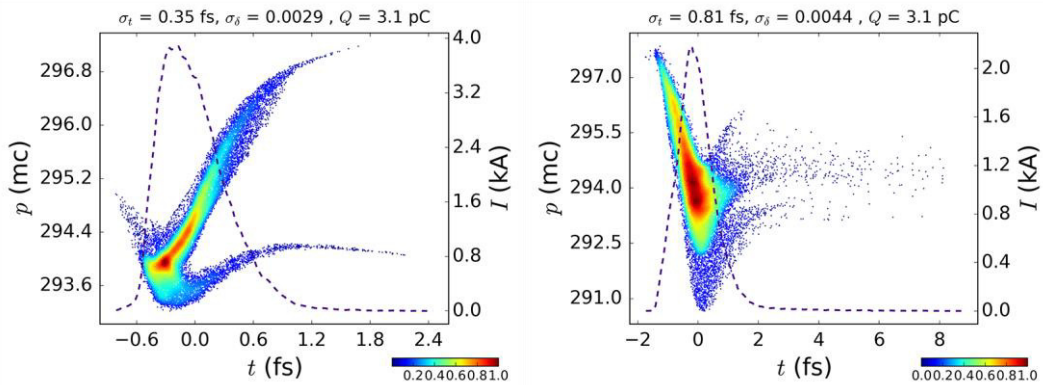


Figure 5.23: Longitudinal and transverse phase-spaces at the exit of the chicane (left column) and at the focus (right column) for the 84 MeV electron bunch. The final bunch charge is ~ 2.9 pC. The Twiss parameters at the focus are $\beta_x \approx 5.3$ mm, $\alpha_x \approx 2.2$, $\beta_y \approx 2.6$ mm and $\alpha_y \approx 0.8$.



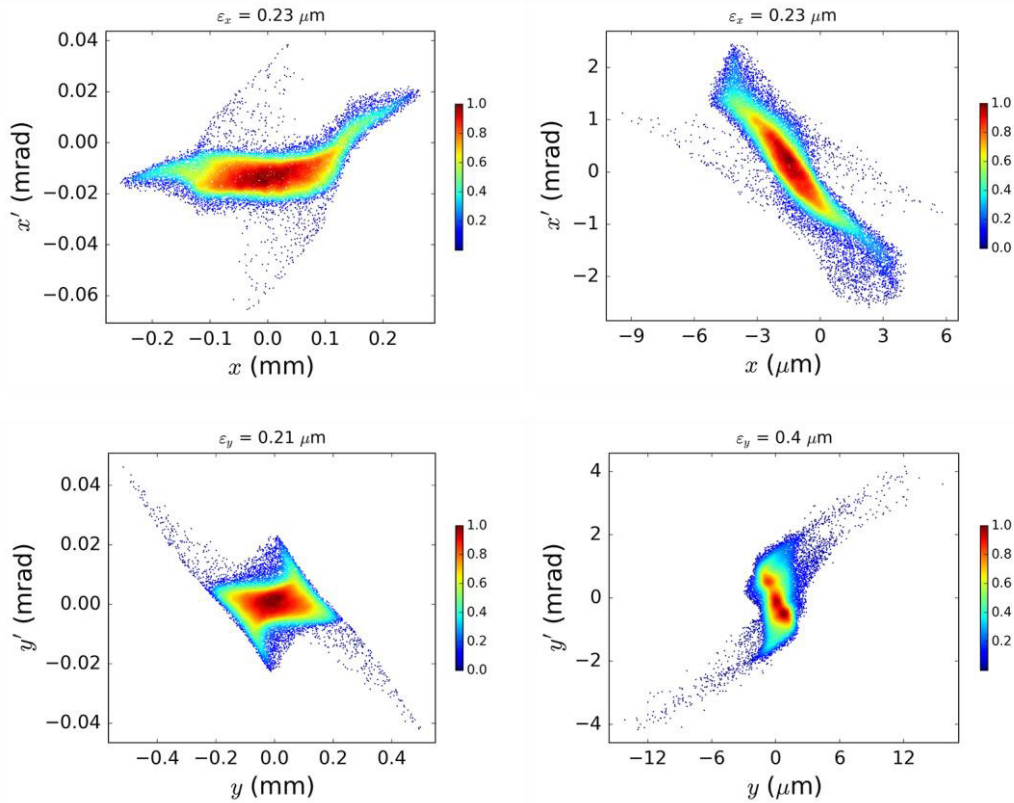


Figure 5.24: Longitudinal and transverse phase-spaces at the exit of the chicane (left column) and at the focus (right column) for the 150 MeV electron bunch. The final bunch charge is about 3.1 pC. The Twiss parameters at the focus are $\beta_x \approx 4.5$ mm, $\alpha_x \approx 2.1$, $\beta_y \approx 1.8$ mm and $\alpha_y \approx -0.4$.

5.3. Design of the dogleg beamline

The dogleg beamline is supposed to deliver ultra-short electron bunches with energies up to 200 MeV to the second beamline, as shown in Figure 5.25. Due to the geometrical constraints inside the SINBAD tunnel, the horizontal displacement between the first and second beamlines is required to be about 5.8 m, and the length of the dogleg should be less than 10 m. In this design, the dogleg consists of four 0.42-m-long rectangular dipole magnets with bending angles of (+, +, -, -) 20° . There are eight quadrupole and two sextupole magnets in between these dipole magnets. The arrangement of the quadrupole magnets and drifts is symmetric about the midpoint of the dogleg. The locations of the two sextupole magnets are also symmetric about the midpoint of the dogleg, while the signs of their currents are opposite. The R_{56} of the dogleg can be varied in the range of -10 mm and 10 mm by adjusting the strengths of the four quadrupole magnets at both ends simultaneously, while the strengths of the other quadrupole magnets need to be tweaked accordingly in order to completely suppress the dispersion at the dogleg exit. The sextupole magnets are able to suppress the second-order longitudinal dispersion term T_{566}^- and cancel the longitudinal phase-

space curvature of the incoming bunch, which is of vital importance for preserving the longitudinal bunch profile and generating ultra-short bunches.

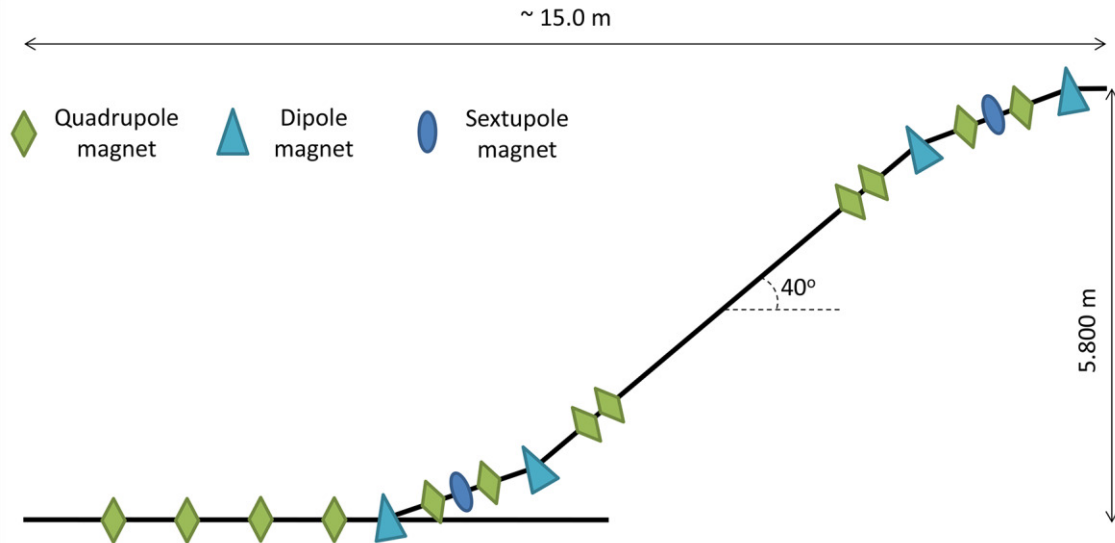


Figure 5.25: Cartoon of the beamline from the exit of the linac to the exit of the dogleg.

The S2E simulations of the beam dynamics from the photocathode to the dogleg exit were performed with ASTRA and ELEGANT. The electron bunch was first accelerated to the entrance of the matching section by using ASTRA and the rest was simulated by using ELEGANT with the CSR effect included.

5.3.1. Isochronous beamline

The dogleg can be used to transfer the velocity-bunched beam from the first beamline to the second one with little impact on the longitudinal phase-space. The optics and the evolutions of the first and second order longitudinal dispersions for the isochronous setup are shown in Figure 5.26 and Figure 5.27, respectively. It should be noted that the R_{56} of the drift space (~ -0.026 mm/m for the 100 MeV beam) is not included in the plot. Simulation shows that the longitudinal phase-space of the 10-pC, 183-fs bunch remains almost unchanged after passing through the dogleg, as shown in Figure 5.28. However, the horizontal projected emittance increases from $0.14 \mu\text{m}$ to $0.41 \mu\text{m}$, while the horizontal slice emittance increases to $0.23 \mu\text{m}$. Although the whole dogleg is nearly isochronous, the R_{56} fluctuates along the beamline. Therefore, the bunch experiences compression or decompression if the chirp of the bunch is non-zero. In this case, the bunch is compressed to about 50 fs after the third dipole magnet, as shown in Figure 5.29, which strongly enhances the CSR effect. It is worth noting that the emittance growth is sensitive to the phase advance between the third and fourth dipole magnets, which is found to be minimized when the phase advance is about 180° .

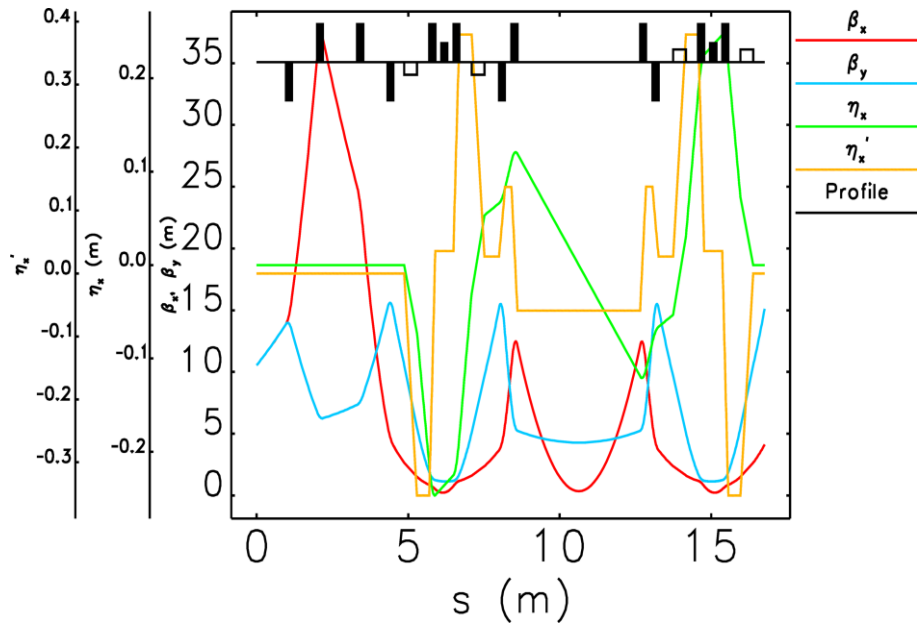


Figure 5.26: Design optics along the isochronous dogleg beamline.

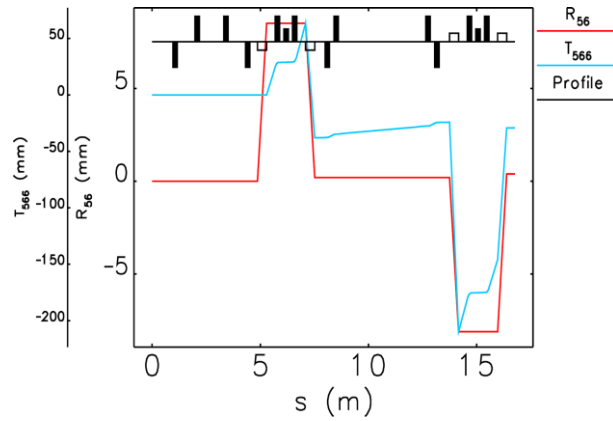


Figure 5.27: Evolutions of the first and second order longitudinal dispersions along the isochronous dogleg beamline.

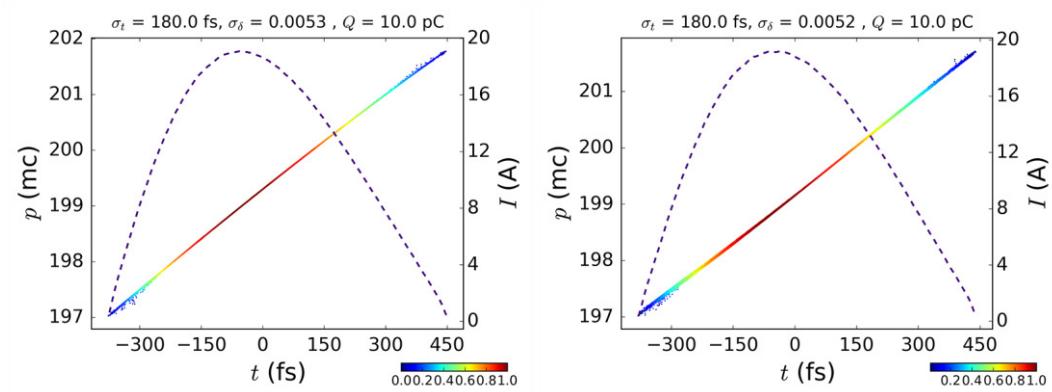


Figure 5.28: Longitudinal phase-spaces of a 10-pC bunch before (left) and after (right) the isochronous dogleg beamline.

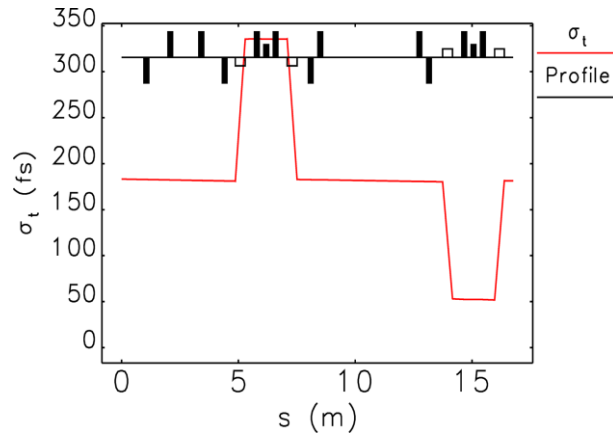


Figure 5.29: Evolution of the bunch length of a 10-pC bunch along the isochronous dogleg beamline.

In another example, a nearly fully compressed 0.5-pC bunch was simulated in the above beamline, and the initial and final longitudinal phase-spaces are shown in Figure 5.30. Since the bunch is largely decompressed and then re-compressed at each pair of dipoles, as shown in Figure 5.31, the CSR effect is considerably mitigated. The bunch becomes even shorter after the dogleg, and the horizontal projected emittance only increases from $0.06 \mu\text{m}$ to $0.08 \mu\text{m}$.

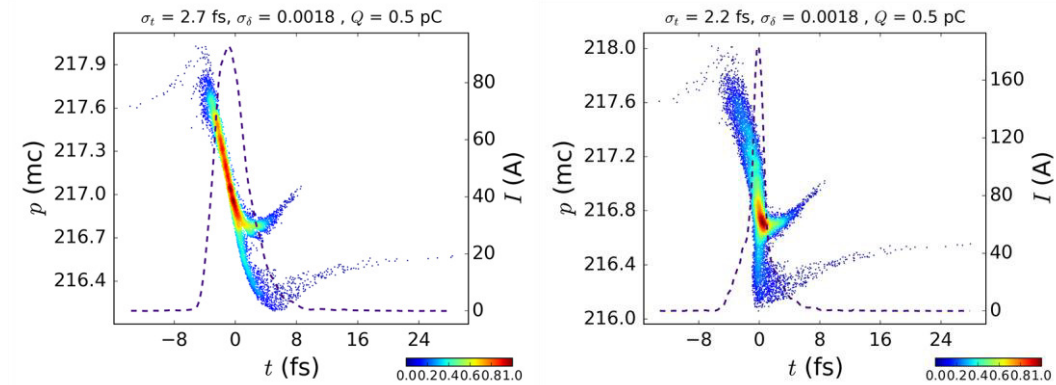


Figure 5.30: Longitudinal phase-spaces of a 0.5-pC bunch before (left) and after (right) the isochronous dogleg beamline.

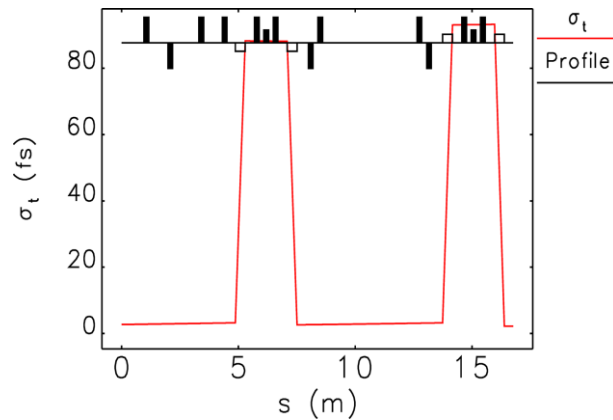


Figure 5.31: Evolution of the bunch length of a 0.5-pC bunch along the isochronous dogleg beamline.

5.3.2. Hybrid compression

The dogleg beamline can also be used to further compress the velocity-bunched beam. The optics and the evolutions of the first and second order longitudinal dispersions for the setup with an overall R_{56} of -9 mm are shown in Figure 5.32 and Figure 5.33, respectively. It is found that the optics changes slightly comparing with Figure 5.26. The same bunch used in Figure 5.28 was simulated through the dogleg beamline with this setup, and the final phase-space is shown in Figure 5.34. The bunch is finally compressed to about 19 fs with a nearly symmetric current profile. It is surprising to find out that the final horizontal projected emittance is about $0.41 \mu\text{m}$, which is almost the same as in the previous case when the bunch is not further compressed. This can be explained by the bunch length evolution along the dogleg, as shown in Figure 5.35. Since the bunch is largely over-compressed in the third dipole magnet, the bunch length is still very long at the entrance of the fourth dipole magnets which mitigates the CSR effect. It should be noted that the final slice emittance only increases to $0.25 \mu\text{m}$.

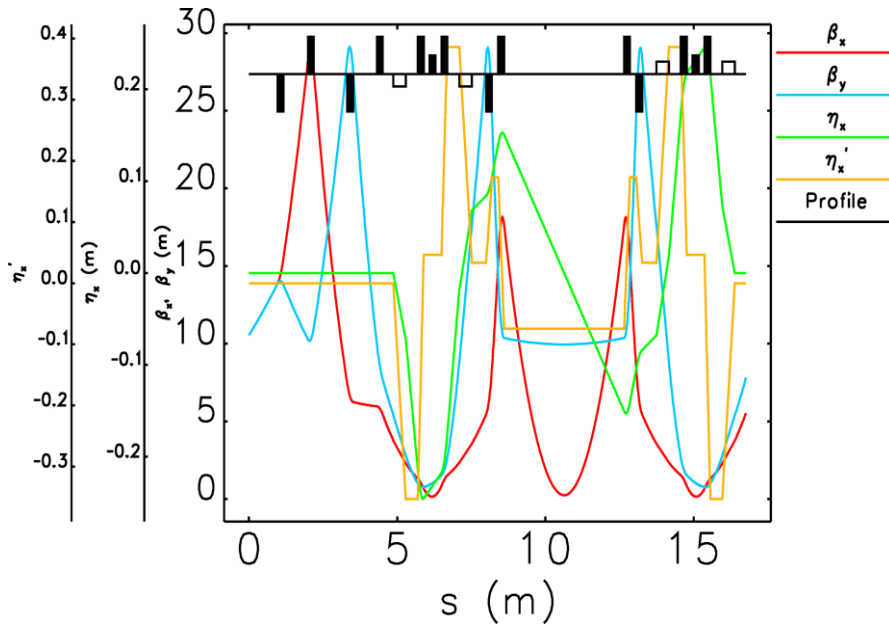


Figure 5.32: Design optics along the dogleg beamline with an overall R_{56} of -9 mm.

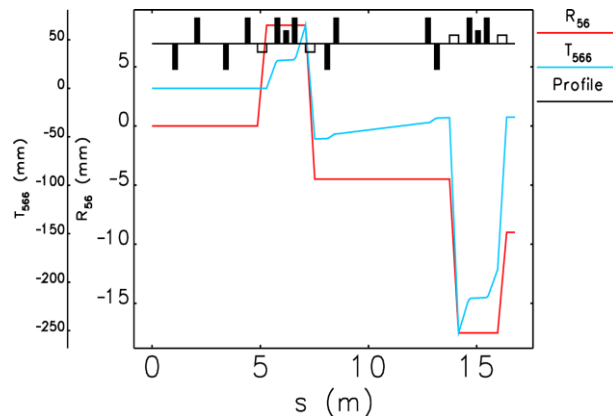


Figure 5.33: Evolutions of the first and second order longitudinal dispersions along the dogleg beamline with an overall R_{56} of -9 mm.

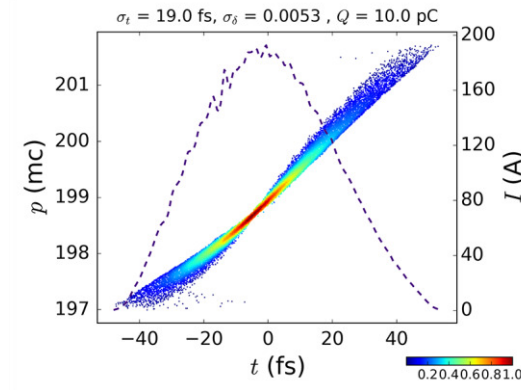


Figure 5.34: Longitudinal phase-space of a 10-pC bunch after the dogleg beamline with an overall R_{56} of -9 mm.

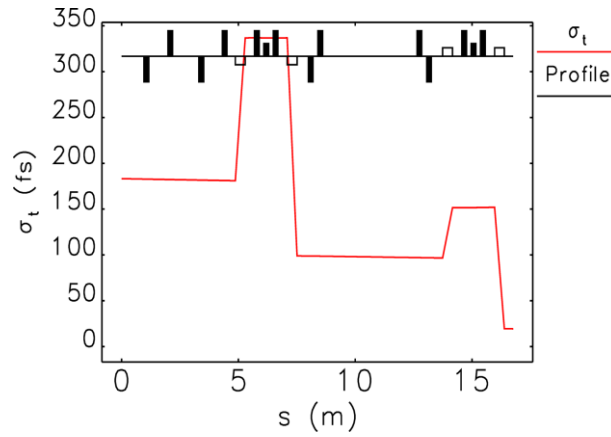


Figure 5.35: Evolution of the bunch length of a 10-pC bunch after the dogleg beamline with an overall R_{56} of -9 mm.

5.4. Summary

In this chapter, three major topics in the ARES lattice design have been investigated: the technical design of the chicane bunch compressor, the final focus beamline and the design of the dogleg.

Various practical issues have been considered during the technical design of the chicane bunch compressor. In order to install a high resolution BMP between the second and the third dipole magnets, a movable chicane design must be adopted. Water cooling is not necessary for the slit collimator system, but the thickness of the slit (Cu) should be at least 3 cm in order to eliminate the influence of the secondary electrons downstream of the chicane for a 200-MeV incoming beam.

A final focus section downstream of the chicane bunch compressor has been designed to focus the ultra-short, space-charge dominated electron bunches into a plasma accelerator. The simulated beta functions can reach as small as several mm. The major consideration in this design is to use a strong PMQ triplet to focus the electron

bunch immediately after the bunch compressor. Therefore, the impact of the space-charge effects can be mitigated, while the beam optics before the PMQ triplet can be adjusted by several quadrupole magnets in the matching section upstream of the chicane. It is of vital importance to have electron bunches with energy spreads much lower than 1%, which makes the slit collimator in the chicane a critical component of the system. In addition, it was found that increasing the electron energy to 150 MeV (adding the third traveling wave structure) can significantly improve the electron bunch quality at the focus.

A dogleg beamline with tunable R_{56} ranging from -10 mm to 10 mm has been designed not only to deliver electron bunches to the second beamline, but also to provide a unique opportunity to compare different compression schemes at the ARES linac. Due to the geometrical constraint in the SINBAD tunnel, the bending angle for each dipole magnet in the dogleg is 20 degree, which makes the CSR effect significant. Moreover, the space for diagnostics is very tight, particularly in between the first and last two dipole magnets.

6 Misalignment Measurement of Femtosecond Electron Bunches with THz Repetition Rate

Generation of a train of drive electron bunches separated by one plasma wavelength followed by a witness bunch is of particular interest for PWFAs [Kallos07] and thus is a possible research interest at the ARES linac in the future. Keeping the individual electron bunches transversely well-aligned is crucial for such a bunch train. It is intuitive that the misalignments between the drive bunches will affect the plasma wake-field generation, which in turn degrades the quality of the witness bunch. Moreover, studies have shown that the misalignment of the electron bunch with respect to the laser beam will result in large emittance growth in LWFAAs [Assmann98][Dornmair15]. Similarly, the misalignment of the witness bunch with respect to the drive bunch (train) has the same effect in PWFAs.

Beam position monitors (BPMs) serve as a non-destructive beam diagnostic device are used in nearly any accelerator operating with bunched beams [Forck08]. However, since the bandwidths of the pick-up electrodes and the readout electronics are limited to several GHz nowadays, BPMs cannot discriminate between bunches with THz repetition rate.

In this chapter, a novel method is proposed to simultaneously measure the relative misalignments of the individual femtosecond electron bunches with THz repetition rate in a train in both planes, which is critical for the control of the alignments of the individual bunches. The measurement was carried out at the SPARC_LAB test facility [Ferrario13], where a train of tens-of-femtosecond-long bunches with THz repetition rate can be generated. The results in this chapter have been published at <https://doi.org/10.1103/PhysRevAccelBeams.20.042801>.

6.1 SPARC_LAB overview

The layout of the SPARC_LAB test facility is shown in Figure 6.1 [Pompili16]. The photoinjector consisting of a 1.6-cell S-band RF gun (2.856 GHz, of the BNL/UCLA/SLAC type) can generate 5.6-MeV electron bunches at 10 Hz repetition rate, with a high-peak field of 120 MV/m on the embedded copper photocathode. These electron bunches are then focused and matched into the following three travelling-wave accelerating sections, which can boost electron energies up to 170 MeV with on-crest

acceleration. The first two sections are surrounded by solenoids in order to provide additional magnetic focusing to better control the beam envelope and the emittance oscillations under velocity bunching schemes. At the end of the linac, a diagnostics section allows to characterize the accelerated beam through both transverse and longitudinal measurements. The diagnostics transfer line, equipped with quadrupoles and an RFD, is also used to match the beam to the undulator in the main line for FEL experiments or, through bending magnets, to the by-pass line for THz radiation experiments.

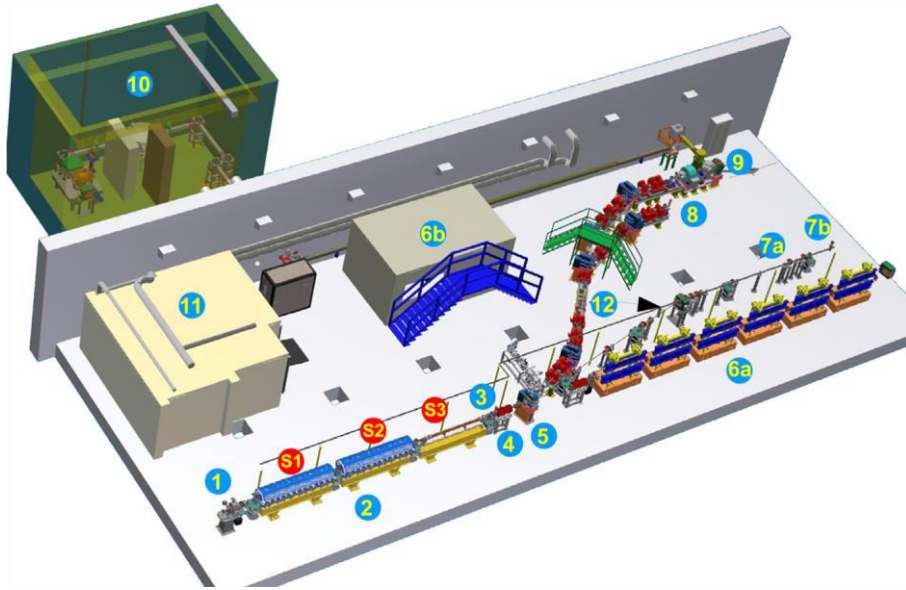


Figure 6.1: Layout of the SPARC_LAB facility. The gun (1) is followed by three travelling-wave structures (2), a THz station (3) and an RFD (4). Four beamlines follow the dipole (5): FEL (6a) both in SASE and with seed laser (6b), beam diagnostics based on THz radiation (7a) and electro-optic sampling (7b), plasma acceleration (8) and X-rays production by Thomson scattering (9) using the FLAME laser (10). Electro-optic sampling shares the laser from the photo-cathode (11) and is delivered by an optical line (12).

6.2 Experimental setup

By illuminating the photocathode with a train of laser pulses and utilizing the velocity bunching technique, a train of femtosecond bunches with THz repetition rate can be generated [Boscolo07] and fully characterized through transverse and longitudinal diagnostics measurements [Cianchi15].

The details of the diagnostics transfer line is shown in Figure 6.2, consisting of three quadrupole magnets followed by a vertical RFD (an S-band five-cell standing-wave RF deflecting cavity) [Alesini06] and a dipole magnet. The maximum power available for the RFD is approximately 2 MW. The view screen U3 is located 2.642 m downstream of the dipole centre in the main beam line, and another view screen D1 is located 3.274 m downstream of the dipole magnet center in the 14° bending arm. Each view screen is composed of a piece of 100- μm -thick YAG:Ce crystal and normal to the

respective beam line, with a 45°-mirror placed on the back. The light is then collected by a 105 mm F11 lens and recorded with a Basler scout A640 CCD camera with pixel size of 7.4 μm (1:3 magnification). The transverse emittance of the beam can be measured at U3 by the quadrupole scan method and the longitudinal phase-space of the beam can be measured at D1 by combining the RFD and the dipole magnet [Emma00]. A typical longitudinal phase-space of the bunch train, which was measured at Flag D1, was shown in Figure 6.3.

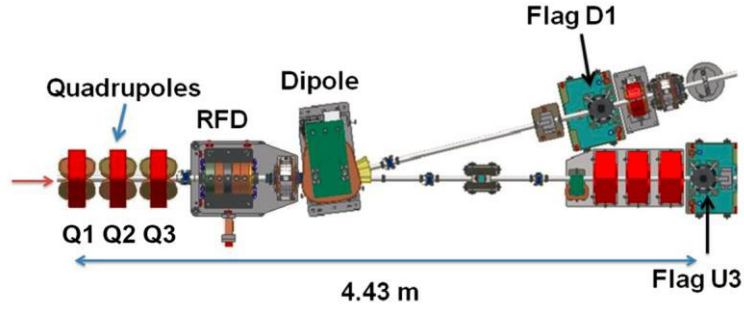


Figure 6.2: Non-scale layout of the SPARC_LAB diagnostic section beam line. The beam is coming from the left side.

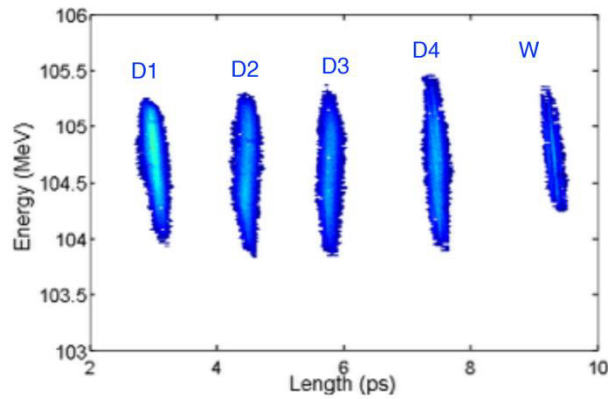


Figure 6.3: Typical measured longitudinal phase-space of the train at Flag D1. The bunch head is on the left. D1, D2, D3, D4 are the four drive bunches while W refers to the witness bunch.

6.3 Theory of misalignment measurement

To first order, considering a beam line composed of non-skew quadrupole magnets, drifts and an RFD streaking the beam in the vertical direction, the transverse coordinates of an electron at the screen are given by

$$x_f = R_{11}x + R_{12}x', \quad (6.1)$$

and

$$y_f \approx R_{33}y + R_{34}y' + B\phi, \quad (6.2)$$

where $[x, x', y, y']$ and $[x_f, y_f]$ are the initial and final transverse coordinates of the electron, respectively, R_{11} , R_{12} , R_{33} and R_{34} are the transfer matrix elements between

the initial and final locations with the RFD switched off, $B \approx eV_{RFD}R_{34}/pc$ [Emma00] and ϕ (=0 for zero crossing) are the strength and the phase of the RFD, respectively.

Since the energy spread of the concerned electron bunch is of the order of 10^{-3} , the misalignment of the bunch at the screen can be obtained by averaging equation (6.1) and (6.2) on both sides. One gets

$$c_{x_f} \approx R_{11}c_x + R_{12}c_{x'} \quad (6.3)$$

$$c_{y_f} - Bc_\phi \approx R_{33}c_y + R_{34}c_{y'}, \quad (6.4)$$

where $[c_x, c_y]$ and $[c_{x_f}, c_{y_f}]$ are the initial and final displacements of the bunch, respectively, $[c_{x'}, c_{y'}]$ are the initial divergences of the bunch, and c_ϕ is the RFD phase for the centroid of the bunch. When the strength of a single quadrupole magnet is scanned, by measuring the final displacements of the bunch (on the screen at the Flag U3), the displacements and divergences of the bunch at the initial location can be derived by linear regression using the vector forms of equation (6.3) and (6.4):

$$\mathbf{c}_{x_f} \approx \mathbf{R}_{11}c_x + \mathbf{R}_{12}c_{x'} \quad (6.5)$$

and

$$c_{y_f} - Bc_\phi \approx \mathbf{R}_{33}c_y + \mathbf{R}_{34}c_{y'}. \quad (6.6)$$

Here we have assumed that \mathbf{R}_{11} and \mathbf{R}_{12} are linearly independent, as are \mathbf{R}_{33} and \mathbf{R}_{34} .

The RFD amplitude and phase of each bunch are required in equation (6.6). However, because of the RFD phase and amplitude jitter as well as the bunch arrival-time jitter, it is impossible to measure the precise RFD phase and amplitude for each bunch. As will be shown in the following, the jitter has a large impact on the measurement in the vertical plane. In order to avoid the measurements of the RFD voltage and the RFD phase for each bunch, equation (6.6) can be transformed into

$$\Delta c_{y_f} \approx \Delta \mathbf{R}_{33}(c_y + \kappa c_{y'}), \quad (6.7)$$

where $\Delta c_{y_f} = c_{y_f} - \bar{c}_{y_f}$, $\Delta \mathbf{R}_{33} = \mathbf{R}_{33} - \bar{\mathbf{R}}_{33}$, the upper bar indicates the average value during the quadrupole scan and we have used the relationship $\Delta \mathbf{R}_{34} = \kappa \Delta \mathbf{R}_{33}$. It is found that only $c_y + \kappa c_{y'}$ can be derived from equation (6.7). Under the condition of $\kappa c_{y'} \ll c_y$, the measured $c_y + \kappa c_{y'}$ is a good approximation to c_y . Considering that the initial location and the scanned quadrupole magnet are connected by a drift space, their distance should be as short as possible since κ is simply the drift length. It should be noted that $c_{y'}$ can be measured instead of c_y by choosing a large κ .

After solving equations (6.5) and (6.7) for every bunch in a train, the misalignment of each bunch with respect to the axis of the train can be calculated by weighting the corresponding bunch charge, i.e.

$$\hat{c}_{X,j} = c_{X,j} - \sum_j q_j c_{X,j}, \quad (6.8)$$

where q_j is the fractional charge of the j -th bunch, X denotes any transverse coordinate and the upper hat indicates the relative value.

In order to quantify the accuracy of the measurement, particularly in the vertical plane, we define the fractional measurement error for the transverse coordinate X as

$$h_X = \sqrt{\frac{\sum_j q_j (\hat{c}_{X,j} - \hat{c}_{X,j,in})^2}{\sum_j q_j \hat{c}_{X,j,in}^2}}, \quad (6.9)$$

where $\hat{c}_{X,j,in}$ denotes the input relative misalignment of the j -th bunch. The intrinsic error of the displacement measurement in the vertical plane is then given by

$$h_y = |\kappa| \sqrt{\frac{\sum_j q_j \hat{c}_{y',j,in}^2}{\sum_j q_j \hat{c}_{y,j,in}^2}}. \quad (6.10)$$

It is apparent that the accuracy of \hat{c}_y improves as κ and $\hat{c}_{y'}$ decrease.

Understanding the influences of the RFD phase and voltage jitter is of importance to explain the measured data in the vertical plane. In the presence of jitter, equation (6.7) can be written as

$$\Delta c_{y_f} = \Delta \mathbf{R}_{33} (c_y + \kappa c_{y'} + K) + \Delta \mathbf{J} - \Delta \mathbf{R}_{33} K, \quad (6.11)$$

where K is an additional effective value for the input displacement to represent the RFD jitter and $\Delta \mathbf{J} = \mathbf{J} - \bar{\mathbf{J}}$ with \mathbf{J} being the actual induced vertical displacements on the screen. The objective of the linear regression is to minimize the residual sum of squares, which is given by

$$\hat{\varepsilon} = (\Delta \mathbf{J} - \Delta \mathbf{R}_{33} K)^T (\Delta \mathbf{J} - \Delta \mathbf{R}_{33} K). \quad (6.12)$$

The minimum $\hat{\varepsilon}$ is achieved when the derivative of equation (6.12) with respect to K is zero, which gives

$$K = \Delta \mathbf{J}^T \Delta \mathbf{R}_{33} / \Delta \mathbf{R}_{33}^T \Delta \mathbf{R}_{33} = \rho_{R_{33},J} \sigma_J / \sigma_{R_{33}}, \quad (6.13)$$

where $\rho_{R_{33},J}$ is the Pearson's correlation coefficient between \mathbf{R}_{33} and \mathbf{J} , $\sigma_{R_{33}}$ and σ_J are the standard deviations of \mathbf{R}_{33} and \mathbf{J} , respectively. Since $\sigma_{R_{33}}$ increases as the scan current range increases, K can be reduced by using a larger scan range.

In the presence of only the phase jitter, $\Delta \mathbf{J}$ is the same for each bunch in a train since each one has the same deflecting voltage increment. $\sigma_{R_{33}}$ and $\rho_{R_{33},J}$ are almost the same for each bunch as well since the energy differences between bunches are small. Consequently, K will be nearly the same for each bunch so that it can be eliminated in

equation (6.8). Therefore, the phase jitter will basically not affect the measurement result.

In the presence of only the voltage jitter, since each bunch in a train has the same voltage jitter but a different phase, ΔJ is different for each bunch. However, $\rho_{R_{33},J}$ is still nearly the same for each bunch since the correlation has nothing to do with the phase which is a constant for each bunch during the scan. Hence K will be different for each bunch so that it cannot be eliminated in equation (6.8). Therefore, the voltage jitter will introduce error into the measurement result.

It should be pointed out that this method in principle ought to be used for relative misalignment measurement. In the horizontal plane, the fitted c_x and $c_{x'}$ will coincide with the absolute misalignment only if the horizontal position of the screen with respect to the accelerator axis has been calibrated. Otherwise, the fitted c_x and $c_{x'}$ will both be the real value plus a constant. For the relative misalignment measurement, the calibration is not necessary since this unknown constant will be eliminated in equation (6.8). While in the vertical plane, equation (6.8) is required to eliminate the RFD phase jitter. Nevertheless, the absolute misalignment of each bunch can be calculated straightforwardly by adding the misalignment of the whole bunch train measured by the BPM.

In addition, the energy of each bunch is required to calculate the transfer matrices from the initial location to the screen. Since the energy differences between bunches are expected to be less than 1%, the average energy of the train can be used to calculate the matrix for every bunch. The simulation result presented in the next section shows that the result is not sensitive to the energy used in the calculation.

6.4 Simulations

In order to validate the proposed method, the beamline used for the misalignment measurement was set up in ELEGANT. The parameters of each bunch at the initial location, which is 0.2 m upstream of the centre of Q1, are summarized in Table 6.1. All the values are either measured or estimated from the experiment. The deflecting strength of the RFD is about 1.46 mm/deg at the screen.

Table 6.1: Summary of the input parameters for every bunch in the train used in the simulations. The parameters were chosen to be similar to the experimental working points. D1-D4 denote the drive bunches and W denotes the witness bunch. The centroid coordinates c_x are the values with respect to the accelerator axis, and t refers to the timing with respect to the zero crossing of the RFD.

	D1	D2	D3	D4	W
Q (pC)	54	58	48	45	20
β_x (m)	72	70	74	85	107
α_x	6.2	8.6	9.2	8.7	9.5
β_y (m)	60	82	92	74	85

α_y	-3.3	-2.6	-2.8	-3.2	-4.8
ε_x (μm)	3.0	3.4	3.3	3.3	1.7
ε_y (μm)	3.0	3.4	3.3	3.3	1.7
E (MeV)	104.68	104.61	104.59	104.66	104.75
$\Delta E_{\text{rms}}/E$	0.0027	0.0032	0.0032	0.0034	0.0024
σ_t (fs)	82	69	62	58	53
t (ps)	-2.40	-0.96	0.35	2.03	3.86
c_x (μm)	-50	150	200	100	-100
c_x (μrad)	10	5	0	15	20
c_y (μm)	200	100	50	100	-100

6.4.1 Simulations without any jitter

We first investigated the case without any jitter. The typical fits in both planes are shown in Figure 6.4, which reveal the linear relationship between the current of the quadrupole magnet and the bunch displacement on the screen. The input and simulated misalignments are compared in Figure 6.5. It is found that the simulated displacements and divergences match the input precisely in the horizontal plane. In the vertical plane, the input and simulated displacements only slightly differ from each other.

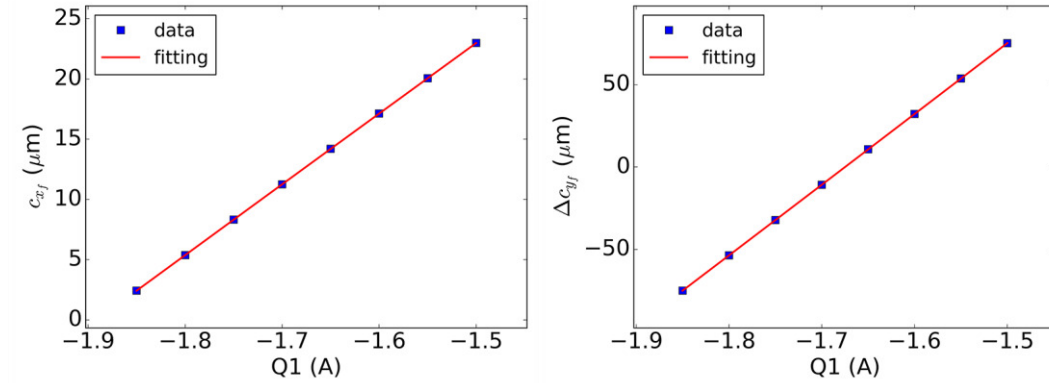


Figure 6.4: Typical fits for a single bunch in both planes without any jitter.

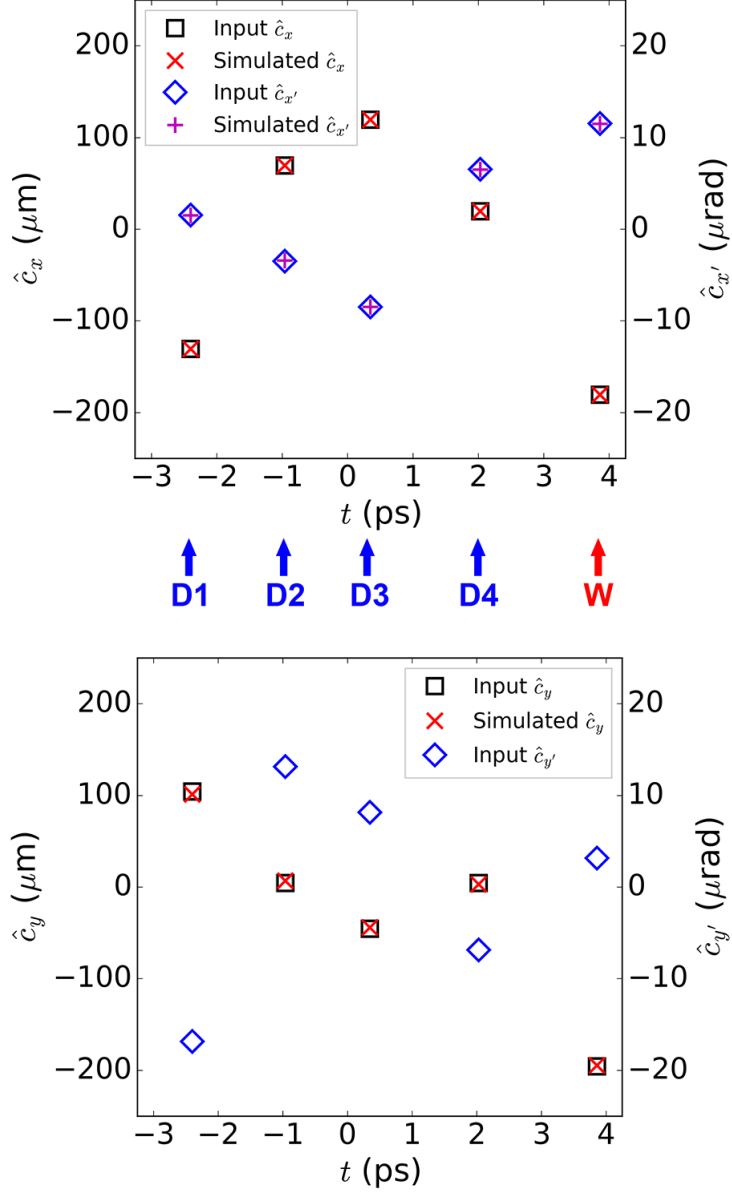


Figure 6.5: Comparisons between the input and simulated misalignments in both planes without any jitter. The bunch train head is on the left. The input $\hat{c}_{y'}$ are also shown in the plot since they affect the accuracies of \hat{c}_y .

For the simulation result shown in Figure 6.5, h_y is about 0.03 ($\kappa \approx 0.20$). As a comparison, h_y will increase to about 0.14 ($\kappa \approx 0.97$) if Q3 is used for scanning instead of Q1. A small κ value is critical when the displacement is small. Considering that every c_y given in Table 6.1 is reduced by an order of magnitude, the measurement error will increase to 0.28 when Q1 is used for scanning. With an error of 0.28 the data can still correctly represent the relative displacements between bunches, as shown in Figure 6.6. In contrast, the error will become as high as 1.41 when Q3 is used for scanning, as shown in Figure 6.7. Although we can still have a general knowledge of how good the relative misalignment is, the simulated relative vertical displacements between different bunches largely deviate from the input.

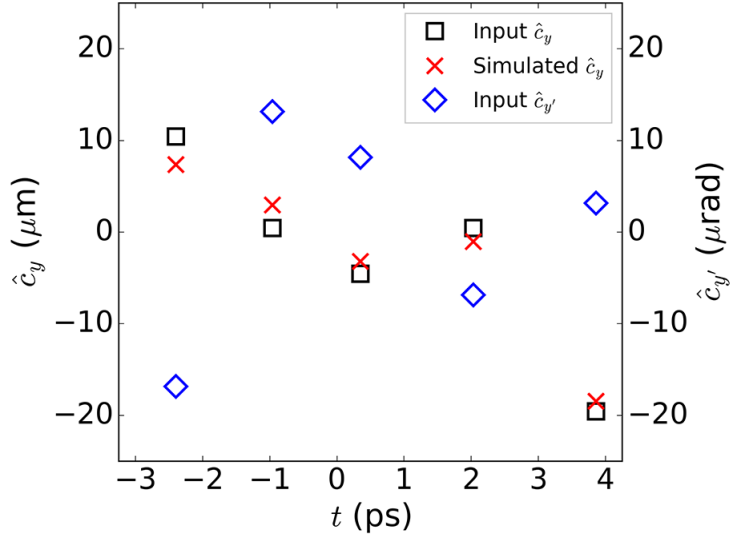


Figure 6.6: Comparison between the input and simulated misalignments in the vertical plane without any jitter. The input displacements are ten times as small as those in Figure 6.5. Q1 is used for scanning. The bunch train head is on the left.

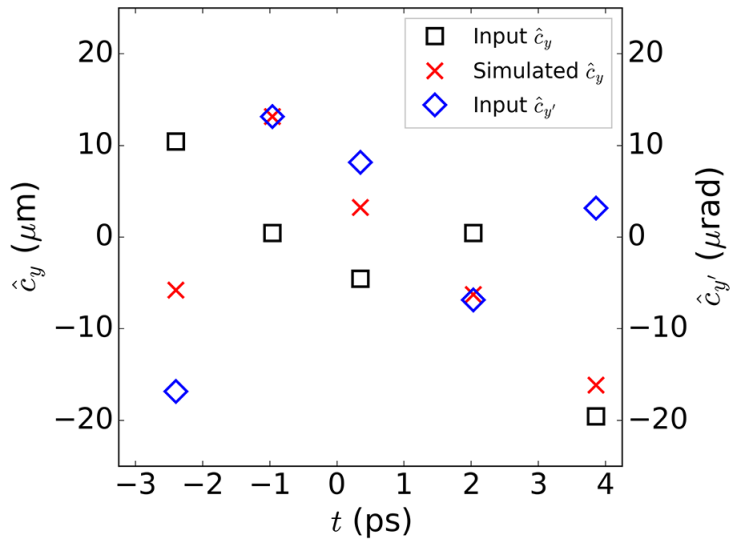


Figure 6.7: Same as Figure 6.6 but Q3 is used for scanning.

In practice, it is convenient to use an identical energy to calculate the transfer matrix for every bunch. Figure 6.8 shows the relationship between the measurement error and the energy used in the calculation. The reference energy is the average energy of the train. It is found that the measurement error is not sensitive to the energy. When Q1 is used for scanning, the optimized energy is slightly larger than the average energy of the train. It is noteworthy that, when Q3 is used for scanning, the measurement error consistently decreases as the energy deviation increases. The decrease in the measurement error is mainly caused by the decrease in κ , which is affected by the transfer matrices of Q1 and Q2.

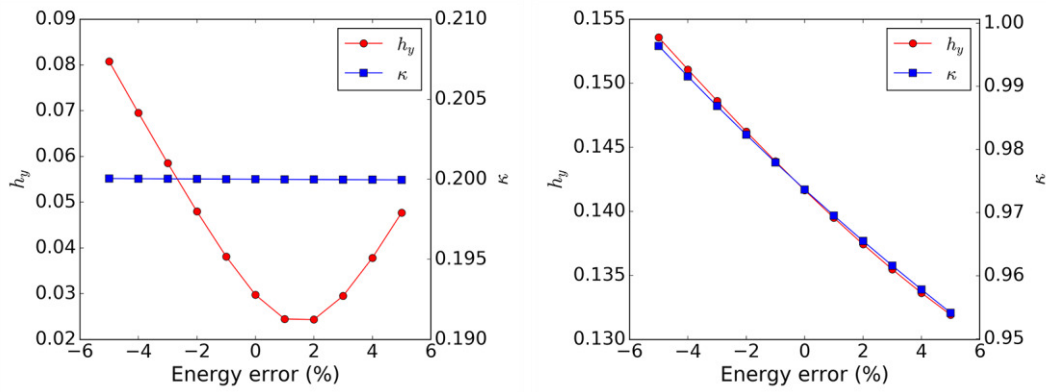


Figure 6.8: Sensitivities of the measurement error to the energy used in the transfer matrix calculation. Left: Q1 is used for scanning; right: Q3 is used for scanning.

6.4.2 Simulations with RFD jitter

The influences of the RFD voltage and phase jitter were demonstrated separately by 300 randomized simulations with a Gaussian distribution for each jitter source. In the simulation, the rms voltage and phase jitter were assumed to be 0.1% and 0.1 deg, respectively, which should be an overestimation for the S-band system nowadays [Craievich13]. The results are shown in Figure 6.9. Consistent with the analytical study, the phase jitter does not increase the measurement error, while the average error due to the voltage jitter increases from 0.03 to about 0.06. In addition, when Q3 is used for scanning, the average error increases to about 0.18 from 0.14 due to the voltage jitter. Simulations also confirm that the error growth halves when the current step increases from 0.05 A to 0.1 A.

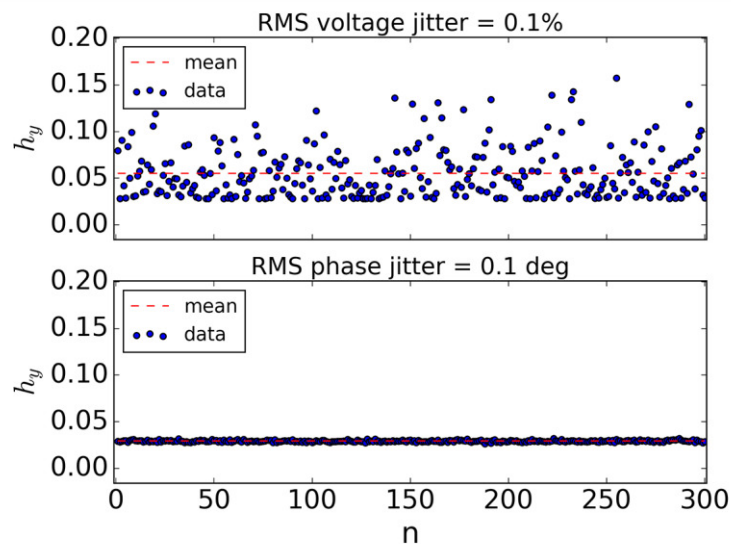


Figure 6.9: Errors of the simulated vertical displacements with 300 random RFD voltages (rms jitter 0.1%) and phases (rms jitter 0.1 degree), respectively. Q1 is used for scanning.

The typical fits including jitter are shown in Figure 6.10 and Figure 6.11. The data points including only the voltage jitter slightly deviate from the fitted line when the

RFD phase is not zero. However, the data points including only the phase jitter widely scattered around the fitted line. It is noteworthy that these data points are always on the same side of the fitted line for each bunch at a given scan current, and the distances are almost the same as well, as shown in Figure 6.12.

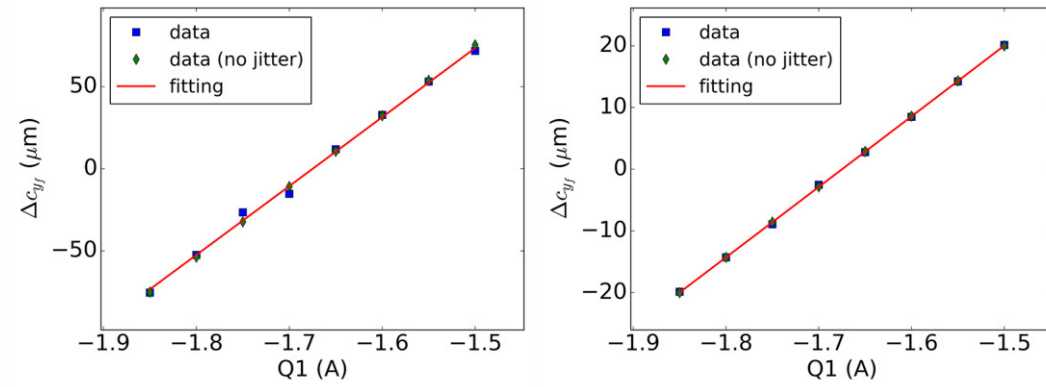


Figure 6.10: Fits in the vertical plane for the first (left) and the third (right) bunches in the train. Only the RFD voltage jitter is included. The data points without any jitter are also plotted together for comparison.

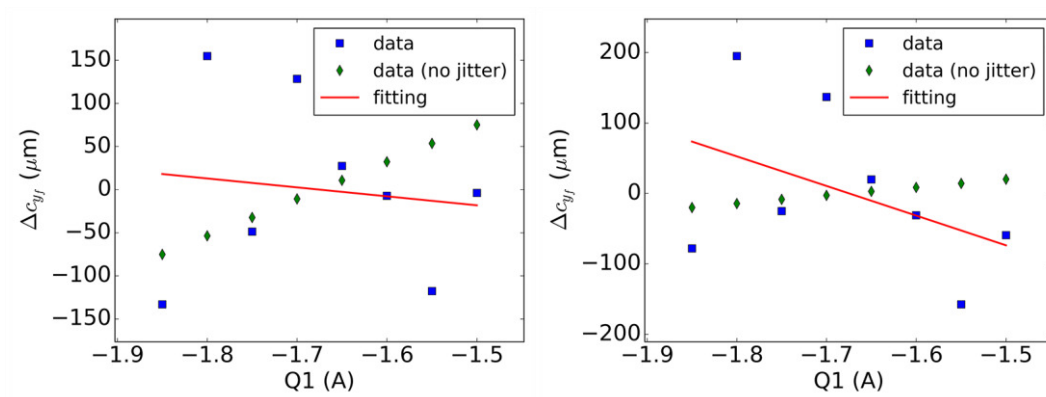


Figure 6.11: Same as Figure 6.10 except only the RFD phase jitter is included.

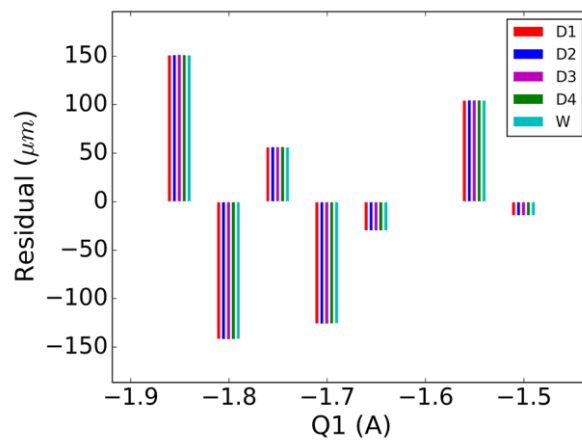


Figure 6.12: Residuals for the fits with only the RFD phase jitter. The residual is defined as the difference between the predicted value and the data.

By combining the jitter used in the simulations shown in Figure 6.10 and Figure 6.11, the input and simulated misalignments with both RFD phase and amplitude jitter included are compared in Figure 6.13. It indicates that the influence is almost negligible.

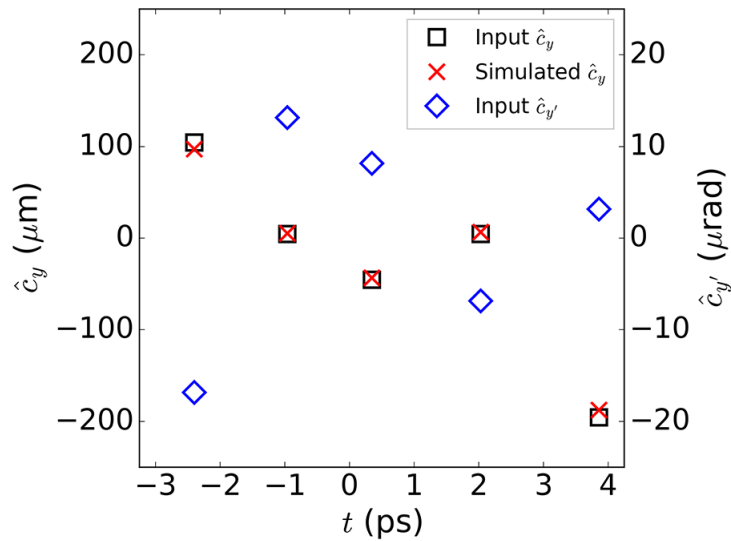


Figure 6.13: Comparisons between the input and simulated misalignments in the vertical plane with both RFD phase and amplitude jitter included. Q1 is used for scanning.

6.4.3 Simulations with beam position and pointing jitter

In real measurements, the initial misalignment of each bunch in a train jitters from shot to shot. The typical fits in the horizontal plane with an initial rms displacement jitter of $10\ \mu\text{m}$ and divergence jitter of $1\ \mu\text{rad}$, respectively, are shown in Figure 6.14. In principle, the position and pointing stabilities of each bunch can be inferred based on the experimental data in the horizontal plane, which are not affected by the RFD jitter. Similar to the RFD phase jitter, the correlated position and pointing jitter will not affect the relative misalignment measurement.

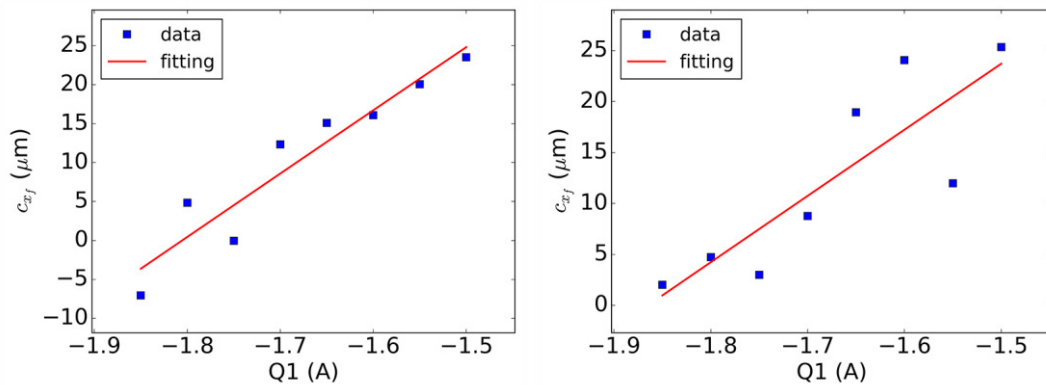


Figure 6.14: Typical fittings in the horizontal plane with an initial rms position jitter of $10\ \mu\text{m}$ and rms pointing jitter of $1\ \mu\text{rad}$.

6.5 Experimental results

In the experiments, we measured the misalignment of each bunch in a train 0.2-m upstream of the centre of Q1, where Q3 was used for scanning. Q3 was used instead of Q1 since we did not realize the difference between different scanning quadrupoles at that time. Ten images of the train were taken for each scan point and the average coordinates of the bunch centroid were calculated. The beam images for the No. 170652 experiment on the screen are shown in Figure 6.15, and the fits for each bunch are shown in Figure 6.16. The fractional charge of each bunch was calculated by weighting the intensity of the corresponding beamlet image.

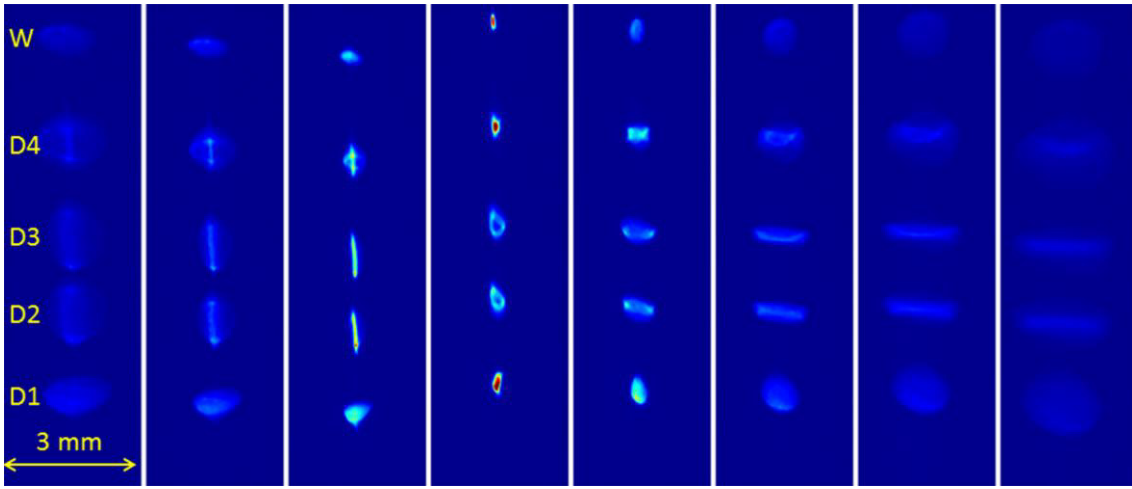
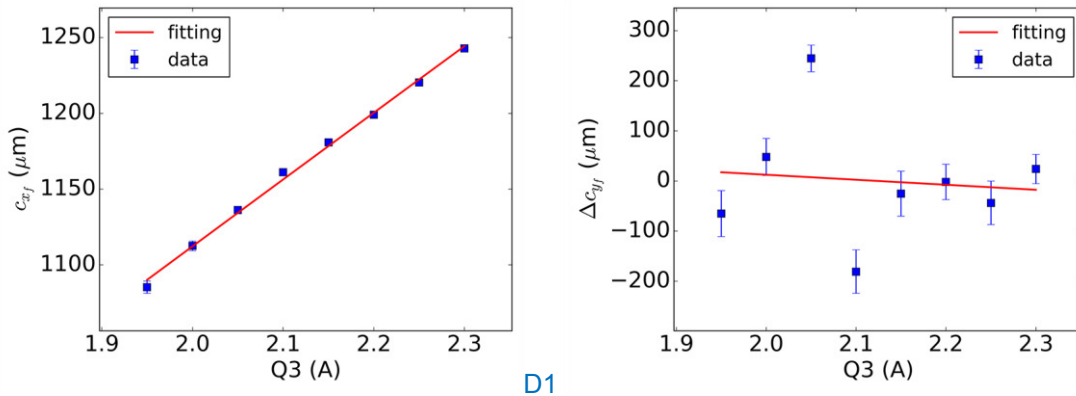


Figure 6.15: Images of the bunch train on the screen (Flag U3) during the quadrupole scan from the No. 170652 experiment.



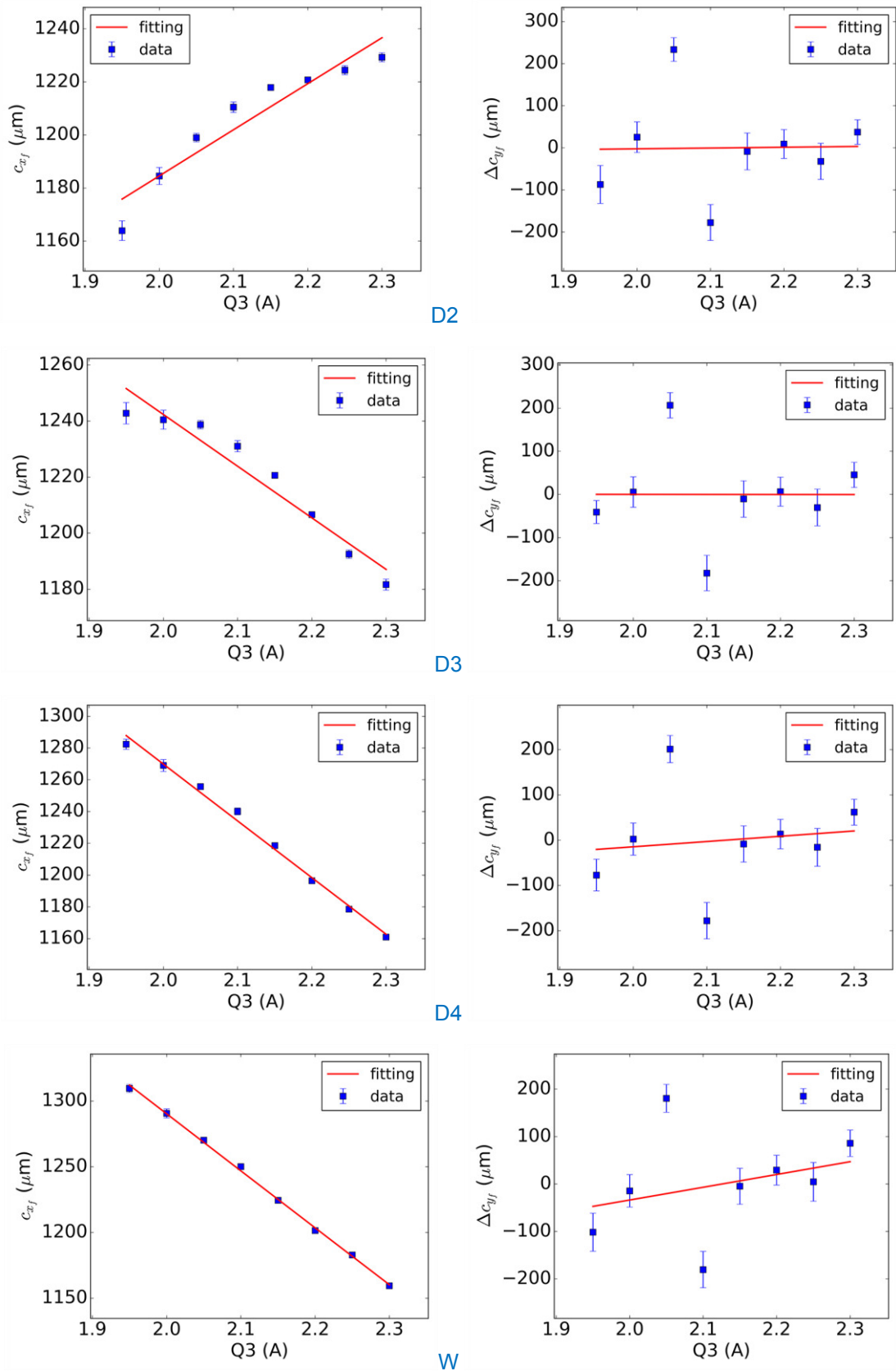


Figure 6.16: Fits for each bunch in the train in the horizontal and vertical planes for the No. 170652 experiment.

We attribute the small scattering of the data in the horizontal plane to the position and pointing jitter of the incoming bunches, and the large scattering of the data in the vertical plane to the RFD phase jitter. It should be noted that the bunch arrival-time jitter will also contribute to the phase jitter. As shown in Figure 6.17, the residuals of the fits are similar for each bunch at a given scan current. According to the previous analytical and simulation studies, this kind of jitter does not affect the relative misalignment measurement.

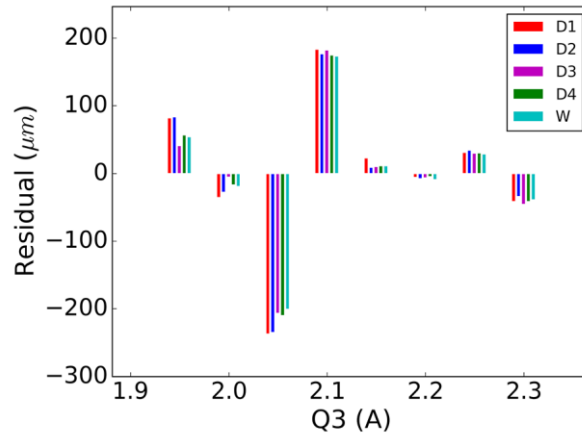


Figure 6.17: Residuals for the fits in the vertical plane shown in Figure 6.16.

The relative misalignment of each bunch was then calculated and the results are shown in Figure 6.18. Assuming the divergences of the individual bunches in the vertical plane are comparable to those in the horizontal plane, the average measurement error in the vertical plane is expected to be smaller than 0.25 without considering the misalignment jitter of the initial bunches. The measured bunch charge, energy, energy spread, bunch length, timing, horizontal emittance and Twiss parameters for each bunch are the same as those listed in Table 6.1.

The measured misalignments for another two experiments are also shown in Figure 6.18. It is apparent that these results from different experiments are very similar. The displacements in both planes are also strongly correlated: they both increase monotonically from the bunch head to tail. Therefore, the misalignments were most likely induced by certain systematic errors during the generation or transportation of the bunch train.

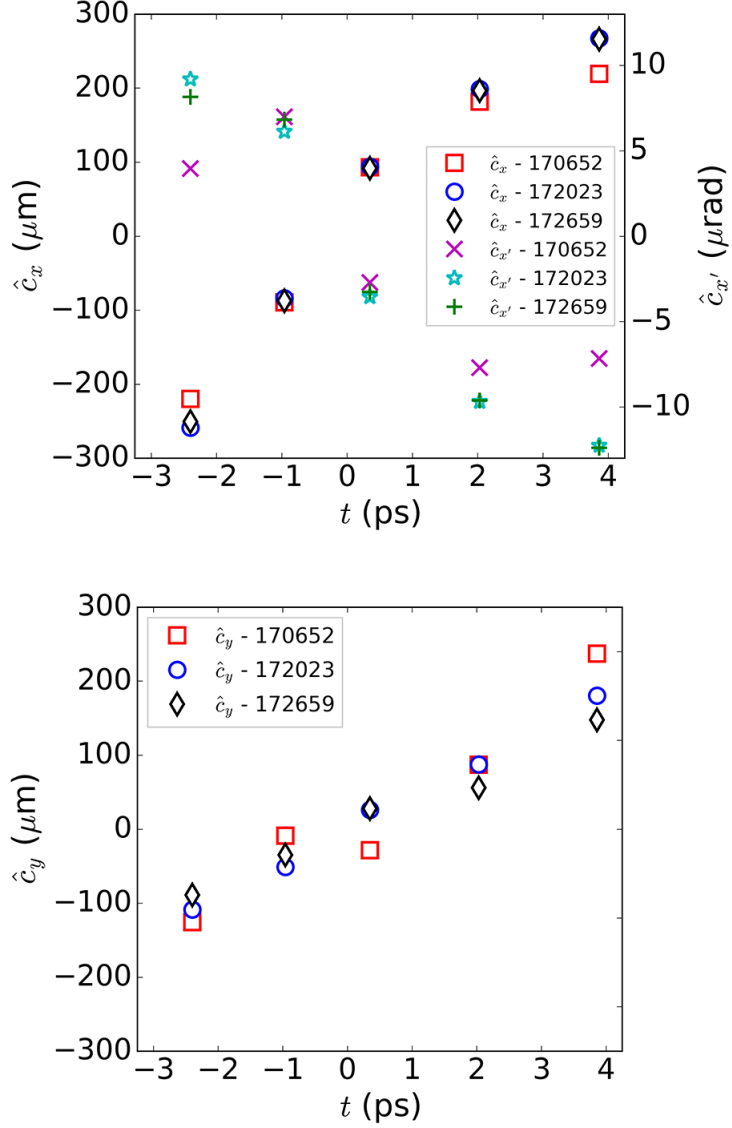


Figure 6.18: Measured misalignments of each bunch in the train for the No.170652, No.172023 and No.172659 experiments. The bunch train head is on the left.

6.6 Discussion

One possible explanation of the misalignments is the method used for generating the bunch train at the cathode. In these experiments, the bunch trains were produced by combining the properties of birefringent crystals and the flexibility of an interferometric-like configuration [Villa16]. This scheme, which allows to fully control and tailor the transverse, longitudinal and energy characteristics of each pulse, however requires a very good alignment in the transverse direction because of the transport optics (e.g. lenses) along the path towards the cathode. Any misalignment will change the relative transverse positions of the pulses over a long travel distance. Therefore, each bunch not only will experience a different energy because of the delayed injection

phase, but will also experience a different radial RF field in the gun because of the misaligned transverse arrival position on the cathode.

6.7 Summary

In this chapter, simultaneous measurement of the horizontal and vertical relative misalignments of the individual femtosecond electron bunches in a train with THz repetition rate, by combining the single quadrupole scan method and an RFD, have been demonstrated. The challenge of the measurement lies in the plane parallel to the deflecting voltage, which was investigated both analytically and numerically. The largely scattered data in this plane, which make the linear regression look very poor, was mainly induced by the RFD phase and bunch arrival-time jitter. However, the study proves that this kind of jitter has barely any influence on the relative misalignment measurement. The RFD voltage jitter, which only induces very small scattering of data, will introduce acceptable measurement error in the vertical plane. This additional error can be mitigated by using a large scan range of the current of the quadrupole magnet. Moreover, the setup between the initial location (where the misalignments are measured) and the scanned quadrupole magnet is important to reduce the measurement error in the vertical plane. In the case of a drift space, for instance, the length should be kept as short as possible. In addition, the average energy of the train can be used to calculate the transfer matrix for each bunch, and the result is not sensitive to this energy. The proposed misalignment measurement method is fast and easy to implement, and the RFD strength and the RFD phase for each bunch do not need to be known. Finally, the absolute misalignment of each bunch can be calculated straightforwardly by adding the misalignment of the whole bunch train measured by the BPM.

7. Final Design Working Points of the ARES Linac

The final design of the ARES linac beamline is being finalized by a trade-off among different beamline components and repeated iterations, for instance, the selection of the traveling-wave structure and the corresponding klystron in favor of the stabilization of the accelerating field, the design of the laser mirror being able to achieve a small laser spot size on the cathode without intercepting the electron bunch, the integration of the “high-charge” solenoid in a limited space around the gun, and so on. The sketch of this final beamline design is shown in Figure 2.2.

In the first half of this chapter, the start-to-end simulation results for four typical working points with this final layout of the ARES linac using different compression schemes are presented. These workings points, covering the design ranges of the bunch charge (0.5 pC ~ 30 pC) and the bunch length (sub-fs ~ dozens of fs), have many different applications, for instance, field sampling for advanced accelerating structures, LWFA-driven FEL generation, beam dynamics studies, R&D on advanced beam diagnostics [Marx17] and so on. These applications are summarized in Figure 7.1. Since the LWFA-driven FEL is one of the most attracting applications, a brief introduction of FEL theory is given in the second half of this chapter. The challenges and potential solutions in beam capture after the plasma and FEL generation are discussed. Moreover, a preliminary analytical study of the foreseen FEL parameters using the working points at ARES is presented.

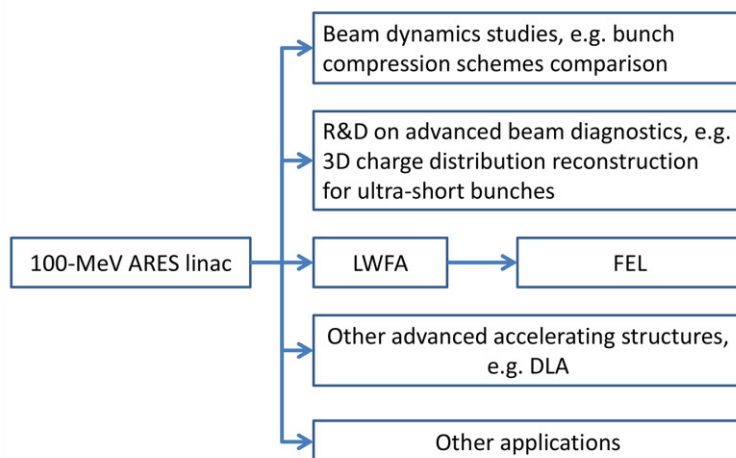


Figure 7.1: Summary of the applications for the ARES linac.

7.1. Working points at ARES linac

Four typical working points (WPs) covering the design ranges of different beam parameters of the ARES linac were simulated. Two of them utilize the pure magnetic compression method, one utilizes the velocity bunching method and the other utilizes the hybrid compression method. The major parameters used in these simulations are listed in Appendix C. The simulated beam parameters at different locations for these working points are summarized in Table 7.1 ~ Table 7.3.

Table 7.1: Summary of beam parameters at the linac exit for different working points.

	WP1	WP2	WP3	WP4
Energy (MeV)	100.6	102.0	99.6	101.2
Bunch charge (pC)	20	200	30	50
Projected horizontal emittance (μm)	0.13	0.40	0.84	0.34
Projected vertical emittance (μm)	0.13	0.40	0.84	0.34
Slice horizontal emittance (μm)	0.094	0.30	0.93	0.32
Slice vertical emittance (μm)	0.094	0.30	0.93	0.32
Bunch length [rms] (fs)	2141	2727	30	184
Peak current (kA)	0.0035	0.025	1.6	0.11
Longitudinal phase-space chirp (1/m)	78.5	76.3	\	106.1
Relative rms energy spread	0.050	0.062	0.0050	0.0058

Table 7.2: Summary of beam parameters at the chicane exit for different working points.

	WP1	WP2	WP3	WP4
Energy (MeV)	100.5	101.8	99.6	100.9
Bunch charge (pC)	0.79	5.8	30	17.3
Projected horizontal emittance (μm)	0.096	0.42	1.0	0.33
Projected vertical emittance (μm)	0.094	0.29	1.0	0.32
Bunch length [rms] (fs)	0.51	1.5	31.8	10.7
Peak current (kA)	2.1	1.4	0.44	1.4
Relative rms energy spread	0.0019	0.0024	0.013	0.0022

Table 7.3: Summary of beam parameters at the plasma entrance for different working points. The bunch tail containing 5% of the particles are not included in the calculation since the parameters of these particles largely deviate from the rest, and will most probably be lost during further acceleration and transportation. Slice properties were calculated for the slice centred at the current peak (WP1, WP3 and WP4) or the bunch centre if the longitudinal current profile has a plateau (WP2). The length of the slice is about 1/10 of the total bunch length.

	WP1	WP2	WP3	WP4
Energy (MeV)	100.5	101.7	99.5	100.8
Bunch charge (pC)	0.75	5.5	28.5	16.5
Projected horizontal emittance (μm)	0.11	0.50	4.8	0.50

Projected vertical emittance (μm)	0.099	0.38	24.9	0.79
Slice horizontal emittance (μm)	0.10	0.32	4.2	0.42
Slice vertical emittance (μm)	0.077	0.37	12.1	0.82
β_x (mm)	1.1	1.8	1.9	2.3
α_x	-0.21	0.69	0.89	1.7
β_y (mm)	1.0	1.8	3.5	1.2
α_y	0.24	-0.58	0.14	-0.60
σ_x (μm)	0.76	2.1	6.9	2.4
σ_y (μm)	0.71	1.9	21.0	2.2
Bunch length [rms] (fs)	0.43	1.7	31.9	8.0
Peak current (kA)	0.62	1.1	0.54	1.5
Relative rms energy spread	0.0017	0.0043	0.0120	0.0027
Slice rms energy spread	0.0010	0.0028	0.0079	0.0021

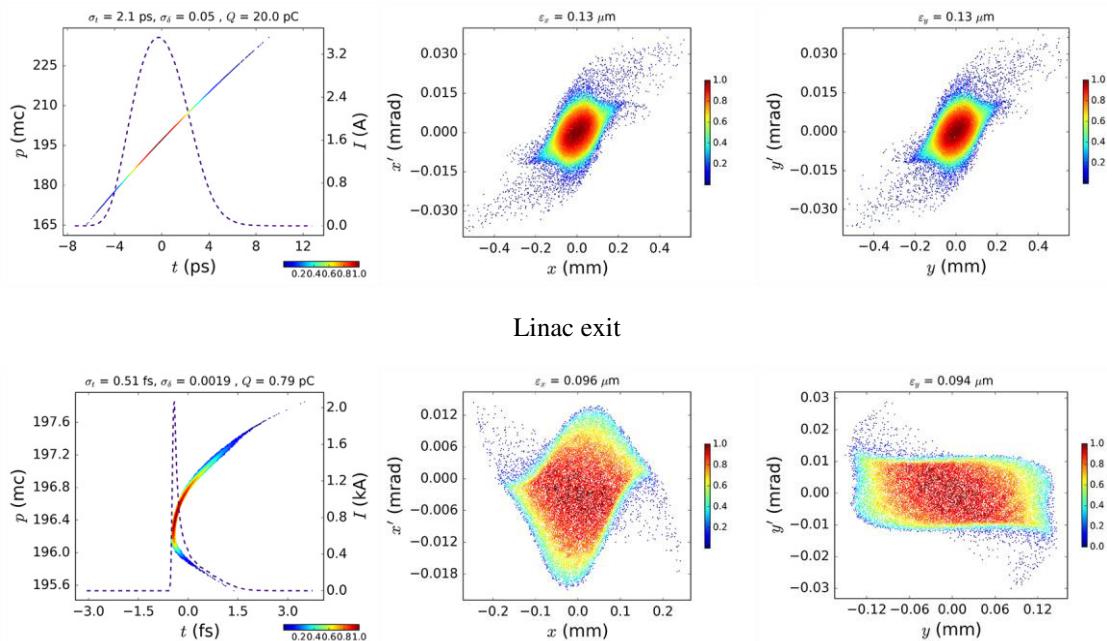
WP1 is defined as the working point for reaching sub-fs bunch length with the smallest bunch arrival-time jitter by using the pure magnetic compression method with the two travelling-wave structures operated at the same amplitude and phase. The simulation result is shown in Figure 7.2. Electron bunches generated at WP1 will provide excellent time resolution as probes in advanced accelerating structures, e.g. inside a plasma chamber. A preliminary simulation for the SINBAD experiment using the similar beam parameters shows that the total rms energy spread of the beam decreased from 0.37% to 0.25% after being accelerated to 226 MeV [Weikum17]. It shows that the bunch length induced energy spread growth does not dominate for such a short electron bunch. The sub-fs bunch is also particularly attracting for the DLA experiment at ARES [Mayet17]. Since the length of one period of the DLA structure is only 2 μm , a sub-fs bunch offers the possibility to sample only a fraction of the accelerating field.

WP2 aims to achieve electron bunches with higher charges by using the same compression scheme in WP1, as shown in Figure 7.3. These two working points can be compared to study the influence of the initial bunch charge to the bunch arrival-time jitter, which was found in the simulations in Chapter 4 but has not been fully understood yet. WP2 can also be used to compare with other working points having similar peak currents but higher bunch charges and longer bunch lengths (e.g. WP4) in FEL generation. Electron bunches longer than a few fs with energy spreads well below 1% are ideal for plasma-driven FELs. However, these demands are conflicting in a plasma accelerator since the energy spread is in principle proportional to the bunch length. Therefore, it is critical to optimize the trade-off in experiments. It is worth mentioning that WP2 (after being accelerated by an LWFA) is similar to the most promising working point at BELLA [Tilborg17], in which the 220-MeV, 6.25-pC, 3.3-fs (rms) electron bunch after an LWFA has an integrated energy spread of 0.25%, a normalized

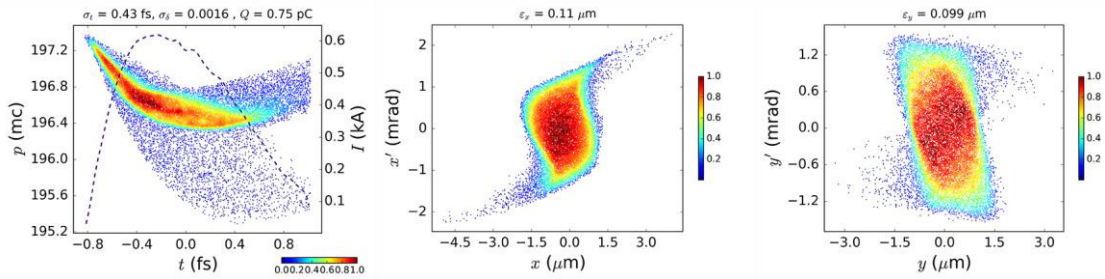
emittance of $0.3 \mu\text{m}$ and a peak current of 0.45 kA . The simulated FEL peak power is above $1 \times 10^7 \text{ W}$ with a resonant wavelength of 87 nm .

WP3 is defined as the working point having both high bunch charge and high peak current, as shown in Figure 7.4. Velocity bunching is suitable for generating such kind of bunches since it does not suffer from the CSR effect. In the current layout, however, it is difficult to transport such space-charge dominated bunches for more than 10 m to reach the final focus PMQ triplet without significantly degrading the beam quality. The emittance growth from the linac exit to the chicane exit (dipoles are switched off) was simulated to be nearly 20% but this is still acceptable. More seriously, the simulated energy spread increases to around 1.3% , which is too high to focus the beam to beta functions of several mm without completely spoiling the beam quality. In fact, the energy spread is already as high as 0.5% at the end of the linac in order to strongly compress the bunch. Nevertheless, such high-charge, high-peak-current electron bunches are still very useful for experiments carried out directly after the linac.

WP4 aims to achieve electron bunches with rms bunch lengths around 10 fs and peak currents higher than 1 kA at the entrance of the plasma, which could be used for generating FEL after acceleration in the plasma. In this case a hybrid compression scheme has been chosen and the result is shown in Figure 7.5. Generating such kind of bunches is indeed difficult for the pure magnetic compression scheme since a very high bunch charge is required to be extracted from the photocathode, which makes it difficult to control the emittance and can lead to radiation protection issues at the bunch compressor. The integrated energy spread of such a long electron bunch after a normal plasma accelerator without any special techniques (e.g. [Brinkmann17]) will be well above 1% . However, it is still possible to achieve FEL gain after acceleration as long as the slice energy spread can be preserved, which will be discussed in the next section.

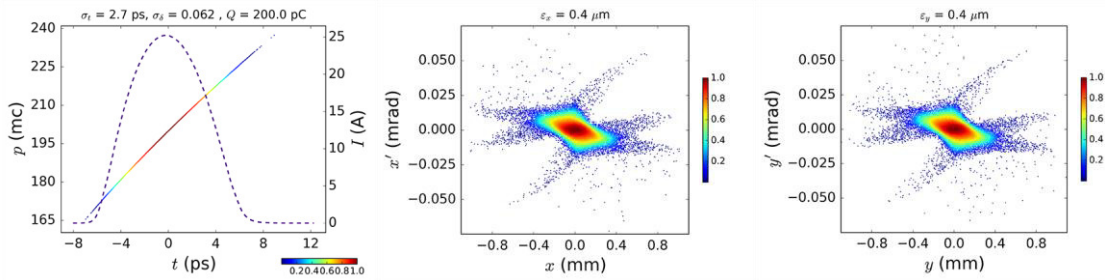


Chicane exit (with a 0.4 mm slit)

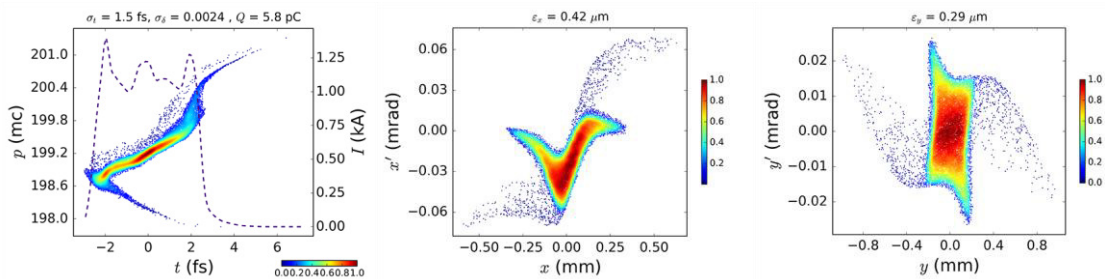


Plasma entrance (the tail containing 5% of the particles are not included)

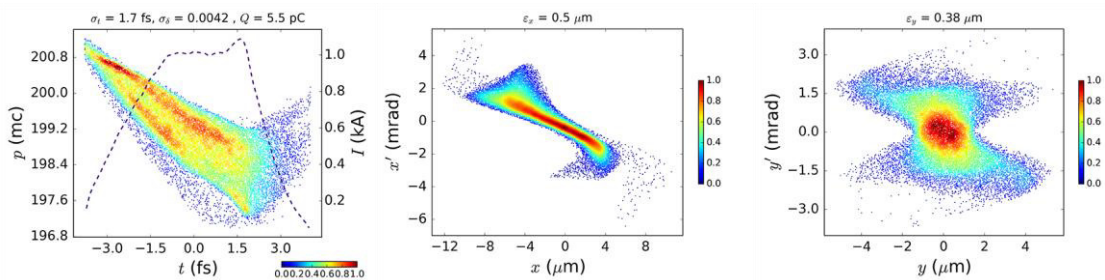
Figure 7.2: Longitudinal and transverse phase-spaces at different locations for WP1.



Linac exit

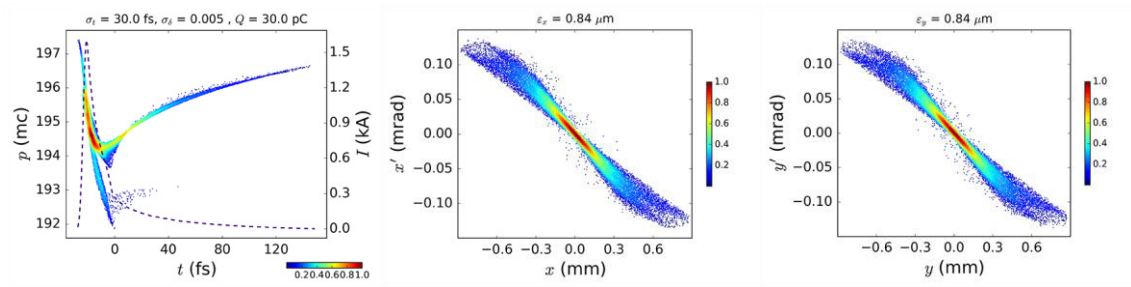


Chicane exit (with a 0.4 mm slit)

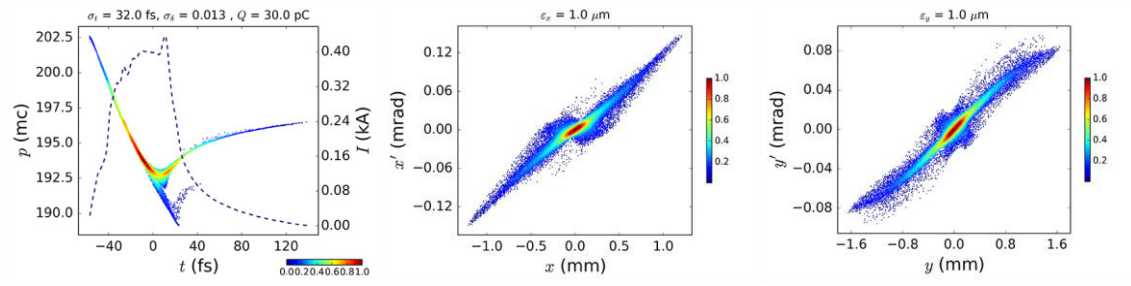


Plasma entrance (the tail containing 5% of the particles are not included)

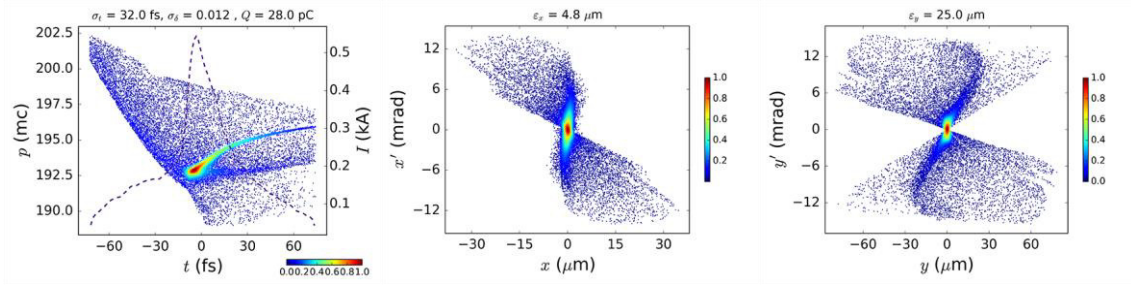
Figure 7.3: Longitudinal and transverse phase-spaces at different locations for WP2.



Linac exit

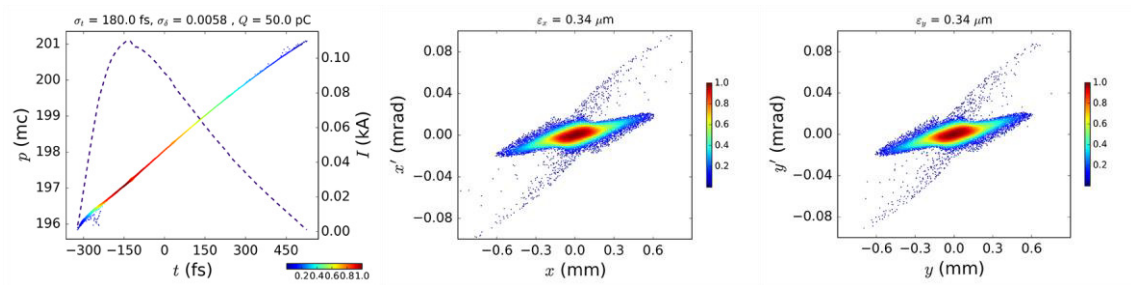


Chicane exit ($R_{56} = 0$, without slit)

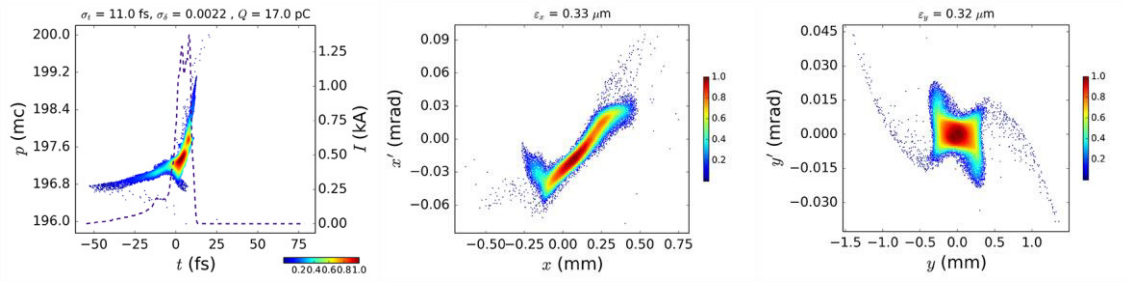


Plasma entrance (the tail containing 5% of the particles are not included)

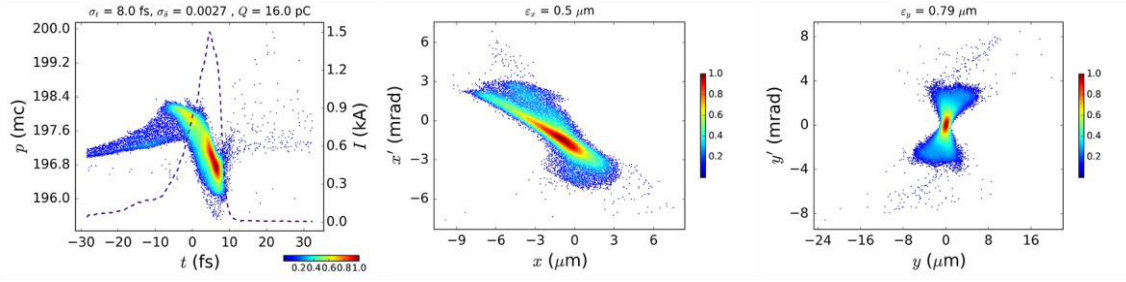
Figure 7.4: Longitudinal and transverse phase-spaces at different locations for WP3. The energy spread increases dramatically during the long drift space from the linac exit to the chicane exit, which results in a huge chromatic aberration in the PMQ triplet. It again demonstrates that 100-MeV electron bunches cannot sustain peak currents higher than 1 kA for a long distance.



Linac exit



Chicane exit (with a 0.4 mm slit)



Plasma entrance (the tail containing 5% of the particles are not included)

Figure 7.5: Longitudinal and transverse phase-spaces at different locations for WP4.

7.2. Application in LWFA driven Free-electron laser

X-ray free-electron lasers (FELs), the fourth generation light source, are the only coherent radiation sources being able to reach a wavelength as small as 1 Ångstrom and a pulse duration as short as 1 femtosecond [Ishikawa12][Behrens14]. The brightness of X-ray FELs is 7 to 10 orders of magnitudes larger than any other source, offering unprecedented capabilities to study the structure and dynamics of atomic and molecular systems and opening up new frontiers across many areas of science.

7.2.1. Basic FEL theory

The most commonly referred FEL radiation is generated in a periodic magnetic device called planar undulator, as shown in Figure 7.6. The vertical magnetic field of a planar undulator is given by

$$B_y = B_0 \sin(k_u z), \quad (7.1)$$

where $k_u = 2\pi/\lambda_u$, λ_u is the undulator period and B_0 is the magnetic pole field. When a relativistic electron enters an undulator, it will oscillate in the horizontal plane and spontaneously emit radiation at the resonant wavelength

$$\lambda_r = \frac{\lambda_u}{2\gamma^2} \left(1 + \frac{K_0^2}{2} + \gamma^2 \phi^2 \right), \quad (7.2)$$

where ϕ is the observation angle relative to the undulator axis and

$$K_0 = \frac{eB_0}{mck_u} \quad (7.3)$$

is the dimensionless undulator strength parameter.

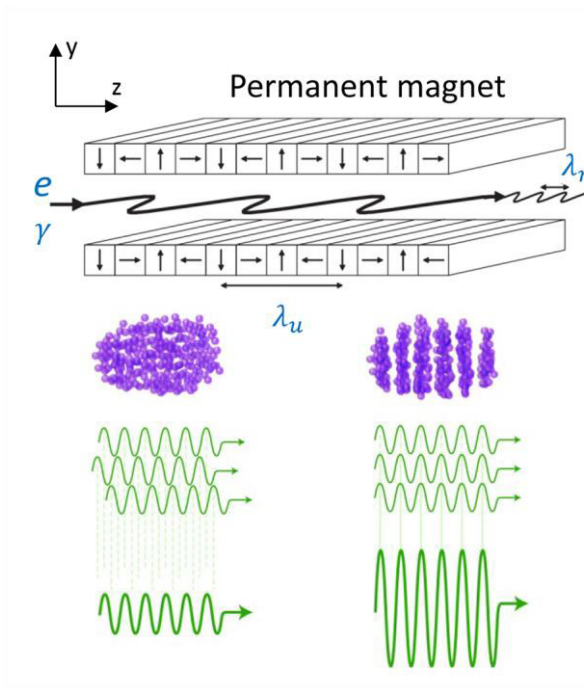


Figure 7.6: Illustration of the spontaneous emission from an electron and the FEL process in a planar undulator.

The FEL equations are rather complicated and details can be found in other literatures [Huang07][Pellegrini16]. Here, a simple physical picture is used to describe the FEL process. The FEL process can be seen as a collective instability of a system consisting of the electron bunch and the electromagnetic radiation. The instability can start from noise (Self-Amplified Spontaneous Emission, SASE) at the radiation wavelength in the longitudinal density distribution of the electron bunch, transforming it from a disordered initial state to one with electrons organized in micro-bunches separated by one radiation wavelength. The radiation intensity is proportional to the number of electrons at the beginning (incoherent emission), while increases dramatically and becomes proportional to the square of the number of electrons with the micro-bunched electrons emitting in phase (coherent emission).

At the initial state of the instability process, the interaction of the electrons with the transverse electric field of the radiation produces periodically energy modulation at the radiation wavelength λ_r along the bunch. The electron energy modulation changes the electron trajectory in the undulator magnetic field. As electrons with higher energies catch up with the electrons with lower energies, a periodic density modulation (micro-bunching) at the radiation wavelength begins to develop in the undulator. The bunched electrons emit radiation in phase at the expense of the electrons' kinetic energy and

increase the intensity of the radiation. The stronger radiation leads to further energy modulation and micro-bunching, leading to exponential growth of the radiation.

The amplitude of the radiation field grows exponentially along the undulator axis only if the following conditions are satisfied:

[1] The undulator length is much longer than the power gain length L_G . The power gain length describes the radiation intensity exponential growth rate and is given by

$$L_G = L_{G,0}(1 + \Lambda). \quad (7.4)$$

Here

$$L_{G,0} = \frac{\lambda_u}{4\pi\sqrt{3}\rho_P} \quad (7.5)$$

is the 1D power gain length for a mono-energetic bunch with

$$\rho_P = \left(\frac{1}{16} \frac{I_{beam} K_0^2}{I_A \gamma_0^3 \sigma_x^2 k_u^2} \right)^{1/3} \left[J_0 \left(\frac{K_0^2}{4 + 2K_0^2} \right) - J_1 \left(\frac{K_0^2}{4 + 2K_0^2} \right) \right]^{2/3} \quad (7.6)$$

being the dimensionless Pierce parameter (J_0 and J_1 are the Bessel functions). Λ is the gain length degradation factor which takes into account of diffraction as well as the emittance and energy spread of the electron beam [Xie00]. The radiation power is then given by $P = P_0 \exp(z/L_G)$ with P_0 being the effective initial noise power. The exponential gain eventually stops when the bunch loses enough energy and the quality of the bunch degrades considerably. Typically an FEL starting from a very low initial noise saturates in about 20 power gain lengths, giving a saturation power of about ρ_P times the electron beam power and a relative radiation bandwidth of approximately ρ_P .

[2] The electron bunch should match the transverse phase-space of the radiation, which gives

$$\varepsilon_{rms} < \frac{\lambda_r}{4\pi}. \quad (7.7)$$

[3] The energy spread of the electron bunch must be sufficiently small because only the electrons inside a narrow energy window (the FEL bandwidth) contribute constructively to the FEL gain process:

$$\delta < \rho_P. \quad (7.8)$$

[4] The radiation generated by the FEL should be greater than that lost by diffraction, that means:

$$L_G < L_R, \quad (7.9)$$

where L_R is the radiation Rayleigh length.

Another important parameter describing the FEL process is the cooperation length L_C . In one undulator period λ_u , the electrons are overtaken by the co-propagating radiation by λ_r . The cooperation length is defined as the slippage in one gain length, that is

$$L_c = \frac{L_G}{\lambda_u} \lambda_r. \quad (7.10)$$

The slippage between the electrons and the radiation is a problem when the electron bunch length is shorter than a few cooperation lengths. The electron bunch and the radiation could be totally separated before the radiation saturates.

7.2.2. Challenges in LWFAs

As candidates for driving the next generation FELs [Gruener07], LWFAs offer the possibility to realize compact and affordable FEL devices. However, there are still several challenging issues that need to be addressed. Besides the problems discussed in this thesis in generating, focusing and synchronizing ultra-short electron bunches with high peak currents at low energies, there are other issues concerning the FEL generation as well as the beam capture and transport after the plasma.

FEL generation

One major obstacle that hinders the realization of a usable plasma-driven FEL is the large energy spread of the electron bunch, as limited by equation (7.8). There are two methods proposed to increase the FEL performance directing at large energy spread electron bunch: decompressing the bunch [Maier12] and utilizing the transverse gradient undulator [Huang12].

Decompressing an electron bunch will linearly reduce its slice energy spread and peak current at the same time. From the scaling of the Pierce parameter $\rho_P \propto I_{beam}^{1/3}$ given by equation (7.6), the local gain length can be reduced by reducing the slice energy spread despite the drop of peak current, if the energy spread dominates the FEL process. On the global scale of the whole bunch, the resonance wavelength changes along the bunch due to the energy chirp. However, as long as ρ_P is large enough, the radiation field can adopt the variation. For ultra-short bunches, the FEL process could be further promoted with the elongated interaction length of the radiation and the electron bunch. However, on the other side, a longer electron bunch will reduce the temporal coherence and increase the FEL bandwidth.

The ideal of the transverse gradient undulator is to cant the magnetic poles, one can generate a linear dependence of the vertical undulator field on the transverse coordinate x so that

$$\frac{\Delta K_0}{K_0} = \alpha x, \quad (7.11)$$

where α is the canting coefficient. By choosing a constant dispersion in the transverse gradient undulator

$$\eta_x = \frac{2 + K_0^2}{\alpha K_0^2}, \quad (7.12)$$

every electron in a bunch will satisfy the resonant equation (7.2). One additional advantage of the transverse gradient undulator is that the impact of the beam energy jitter can be potentially reduced or eliminated, which in turn reduces the requirement of the timing jitter between the electron bunch and the plasma. One potential disadvantage of this method is the loss of transverse coherence on the SASE mode because of the large transverse bunch size.

Beam capture and matching to the undulator

Although the large energy spread problem could be solved by the aforementioned methods, it is still challenging to transport such an electron bunch from the exit of the plasma to the entrance of the undulator.

At the exit of the plasma, the intense transverse focusing field vanishes while the transverse bunch size remains on the order of a few μm or even smaller due to the ultra-small beta function (mm \sim cm). Hence the transverse bunch size will increase rapidly in a drift space because of the emittance pressure. The final emittance of an electron bunch after drifting a distance L is given by [Migliorati13]

$$\varepsilon_f \cong \sqrt{\varepsilon_i^2 + \gamma^2 L^2 \sigma_\delta^2 \sigma_x^4}, \quad (7.13)$$

assuming there is no correlation between the energy and transverse position. The emittance growth is not negligible for a typical electron bunch at the exit of a plasma accelerator. Assuming a 1-GeV electron bunch with 1% rms energy spread and 1 μm normalized emittance leaves the plasma with a beta function of 1 mm at its waist, the emittance will increase to 2.2 μm after drifting 0.2 m. A proper tailored longitudinal plasma profile (down-ramp) could produce an adiabatic defocusing of the bunch, i.e. an increase of the transverse beam size without spoiling the emittance [Dornmair15]. If the beta function at the plasma exit increases to 1 cm in the previous example, the emittance will only increase to 1.02 μm after a 0.2-m drift. It should be pointed out that electron bunches shorter than a few fs are required to achieve an energy spread of $\sim 1\%$ in order to be able to match the FEL requirements.

After being captured by strong quadrupole magnets, the electron bunch could experience emittance growth because of the chromatic aberration. If a transverse gradient undulator is employed, the nonlinearity in the transverse coordinate and momentum introduced by the chromatic effect in quadrupoles could degrade the FEL gain [Liu17]. These problems can be partially overcome by a carefully designed transport beamline with sextupole magnets included [Liu17].

7.2.3. More discussions on LWFA-driven FEL at ARES

By using equation (7.4), the 3D power gain length of the aforementioned BELLA experiment for the 6.25-pC working point was calculated to be about 0.19 m with $\lambda_r \approx$

88.5 nm. The cooperation length is about 0.94 μm , which is comparable with the rms bunch length of 1.0 μm . Here we have used the parameters $\lambda_u = 1.8$ cm, $K_0 = 1.28$, $\bar{\beta}_x = 0.7$ m, $\gamma = 430$, $I_{beam} = 0.45$ kA, $\varepsilon_{x,slice} = 0.25$ μm and $\sigma_{\delta,slice} = 0.18\%$. The average beta function is very small due to the distributed FODO lattice (0.25 m period) along the 4-m-long undulator. It should be noted that the simulated power gain length is twice as long as the analytical one due to the time-dependent and slippage effects. Nevertheless, such a power gain length is still short enough to see significant FEL output at BELLA.

The WP2 at ARES has slightly smaller bunch charge and higher slice emittance compared to the above BELLA working point. By using $I_{beam} = 0.4$ kA and $\varepsilon_{x,slice} = 0.32$ μm , the calculated 3D power gain length and cooperation length are 0.22 m and 1.07 μm , respectively, which are both slightly longer than those for the BELLA working point. Here we have assumed that the electron bunch can be accelerated to 220 MeV by an LWFA and then decompressed slightly afterwards with negligible emittance growth. We have also assumed that the accelerated electron bunch has the same slice energy spread as the BELLA beam. Since the slice energy spread of the electron bunch for the WP2 before the plasma is about 0.28% and the decompression will further reduce it, this assumption holds if the plasma can at least preserve the relative energy spread of the bunch. For a strongly chirped bunch, rigorously speaking, it is an iterative process to find the correct “slice energy spread” since it refers to the energy spread within one cooperation length. However, for simplicity, this effect has not been taken into account here. As a comparison, we also repeated the calculation using parameters ($\lambda_u = 1.5$ cm, $K_0 = 1.0$) of a possible candidate undulator for the ATHENA project [Maier15]. It is found that the 3D gain length further increases to 0.25 m with the radiation wavelength reducing to 60.8 nm and the cooperation length decreasing to 1.01 μm .

Another scenario for the WP2 is accelerating the electron bunch to a higher energy, e.g. 850 MeV. Again, we assume that the emittance and the relative slice energy spread are both preserved. However, the average beta function inside the undulator is scaled up to 2.7 m due to the energy increase. By using the latter undulator, the 3D gain length increases to 4.45 m. Also, we notice that equation (7.8) is violated and the cooperation length is 21% longer than the rms bunch length. Therefore, this option is not reliable. On the other hand, if the slice energy spread can be improved to 0.05% (in the ideal case, the slice energy spread should decrease after acceleration), then the 3D gain length will reduce to 0.74 m. More importantly, the cooperation length will reduce to 0.20 μm , which is much shorter than the rms bunch length. Hence, the slice energy spread is much more critical when the electron energy becomes higher. These results for the WP2 are summarized in Table 7.4.

The WP4 at ARES has much higher peak current but smaller slice emittance compared with the WP2, which makes it potentially more suitable for the LWFA-driven FEL application if the slice emittance and at least the relative energy spread can be preserved, as shown in Table 7.5. Compared to the results for WP2 using the same

electron energies and undulator parameters, the 3D gain lengths and cooperation lengths are much shorter. Since the bunch is long enough, it saves the effort to decompress it after the plasma. It is worth mentioning that the CSR effect can spoil the slice emittance during the decompression of a high-charge and high-peak current bunch, which will hinder the FEL generation [Tilborg17]. Nevertheless, the integrated energy spread of the bunch is expected to be larger than a few percent, which will result in significant projected emittance growth in the beam capture section as well as the matching section, and could make the beam transport difficult.

Table 7.4: Summary of the discussed FEL parameters using the WP2 at ARES.

Q (pC)	I_{beam} (kA)	σ_t (fs)	$\varepsilon_{x,slice}$ (μm)	$\bar{\beta}_x$ (m)	$\sigma_{\delta,slice}$ (%)	γ	λ_u (cm)	K_0	λ_r (nm)	ρ_P	L_G (m)	L_c (μm)
5.5	0.4	3.3	0.32	0.7	0.18	430	1.8	1.28	88.5	0.0072	0.22	1.07
							1.5	1.00	60.8	0.0055	0.25	1.01
				2.7	0.18	1663	1.5	1.00	4.1	0.0014	4.45	1.21
	0.05						0.74	0.20				

Table 7.5: Summary of the discussed FEL parameters using the WP4 at ARES.

Q (pC)	I_{beam} (kA)	σ_t (fs)	$\varepsilon_{x,slice}$ (μm)	$\bar{\beta}_x$ (m)	$\sigma_{\delta,slice}$ (%)	γ	λ_u (cm)	K_0	λ_r (nm)	ρ_P	L_G (m)	L_c (μm)
16.5	1.5	8.0	0.42	0.7	0.21	430	1.5	1.00	60.8	0.0078	0.14	0.55
				2.7	0.21	1663	1.5	1.00	4.1	0.0020	1.43	0.39

In conclusion, both the WP2 and WP4 at ARES are good candidates for the pilot LWFA-driven FEL experiment. The proposed parameters can serve as good starting points for detailed start-to-end simulations.

7.3. Summary

In this chapter, start-to-end simulation results with the final design of the ARES linac, from the photocathode to the plasma entrance, are presented. Pure magnetic compression, pure velocity bunching and hybrid compression methods are used for four different working points. The electron bunch energies are all around 100 MeV. The final bunch charges range from 0.75 pC to 28.5 pC and the final bunch lengths range from 0.43 fs to 31.9 fs (the tail containing 5% of the particles are not included), which cover the design parameters of the ARES linac. In addition, the beta functions at the plasma entrance are less than a few mm. These working points have applications in field sampling for advanced accelerating structures, LWFA-driven FEL generation, bunch compression schemes comparison, R&D on advanced beam diagnostics, etc.

Compression and focusing electron bunches at ~ 100 MeV limits the maximum peak current to approximately 1.5 kA at the plasma entrance due to strong space-charge effects. The impact of the space-charge effects can be mitigated by adding another traveling-wave structure at the ARES linac to further boost the beam energy. As shown

in Chapter 5, the peak current of the electron bunch at the plasma entrance can reach higher than 2 kA when the electron energy increases to about 150 MeV. Moreover, the emittance growth can also be significantly mitigated.

Summary

The ARES linac at the SINBAD facility is aiming to generate ~ 100 MeV, low charge ($0.5 \sim 30$ pC) and ultra-short (sub-fs \sim dozens of fs) electron bunches with ultra-small spot sizes (less than a few μm) and excellent timing stability (rms bunch arrival-time jitter < 10 fs), as required by novel compact accelerators. Design studies have been presented in this thesis to address the problems in generating such electron bunches, particularly for LWFA experiments. It is foreseen to have two experimental beamlines at the ARES linac. The research results presented in this thesis mainly focus on the design of the main straight beamline, while the expected results from the second dogleg beamline with tunable R_{56} between -10 mm to 10 mm have also been concluded briefly.

As a major feature of the ARES linac, sub-fs electron bunches are foreseen to be produced at the main beamline via a weak magnetic chicane ($R_{56} \sim -10$ mm) with a sub-mm-wide slit collimator between the 2nd and the 3rd dipole magnets. A weak magnetic chicane is also critical to achieve an excellent timing stability. Beam dynamics of such extreme bunches have been investigated meticulously by using IMPACT-T and CSRTrack with different space-charge and CSR models. Moreover, interactions between the electrons and the slit have been simulated by the Monte-Carlo code EGS4, validating the use of an ideal knife edge in the beam dynamics simulations. In addition, imperfections including the field quality of the dipole magnet and misalignment have also been considered.

As required by the matching condition of LWFAs, external injected electron bunches must be focused to a spot size smaller than a few μm at the plasma entrance. Due to the strong space-charge effects, compressed electron bunches with peak currents around 1 kA or higher cannot be transported for a long distance without significantly degrading the beam quality (e.g. emittance, energy spread and peak current). Therefore, the magnetic lattice at the ARES linac was designed in such a way that the compressed electron bunch will be focused into the plasma immediately downstream of the chicane by a PMQ triplet. It must be emphasized that the slit collimator in the chicane plays an important role in the final focus. Since a significant energy spread must be introduced to strongly compress the electron bunch, the slit collimator can be used to control the energy spread of the final bunch and avoid serious chromatic aberration at the PMQ triplet. It is also worth mentioning that the space-charge effects can be significantly mitigated by adding another traveling-wave structure.

At the ARES linac, pure magnetic compression is the best choice for generating sub-pC, sub-fs electron bunches since the bunch arrival-time jitter can be relaxed by driving each of the traveling-wave structures with independent klystrons. The tolerance budget for a 10-fs bunch arrival-time jitter requires the phase and amplitude jitter of the traveling-wave structure being 0.013 degree and 0.013% respectively, which are more relaxed compared to the requirements of 0.009 degree and 0.009% in the hybrid compression and velocity bunching cases. The pure magnetic compression method can also be used to generate several pC and sub-fs- to fs- long electron bunches. However, the extracted charge jitter at the photocathode or the phase and amplitude of the traveling-wave structures need to be further stabilized to maintain a 10-fs bunch arrival-time jitter.

Pure velocity bunching is suitable for generating high-charge and high-peak-current (e.g. 30 pC and ~ 1.6 kA) electron bunches since it does not suffer from the CSR effect. However, it is difficult to transport such space-charge dominated bunches from the linac exit to the final focus PMQ triplet without significantly degrading the beam quality. Therefore, such electron bunches can only be used for experiments carried out directly after the linac.

Hybrid compression can be used to generate not only several pC and sub-fs- to fs- long electron bunches with significantly less charge loss at the slit collimator but also longer (~ 10 fs) electron bunches with 10 to 20 pC bunch charges. Moreover, the bunch arrival-time jitter is not sensitive to the gun charge jitter. In addition, compared with the other two compression methods, the final bunch length and momentum jitters are significantly smaller. These characteristics make the hybrid compression scheme more suitable for generating ultra-short and low-jitter electron bunches with relatively high bunch charges.

Generation of femtosecond electron bunches in a train with THz repetition rate is of particular interest for PWFAs and thus is a possible research interest at the ARES linac in the future. Since the bandwidths of the pick-up electrodes and the readout electronics are limited to several GHz nowadays, it is impossible to measure the misalignments of the individual bunches with BPMs. In this thesis, a novel method was proposed to simultaneously measure the relative misalignments of the individual bunches in both transverse planes by combining the single quadrupole scan method and an RFD. The method was not only investigated analytically and numerically in details, but also experimentally demonstrated at the SPARC_LAB test facility. The challenge of the measurement lies in the plane parallel to the deflecting voltage, in which the experimental data are dominated by the noise introduced by the bunch arrival-time as well as the RFD voltage and phase jitter. The proposed method is fast and easy to implement. The absolute misalignment of each bunch can be obtained straightforwardly by adding the misalignment of the whole bunch train measured by the BPM.

A Thin lens focusing

Figure A.1 illustrates the focusing of a beam by a thin lens with focal length f . By taking into account the beam emittance and chromatic aberration, the beta function at the focus is given by

$$\beta_{x_f} = \frac{f^2}{\beta_{x_i}} + \sigma_\delta^2 \beta_{x_i}. \quad (\text{A.1})$$

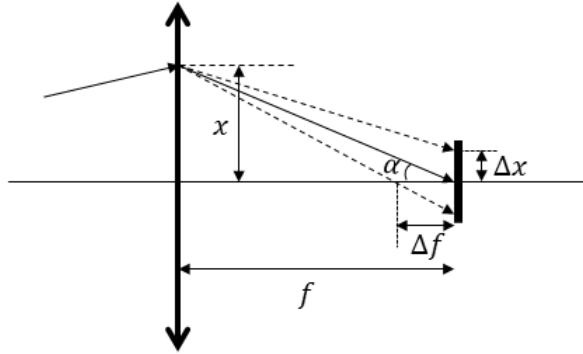


Figure A.1: Illustration of the change of focus resulting from the chromatic aberration.

A.1 Emittance term

The rms envelope equation of a beam in the free space is given by

$$\sigma_x'' = \frac{\varepsilon_x^2}{\sigma_x^3}. \quad (\text{A.2})$$

Integrating equation (A.2) after multiplying both sides by σ_x' yields

$$\sigma_{x_f}'^2 - \sigma_{x_i}'^2 = \frac{\varepsilon_x^2}{\sigma_{x_i}^2} - \frac{\varepsilon_x^2}{\sigma_{x_f}^2}. \quad (\text{A.3})$$

It should be noted that the integration starts from the right side of the thin lens. By considering $\sigma_{x_f}' = 0$ at the focal point, the final spot size is

$$\sigma_{x_f}^2 = \frac{\varepsilon_x^2 \sigma_{x_i}^2}{\varepsilon_x^2 + \sigma_{x_i}^2 \sigma_{x_i}'^2} \approx \frac{\varepsilon_x^2}{\sigma_{x_i}'^2}, \quad (\text{A.4})$$

where the assumption $\varepsilon_x^2 \ll \sigma_{x_i}^2 \sigma_{x_i}'^2$ has been used since the strongly focused beam has a large convergent angle. Under thin lens approximation, it is obvious that

$$\sigma'_{x_i} = \frac{\sigma_{x_i}}{f}. \quad (\text{A.5})$$

Substituting equation (A.5) into (A.4) yields

$$\sigma_{x_f} = \frac{f \varepsilon_x}{\sigma_{x_i}}. \quad (\text{A.6})$$

Assuming the emittance is conserved, from equation (A.6) we have

$$\beta_{x_f} = \frac{f^2}{\beta_{x_i}}. \quad (\text{A.7})$$

A.2 Chromatic aberration

To first order, the change of focal length due to a small energy change δ is given by

$$\Delta f = f \delta. \quad (\text{A.8})$$

As shown in Figure A.1, the blur on the image plane can be written as

$$\Delta x \approx \Delta f \alpha = \delta x. \quad (\text{A.9})$$

Taking the rms values of the both sides of equation (A.9) yields

$$\sigma_{x_f} \approx \sigma_\delta \sigma_{x_i}. \quad (\text{A.10})$$

Again, assuming the emittance is conserved, from equation (A.10) we have

$$\beta_{x_f} \approx \sigma_\delta^2 \beta_{x_i}. \quad (\text{A.11})$$

In addition, under thin lens approximation, the emittance growth due to the chromatic aberration is given by [Buon94]

$$\frac{\Delta \varepsilon_x}{\varepsilon_x} \approx \frac{\sigma_\delta^2 \beta_{x_i}^2}{2f^2}. \quad (\text{A.12})$$

B Mismatch factor

Suppose the matched beam ellipse is given by

$$\varepsilon_x = \gamma_m x_m^2 + 2\alpha_m x_m x'_m + \beta_m x'^2_m \quad (\text{B.1})$$

and the mismatched beam ellipse with the same emittance is given by

$$\varepsilon_x = \gamma x^2 + 2\alpha x x' + \beta x'^2, \quad (\text{B.2})$$

the mismatch parameter B_{mag} is defined as the ratio of the area of the decohered beam to the area of the matched beam [Minty03], which gives

$$\begin{aligned} B_{mag} &= \frac{1}{2} \frac{\gamma_m \langle x^2 \rangle + 2\alpha_m \langle x x' \rangle + \beta_m \langle x'^2 \rangle}{\varepsilon_x} \\ &= \frac{1}{2} (\beta \gamma_m + \beta_m \gamma - 2\alpha \alpha_m). \end{aligned} \quad (\text{B.3})$$

The phase plane (x, x') can be transferred to a normalized phase plane (u, v) by the following transfer matrix

$$\begin{bmatrix} u \\ v \end{bmatrix} = \frac{1}{\sqrt{\beta_m}} \begin{bmatrix} 1 & 0 \\ \alpha_m & \beta_m \end{bmatrix} \begin{bmatrix} x \\ x' \end{bmatrix}, \quad (\text{B.4})$$

and equation (B.2) becomes

$$\varepsilon_x = u^2 + v^2. \quad (\text{B.5})$$

The phase space of the beam in the so-called normalized phase plane will occupy a circle with unit radius.

Applying the same transformation to the mismatched beam, the normalized C-S parameters are given by

$$\tilde{\beta} = \beta/\beta_m, \quad \tilde{\gamma} = 2B_{mag} - \beta/\beta_m. \quad (\text{B.6})$$

The mismatch factor defined by Sands [Sands91] is thus written as

$$\begin{aligned}
M_S &= \frac{1}{2} \left(\tilde{\beta} + \tilde{\gamma} + \sqrt{(\tilde{\beta} + \tilde{\gamma})^2 - 4} \right) \\
&= B_{mag} + \sqrt{B_{mag}^2 - 1},
\end{aligned} \tag{B.7}$$

which is the area of the circle if it is enlarged to enclose the eclipse.

The mismatch factor can also be defined as the difference between the length of the major semi-axis of the eclipse and the radius of the circle [Crandall90]

$$M_E = (M_S)^{1/2} - 1. \tag{B.8}$$

Assuming the matched Twiss parameters are $\beta_m = 40$ mm and $\alpha_m = 1.6$, the allowed Twiss parameters for a 1% mismatch is shown in Figure B.1. It is obvious that M_S has the strongest constraint, while B_{mag} is not suitable to be used in matching Twiss parameters.

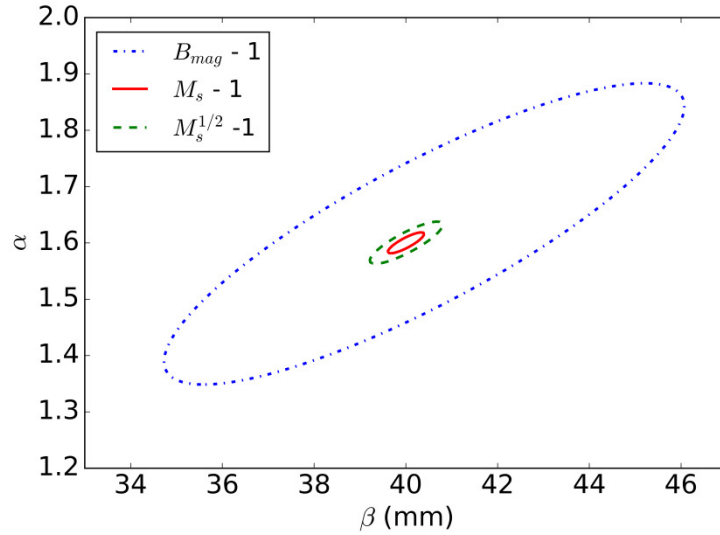


Figure B.1: Area of Twiss parameters with a 1% mismatch for different definitions. The matched Twiss parameters are $\beta_m = 40$ mm and $\alpha_m = 1.6$.

C Parameters used in the final working points

Table C.1: Summary of parameters used in ASTRA simulations (linac part) for different working points.

	WP1	WP2	WP3	WP4
Initial bunch charge (pC)	20	200	30	50
RMS laser spot size (mm)	0.088	0.181	0.246	0.169
RMS laser pulse length (ps)	3.0	3.0	0.142	2.9
Gun peak gradient (MV/m)	110			
Gun phase (deg)	0.0			
TWS1 peak gradient (MV/m)	25.5			
TWS1 phase (deg)	-53.0	-53.0	-90.85	-87.00
TWS2 peak gradient (MV/m)	25.5			
TWS2 phase (deg)	-53.0	-53.0	0.0	0.0
High charge solenoid B_z (T)	0.21069	0.23999	0.23609	0.23985
Low charge solenoid B_z (T)	0.14029	0.11835	0.11153	0.10808
TWS1 solenoids B_z (T)	0.06125	0.02493	0.02311	0.03790
TWS2 solenoids B_z (T)	0.01000	0.07818	0.04000	0.03178

Table C.2: Summary of key parameters used in IMPACT-T simulations (lattice part) for different working points.

	WP1	WP2	WP3	WP4
Chicane R_{56} (mm)	-12.4	-12.8	0.0	-9.1
Slit full-open width (mm)	0.4	0.4	\	0.4
z_{focus} (m)	30.5052	30.5054	30.5040	30.5046
PMQ-1 length (cm)	1.5			
PMQ-1 gradient (T/m)	250			
PMQ-2 length (cm)	1.5			
PMQ-2 gradient (T/m)	500			
PMQ-3 length (cm)	1.5			
PMQ-3 gradient (T/m)	500			

Bibliography

- [Abrahamyan04] K. Abrahamyan, et al., “Characterization of the electron source at the photo injector test facility at DESY Zeuthen”, *Nucl. Instrum. Methods Phys. Res., Sect. A* 528, 360 (2004).
- [Adelmann] A. Adelmann, et al., “Object Oriented Parallel Accelerator Library (OPAL) Manual”, http://amas.web.psi.ch/docs/opal/opal_user_guide.pdf.
- [Agustsson04] R. Agustsson, “Design, Construction, Simulation and Implementation of a Magnetic Electron Bunch Compressor”, Master thesis (2004).
- [Alesini06] D. Alesini, et al., “RF deflector design and measurements for the longitudinal and transverse phase space characterization at SPARC”, *Nucl. Instrum. Methods Phys. Res., Sect. A* 568, 2 (2006).
- [Anderson02] S. G. Anderson, et al., Space-charge effects in high brightness electron beam emittance measurements, *Phys. Rev. ST Accel. Beams* 5, 014201 (2002)
- [Assmann98] R. Assmann and K. Yokoya, “Transverse beam dynamics in plasma-based linacs”, *Nucl. Instrum. Methods Phys. Res., Sect. A* 410, 544 (1998).
- [Bacci14] A. Bacci, et al., “Ultra-short electron bunches by Velocity Bunching as required for plasma wave accelerations”, *Nucl. Instrum. Methods Phys. Res., Sect. A* 740, 42 (2014).
- [Bartolini12] R. Bartolini, et al., “Multiobjective genetic algorithm optimization of the beam dynamics in linac drivers for free electron lasers”, *Phys. Rev. ST Accel. Beams* 15, 030701 (2012).
- [Bayesteh14] S. Bayesteh, “Transverse electron beam diagnostics at REGAE”, PhD thesis (2014).
- [Bazarov05] I. V. Bazarov and C. K. Sinclair, “Multivariate optimization of a high brightness dc gun photoinjector”, *Phys. Rev. ST Accel. Beams* 8, 034202 (2005).
- [Behrens14] C. Behrens et al., “Few-femtosecond time-resolved measurements of X-ray free-electron lasers”, *Nat. Comm.* 5, 3762 (2014).
- [Beringer13] J. Beringer et al., “Particle Detectors at Accelerators”, <http://pdg.lbl.gov/2013/reviews/rpp2013-rev-particle-detectors-accel.pdf> (2013).
- [Beutner10] B. Beutner, et al., “Sensitivity and Tolerance Study for the SwissFEL”, WEPB17, *Proceedings of FEL2010*, Malmö, Sweden (2010).
- [Beutner13] B. Beutner, “Status of the SwissFEL and its Injector Test Facility”, Accelerator Physics Seminar DESY (2013).
- [Blumenfeld07] I. Blumenfeld, et al., “Energy doubling of 42 GeV electrons in a metre-scale plasma wakefield accelerator”, *Nature* (London) 445, 741 (2007).
- [Borland00] M. Borland, “Elegant: A Flexible SDDS-Compliant Code for Accelerator Simulation”, Advanced Photon Source LS-287, September 2000.
- [Borland01] M. Borland, “Simple method for particle tracking with coherent synchrotron radiation”, *Phys. Rev. ST Accel. Beams* 4, 070701 (2001).
- [Borland01+] M. Borland, “Potential production of ultrashort electron bunches with the advanced photon source linac”, *Proceedings of PAC’01*, Chicago, IL, USA (2001).

- [Boscolo07] M. Boscolo, et al., “Generation of short THz bunch trains in a RF photoinjector”, *Nucl. Instrum. Methods Phys. Res., Sect. A* 577, 409 (2007).
- [Brinkmann17] R. Brinkmann, et al., “Chirp Mitigation of Plasma-Accelerated Beams by a Modulated Plasma Density”, *Phys. Rev. Lett.* 118, 214801 (2017).
- [Brown84] K. L. Brown, “First and second order charged particle optics”, SLAC-PUB-3381 (1984).
- [Buon94] J. Buon, “Beam phase space and emittance”, LAURT92-03 (1992).
- [Carlsten89] B. E. Carlsten, “New photoelectric injector design for the Los Alamos National Laboratory XUV FEL accelerator”, *Nucl. Instrum. Methods Phys. Res., Sect. A* 285, 313 (1989).
- [Carlsten11] B.E. Carlsten, et al., “Using an emittance exchanger as a bunch compressor”, *Phys. Rev. ST Accel. Beams* 14, 084403 (2011).
- [Cesar16] D. Cesar, et al., “Demonstration of Single-Shot Picosecond Time-Resolved MeV Electron Imaging Using a Compact Permanent Magnet Quadrupole Based Lens”, *Phys. Rev. Lett.* 117, 024801 (2016).
- [Castellano99] M. Castellano, et al., “Beam Characteristics Control Using Optical Transition Radiation (OTR)”, LAL/RT 99-01 (1999).
- [Cianchi15] A. Cianchi, D. Alesini, M. P. Anania, “Six-dimensional measurements of trains of high brightness electron bunches”, *Phys. Rev. ST Accel. Beams* 18, 082804 (2015).
- [CLIC12] “CLIC conceptual design report”, CERN-2012-007 (2012).
- [Corde15] S. Corde, et al., “Multi-gigaelectronvolt acceleration of positrons in a self-loaded plasma wakefield”, *Nature* 524 442 (2015).
- [Cornacchia] M. Cornacchia, et a., “Transverse to longitudinal emittance exchange”, *Phys. Rev. ST Accel. Beams* 5, 084001 (2002)
- [Courant58] E. D. Courant AND H. S. Snyder, “Theory of the Alternating-Gradient Synchrotron”, *Annals of Physics* 3, 1-48 (1958).
- [Craievich13] P. Craievich, et al., “Modeling and experimental study to identify arrival-time jitter sources in the presence of a magnetic chicane”, *Phys. Rev. ST Accel. Beams* 16, 090401 (2013).
- [Crandall90] K. R. Crandall, “TRACE 3-D Documentation”, 2nd ed., Los Alamos Report LA-UR-90-4146, December, 1990.
- [Curtoni01] A. Curtoni, et al., “Study of the TESLA preaccelerator for the polarised electron beam”, TESLA-2001-22 (2001)
- [Decking11] W. Decking, et al., “XFEL Bunch Compressor Chicane Layout”, FEL beam dynamics meeting (2011).
- [Decking13] W. Decking and T. Limberg, “European XFEL Post-TDR Description”, XFEL.EU TN-2013-004-01.
- [Derbenev95] Y. S. Derbenev, et al., Report No. TESLA-FEL 95-05.
- [DiMitri13] S. Di Mitri, et al., “Cancellation of Coherent Synchrotron Radiation Kicks with Optics Balance”, *Phys. Rev. Lett.* 110, 014801 (2013).
- [DiMitri13-1] S. Di Mitri, et al., “Electron slicing for the generation of tunable femtosecond soft x-ray pulses from a free electron laser and slice diagnostics”, *Phys. Rev. ST Accel. Beams* 16, 042801 (2013).
- [Ding11] Y. Ding, et al., “Femtosecond x-ray pulse temporal characterization in free-electron lasers using a transverse deflector”, *Phys. Rev. ST Accel. Beams* 14, 120701 (2011).
- [Dohlus00] M. Dohlus, A. Kabel, T. Limberg, “Efficient field calculation of 3D bunches on general trajectories”, *Nucl. Instrum. Methods Phys. Res., Sect. A* 445, 338 (2000).
- [Dohlus03] M. Dohlus, “Two Methods for the Calculation of CSR Fields”, TESLA-FEL-2003-05 (2003).

- [Dohlus04] M. Dohlus, T. Limberg, “CSRtrack: faster calculation of 3-D CSR effects”, *Proceedings of the 2004 FEL Conference*, 18-21 (2004).
- [Dohlus05] M. Dohlus et al., “Electron bunch length compression”, *ICFA Beam Dynamics Newsletter* 38, 39 (2005).
- [Dohlus06] M. Dohlus, “Modelling of space charge and CSR effects in bunch compression systems”, *Proceedings of EPAC 2006*, Edinburgh, Scotland (2006).
- [Dorda16] U. Dorda, et al., “SINBAD—The accelerator R&D facility under construction at DESY”, *Nucl. Instrum. Methods Phys. Res., Sect. A* 829, 233 (2016).
- [Dornmair15] I. Dornmair, K. Floettmann, and A. R. Maier, “Emittance conservation by tailored focusing profiles in a plasma accelerator”, *Phys. Rev. ST Accel. Beams* 18, 041302 (2015).
- [Emery03] L. Emery, “User’s Guide to shower version 1.0, an EGS4 Interface”, Advanced Photon Source (2003).
- [Emma00] P. Emma, J. Frisch and P. Krejcik, “A Transverse RF Deflecting Structure for Bunch Length and Phase Space Diagnostics”, LCLS-TN-00, 12 (2000).
- [Emma04] P. Emma, et al., “Femtosecond and Subfemtosecond X-Ray Pulses from a Self-Amplified Spontaneous-Emission-Based Free-Electron Laser”, *Phys. Rev. Lett.* 92, 074801 (2004).
- [Emma10] P. Emma, et al., “First lasing and operation of an ångstrom-wavelength free-electron laser”, *Nat. Photonics* 4, 641 (2010).
- [England05] R. J. England, et al., “Sextupole correction of the longitudinal transport of relativistic beams in dispersionless translating sections”, *Phys. Rev. ST Accel. Beams* 8, 012801 (2005).
- [England14] R. J. England, et al., “Dielectric laser accelerators”, *Rev. Mod. Phys.* 86, 1337 (2014).
- [England16] R. J. England, et al., “Review of laser-driven photonic structure-based particle acceleration”, *IEEE Journal of Selected Topics in Quantum Electronics*, 22 4401007 (2016).
- [Esarey09] E. Esarey, et al., “Physics of laser-driven plasma-based electron accelerators”, *Rev. Mod. Phys.* 81, 1229 (2009).
- [EuXFEL06] “The European X-Ray Free-Electron Laser Technical design report”, DESY-2006-097 (2006).
- [Faure04] J. Faure, et al., “A laser–plasma accelerator producing monoenergetic electron beams”, *Nature* (London) 431, 541 (2004).
- [Felber12] M. Felber, et al., “Laser Synchronization at REGAE Using Phase Detection at an Intermediate Frequency”, WEPPD048, *Proceedings of IPAC’12*, New Orleans, Louisiana, USA (2012).
- [Ferrario00] M. Ferrario, et al., “HOMDYN Study for the LCLS RF Photoinjector”, SLAC-PUB-8400 (2000).
- [Ferrario10] M. Ferrario, et al., “Experimental Demonstration of Emittance Compensation with Velocity Bunching”, *Phys. Rev. Lett.* 104, 054801 (2010).
- [Ferrario13] M. Ferrario, et al., “SPARC_LAB present and future”, *Nucl. Instrum. Methods Phys. Res., Sect. B* 309, 183 (2013).
- [Floettmann01] K. Floettmann, et al., “Generation of Ultrashort Electron Bunches by Cancellation of Nonlinear Distortions in the Longitudinal Phase Space”, report TESLAFEL-2001-06, DESY Hamburg (2001).
- [Floettmann-website] K. Floettmann, ASTRA particle tracking code <http://tesla.desy.de/~meykopff/>.
- [Floettmann03] K. Floettmann, “Some basic features of the beam emittance”, *Phys. Rev. ST Accel. Beams* 6, 034202 (2003).

- [Floettmann17] K. Floettmann, “Emittance compensation in split photoinjectors”, *Phys. Rev. ST Accel. Beams* 20, 013401 (2017).
- [Fonseca03] C. M. Fonseca, et al., “PISA — a platform and programming language independent interface for search algorithms”, *Evolutionary Multi-Criterion Optimization (EMO 2003)*, Lecture Notes in Computer Science, pages 494 – 508, Berlin (2003).
- [Forck08] P. Forck, et al., “Beam position monitors”, *CERN accelerator school on beam diagnostics*, pp. 187—228 (2008).
- [Geddes04] C. G. R. Geddes, et al., “High-quality electron beams from a laser wakefield accelerator using plasma-channel guiding”, *Nature (London)* 431, 538 (2004).
- [Giannessi03] L. Giannessi, et al., “TREDI simulations for high-brilliance photoinjectors and magnetic chicanes”, *Phys. Rev. ST Accel. Beams* 6, 120101 (2003).
- [Gonsalves15] A. J. Gonsalves, et al., “Generation and pointing stabilization of multi-GeV electron beams from a laser plasma accelerator driven in a pre-formed plasma waveguide”, *Phys. Plasmas*, 22, 056703 (2015).
- [Gruener07] F. Gruener, et al., “Design Considerations for Table-Top, Laser-Based VUV and X-Ray Free Electron Lasers”, *Appl. Phys. B* 86, 431 (2007).
- [Ha16ppt] G. Ha, “Demonstration of current profile shaping using EEX beam line at Argonne Wakefield Accelerator”, ppt at the 7rd International Particle Accelerator Conference (2016).
- [Ha16] G. Ha, et al., “Perturbation-minimized triangular bunch for high-transformer ratio using a double dogleg emittance exchange beam line”, *Phys. Rev. Accel. Beams* 19, 121301 (2016).
- [Hachmann16] M. Hachmann, et al., “Measurement of ultra-low transverse emittance at REGAE”, *Nucl. Instrum. Methods Phys. Res., Sect. A* 829, 318–320 (2016).
- [Hacker10] K. Hacker, “Measuring the Electron Beam Energy in a Magnetic Bunch Compressor”, PhD thesis (2010).
- [Hada12] M. Hada et al., “REGAE, New Source for Atomically Resolved Dynamics”, *Int. Conf. Ultrafast Struc. Dyn.*, Berlin (2012).
- [Hall15] C. C. Hall, et al., “Measurement and simulation of the impact of coherent synchrotron radiation on the Jefferson Laboratory energy recovery linac electron beam”, *Phys. Rev. ST Accel. Beams* 18, 030706 (2015).
- [He15] A. He, et al., “Design of low energy bunch compressors with space charge effects”, *Phys. Rev. ST Accel. Beams* 18, 014201 (2015).
- [Huang04] Z. Huang, et al., “Suppression of microbunching instability in the linac coherent light source”, *Phys. Rev. ST Accel. Beams* 7, 074401 (2004).
- [Huang07] Z. Huang, et al., “Review of x-ray free-electron laser theory”, *Phys. Rev. ST Accel. Beams* 10, 034801 (2007).
- [Huang12] Z. Huang, et al., “Compact X-ray Free-Electron Laser from a Laser-Plasma Accelerator Using a Transverse-Gradient Undulator”, *Phys. Rev. Lett.* 109, 204801 (2012).
- [Huck15] H. Huck, et al., “First Results of Commissioning of the PITZ Transverse Deflecting”, MOP039, *Proceedings of FEL2015*, Daejeon, Korea (2015).
- [Huck16] H. Huck, et al., “Progress on the PITZ TDS”, WEPG47, *Proceedings of IBIC2016*, Barcelona, Spain (2016).
- [Huening03] M. Huening et al., “Measurement of the beam energy spread in the TTF photo-injector”, *Proceedings of the 2003 particle accelerator conference* (2003).

- [Humphries99] S. Humphries, Jr., “Principles of charged particle acceleration”, University of New Mexico (1999).
- [Inoue08] Y. Inoue, et al., “Development of a high-resolution cavity-beam position monitor”, *Phys. Rev. Accel. Beams* 11, 062801 (2008).
- [Ishikawa12] T. Ishikawa, et al., “A compact X-ray free-electron laser emitting in the sub-ångström region”, *Nat. Photonics* 6, 540 (2012).
- [Jackson75] J.D. Jackson, *Classical Electrodynamics*, Wiley, New York, 1975.
- [Jenson11] P.W. Jenson, R.E. Perez, “Constrained structural design optimization via a parallel augmented Lagrangian particle swarm optimization approach”, *Computers & Structures* 89, 1352 (2011).
- [Jing07] C. Jing, et al., “Observation of Enhanced Transformer Ratio in Collinear Wakefield Acceleration”, *Phys. Rev. Lett.* 98, 144801 (2007).
- [Kan10] K. Kan, et al., “Simulation study of sub-femtosecond electron bunch generation using photocathode RF gun linac”, *Nucl. Instrum. Methods Phys. Res., Sect. A* 622, 35 (2010).
- [Kaertner16] F. X. Kaertner, et al., “AXSIS: Exploring the frontiers in attosecond X-ray science, imaging and spectroscopy”, *Nucl. Instrum. Methods Phys. Res., Sect. A* 829, 233 (2016).
- [Kallos07] E. Kallos, al., “Plasma wakefield acceleration utilizing multiple electron bunches“, THPMS031, in *proceedings of PAC07* (2007).
- [Keil2015] B. Keil, et al., “Status of the SwissFEL BPM System”, TUPB065, *Proceedings of IBIC2015*, Melbourne, Australia (2015).
- [Kennedy95] J. Kennedy and R. C. Eberhart, “Particle swarm optimization”, *Proceedings of the 1995 IEEE International Conference on Neural Networks*, 4, 1942 (1995).
- [Kim03] K. J. Kim, “Round-to-flat transformation of angular-momentum-dominated beams”, *Phys. Rev. ST Accel. Beams* 6, 104002 (2003)
- [Koltenbah02] B. E. C. Koltenbah, et al., “PARMELA_B: A new version of PARMELA with coherent synchrotron radiation effects and a finite difference space charge routine”, *Nucl. Instrum. Methods Phys. Res., Sect. A* 487, 249 (2002).
- [Krasilnikov12] M. Krasilnikov, et al., “Experimentally minimized beam emittance from an L-band photoinjector”, *Phys. Rev. ST Accel. Beams* 15, 100701 (2012).
- [Kube10] G. Kube, et al., “Resolution Studies of Inorganic Scintillation Screens for High Energy and High Brilliance Electron Beams”, MOPD088, *Proceedings of IPAC'10*, Kyoto, Japan (2010).
- [LCLS02] Linac Coherent Light Source (LCLS) Conceptual Design Report, SLAC-R-593 (2002).
- [Lacivita10] D. Lacivita, et al., “FERMI@ELETTRA bunch compressor chicane mechanical design”, *Diamond Light Source Proceedings* 1, e19, MEDSI-6 (2010).
- [Larsen64] R. R. Larsen, et al., “Investigations of Traveling-Wave Separators for the Stanford Two-Mile Linear Accelerator”, *Rev. Sci. Instrum.* 35, 4 (1964).
- [Lechner14] C. Lechner, et al., “Measurements of the timing stability at the FLASH1 seeding experiment”, *Proceedings of FEL2014*, Basel, Switzerland THP076 (2014).
- [Lee14] H.G.Lee, et al., “Design and fabrication of bunch compressor support system for PAL XFEL”, *proceedings of IPAC14*, THPRI104, Dresden, Germany (2014).
- [Leemans06] Leemans, et al., “GeV electron beams from a centimetre-scale accelerator”, *Nature Physics* 2, 696 - 699 (2006).
- [Leemans14] Leemans, et al., “Multi-GeV Electron Beams from Capillary-Discharge-Guided Subpetawatt Laser Pulses in the Self-Trapping Regime”, *Phy. Rev. Lett.* 113, 245002 (2014).
- [LHC] <https://home.cern/topics/large-hadron-collider>

- [Liu17] T. Liu, et al., “Compact beam transport system for free-electron lasers driven by a laser plasma accelerator”, *Phys. Rev. Accel. Beams* 20, 020701 (2017).
- [Liuzzi10] G. Liuzzi, et al., “Sequential Penalty Derivative-free Methods for Nonlinear Constrained Optimization”. *SIAM J. Optim.* 20, 5, 2614 (2010).
- [Lim05] J. K. Lim, et al., “Adjustable, short focal length permanent-magnet quadrupole based electron beam final focus system”, *Phys. Rev. ST Accel. Beams* 8, 072401 (2005).
- [Litos14] M. Litos, et al., “High-efficiency acceleration of an electron beam in a plasma wakefield accelerator”, *Nature* (London) 515, 92 (2014).
- [Lu06] W. Lu, et al., “A nonlinear theory for multidimensional relativistic plasma wave wakefields”, *Phys. Plasmas* 13, 056709 (2006).
- [LUX] <http://lux.cfel.de/>
- [Malyutin14] Dmitriy Malyutin, “Time resolved transverse and longitudinal phase space measurements at the high brightness photo injector PITZ”, PhD thesis (2014).
- [Maier12] A. Maier, et al., “Demonstration Scheme for a Laser-Plasma-Driven Free-Electron Laser”, *Phys. Rev. X*, 2, 031019 (2012).
- [Maier15] A. Maier, “FEL applications”, presentation in Matter and Technologies Kickoff Meeting, DESY Hamburg (2015).
- [Maltezopoulos14] T. Maltezopoulos, et al., “A high-harmonic generation source for seeding a free-electron laser at 38 nm”, *Appl. Phys. B* 115, 45 (2014).
- [Mangles04] S. P. D. Mangles, et al., “Monoenergetic beams of relativistic electrons from intense laser-plasma interactions”, *Nature* (London) 431, 535 (2004).
- [Marchetti16-2] B. Marchetti, et al., “Technical design considerations about the SINBAD-ARES linac”, MOPMB015, *Proceedings of IPAC2016*, BUSAN, Korea (2016)
- [Marchetti16] B. Marchetti, et al., “Electron-beam manipulation techniques in the SINBAD Linac for external injection in plasma wake-field acceleration”, *Nucl. Instrum. Methods Phys. Res., Sect. A* 829, 278 (2016).
- [Marx17] D. Marx, et al., “Reconstruction of the 3D charge distribution of an electron bunch using a novel variable polarization transverse deflecting structure (TDS)”, *Proceedings of IPAC2017*, Copenhagen, Denmark (2017)
- [Mayet17] F. Mayet, et al., “Simulations and plans for a dielectric laser acceleration experiment at SINBAD”, *Proceedings of IPAC17*, Copenhagen, Denmark (2017).
- [McDonald89] K. T. McDonald, et al., “Methods of emittance measurement”, in *Frontiers of Particle Beams: Observation, Diagnosis, and Correction*, edited by M. Month and S. Turner (Springer, New York, 1989).
- [Mehrling14] T. Mehrling, “Theoretical and numerical studies on the transport of transverses e-beam quality in plasma-based”, PhD thesis (2014).
- [Migliorati13] M. Migliorati, et al., “Intrinsic normalized emittance growth in laser-driven electron accelerators”, *Phys. Rev. ST Accel. Beams* 16, 011302 (2013).
- [Milas10] N. Milas et al., “Design of the SwissFEL Switchyard”, *Proceedings of FEL2010*, Malmoe, Sweden (2010).
- [Minty03] M. G. Minty and F. Zimmermann, “Beam Techniques - Beam Control and Manipulation”, SLAC-R-621, 2003.
- [Mitchell13] C. E. Mitchell, J. Qiang, R. D. Ryne, *Nucl. Instrum. Methods Phys. Res., Sect. A* 715, 119 (2013).

- [Moore14] T. Moore, et al., “Fast wire scanner for intense electron beams”, *Phys. Rev. Accel. Beams* ST 17, 022801 (2014).
- [Murokh00] A. Murokh, et al., Limitations on the resolution of YAG:CE beam profile monitor for high brightness electron beam, *2nd ICFA Advanced Accelerator Workshop on the Physics of High Brightness Beams* (2000).
- [Nanni15] E. Nanni, et al., “Terahertz-driven linear electron acceleration”, *Nat. Comm.* 6, 8486 (2015).
- [Nelson85] W. R. Nelson, et al., “The EGS4 Code System”, SLAC-265 (1985).
- [Pellegrini16] C. Pellegrini, et al., “The physics of x-ray free-electron”, *Rev. Mod. Phys.* 88, 015006 (2016).
- [Peralta13] E. A. Peralta, et al., “Demonstration of electron acceleration in a laser-driven dielectric microstructure”, *Nature* 503, 91 (2013).
- [Pompili16] R. Pompili, et al., “Beam manipulation with velocity bunching for PWFA applications”, *Nucl. Instrum. Methods Phys. Res., Sect. A* 829, 17 (2016).
- [Prokop13] C. Prokop, et al., “Beam dynamics performances and applications of a low-energy electron-beam magnetic bunch compressor”, *Nucl. Instrum. Methods Phys. Res., Sect. A* 719, 17 (2013).
- [pyopt-website] <http://www.pyopt.org/>
- [Qiang06] J. Qiang, et al., “Three-dimensional quasistatic model for high brightness beam dynamics simulation”, *Phys. Rev. ST Accel. Beams* 9, 044204 (2006).
- [Qiang12] J. Qiang, et al., “A fast high-order method to calculate wakefields in an electron beam”, *Nucl. Instrum. Methods Phys. Res., Sect. A* 682, 49 (2012).
- [Qiang-website] <http://amac.lbl.gov/~jqiang/impact/>.
- [Rao12] T. Rao, et al., “An engineering guide to photoinjectors” (2012).
- [Raguin12] J. Y. Raguin, “The Swiss FEL S-Band and Accelerating Structure: RF Design”, TUPB011, *Proceedings of LINAC12*, Tel-Aviv, Israel (2012).
- [Raubenheimer00] T. O. Raubenheimer et al., “Final-focus systems in linear colliders”, *Rev. Mod. Phys.* 72, 95 (2000).
- [Reiser08] M. Reiser, “Theory and Design of Charged Particle Beams”, 2nd edition (2008).
- [Rimjaem11] S. Rimjaem, et al., “Comparison of different radiators used to measure the transverse characteristics of low energy electron beams at PITZ”, TUPD54, *Proceedings of DIPAC2011*, Hamburg, Germany (2011).
- [Ruan11] J. Ruan, et al., “First Observation of the Exchange of Transverse and Longitudinal Emittances”, *Phys. Rev. Lett.* 106, 244801 (2011).
- [Ryne12] R. D. Ryne et al., “Large scale simulation of synchrotron radiation using a Lienard-Wiechert approach”, in *Proceedings of the 3rd International Particle Accelerator Conference*, New Orleans, LA, 2012 (IEEE, Piscataway, NJ, 2012).
- [Ryne13] R. D. Ryne, et al., “Using a Lienard-Wiechert solver to study coherent synchrotron radiation effects”, *Proceedings of FEL2013* (JACoW, New York, NY, 2013).
- [Saldin97] E. L. Saldin, et al., “On the coherent radiation of an electron bunch moving in an arc of a circle”, *Nucl. Instrum. Methods Phys. Res., Sect. A* 398, 373 (1997).
- [Sands91] M. Sands, “A Beta Mismatch Parameter”, SLAC-AP-85 (1991).
- [Saint-gobain] http://www.crystals.saint-gobain.com/sites/imdf.crystals.com/files/documents/yag-material-data-sheet_69775.pdf
- [Schietinger16] T. Schietinger, et al., “Commissioning experience and beam physics measurements at the SwissFEL Injector Test Facility”, *Phys. Rev. Accel. Beams* 19, 100702 (2016).

- [Sedlaczek06] Kai Sedlaczek, “Using augmented Lagrangian particle swarm optimization for constrained problems in engineering”, *Struct. Multidisc. Optim.* 32, 277 (2006).
- [Serafini97] Luca Serafini, et al., “Envelope analysis of intense relativistic quasilaminar beams in rf photoinjectors: A theory of emittance compensation”, *Phys. Rev. E* 55, 7565(1997).
- [Serafini01] L. Serafini, et al., “Velocity bunching in photo-injectors”, in: *American Institute of Physics Conference Series*, 581, 87–106 (2001).
- [Sharma09] A. Sharma, et al., “Optics design and second order longitudinal dispersion minimization in a bunch compressor transfer line for CTF3”, *Nucl. Instrum. Methods Phys. Res., Sect. A* 602, 342 (2009).
- [Smith09] S. Smith, et al., “Commissioning and Performance of LCLS Cavity”, TU3GRC05, *Proceedings of PAC09*, Vancouver, BC, Canada (2009).
- [Sun11] Y. Sun et al., Emittance growth in the NLCTA first chicane, SLAC-PUB-14323 (2011).
- [Tajima79] T. Tajima, J.M. Dawson, “Laser Electron Accelerator”, *Phy. Rev. Lett.* 43, 267 (1979).
- [Tenenbaum99] P. Tenenbaum, et al., “Measurement of Small Electron Beam Spots”, *Annu. Rev. Nucl. Part. Sci.* 49, 125 (1999).
- [Tenenbaum07] P. Tenenbaum, et al., “Direct measurement of the transverse wakefields of tapered collimators”, *Phys. Rev. ST Accel. Beams* 10, 034401 (2007).
- [Tilborg17] J. van Tilborg, et al., “Free-electron lasers driven by laser plasma accelerators”, *AIP Conference Proceedings* 1812, 020002 (2017).
- [Titberidze15] M. Titberidze, et al., “Present and future optical-to-microwave synchronization systems at REGAE facility for electron diffraction and plasma acceleration experiments”, MOPHA026, *Proceedings of IPAC2015*, Richmond, VA, USA (2015).
- [TraFiC4] <http://www-mpy.desy.de/trafic4/TraFiC4/>.
- [Treyer13] D. M. Treyer, et al., “Design and Beam Test Results of Button BPMs for the European XFEL”, WEPC21, *Proceedings of IBIC2013*, Oxford, UK (2013).
- [Veronese06] M. Veronese, et al., “The diagnostics of the FERMI@ELETTRA bunch compressors”, *Proceedings of FEL 2006*, THPPH029, BESSY, Berlin, Germany (2006).
- [Villa16] F. Villa, et al., “Laser pulse shaping for high gradient accelerators”, *Nucl. Instrum. Methods Phys. Res., Sect. A* 829, 446 (2016).
- [Vogt13] M. Vogt, et al., “The free-electron laser FLASH at DESY”, *Proceedings of IPAC2013*, Shanghai, China (2013).
- [Wang07] C. Wang, “Criteria for emittance compensation in high-brightness photoinjectors”, *Phys. Rev. ST Accel. Beams* 10, 104201 (2007).
- [Wangler08] T. P. Wangler, “RF Linear Accelerator”, 2nd completely revised and enlarged edition (2008).
- [Weikum17] M. K. Weikum, et al., “Improved Electron Beam Quality from External Injection in Laser-driven Plasma Acceleration at SINBAD”, *Proceedings of IPAC2017*, Copenhagen, Denmark (2017).
- [Welch07] J. Welch, et al., “Report on Modifications to the BX12 and BX13 BC1 Dipoles”, LCLS-TN-07-12 (2007).
- [Wiebers13] C. Wiebers, et al., “Scintillating Screen Monitors for Transverse Electron Beam Profile Diagnostics at the European XFEL”, *Proceedings of IBIC2013*, Oxford, UK (2013).
- [Wiedemann] H. Wiedemann, “Particle Accelerator Physics: Basic Principles and Linear Beam Dynamics”, Springer-Verlag, New York (1993).
- [Xie00] M. Xie, “Exact and variational solutions of 3D eigenmodes in high gain FELs”, *Nucl. Instrum. Methods Phys. Res., Sect. A* 445, 59 (2000).

- [Zeitler17] B. M. G. Zeitler, “Phase Space Linearization and External Injection of Electron Bunches into Laser-Driven Plasma Wakefields at REGAE”, PhD thesis (2017).
- [Zholents07] A. Zholents, et al., “Spreader Design for FERMI@Elettra Free Electron Laser”, LBNL-62345 (2007).
- [Zholents11] A. A. Zholents, et al., “A New Type of Bunch Compressor and Seeding of a Short Wave Length Coherent Radiation”, Report No. ANL/APS/LS-327 (2011).
- [Zhou15] F. Zhou, et al., “Measurements and analysis of a high-brightness electron beam collimated in a magnetic bunch compressor”, *Phys. Rev. ST Accel. Beams* 18, 050702 (2015).
- [Zhou16] F. Zhou, private communication.
- [Zhu14] J. Zhu, et al., “Formation of compressed flat electron beams with high transverse emittance ratios”, *Phys. Rev. ST Accel. Beams* 17, 084401 (2014).
- [Zhu15-1] J. Zhu, et al., “Sub-fs electron bunch generation using magnetic compressor at SINBAD”, MOPWA042, *Proceedings of IPAC2015*, Richmond, VA, USA (2015).
- [Zhu15-2] J. Zhu, et al., “Timing jitter studies for sub-fs electron bunch generation at SINBAD”, WEPMA031, *Proceedings of IPAC2015*, Richmond, VA, USA (2015).
- [Zhu16] J. Zhu, et al., “Matching sub-fs electron bunches for laser-driven plasma acceleration at SINBAD”, *Nucl. Instrum. Methods Phys. Res., Sect. A* 829, 229 (2016).

Acknowledgements

My sincere acknowledgements go to:

Dr. Barbara Marchetti at DESY

Dr. Ralph W. Assmann at DESY

Dr. Enrica Chiadroni at SPARC LAB

Dr. Martin Dohlus at DESY

Dr. Ulrich Dorda at DESY

Dr. Massimo Ferrario at SPARC LAB

Prof. Dr. Florian Grüner at the University of Hamburg

Dr. Elvin Harms at Fermi National Accelerator Laboratory

Frank Mayet at DESY

Dr. Riccardo Pompili at SPARC LAB

Ángel Ferran Pousa at DESY

Prof. Philippe Piot at Northern Illinois University

Maria Weikum at the University of Strathclyde and DESY

and my family.

List of publications

Journal papers

- [1] **J. Zhu**, E. Chiadroni, R. Assmann, M. Bellaveglia, A. Cianchi, M. Ferrario, A. Giribono, B. Marchetti, A. Mostacci, L. Piersanti, R. Pompili, and F. Villa, “Misalignment Measurement of Femtosecond Electron Bunches with THz Repetition Rate”, *Phys. Rev. Accel. Beams* 20, 042801 (2017).

[10.1103/PhysRevAccelBeams.20.042801](https://doi.org/10.1103/PhysRevAccelBeams.20.042801)

- [2] **J. Zhu**, R. Assmann, M. Dohlus, U. Dorda, B. Marchetti, “Sub-fs Electron Bunch Generation with sub-10-fs Bunch Arrival-time Jitter via Bunch Slicing in a Magnetic Chicane”, *Phys. Rev. Accel. Beams* 19, 054401 (2016).

[10.1103/PhysRevAccelBeams.19.054401](https://doi.org/10.1103/PhysRevAccelBeams.19.054401)

- [3] **J. Zhu**, R. Assmann, U. Dorda, B. Marchetti, "Matching sub-fs electron bunches for laser-driven plasma acceleration at SINBAD", *Nucl. Instrum. Methods Phys. Res., Sect. A* 829, 229 (2016).

<https://doi.org/10.1016/j.nima.2016.01.066>

- [4] B. Marchetti, R. Assmann, C. Behrens, R. Brinkmann, U. Dorda, K. Floettmann, I. Hartl, M. Huening, Y. Nie, H. Schlarb, **J. Zhu**, “Electron-beam manipulation techniques in the SINBAD Linac for external injection in plasma wake-field acceleration”, *Nucl. Instrum. Methods Phys. Res., Sect. A*, 829, 278 (2016).

<https://doi.org/10.1016/j.nima.2016.03.041>

- [5] U. Dorda, R. Assmann, R. Brinkmann, K. Flöttmann, I. Hartl, M. Hüning, F. Kärtner, A. Fallahi, B. Marchetti, Y. Nie, J. Osterhoff, H. Schlarb, **J. Zhu**, A. R. Maier, “SINBAD — The accelerator R&D facility under construction at DESY”, *Nucl. Instrum. Methods Phys. Res., Sect. A*, 829, 233 (2016).

<https://doi.org/10.1016/j.nima.2016.01.067>

- [6] R. Pompili, M. P. Anania, M. Bellaveglia, A. Biagioni, F. Bisesto, E. Chiadroni, A. Cianchi, M. Croia, A. Curcio, D. DiGiovenale, M. Ferrario, F. Filippi, M. Galletti, A. Gallo, A. Giribono, W. Li, A. Marocchino, A. Mostacci, M. Petrarca, V. Petrillo, G. DiPirro, S. Romeo, A. R. Rossi, J. Scifo, V. Shpakov, C. Vaccarezza, F. Villa, **J. Zhu**, “Beam manipulation with velocity bunching for PWFA applications”, *Nucl. Instrum. Methods Phys. Res., Sect. A* 829, 17 (2016).

<https://doi.org/10.1016/j.nima.2016.01.061>

- [7] Y. C. Ni, R. Assmann, U. Dorda, B. Marchetti, M. Weikum, **J. Zhu**, M. Hüning, “Potential applications of the dielectric wake field accelerators in the SINBAD facility at DESY”, *Nucl. Instrum. Methods Phys. Res., Sect. A* 829, 183 (2016).

<https://doi.org/10.1016/j.nima.2016.01.038>

Conference papers

- [1] J. Zhu, R. Assmann, U. Dorda, B. Marchetti, “Matching space-charge dominated electron bunches into the plasma accelerator at SINBAD”, THPVA007, *Proceedings of IPAC2017*, Copenhagen, Denmark (2017).
- [2] J. Zhu, R. Assmann, U. Dorda, B. Marchetti, R. Rossmanith, “Dogleg design for the SINBAD linac”, THPMB010, *Proceedings of IPAC2016*, Busan, Korea (2016).
- [3] J. Zhu, R. Assmann, U. Dorda, J. Grebenyuk, B. Marchetti, “Timing jitter studies for sub-fs electron bunch generation at SINBAD”, WEPMA031, *Proceedings of IPAC2015*, Richmond, VA, USA (2015).
- [4] J. Zhu, R. Assmann, U. Dorda, J. Grebenyuk, B. Marchetti, “Sub-fs electron bunch generation using magnetic compressor at SINBAD”, MOPWA042, *Proceedings of IPAC2015*, Richmond, VA, USA (2015).

Declaration

Eidesstattliche Versicherung

Hiermit erkläre ich an Eides statt, dass ich die vorliegende Dissertationsschrift selbst verfasst und keine anderen als die angegebenen Quellen und Hilfsmittel benutzt habe.

Jun Zhu

Hamburg, December 23, 2017